A Tensor Calculus Formulation of the Lumley Decomposition applied to the Turbulent Axi-symmetric Jet Far-eld

Hodzic, Azur

Publication date:
2018

Document Version
Publisher's PDF, also known as Version of record

Ph.D. Thesis
Submitted 26th of November 2018
Defended 24th of January 2019

DTU Mechanical Engineering
Department of Mechanical Engineering

A Tensor Calculus Formulation of the Lumley Decomposition applied to the Turbulent Axi-symmetric Jet Far-field

Azur Hodžić

Kgs. Lyngby, Denmark 2019

DTU MEK
Department of Mechanical Engineering
Technical University of Denmark

Nils Koppels Allé
Building 404
2800 Kongens Lyngby, Denmark
Phone +45 45 25 19 60
Fax +45 45 25 19 61
mek@mek.dtu.dk
www.mek.dtu.dk

Preface

This Ph.D. thesis was prepared at the department of Mechanical Engineering at the Technical University of Denmark in partial fulfillment of the requirements for acquiring a Ph.D. degree in Mechanical Engineering.

Kgs. Lyngby, Denmark, January 25th, 2019

Azur Hodžić

Abstract

The current work studies the far-field of the turbulent round jet at a Reynolds number of 20 000. A formalism based on tensor calculus is introduced for the study of flows for which equilibrium similarity holds, motivated by the complexity of the coordinate system that the far-field region is represented in. The tensor-based approach ensures that the invariance of the field is preserved and allows for a formulation of the Lumley Decomposition (LD) in tensor form, which is valid in any well-defined coordinate system. This expression of the LD reveals that the inner product space must be equipped with a specific weight function in order to conclude that the modes in the streamwise direction are Fourier modes. It is furthermore shown that the use of the so-called similarity coordinates introduced by Ewing et al. 2007 fails to yield a Hermitian form of the LD matrix operator due to the non-orthogonality of this coordinate system. The orthogonal stretched spherical coordinates (SSC) are therefore proposed as an alternative, since they ensure the Hermitian property of the LD operator and allow the LD to be performed on the turbulent jet with a amplitude decaying stretched Fourier decomposition along the streamwise coordinate.

The energy equation is spanned by the LD eigenfunctions coupling the eigenfunctions to the various energy transport mechanisms for a solenoidal fluid in curvilinear coordinates. This allows for a reconstruction of the energy production term leading to energy production and transport analysis. The reconstructions of the component energy spectra in the $-5/3$-range reveal the varying spectral fluxes for each individual modal component across the jet. This indicates the presence of a more complex underlying energy transfer mechanism across modes than what is usually assumed by the Richardson cascade. The reconstruction of the energy production is then performed in order to quantify the hypothesis stated in Wänström 2009 that multiple modes have the ability to obtain energy directly from the mean flow. It is demonstrated that every mode must participate in the energy production in some way, for flows where the LD operator is self-adjoint. Furthermore, each mode's production of energy is shown to vary over wave and mode number across the span of the flow. In particular, it is demonstrated that the relative energy production of modes is substantial even in the $-5/3$-range. This means that modes in this region obtain a substantial part of their energy directly from the mean flow.

Resumé

Nærværende afhandling rapporterer studier af fjernfeltet af den turbulente runde jet-strømning ved et Reynolds-tal svarende til 20 000. En formalisme baserede på tensor analyse er introduceret der kan anvendes på strømninger for hvilke den såkaldte ligevægtssimilaritetsteori er gældende, motiveret af det komplekse koordinatsystem som fjernfeltet er repræsenteret i. Den tensor-baserede tilgang sikrer at invariansen af feltet bibevares og tillader en formulering af Lumley Dekompositionen (LD) i tensorform, som er valid i ethvert veldefineret koordinatsystem. Dette udtryk af LD afslører at det pågældende indre produktrum skal udstyres med en specifik vægtfunktion for at tillade konklusionen at blive draget at basisfunktionerne i strømningsretning er Fourier basisfunktioner. Det er derudover vist at brugen af såkaldte similaritetskoordinater introduceret i Ewing et al. 2007 ikke producerer en Hermitisk form af LD matrixoperatoren, grundet koordinaternes ikke-ortogonalitet. De ortogonale strukkede sferiske koordinater (SSC) er derfor foreslået som et alternativ, da disse sikrer den Hermitiske egenskab af LD operatoren og tillader LD at blive anvendt på den turbulente jet med en amplitudeaftagende og strukket Fourier dekomposition langs koordinaten i strømningsretningen.

Energiligningen er udspændt af LD egenfunktionerne, hvilket kobler disse til de forskellige energitransportmekanismer for en divergensfri fluid i bueliniede koordinater. Dette tillader en rekonstruktion af energiproduktionsleddet, hvilket fører til analysen af energiproduktionen og energitransporten. Rekonstruktionen af energispektraerne i $-5/3$-båndet afslører de varierende spektrale flukser for hver modal komponent på tværs af jet-strømningen. Dette indikerer at der eksisterer en mere kompleks energioverførsel over bølgetal end hvad der ellers antages i Richardsonkaskaden. Rekonstruktionen af energiproduktionen er derefter udført for at kvantificere hypotesen formuleret i Wänström 2009, at flere egenfunktioner har evnen til at opnå energi direkte fra det midlede felt. Det er demonstreret at alle egenfunktioner deltager i energiproduktionen, for strømninger, hvor LD operatoren er selvadjungeret. Derudover er det vist at enhver egenfunktion's energiproduktion varierer over bølgetal og egenfunktionsnummer på tværs af strømningen. Det er demonstreret at den relative energiproduktion af egenfunktionerne er betydelig selv i $-5/3$-båndet. Dette betyder at egenfunktionerne i denne region opnår en betydelig del af deres energi direkte fra det midlede felt.

Nomenclature

Abbreviations

l	Wavelength as a function of mode number and η.
ENP	Eigenvalue normalized production.
EST	Equilibrium similarity theory
LD	Lumley Decomposition
LES	Large eddy simulation
NSE	Navier-Stokes equations
pdf	Probability density function
POD	Proper Orthogonal Decomposition
RANS	Reynolds Averaged Navier-Stokes
SAPD	Self-adjoint positive definite operator
SSC	Stretched spherical coordinates
TKE	Turbulence kinetic energy

Symbols - Greek

δ	Jet half-width
δ^i_j	Kroenecker delta
Γ^k_{ij}	Christoffel-symbol of the second kind
∇^i	Contravariant derivative
∇_i	Covariant derivative
τ^{ij}	Contravariant stress tensor
ξ, η, θ	Similarity coordinates

Symbols - Roman

$\mathcal{P}$	Turbulence kinetic energy production term.

$\mathcal{P}^{11}$	Turbulence kinetic energy production related to $\left\langle v^{\xi} v^{\xi} \right\rangle$.
$\mathcal{P}^{12}$	Turbulence kinetic energy production related to $\left\langle v^{\xi} v^{\eta} \right\rangle$.
$\mathcal{P}^{22}$	Turbulence kinetic energy production related to $\langle v^{\eta} v^{\eta} \rangle$.
$\overline{e}_i$	Unit basis vectors
$\overline{V}$	Velocity vector
$\overline{z}^i$	Contravariant basis vector
$\overline{z}_i$	Covariant basis vector
$J^i_{i'}$	Jacobian operator
s^{ij}	Contravariant strain tensor
$V[i]$	Physical velocity components in similarity coordinates
$V^{\xi}, V^{\eta}, V^{\theta}$	Contravariant velocity components in similarity coordinates
V^i	Contravariant velocity component
v_i	Covariant velocity component
x, y, z	Cartesian coordinates
z^i	Curvilinear coordinates
z^{ij}	Contravariant metric tensor
z_{ij}	Covariant metric tensor

Acknowledgments

Firstly, I would like to thank my supervisor Associate Professor Clara Marika Velte at DTU, for reaching out to me at the end of my Bachelor studies and inspiring me to strive for a PhD-degree in turbulence. Thank you for the endless support provided and the freedom you have given me to find my own way in this highly untamed research field.

I would like to thank Professor William Kenneth George, who throughout his career has been a pioneer in turbulence research and has propelled the field into the 21st century. Always generous with his ideas, Bill has inspired countless researchers around the world. He is the gold standard that we measure ourselves against and it has been my great honor to work with him. Thank you for the countless inspiring discussions we have had over the course of this project.

I would like to thank Professor Berend Van Wachem, at the University of Magdeburg, for graciously accepting me into his research group - from November 2015 to April 2016 as a visiting PhD-student - which at the time was situated at Imperial College London. I would like to thank all the guys from the Multiflow Lab, but especially Dr. Paul Bartholomew, Dr. Fabien Evrard, Dr. Thomas Curran, and Assistant Professor Fabian Denner for all of their support regarding the application of their numerical flow solver *Multiflow*.

I would like to thank my co-supervisor, Associate Professor Knud Erik Meyer for sparking my interest for fluid mechanics in my early studies at DTU, and for his support in the early stages of this project.

A special thanks goes to my fellow students Nikolas Karvounis, Henrik Juul Spietz, and Seyed Saeed Asadzadeh in the Fluid Mechanics group at DTU MEK, for striving to make each other laugh every day.

A heartfelt thanks goes to my family for always supporting me in my endeavors. Finally, I would like to thank my wife, Anela, for your endless support and for all the great experiences we have shared together.

Contents

CHAPTER 1

Introduction

'Turbulence' is the term used to describe the chaotic state of a fluid. The state occurs when the kinetic forces are significantly larger than the viscous forces. In this situation a small perturbation of the velocity field initiates a chain reaction that disrupts the parallel, laminar flow and breaks it up into a wide variety of turbulent structures. Most of the flows surrounding us are turbulent, since the transition to turbulence occurs at relatively low Reynolds numbers. Turbulent flows engulf the cars on the roads, airplane and wind turbine wings, ships and most other objects moving at a relative velocity to the fluid which they are in contact with. Internal combustion engines rely on turbulent processes to facilitate a proper mixing of the fuel and air composition in order to optimize the efficiency of the engine. A variety of mixing processes occur in the food and chemical industry require optimizations in order to increase mixing relative to the energy input that is required. The efficiency of wind farms relies on optimizing blade designs using numerical solvers that often apply turbulence models for the simulation of the flow.

Turbulence occurs in a wide variety of natural processes, involving a wide range of turbulent scales. Turbulent plumes are produced by active vulcanos, and turbulence is responsible for the redistribution of heat in the atmosphere impacting the weather on the planet.

Figure 1.1: A picture of Jupiter's northern hemisphere, named *Jupiter Blues*, taken from the spacecraft Juno at 10:24 (PDT) on October 24th, 2017.

Turbulence is also found in extraterrestrial regions of space, such as the sun's atmosphere and on the gas giant, Jupiter. A picture of turbulent structures on the northern hemisphere of Jupiter are seen in Figure 1.1, captured at 10:24 (PDT) on October 24th, 2017. These are but a few examples of turbulent flows illustrating that the turbulence problem is one of great importance, not least due to its presence in the vast range of dynamical systems it manifests itself in. We hope to some day control at least some parts of the turbulent flow, perhaps by changing the coherent structures within it. In order to make better and more efficient turbulence models, we are faced with the task of first understanding the turbulence to a higher degree. The subject, however, suffers from the fundamental deficiency of lacking a precise definition of what a *turbulent structure* is. This inevitably forces a great deal of ambiguity onto the field, often demanding experience and intuition on behalf of the investigator in order to address the issues at hand.

Over the last few centuries, fluid mechanics has played a significant role in developing the field of mathematics. The complexity of the physics of fluids required more advanced methods for characterization and analysis of fields. In the first half of the 20th century well known figures in science, such as Schrödinger and Heisenberg were addressing the turbulence problem. After the attempts of Andrey Kolmogorov to describe the smallst turbulence scales, the problem began to look somewhat intractable and the subject became viewed by some as *an unwise field for physicists to enter*. This, however, is something the author strongly disagrees with. If, we are to make significant contributions to the subject of turbulence, developing objective mathematical methods for the analysis of fields must be an important part of the solution. The subject demands advanced mathematical tools in order to harness it and to address the fundamental questions that lie ahead of us.

There are those that regard the field of turbulence as a somewhat philosophical one due to its inherent ambiguities. This ambiguity is, however, rooted in our naive perceptions of turbulent coherent structures and the vague definitions of these. Inspiration for tackling this issue may be found in an other well-known field of science, namely quantum mechanics. The ambiguity of quantum mechanics is rooted in the fact that solutions to the Schrödinger equation are the so-called wave functions, which are intimately related to probability density functions (pdf's) describing a quantum particle's location or velocity. This means that the solution to the governing equation of quantum mechanics is not the location- and velocity of a particle, but functions related to a pdf describing the *likelihood* of the location and velocity as a function of space and time.

In the current work turbulence is analyzed in the far-field of the turbulent axi-symmetric jet by expanding it by an energy-optimized orthog-

onal basis. The method was introduced to the turbulence community by John L. Lumley and is generally referred to under the somewhat incorrect rubric of the Proper Orthogonal Decomposition (POD), Lumley 1967b. In this work we will refer to a more general method, namely the *Lumley Decomposition* (LD), George 2017. Since Lumley did not refer to any specific weight function in Lumley 1967b in relation to the inner-product that defined the POD, it is naturally assumed that the weight function in the definition of the inner product is unity. For this type of weight function, the well-definedness criteria of the inner-product relies on the asymptotic decay of the eigenfunctions as the boundaries of the flow tend towards infinity. Note that this is formulated in a slightly different way by George 2017, but essentially the criteria for the LD to reduce to the POD is that the eigenfunctions converge towards zero as the domain of integration tends towards infinity for a constant weight function in the inner-product definition. As noted in George 2017, this means e.g. that the LD reduces to the POD in flows where the fluid domain is finite.

The LD is a linear dimensionality reduction method that is based on the maximization of parallelism between vectors in Hilbert spaces and the method yields an optimized orthogonal basis in L^2 vector spaces. It represents an objective way of decomposing the turbulent field into modes from a given data set, and yields a statistical representation of the dynamics that characterize the flow. The modes consist of a pair; eigenfunctions and eigenvalues. The eigenfunctions are somewhat analogous to the wave equation of quantum mechanics, in that the eigenfunctions of the POD are closely related to pdf's as well. Inspired from the abstractness of quantum mechanics, the solution to the turbulence problem in general, may appear in the form of POD modes, describing the dynamics of the flow statistically. Following their lead we refrain ourselves from the imprecise notion of *coherent structures* whenever possible, by instead referring to eigenfunctions or POD modes of a given flow.

1.1 Past Studies of Turbulent Jets

Due to its symmetry and absence of solid boundaries, the turbulent round jet is in many ways an ideal flow for studying turbulence. Turbulent jets have been studied for almost half a century. The first detailed turbulence measurements (using hot-wires) in jet mixing layers were initially investigated by Corrsin and Kistler 1955 and Townsend 1956. They reported an intermittency surface dividing the turbulent/non-turbulent interface at the periphery of the jet (see Figure 1.2). Wygnanski and Fiedler 1969 explored the similarity region of the jet measuring first- and second order moments. Subsequent experiment using flying hot-wire to

reduce cross-flow errors by Panchapakesan and Lumley 1993a and Hussein, Capp, and George 1994 gave very different results, in large part because of the size of the enclosure relative to the jet. Hussein, Capp, and George 1994 performed extensive measurements and analysis of the jet flow, in particular, and demonstrated the impact of back-flow for confined jets, and its impact on statistics and self-similarity. The latter also demonstrated the non-isotropy of the velocity derivatives and dissipation.

The appendix of George 2017 provides an extensive review of the application of POD since 1967, so we provide only a brief summary here. Past investigations conducted in the vicinity of the potential core (figure 1.2) utilizing the POD were conducted by Leib, Glauser, and George 1984, Glauser, Leib, and George 1987, Citriniti and George 2000, Gamard et al. 2002. The measurements were performed with hot-wire rakes allowing a spatio-temporal decomposition of the flow field cross-plane. The decomposition was applied in order to identify turbulent structures and their relation to noise issues. These works demonstrated conclusively that energy was concentrated in a small number of modes. The results of Citriniti and George 2000 identified vortex rings participating in rapid ejection events, confirming the conjecture of Glauser, Leib, and George 1987. Furthermore, the reconstructed fields indicated the presence of stream-wise vortex filaments in relation to the ejection events. Jung, Gamard, and George 2004 expanded these studies to cover the $2-6\,\mathrm{D}$ range from the nozzle, for three different Reynolds numbers, and identified the evolution of the dynamics of the flow.

The intermediate and far-field cross-planes (the *developing* and *fully developed* regions in figure 1.2) were investigated by Gamard, Jung, and George 2004, and sampled with a hot-wire rake. The POD modes projected self-similar behavior in the far-field but showed similar trends to those obtained as close as 6 diameters from the nozzle. Iqbal and Thomas 2007 investigated the streamwise evolution of the energy concentration of azimuthal mode numbers in the near field, and extended the studies to include all components of velocity. The primary reported difference was that the energy peaked in azimuthal mode 1, as opposed to azimuthal mode 2 when the streamwise component alone was considered. Wänström 2009 and Wänström, George, and Meyer 2006 obtained similar results using stereo PIV in crossplane measurements in the same jet employed in the present thesis.

Wänström 2009 took advantage of the self-similar nature of the far-field turbulence in order to perform a Fourier deocomposition of the flow in the streamwise and azimuthal. Her work (see also Wänström, George, and Meyer 2006, Wanstrom et al. 2007, Wänström, George, and Meyer 2012) revealed that, when scaled by the centerline velocity and interpolated onto the similarity coordinate system, the resulting flow field

becomes homogeneous. This confirmed the results of Ewing et al. 2007 who showed that the correlation function of the scaled velocities is independent of the streamwise similarity coordinate. As originally suggested in the work of Ewing 1995, Wänström 2009 concluded that the modes in the streamwise direction of the scaled field were Fourier modes. The main contribution of the work of Wänström 2009 was in the decomposition of the turbulent flow field in the streamwise and cross-plane direction. Wänström 2009 further hypothesized that multiple modes could tap into the energy extraction process from the mean flow, directly.

Most recently the studies of Towne, Schmidt, and Colonius 2018 and Schmidt et al. 2018 performed space-time decompositions of the turbulent jet from LES data in order to demonstrate the effects of missing dimensions of the decompositions as well as to characterize the modal decomposition of the flow in the near- and intermediate region.

1.2 The Turbulent Axi-symmetric Jet

The jet is often characterized in terms of the three regions: *the near-field*, *the developing region*, and *the fully developed region*. The near-field region is characterized by the presence of a potential core, surrounded by a mixing layer. Assuming a top-hat velocity profile at the nozzle lip, the velocity profile within the potential core closely resembles a top-hat profile. The developing region, begins after the potential core ends and the flow is here in an intermediate state before entering the fully developed, self-similar region. Self-similarity entails that the moments of velocity collapse along certain coordinate lines, when the velocity field is normalized with a local characteristic velocity. This implies that a particular choice of coordinate system can simplify the problem at hand. This characteristic of the flow is an asymptotic state that jets and very few other flows can attain, George 1989. For the turbulent axi-symmetric jet the coordinate system is defined in terms of the jet half-width (Figure 1.2). The jet half-width defines the local distance from the centerline where the velocity is 50% of the local centerline velocity. Self-similarity indicates that the flow is in an asymptotic state, since all significant processes such as the energy production and energy dissipation scale linearly with the distance from the nozzle. This implies, that the velocity far-field can be scaled with the local centerline velocity, such that the data collapse in the similarity coordinate system. This property is at the core of equilibrium similarity theory, and is what the current work relies heavily upon.

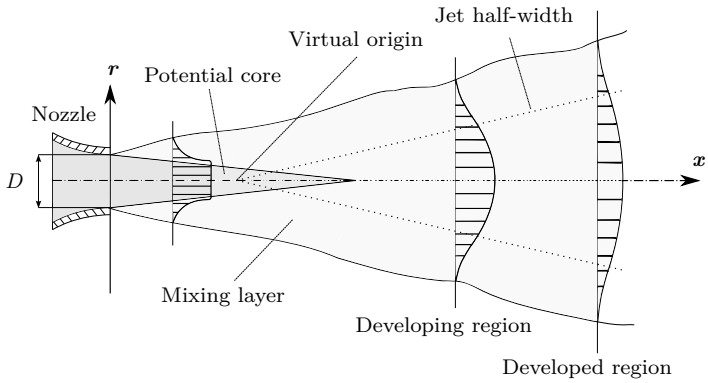

Figure 1.2: Sketch of the turbulent round jet. The virtual origin is denoted by x_0 and the jet half-width is defined as $\delta = A\,(x - x_0)$, where A is the jet spreading rate.

It was the initial aim of the work to perform a decomposition of DNS data of the jet far-field $x/D = 30 : 100$. Simulations were performed but due to low convection velocities in the far-field region the DNS required a large computational effort in order to obtain converged statistics in the domain. The intended decomposition was therefore not implemented for the simulated field, and the current thesis only includes the experimental work performed. The DNS, which for practical purposes consists of records of shorter flow development, will in the future be used in combination with experiments.

1.3 The Contributions of the Current Work

The current work introduces a new formalism for decomposing the self-self similar velocity field. This is achieved through the use of tensor calculus in order to obtain a mathematical formulation of the Lumley Decomposition (LD) integral in tensor form valid in any well-defined curvilinear coordinate system. Multiple new insights in this work are a direct result of the use of tensor analysis. Inconsistencies are identified in the representation of velocity components in similarity coordinates in the literature in general, as well as in Ewing 1995, Ewing et al. 2007, Wänström 2009, Wänström, George, and Meyer 2009, for which these are more critical. These inconsistencies have blurred the physical interpretations of the field in similarity coordinates.

Since the similarity coordinates are non-orthogonal it follows that the LD matrix operator is not self-adjoint when velocity components are

expressed with respect to these bases. This motivated the introduction of an alternative coordinate system to the one proposed in Ewing et al. 2007, named the stretched spherical coordinate system (SSC), which ensures the self-adjointedness of the LD matrix operator. The current work inevitably makes use of the self-similar behavior of the turbulent axi-symmetric jet in order to formally deduce that the optimal LD modes in the streamwise direction are Fourier modes with a decaying amplitude. This, however, is shown only to be possible if a specific weight function is introduced in the L^2-inner product of the vector space, which has gone unnoticed prior to this work. Nevertheless, the introduction of the weight appears to be quite critical for the physical interpretation of the modal expansion of the governing equations using Fourier-related modes, since it defines the vector space in which the physical field is expanded. From this follows the reconstruction of the single-point statistics and energy density spectra in stretched-spherical coordinates, in order to yield how various LD modes can be related to the turbulent energy production and energy transport.

A motivation for applying the formalism introduced in the current work, is that it resolves the issue initially raised by Daniel Ewing (private communication) concerning the formulation of the instantaneous Navier-Stokes equations for the jet far-field in similarity coordinates in non-dimensional form. Ewing's critique was directed towards the idea of non-dimensionalizing time using the characteristic velocity, which in this case is the spatially decaying mean centerline velocity. This inevitably suggest that the dimensionless time variable would be a function of space, implying that time and space are interlinked. The current work circumvents this issue by expressing the velocities in tensor form, and decomposing the flow in terms of the amplitude decaying stretched Fourier modes.

The reconstruction of the velocity field reveals that the most energetic region is located around one jet-half width, where the mean shear peaks, and where most of the energy is concentrated. It is also seen that in this region the cross-spectra collapse for all wave-numbers, supporting the model of Lumley 1967a of scale-to-scale similarity in the case of constant shear flow. In the streamwise experiment the Reynolds stresses are shown to be nearly fully reconstructed using a single LD mode, indicating that this mode is the dominant energy extraction mechanism from the mean flow. This implies that the energy production and the energy transport related to the shear-stresses are dominated by the first LD mode which is self-similar across wavenumbers. Both the streamwise and crossplane data demonstrate that the eigenvalue-normalized production term in the turbulence kinetic energy transport equation is constant for a range of the most energetic modes, in support of the hypothesis posed in Wänström 2009 that multiple modes are able to directly tap

into the energy production of the flow.

The current work, paves the way for a full decomposition in space and time of the jet far-field analogous to the recent works of Schmidt et al. 2018, Towne, Schmidt, and Colonius 2018, and Muralidhar et al. 2018. It furthermore serves as an inspiration for the decomposition of other more general flow fields in complex coordinate systems.

1.4 Outline of the Thesis

The decomposition of the jet far-field represents a compound problem, since the identification of the family of optimal basis functions can only be achieved by expressing the velocity field in curvilinear similarity coordinates, prior to applying the LD. The governing equations are therefore introduced in in similarity coordinates in chapter 2, and the formulation of the LD integral in tensor form is introduced in Chapter 3, where the family of eigenfunctions that satisfies the LD integral in siimilarity coordinates is identified. Chapters 4 and 5 present the results from the streamwise- and cross-plane measurement campaigns where the decomposition and reconstruction of the flow is presented. Chapter 6 summarizes the conclusions of the work.

CHAPTER 2

Governing Equations of Motion

In this chapter the governing equations of fluid motion are formulated. The chapter is divided into two parts: the first part reviews the formulation of the governing equations in general coordinates, including the momentum and mass conservation, the transport equations, and the two-time, two-point correlations equations in general coordinates. The second part of the chapter is the formulation of the governing equations in two specific coordinate systems; the similarity coordinates proposed by Ewing et al. 2007 and the stretched spherical coordinates. For the purpose of formulating governing equations in complex coordinate systems tensor analysis is applied. The following section will introduce the tensor notation applied in this work. For a review on tensor analysis the reader is referred to Weyl 1952, Aris 1962, Lumley 1970, Dirac 1975, and Grinfeld 2013. In this work the tensor notation from Grinfeld 2013 will be applied.

2.1 Tensor notation

In the current chapter we restrict the term *vector* to an operator denoted by an overline defined as

$$\overline{T} : \Omega \to \mathbb{C}^n \ , \ \Omega \subseteq \mathbb{R}^3 \times t \tag{2.1}$$

Any object without an index is considered a zeroth-order tensor and tensors with indicies in the super-, subscript, and those with a combination of both, are called contravariant, covariant, and mixed tensors, respectively. A vector field, $\overline{V}$, can be decomposed with respect to a curvilinear basis in the following way

$$\overline{V} = \sum_{i=1}^{n} V^i \overline{z}_i = V^i \overline{z}_i, \tag{2.2}$$

where V^i is the contravariant vector component, $\overline{z}_i$ is the covariant basis vector, and n is the dimension of the space spanned by the basis. Whenever an index is repeated in the sub- and superscript in a given term, the Einstein summation convention (a contraction over that index) is invoked, as demonstrated in (2.2). Repeated indices in the same script position must therefore be accompanied by the an explicit summation sign if an summation is implied, since this in general is a violation of

the tensor notation. Two identical indices in the subscript will, however, appear without a summation sign in relation to *physical velocity components*. In this case the reader should note that the resulting expression containing the repeated indices is not a tensor, and the repeated indices are to be substituted with the corresponding index of the respective component.

Coordinates are always indicated by superscripted indices, z^i and two different coordinate systems are distinguished by introducing a prime on the index, such that z^i and $z^{i'}$ are recognized as coordinates belonging to two different coordinate systems. The Jacobian operators are denoted by the letter, J,

$$J^i_{i'} = \frac{\partial z^i}{\partial z^{i'}} \quad , \quad J^{i'}_i = \frac{\partial z^{i'}}{\partial z^i} \tag{2.3}$$

such that

$$V^{i'} = V^i J^{i'}_i \quad , \quad V^i = V^{i'} J^i_{i'}. \tag{2.4}$$

The covariant- and contravariant metric tensors are defined by the following

$$z_{ij} = \overline{z}_i \cdot \overline{z}_j \quad , \quad z^{ij} = \overline{z}^i \cdot \overline{z}^j, \tag{2.5}$$

and the contraction of the covariant- and contravariant metric tensor is the identity operator,

$$\delta^i_j = z^{ik} z_{kj}, \tag{2.6}$$

where δ^i_j is the Kronecker delta. The Christoffel-symbol of the second kind is denoted by $\Gamma^k_{ij} = \overline{z}^k \cdot \partial \overline{z} / \partial z^k$, and $\nabla_j V^k = \partial V^k / \partial z^j + \Gamma^k_{ij} V^i$ is the covariant derivative of the contravariant tensor V^k. The contravariant derivative is defined as $\nabla^i = z^{ij} \nabla_j$. The volume element is defined as the determinant of the covariant metric tensor

$$\sqrt{Z} = \sqrt{|z_{..}|}, \tag{2.7}$$

which for curvilinear coordinates defined with respect to a Cartesian coordinate system reduces to the determinant of the Jacobian operator.

In order to gain a more intuitive understanding of the vector field, it can be useful to sometimes work with what are commonly known as *physical components* of a vector field. These are obtained by normalizing the basis vectors and adjusting the components accordingly in order to preserve invariance. The drawback of this operation is that the components and bases are no longer tensors, which complicates operations in complex coordinate systems, since the rules of tensor analysis cannot be applied in this case. The advantage is that the physical components are

more intuitive and will be used in cases where fields need to be evaluated. The physical components of a tensor are obtained by projecting the vector field onto the set of unit vectors $\overline{e}_i$, pointing in the corresponding directions of the $\overline{z}_i$-bases, (note that the Einstein summation convention does not apply in the following), Truesdell 1953

$$V[i] = \overline{V} \cdot \overline{e}_i, \tag{2.8}$$

where the index is placed in a square bracked in order to accentuate that the object is not a tensor. The unit vectors are defined as the normalized covariant basis vectors

$$\overline{e}_i = \frac{\overline{z}_i}{\sqrt{z_{ii}}} \tag{2.9}$$

and the physical components can then be obtained by the explicit form through the contravariant velocity component

$$V[i] = V^i \sqrt{z_{ii}}. \tag{2.10}$$

It is apparent that the multiplier in (2.10) is simply the length of the i-th basis component. It therefore effectively rescales the contravariant component such that it reflects the full magnitude of the field in that direction.

2.2 Governing equations in curvilinear coordinates

For an incompressible Newtonian isothermal fluid with constant material properties the Navier-Stokes equation with no body forces take on the following invariant form

$$\frac{\partial \overline{V}}{\partial t} + \overline{V} \cdot \nabla \overline{V} = -\frac{1}{\rho} \nabla P + \nu \nabla^2 \overline{V}, \tag{2.11}$$

which together with the divergence free condition comprise the governing equations of fluid motion

$$\nabla \cdot \overline{V} = 0. \tag{2.12}$$

In curvilinear coordinates the Navier-Stokes equations take the following form, Appendix B

$$\frac{\partial V^i}{\partial t} + V^j \nabla_j V^i = -\frac{1}{\rho} \nabla^i P + \nu \nabla^j \nabla_j V^i. \tag{2.13}$$

where the Voss-Weyl formula yields the expression for the continuity equation in terms of the squared volume element, Z (see (2.49), p. 19)

$$\nabla \cdot \overline{V} = \frac{\partial V^i}{\partial z^i} + \frac{V^i}{2Z} \frac{\partial Z}{\partial z^i}. \tag{2.14}$$

The formulations (2.13) and (2.14) are valid in any well-defined coordinate system defined in Euclidean space. The transport equations can now be formulated from these expressions.

2.2.1 Transport equations

Denoting equation (2.13) by M^i, the Reynolds averaged Navier-Stokes (RANS) equations can be denoted by $\langle M^i \rangle$, where angle brackets denote ensemble averaging and the Reynolds-Decomposition has been employed

$$\frac{\partial \langle V^i \rangle}{\partial t} + \langle V^j \rangle \nabla_j \langle V^i \rangle + \nabla_j \langle v^i v^j \rangle = -\frac{1}{\rho} \nabla^i \langle P \rangle + \nu \nabla^j \nabla_j \langle V^i \rangle . \quad (2.15)$$

Note that v^i denotes the fluctuating part of the velocity and $\langle V^i \rangle$ and $\langle P \rangle$, denote ensemble averaging of the velocity components and pressure field. In order to obtain the energy equation for laminar flow we have to perform the following operation, which represents the single-point velocity correlation

$$V^j M^i + V^i M^j . \quad (2.16)$$

After collecting terms the following form of the single-point equations is obtained for laminar flow

$$\begin{aligned} \frac{\partial \left(V^i V^j\right)}{\partial t} + V^k \nabla_k V^i V^j &= -\frac{1}{\rho} \left(V^j \nabla^i P + V^i \nabla^j P\right) \\ &+ \nu \left(V^j \nabla^k \nabla_k V^i + V^i \nabla^k \nabla_k V^j\right) . \end{aligned} \quad (2.17)$$

The single-point correlation for the mean flow is obtained by the following procedure

$$\langle V^j \rangle \langle M^i \rangle + \langle V^i \rangle \langle M^j \rangle , \quad (2.18)$$

which yields

$$\begin{aligned} & \frac{\partial \left(\langle V^i \rangle \langle V^j \rangle\right)}{\partial t} + \langle V^k \rangle \nabla_k \langle V^i \rangle \langle V^j \rangle + \nabla_k \langle V^j \rangle \langle v^i v^k \rangle \\ + \quad & \nabla_k \langle V^i \rangle \langle v^j v^k \rangle - \langle v^i v^k \rangle \nabla_k \langle V^j \rangle - \langle v^j v^k \rangle \nabla_k \langle V^i \rangle = \\ - \quad & \frac{1}{\rho} \left(\langle V^j \rangle \nabla^i P + \langle V^i \rangle \nabla^j P\right) \\ + \quad & \nu \left(\langle V^j \rangle \nabla^k \nabla_k \langle V^i \rangle + \langle V^i \rangle \nabla^k \nabla_k \langle V^j \rangle\right) . \end{aligned} \quad (2.19)$$

The single-point correlation of the fluctuating field is obtained by taking the laminar correlation field and subtracting the mean correlation field. This is formulated compactly by the following

$$\langle V^j \left(M^i - \langle M^i \rangle\right) + V^i \left(M^j - \langle M^j \rangle\right) \rangle , \quad (2.20)$$

where manipulation with terms yields the final form of the Reynolds-stress transport equation

$$\begin{aligned}\frac{\partial \left\langle v^i v^j \right\rangle}{\partial t} &+ \left\langle V^k \right\rangle \nabla_k \left\langle v^i v^j \right\rangle + \left\langle v^i v^k \right\rangle \nabla_k \left\langle V^j \right\rangle + \left\langle v^j v^k \right\rangle \nabla_k \left\langle V^i \right\rangle + \\ &+ \nabla_k \left\langle v^i v^j v^k \right\rangle = -\frac{1}{\rho}\left(\left\langle v^j \nabla^i p \right\rangle + \left\langle v^i \nabla^j p \right\rangle\right) + \\ &+ \nu\left(\left\langle v^j \nabla^k \nabla_k v^i \right\rangle + \left\langle v^i \nabla^k \nabla_k v^j \right\rangle\right),\end{aligned} \tag{2.21}$$

from which the energy equations can be obtained.

2.2.2 Energy equations

The energy equations for the laminar-, mean-, and fluctuating parts of the velocity field are obtained by contracting (2.18), (2.19), and (2.21) with z_{ij} and multiplying by one half. This operation yields the corresponding energy equations

$$\frac{DK}{Dt} = -\frac{1}{\rho}\nabla_i V^i P + \nu\left(\nabla^j \nabla_j K - \left(\nabla^j V_i\right)\nabla_j V^i\right), \tag{2.22}$$

$$\begin{aligned}\frac{DK_0}{Dt} &+ \nabla_j \left\langle V^i \right\rangle \left\langle v_i v^j \right\rangle - \left\langle v_i v^j \right\rangle \nabla_j \left\langle V^i \right\rangle = -\frac{1}{\rho}\nabla_i \left\langle V^i \right\rangle P + \\ &+ \nu\left(\nabla^j \nabla_j K_0 - \left(\nabla^j \left\langle V^i \right\rangle\right)\nabla_j \left\langle V_i \right\rangle\right),\end{aligned} \tag{2.23}$$

$$\begin{aligned}\frac{DK_t}{Dt} &+ \left\langle v_i v^j \right\rangle \nabla_j \left\langle V^i \right\rangle + \frac{1}{2}\nabla_j \left\langle v_i v^i v^j \right\rangle = -\frac{1}{\rho}\nabla_i \left\langle v^i p \right\rangle + \\ &+ \nu\left(\nabla^j \nabla_j K_t - \left\langle \left(\nabla^j v^i\right)\nabla_j v_i \right\rangle\right),\end{aligned} \tag{2.24}$$

where the material derivative is defined as

$$\frac{D}{Dt} = \frac{\partial}{\partial t} + \left\langle V^j \right\rangle \nabla_j. \tag{2.25}$$

and the density-normalized kinetic energy for the laminar, mean, and fluctuating part are defined as

$$K = \frac{1}{2} V^i V_i \tag{2.26}$$

$$K_0 = \frac{1}{2}\left\langle V^i \right\rangle \left\langle V_i \right\rangle \tag{2.27}$$

$$K_t = \frac{1}{2}\left\langle v^i v_i \right\rangle. \tag{2.28}$$

Note that the viscous term was separated into two parts, since the following relation holds

$$V_i \nabla_j \nabla^j V^i = \frac{1}{2}\nabla^j \nabla_j V^i V_i - \left(\nabla^j V^i\right)\nabla_j V_i. \tag{2.29}$$

However, in (2.24) the viscous dissipation can be expressed explicitly by rewriting the viscous part of the equation as follows

$$\nu \left\langle v_i \nabla_j \nabla^j v^i \right\rangle = \left\langle v_i \nabla_j \tau^{ij} \right\rangle = \nabla_j \left\langle v_i \tau^{ij} \right\rangle - \left\langle \tau^{ij} \nabla_j v_i \right\rangle , \tag{2.30}$$

where the last term is the viscous dissipation. The deviatoric stress tensor is defined as

$$\tau^{ij} = 2\nu s^{ij}, \tag{2.31}$$

and the strain tensor is

$$s^{ij} = \frac{1}{2} \left(\nabla^j v^i + \nabla^i v^j \right) . \tag{2.32}$$

In the energy equation for the fluctuating part, (2.24), the physical meaning of the terms can now be identified - note that the viscous terms have been expressed in terms of (2.30)

$$\begin{aligned} \underbrace{\frac{DK_t}{Dt}}_{I} \quad + \quad & \underbrace{\left\langle v_i v^j \right\rangle \nabla_j \left\langle V^i \right\rangle}_{II} + \underbrace{\frac{1}{2} \nabla_j \left\langle v_i v^i v^j \right\rangle}_{III} = - \underbrace{\frac{1}{\rho} \nabla_i \left\langle v^i p \right\rangle}_{IV} + \\ + \quad & \underbrace{\nabla_j \left\langle v_i \tau^{ij} \right\rangle}_{V} - \underbrace{\left\langle \tau^{ij} \nabla_j v_i \right\rangle}_{VI} . \end{aligned} \tag{2.33}$$

I is the material derivative of the turbulence kinetic energy (TKE), II represents the turbulence-energy production by mean shear, III is the diffusion due to velocity fluctuations, IV is the diffusion due to pressure fluctuations, V is the viscous transport, and VI is the viscous dissipation.

2.2.3 Two-time, two-point correlation equations

In order to obtain the two-time, two-point correlation equations, we apply the following procedure

$$\left\langle U^j \left(M^i - \left\langle M^i \right\rangle \right) + V^i \left(N^j - \left\langle N^j \right\rangle \right) \right\rangle . \tag{2.34}$$

where M^i and N^j are the momentum equations at point (point designates space and time collectively) A and B, respectively. The parameters t, ∇_k, z_{ij}, v^i and p designate the time, the covariant derivative, the covariant metric tensor, the contravariant velocity component and pressure at point A, new variables are introduced at point B and are designated in the corresponding order as: τ, Δ_k, g_{ij}, u^j and q, respectively.

The procedure $M^i - \langle M^i \rangle$ evaluates to

$$\begin{aligned} \frac{\partial v^i}{\partial t} &+ v^k \nabla_k \langle V^i \rangle + \langle V^k \rangle \nabla_k v^i \\ &+ \nabla_k \left(v^i v^k - \langle v^i v^k \rangle \right) = -\frac{1}{\rho} \nabla^i p + \nu \nabla^k \nabla_k v^i, \end{aligned} \tag{2.35}$$

and analogously $N^j - \langle N^j \rangle$ is evaluated as

$$\begin{aligned} \frac{\partial u^j}{\partial \tau} &+ u^k \Delta_k \langle U^j \rangle + \langle U^k \rangle \Delta_k u^j \\ &+ \Delta_k \left(u^j u^k - \langle u^j u^k \rangle \right) = -\frac{1}{\rho} \Delta^j q + \nu \Delta^k \Delta_k u^j. \end{aligned} \tag{2.36}$$

By applying the procedure (2.34), noting that the spatial and temporal derivatives at point B of variables at point A are zero and vice versa, we obtain the two-time, two-point correlation equations in general coordinates

$$\begin{aligned} & \frac{\partial \langle v^i u^j \rangle}{\partial t} + \frac{\partial \langle v^i u^j \rangle}{\partial \tau} + \langle v^k u^j \rangle \nabla_k \langle V^i \rangle + \langle v^i u^k \rangle \Delta_k \langle U^j \rangle + \\ + \; & \langle V^k \rangle \nabla_k \langle v^i u^j \rangle + \langle U^k \rangle \Delta_k \langle v^i u^j \rangle + 2 \langle U^j \rangle \nabla_k \langle v^i v^k \rangle + \\ + \; & 2 \langle V^i \rangle \Delta_k \langle u^j u^k \rangle + \nabla_k \langle v^i v^k u^j \rangle + \Delta_k \langle v^i u^j u^k \rangle = \\ - \; & \frac{1}{\rho} \left(\nabla^i \langle u^j p \rangle + \Delta^j \langle v^i q \rangle \right) + \nu \left(\nabla^k \nabla_k \langle v^i u^j \rangle + \Delta^k \Delta_k \langle v^i u^j \rangle \right). \end{aligned} \tag{2.37}$$

The expression is also valid for $A = B$ and reduces to the single-point single- time correlation equations by replacing $u^j = v^j$ and by renaming the operators at point B to those at point A. The two-time, two-point equations are valuable for the analysis of the energy transport over a distance in space or time. These may prove to be particularly useful when combined with the LD introduced in Chapter 3 in order to characterize the energy transport across LD modes. This analysis was not included in the current work, but may prove to be of significant importance for future turbulence studies. Due to the tensor form of (2.37) the expression is valid in any well-defined coordinate system.

2.3 Transformation to curvilinear coordinates

The purpose of coordinate transformations is to utilize any symmetries of a system, in order to simplify the problem at hand. The far-field of the turbulent jet reveals a particular type of symmetry, defined in terms of self-similarity or self-preservation. Experimental data has revealed,

Ewing et al. 2007, Wänström 2009, that when the velocity components are scaled with the local centerline velocity and interpolated onto the similarity coordinate system $\xi = \ln(x - x_0)/D$ and $\eta = r/\delta$ (see (2.40)-(2.42), p. 18) the resulting field is statistically homogeneous along the streamwise coordinate, ξ (see definition in (2.40), p. 18). These observations confirm that the jet far-field is in a state of equilibrium as predicted by equilibrium similarity theory (EST), George 1989, Ewing 1995, Wänström 2009, Wänström, George, and Meyer 2012. The underlying assumption of EST is the hypothesis that the velocity components in similarity coordinates can be written as

$$U(\xi, \eta) = f(\eta)U_c(\xi), \tag{2.38}$$
$$V(\xi, \eta) = g(\eta)U_c(\xi). \tag{2.39}$$

While the aforementioned approach of scaling and interpolation proposed by Ewing et al. 2007 and implemented by Wänström 2009 do yield a simplified velocity field, the current work shows that it violates the fundamental requirement of preserving the invariance of the vector field itself when seeking a similarity solution. From the ansätze (2.38) and (2.39), f and g have traditionally been perceived in the fluid dynamics community as cylindrical velocity components scaled by the local centerline velocity. The reason for this is because (2.38) and (2.39) do not state how to determine f and g in order to preserve the invariance of the field. This has given rise to some confusion regarding the physical interpretation of the scaled velocity field in similarity coordinates. By assuming f and g to be the scaled cylindrical velocity components in the streamwise- and radial direction, the invariance of the velocity field is in fact only preserved along the centerline of the jet, due to the orthogonality of the similarity coordinates along this line. It can therefore only be considered as an approximation to the invariant transformations. The error related to this assumption increases with increasing distance from the centerline due to the missing effect of the change of the basis in the governing equations.

These assumption span back to some of the very first studies of jets documented in literature. In most cases these assumptions have had no major consequences for the documented work, since the primary concern of the corresponding authors has been to confirm the *collapse* of single- and (in more recent cases) multi-point statistics. However, for understanding the physics of the flow through single- and multipoint statistics in curvilinear coordinates, the direct consequences of these assumptions result in misestimations of Reynolds stresses and mainly cross-spectra which are relevant for the analysis of the flow. The mean η-velocity component and the shear-stresses have also been misrepresented due to these assumptions, and it will be demonstrated that in similarity coordinates

the mean η velocity component is negative across the entire span of the flow, contrary to what the scaled cylindrical profiles suggest. In similarity coordinates, the shear-stresses have been overestimated as well, by an amount of 35% at one jet-half width, and by an order of magnitude at two half-widths. From Plancherel's equation, Christensen 2010, it is evident that the spectra and the LD kernel are also affected to some degree.

The current work also demonstrates that a straightforward numerical implementation of the LD is not possible in similarity coordinates. This is due to the lack of self-adjointedness of the matrix representation of the LD operator in similarity coordinates, which is rooted in the non-orthogonality of the coordinate system. The self-adjointedness may, however, be possible to recover through a similarity transformation of the matrix operator - i.e. a formulation of the non-Hermitian matrix operator in terms of a product of two Hermitian matrices. The identification of this pair of Hermitian matrices, however, remains an open issue at the time of the writing of this thesis.

As a solution to this problem, the current work introduces an alternative approach for the analysis of the far-field, by introducing a logarithmically stretched spherical coordinate system, which due to its orthogonality does not suffer from the aforementioned disadvantages of the similarity coordinates and produces a self-adjoint matrix representation of the LD operator. The approach of decomposing the velocity field in the current work can be summarized by the following three steps

1. A transformation from Cartesian to curvilinear coordinates

2. A scaling of the instantaneous contravariant velocity components

3. Identification of the optimal family of functions to span the velocity field by means of the LD integral formulation in curvilinear coordinates.

It is important to note that the scaling of the contravariant velocity components is a necessary step, since homogeneity is not obtained by a coordinate transformation alone (step 1). This is essentially due to two reciprocal characteristics in the jet far-field: a linear *decay* of mean velocity and a linear *growth* of turbulent structures. For a hypothetical flow where the scale growth is proportional to the velocity, a mere coordinate transformation yields a vastly simplified velocity field. It will be demonstrated, however, that the coordinate transformations have a 'neutralizing' effect on the scale growth, but an opposite effect on the decay of the contravariant velocity components.

The outlined approach preserves the invariance of the vector field, and enables us to express the governing equations in curvilinear coordinates in terms of the contravariant velocity components, for which the identified family of functions is directly applicable. Although the LD implementation in similarity coordinates remains impractical this work will provide the formulation of the governing equations as well as results in similarity coordinates, alongside the results in SSC. This is mainly due to the fact that the advantages of similarity coordinates may be useful for the analysis of data sampled in the cross-plane of the turbulent jet, since the measurement plane in this case represents a constant ξ-component. Note that this is not the case in SSC, where a constant ξ-coordinate represents a spherical shell (see section 2.3.3), which cannot be sampled using stereoscopic PIV measurements. The following sections will introduce the objects and metrics for performing the coordinate transformations as well as the formulation of the governing equations in these coordinates.

2.3.1 Evaluation of objects for similarity coordinates

The current section introduces the mathematical objects relevant for reducing the governing equations to the form specified by the similarity coordinates. The term *similarity coordinates* refer to a specific set of curvilinear coordinates $(z^1, z^2, z^3) = (\xi, \eta, \theta)$ which are here expressed in terms of the Cartesian coordinates, $(z^{1'}, z^{2'}, z^{3'}) = (x, y, z)$. These coordinate systems are related by the following relations, Ewing et al. 2007

$$\xi(x) = \ln\left((x - x_0)/D\right), \tag{2.40}$$

$$\eta(x, y, z) = \left(y^2 + z^2\right)^{\frac{1}{2}}/\delta(x), \tag{2.41}$$

$$\theta(y, z) = \arctan z/y, \tag{2.42}$$

where $\delta(x) = A(x - x_0)$ is the jet half-width. The similarity coordinates are expressed in terms of Cartesian coordinates by the relations (2.40)-(2.42). The Jacobian operators relating the two systems are defined by the following

$$J_i^{i'} = \begin{Bmatrix} \delta/A & 0 & 0 \\ \delta\eta\cos\theta & \delta\cos\theta & -\delta\eta\sin\theta \\ \delta\eta\sin\theta & \delta\sin\theta & \delta\eta\cos\theta \end{Bmatrix}, \tag{2.43}$$

$$J_{i'}^{i} = \begin{Bmatrix} A/\delta & 0 & 0 \\ -\eta A/\delta & \cos\theta/\delta & \sin\theta/\delta \\ 0 & -\sin\theta/(\delta\eta) & \cos\theta/(\delta\eta) \end{Bmatrix}, \tag{2.44}$$

where $\delta = ADe^{\xi}$. We then define the Cartesian covariant basis vectors as the canonical set

$$\overline{z}_{1'} = \begin{pmatrix} 1 \\ 0 \\ 0 \end{pmatrix}, \overline{z}_{2'} = \begin{pmatrix} 0 \\ 1 \\ 0 \end{pmatrix}, \overline{z}_{3'} = \begin{pmatrix} 0 \\ 0 \\ 1 \end{pmatrix}. \tag{2.45}$$

such that the covariant basis vectors of the curvilinear system can be expressed as

$$\overline{z}_1 = \begin{pmatrix} \delta/A \\ \delta\eta\cos\theta \\ \delta\eta\sin\theta \end{pmatrix}, \overline{z}_2 = \begin{pmatrix} 0 \\ \delta\cos\theta \\ \delta\sin\theta \end{pmatrix}, \overline{z}_3 = \begin{pmatrix} 0 \\ -\delta\eta\sin\theta \\ \delta\eta\cos\theta \end{pmatrix}. \tag{2.46}$$

The form of the covariant basis (2.46) reveals that these are increasing with increasing ξ and η. This means that the basis vectors are increasing with downstream position and with distance from the jet centerline. The covariant- and contravariant metric tensors are then

$$z_{ij} = \begin{Bmatrix} \delta^2\left(\eta^2 + A^{-2}\right) & \eta\delta^2 & 0 \\ \eta\delta^2 & \delta^2 & 0 \\ 0 & 0 & \delta^2\eta^2 \end{Bmatrix}, \tag{2.47}$$

$$z^{ij} = \begin{Bmatrix} A^2\delta^{-2} & -\eta A^2\delta^{-2} & 0 \\ -\eta A^2\delta^{-2} & (A^2\eta^2+1)\delta^{-2} & 0 \\ 0 & 0 & \delta^{-2}\eta^{-2} \end{Bmatrix}. \tag{2.48}$$

Since the metric tensors have non-zero off-diagonal components they reveal that the ξ- and η bases in general are non-orthogonal. The similarity coordinates are only orthogonal when η is zero, corresponding to the the centerline of the jet. The determinant of the covariant metric tensor is the volume element squared

$$Z = \frac{\delta^6\eta^2}{A^2}. \tag{2.49}$$

The contravariant bases are defined as

$$\overline{z}^1 = \begin{pmatrix} A/\delta \\ 0 \\ 0 \end{pmatrix}, \overline{z}^2 = \begin{pmatrix} -\eta A/\delta \\ \cos\theta/\delta \\ \sin\theta/\delta \end{pmatrix}, \overline{z}^3 = \begin{pmatrix} 0 \\ -\sin\theta/(\delta\eta) \\ \cos\theta/(\delta\eta) \end{pmatrix}, \tag{2.50}$$

and the non-zero elements of the Christoffel-symbol for Z' are

$$\Gamma^1_{11} = 1 \tag{2.51}$$

$$\Gamma^2_{12} = 1 \ , \ \Gamma^2_{33} = -\eta \tag{2.52}$$

$$\Gamma^3_{13} = 1 \ , \ \Gamma^3_{23} = \frac{1}{\eta}. \tag{2.53}$$

Since the Christoffel-symbol is symmetric in its lower indices (2.51)-(2.53) represent eight non-zero elements in total.

Figure 2.1 illustrates the covariant basis vectors along the coordinate lines described by (2.40)-(2.42) for $\theta = const$. For the bases (2.46), it is apparent that the magnitude increases with downstream- and radial position. This is illustrated in Figure 2.1 where the covariant bases are shown at two different locations in the field. It is convenient to view these bases as a vector field in their own right. From this perspective we find that our goal is to find the correct coefficients, V^i, in order to span the velocity field that we have measured. In order to preserve the invariance of a measured velocity field, the corresponding components, V^i, must vary with downstream- and radial position in a manner such that the velocity field $\overline{V} = V^i \overline{z}_i$, evaluated at a given point (z^1, z^2, z^3), has the same length and direction had it been spanned by Cartesian bases, (2.45). This then implies that the contravariant components V^i are the velocity components *with respect to this new field of basis vectors*. Note that the bases are also a geometric representation of the distance measure, which is the property that impacts the representation of the scale growth in this coordinate system.

One of the drawbacks of working in similarity coordinates is that the velocity components vary differently than what we are accustomed to in cylindrical or Cartesian coordinates. The physical velocity field in similarity coordinates is obtained from the contravariant bases, and (2.10) in order to yield

$$V[1] = V^{1'} A\sqrt{\eta^2 + A^{-2}}, \tag{2.54}$$

$$V[2] = V^{2'} \cos\theta + V^{3'} \sin\theta - A\eta V^{1'}, \tag{2.55}$$

$$V[3] = V^{3'} \cos\theta - V^{2'} \sin\theta. \tag{2.56}$$

Note that $V[2]$ includes a component from the streamwise velocity component. This has a profound impact on the mean velocity profile for the η-component, but also affects the normal Reynolds stresses in the η-direction as well the shear-stresses, as will be seen in Chapter 4. The reason is seen by examining the last term of (2.55) where the multiplier, $A \approx 0.1$, suppresses the effect of $V^{1'}$ on $V[2]$. The streamwise mean velocity component, is an order of magnitude larger than $V^{2'}$ and $V^{3'}$, and therefore impacts the profile profoundly. This, as will be seen later, yields a negative mean profile for $V[2]$ for $\eta > 0$, which is monotonically much simpler than the scaled radial velocity profile in scaled cylindrical coordinates shown in Panchapakesan and Lumley 1993a and Wänström 2009. This is an additional advantage for this choice of coordinates in terms of simplifying the representation of the flow.

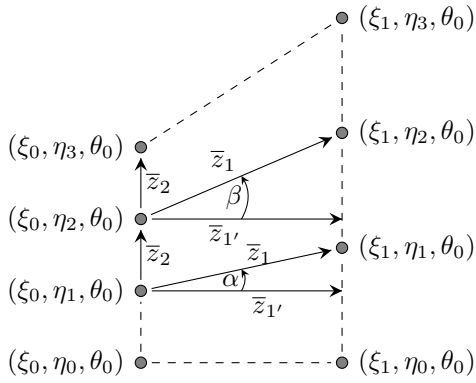

Figure 2.1: Superimposed covariant basis vectors, $\overline{z}_i$ and $\overline{z}_{i'}$, of the similarity coordinate system and the cylindrical coordinates in Euclidean space. It is illustrated that the angle between the bases changes with increasing η-coordinates.

2.3.2 Governing equations in similarity coordinates

The continuity equation is obtained from (2.14) for the contravariant velocity components in similarity coordinates as

$$\frac{\partial V^i}{\partial z^i} + 3V^1 + \frac{V^2}{z^2} = 0. \tag{2.57}$$

We replace the numerical indices for clarification purposes, in order to obtain the continuity equation in similarity coordinates

$$\frac{\partial V^\xi}{\partial \xi} + \frac{1}{\eta}\frac{\partial \left(V^\eta \eta\right)}{\partial \eta} + \frac{\partial V^\theta}{\partial \theta} + 3V^\xi = 0, \tag{2.58}$$

where V^ξ, V^η, V^θ are the contravariant velocity components. In the following, the terms of (2.13) will be evaluated in similarity coordinates.

2.3.2.1 The advective term

The non-linear advective term in (2.13) is a contraction between the contravariant velocity component and the covariant derivative

$$V^j \nabla_j V^i \quad = \quad V^j \left(\frac{\partial V^i}{\partial z^j} + \Gamma^i_{jk} V^k \right). \tag{2.59}$$

These are evaluated in component form as

$$V^j \nabla_j V^1 = V^j \frac{\partial V^1}{\partial z^j} + \left(V^1\right)^2, \tag{2.60}$$

$$V^j \nabla_j V^2 = V^j \frac{\partial V^2}{\partial z^j} + 2V^1 V^2 - z^2 (V^3)^2, \tag{2.61}$$

$$V^j \nabla_j V^3 = V^j \frac{\partial V^3}{\partial z^j} + 2V^1 V^3 + \frac{2}{z^2} V^2 V^3, \tag{2.62}$$

where the power operator on the components is denoted in connection with a parenthesis, in order to distinguish it from a superscript.

2.3.2.2 The pressure gradient

Since the pressure is a scalar, the covariant derivative reduces to a partial derivative

$$\nabla^i P = z^{ij} \nabla_j P \tag{2.63}$$

$$= z^{ij} \frac{\partial P}{\partial z^j}. \tag{2.64}$$

Evaluating the pressure term for the three components and neglecting the terms with zero elements of the contravariant metric tensor, we obtain

$$\nabla^1 P = z^{11} \frac{\partial P}{\partial z^1} + z^{12} \frac{\partial P}{\partial z^2} \tag{2.65}$$

$$\nabla^2 P = z^{21} \frac{\partial P}{\partial z^1} + z^{22} \frac{\partial P}{\partial z^2} \tag{2.66}$$

$$\nabla^3 P = z^{33} \frac{\partial P}{\partial z^3}. \tag{2.67}$$

As for the convective term, we notice that the non-zero off-diagonal elements elements of the contravariant metric tensor result in a cross-coupling between the pressure gradients for the ξ- and η-components. This is due to the non-orthogonality of the coordinate system.

2.3.2.3 The Laplacian

In curvilinear coordinates the Laplacian of the contravariant velocity component takes the following form (Appendix B)

$$\nabla^j \nabla_j V^i = z^{jk} \left(\frac{\partial^2 V^i}{\partial z^j z^k} - \Gamma^l_{jk} \frac{\partial V^i}{\partial z^l} + 2\Gamma^i_{jl} \frac{\partial V^l}{\partial z^k} + \right.$$

$$\left. + v^m \left(\frac{\partial \Gamma^i_{jm}}{\partial z^k} + \Gamma^i_{kl} \Gamma^l_{jm} - \Gamma^l_{jk} \Gamma^i_{lm} \right) \right). \tag{2.68}$$

Evaluating (2.68) for each similarity component yields the following form for the contravariant metric tensor defined by (2.48)

$$\nabla^j \nabla_j V^1 = z^{ij} \frac{\partial^2 V^1}{\partial z^i \partial z^j} + z^{11} \frac{\partial V^1}{\partial z^1} + z^{33} z^2 \frac{\partial V^1}{\partial z^2}, \tag{2.69}$$

$$\begin{aligned} \nabla^j \nabla_j V^2 &= z^{ij} \frac{\partial^2 V^2}{\partial z^i \partial z^j} + z^{11} \frac{\partial V^2}{\partial z^1} + 2 z^{22} \frac{\partial V^1}{\partial z^2} + 2 z^{12} \frac{\partial V^1}{\partial z^1} + \\ &+ z^{33} \left(z^2 \frac{\partial V^2}{\partial z^2} - 2 z^2 \frac{\partial V^3}{\partial z^3} - V^2 + z^2 V^1 \right), \end{aligned} \tag{2.70}$$

$$\begin{aligned} \nabla^j \nabla_j V^3 &= z^{ij} \frac{\partial^2 V^3}{\partial z^i \partial z^j} + z^{11} \frac{\partial V^3}{\partial z^1} + 2 \frac{z^{22}}{z^2} \frac{\partial V^3}{\partial z^2} + \\ &+ z^{33} \left(z^2 \frac{\partial V^3}{\partial z^2} + 2 \frac{\partial V^1}{\partial z^3} + \frac{2}{z^2} \frac{\partial V^2}{\partial z^3} \right) + 2 \frac{z^{12}}{z^2} \frac{\partial V^3}{\partial z^1}. \end{aligned} \tag{2.71}$$

The Navier-Stokes equations can now be written in similarity coordinates.

2.3.2.4 Navier-Stokes equations in similarity coordinates

Equilibrium similarity theory, Ewing 1995, George 1989, Wänström 2009, Wänström, George, and Meyer 2012, hypothesized that the far-field of the round turbulent jet can be scaled by the local centerline velocity in order to obtain a simplified velocity field, and was confirmed by the results of Ewing et al. 2007 and Wänström 2009. This demonstrates the potential of obtaining a simplified expression for the governing equations by obtaining homogeneity in the ξ-direction in addition to the homogeneous-periodic field along the θ-coordinate.

Writing the Navier-Stokes in non-dimensional form by scaling the field by the local centerline velocity and the jet half-width implies expressing the dimensionless time, t', in terms of these parameters. This would seem to be the natural velocity scale in this regard. It would mean that the time is to be non-dimensionalized in the following way

$$t' = \frac{t U_c}{\delta}. \tag{2.72}$$

As pointed out by Daniel Ewing (private communication) this however introduces the problem of t' being a function of space through δ and U_c. This in turn creates issues of causality and simultaneity, since it is not clear how to associate a point in time at two different spatial locations, or vice versa. An alternative approach analogous to special relativity is to consider a space-time metric. The reason for this is that space and the new time variable, t', are coupled. This means that we are modifying the metric tensors, (2.47) and (2.48), through our

definition of time, (2.72) as we are in fact extending them to $\mathbb{R}^4$ as a space-time manifold. We are implicitly defining a metric tensor that in some ways resembles the Minkowski metric, as t' in (2.72) can be viewed as the time in a moving frame of reference. Note that a moving frame of reference must be distinguished from a convected coordinate system in $\mathbb{R}^3$, where the spatial basis vectors are time-dependent. In the latter time remains constant for all points in space unlike the case of the former where time varies with spatial coordinates. The alternative for formulating the Navier-Stokes equations in the far-field region of the jet, is to formulate the equations in curvilinear coordinates defined in Euclidean space, and work with similarity coordinates and physical time, t, as in (2.37), using physical velocity components. This is in many ways more straightforward, since the initial motivation for introducing the similarity coordinates was to obtain homogeneity through the stretching of the coordinates. The analogue to homogeneity in space, is stationarity in time, which is also a desirable trait from an analysis-perspective. In this regard as noted in the paragraph above the flow of interest is in fact already stationary, and therefore requires no further transformation of the time-variable if we wish to decompose the flow in frequency domain. This approach is applied in the current work.

In section 3.1.1 the LD will be formulated in tensor form, in order to enable us to apply it in similarity coordinates, and identify the family of analytical functions in the ξ-direction. It will be derived that the physical ξ-components are indeed analytical functions, namely Fourier coefficients with a decaying amplitude, which will follow from the introduction of a weight function in the inner-product definition of the vector space. This will provide the opportunity for expanding the governing equations in terms of these optimal eigenfunctions, and for analyzing the physics of the flow through modal interactions.

In order to write the instantaneous momentum equations in similarity coordinates in physical form, we invoke the definition of the physical components, (2.10), in order to express the contravariant components as

$$V^i = \frac{V[i]}{\sqrt{z_{ii}}}. \tag{2.73}$$

These are substituted into (2.13), in order to obtain an expression for the momentum equations for the ξ, η, and θ-components. The physical components are expressed as (2.77)-(2.79), and denoted for the sake of clarity in terms of coordinate-designations in the superscripts

$$V^\xi = V[1], \tag{2.74}$$
$$V^\eta = V[2], \tag{2.75}$$
$$V^\theta = V[3]. \tag{2.76}$$

After multiplying the velocity components with $\sqrt{z_{11}}$, $\sqrt{z_{22}}$, and $\sqrt{z_{33}}$, respectively, the ξ-component reduces to the following expression

$$\begin{aligned}
\frac{\partial V^\xi}{\partial t} &+ \frac{V^\xi}{\sqrt{z_{11}}}\left(\frac{\partial V^\xi}{\partial \xi} - V^\xi\right) + \frac{V^\eta}{\sqrt{z_{22}}}\left(\frac{\partial V^\xi}{\partial \eta} + V^\xi\right) + \frac{V^\theta}{\sqrt{z_{33}}}\frac{\partial V^\xi}{\partial \theta} = \\
&- \frac{\sqrt{z_{11}}}{\rho}\left(z^{11}\frac{\partial P}{\partial \xi} + z^{12}\frac{\partial P}{\partial \eta}\right) + \nu\left[z^{11}\left(\frac{\partial^2 V^\xi}{\partial \xi^2} - \frac{\partial V^\xi}{\partial \xi}\right) + \right. \\
&+ z^{22}\left(\frac{\partial^2 V^\xi}{\partial \eta^2} - \frac{2\delta^2\eta}{z_{11}}\frac{\partial V^\xi}{\partial \eta} + \left(\frac{3\delta^4\eta^2}{(z_{11})^2} - \frac{\delta^2}{z_{11}}\right)V^\xi\right) + \\
&+ z^{33}\left(\frac{\partial^2 V^\xi}{\partial \theta^2} + \eta\frac{\partial V^\xi}{\partial \eta} - \frac{\delta^2\eta^2}{z_{11}}V^\xi\right) + \\
&+ \left. 2z^{12}\left(\frac{\partial^2 V^\xi}{\partial \xi \partial \eta} - \frac{\delta^2\eta}{z_{11}}\left(\frac{\partial V^\xi}{\partial \xi} - V^\xi\right) - \frac{\partial V^\xi}{\partial \eta}\right)\right], \qquad (2.77)
\end{aligned}$$

the η-component becomes,

$$\begin{aligned}
\frac{\partial V^\eta}{\partial t} &+ \frac{V^\xi}{\sqrt{z_{11}}}\left(\frac{\partial V^\eta}{\partial \xi} - V^\eta\right) + \frac{V^\eta}{\sqrt{z_{22}}}\frac{\partial V^\eta}{\partial \eta} + \frac{V^\theta}{\sqrt{z_{33}}}\frac{\partial V^\eta}{\partial \theta} + \frac{2V^\xi V^\eta}{\sqrt{z_{11}}} + \\
&- \eta\frac{\sqrt{z_{22}}}{z_{33}}\left(V^\theta\right)^2 = -\frac{\sqrt{z_{22}}}{\rho}\left(z^{12}\frac{\partial P}{\partial \xi} + z^{22}\frac{\partial P}{\partial \eta}\right) + \nu\left[z^{11}\left(\frac{\partial^2 V^\eta}{\partial \xi^2} - \frac{\partial V^\eta}{\partial \xi}\right)\right. \\
&+ z^{22}\left(\frac{\partial V^\eta}{\partial \eta} + 2\sqrt{\frac{z_{22}}{z_{11}}}\left(\frac{\partial V^\xi}{\partial \eta} - \frac{\delta^2\eta}{z_{11}}V^\xi\right)\right) \\
&+ z^{33}\left(\frac{\partial^2 V^\eta}{\partial \theta^2} + \eta\frac{\partial V^\eta}{\partial \eta} - 2\eta\sqrt{\frac{z_{22}}{z_{33}}}\frac{\partial V^\theta}{\partial \theta} - V^\eta + \eta\frac{V^\xi}{\sqrt{z_{11}}}\right) + \\
&+ \left. 2z^{12}\left(\frac{\partial^2 V^\eta}{\partial \xi \partial \eta} - V^\eta + \sqrt{\frac{z_{22}}{z_{11}}}\left(\frac{\partial V^\xi}{\partial \xi} - V^\xi\right)\right)\right], \qquad (2.78)
\end{aligned}$$

and the θ-component is,

$$\begin{aligned}
\frac{\partial V^\theta}{\partial t} &+ \frac{V^\xi}{\sqrt{z_{11}}}\left(\frac{\partial V^\theta}{\partial \xi} - V^\theta\right) + \frac{V^\eta}{\sqrt{z_{22}}}\left(\frac{\partial V^\theta}{\partial \eta} - \frac{V^\theta}{\eta}\right) + \frac{V^\theta}{\sqrt{z_{33}}}\frac{\partial V^\theta}{\partial \theta} + \\
&+ 2V^\theta\left(\frac{V^\xi}{\sqrt{z_{11}}} + \frac{V^\eta}{\eta\sqrt{z_{22}}}\right) = -\frac{\sqrt{z_{33}}}{\rho}\frac{\partial P}{\partial \theta} + \nu\left[z^{11}\left(\frac{\partial^2 V^\theta}{\partial \xi^2} - V^\theta\right)\right. \\
&+ z^{22}\frac{\partial^2 V^\theta}{\partial \eta^2} + z^{33}\left(\frac{\partial^2 V^\theta}{\partial \theta^2} + \eta\frac{\partial V^\theta}{\partial \eta} - \frac{V^\theta}{\eta} + 2\sqrt{\frac{z_{33}}{z_{11}}}\frac{\partial V^\xi}{\partial \theta} + \frac{2}{\eta}\sqrt{\frac{z_{33}}{z_{22}}}\frac{\partial V^\eta}{\partial \theta}\right) \\
&+ \left. 2z^{12}\left(\frac{\partial^2 V^\theta}{\partial \xi \partial \eta} - \frac{\partial V^\theta}{\partial \eta}\right)\right], \qquad (2.79)
\end{aligned}$$

where the covariant- and contravariant metric tensor elements are found in (2.47) and (2.48), respectively. The formulation of the equations, (2.77)-(2.79) demonstrates the complications introduced by the choice of coordinate system in the form of additional cross-coupling terms between the the ξ- and η- components. These are found in terms with z^{12}-multipliers. At the centerline the off-diagonal components of the metric tensor vanish, along with the ξ-η-cross-coupling. The second complication introduced by the coordinate stretching remains at the centerline, however. It is manifested by the additional terms in relation to the spatial velocity derivatives in the ξ-direction, which are seen e.g. in the advective terms of all three momentum equations.

2.3.3 Evaluation of objects for stretched spherical coordinates

The similarity coordinates proposed in the preceding section are disadvantaged due to the non-orthogonality of the coordinate system. The non-orthogonality introduces additional cross-coupling terms between in the momentum equations and, as will be demonstrated in section 3.1.2, introduce an asymmetry in the cross-correlation matrix such that it cannot be written in a Hermitian form. In order to circumvent these difficulties stretched spherical coordinates (SSC) will be introduced which are a set of orthogonal curvilinear coordinates. Orthogonality of the coordinate system ensures Hermitian symmetry of the cross-correlation matrix from which follows that the eigenvalues of the matrix are real and the eigenvectors are orthogonal. The relation between Cartesian, $z^{i'}$, and SSC, $z^{i''}$, can be written as follows

$$x(\xi,\theta,\phi) = De^{\xi}\cos\theta + x_0, \tag{2.80}$$

$$y(\xi,\theta,\phi) = De^{\xi}\sin\theta\cos\phi, \tag{2.81}$$

$$z(\xi,\theta,\phi) = De^{\xi}\sin\theta\sin\phi, \tag{2.82}$$

which resembles a regular spherical coordinate system, but with a logarithmically stretched radial coordinate. Figure 2.2 shows a sketch of the SSC together with the Cartesian coordinates. The center of the nozzle is then located at the Cartesian origo, and $\theta = 0$ is the centerline of the jet.

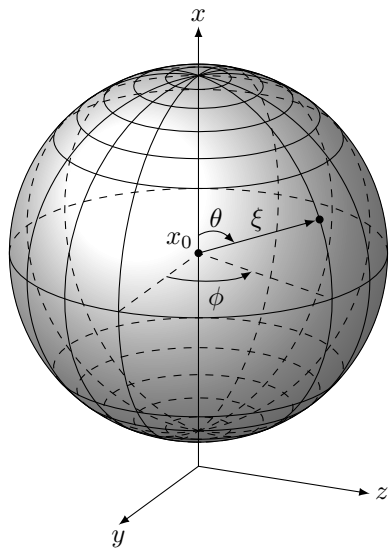

Figure 2.2: Sketch of the stretched spherical coordinate system, (ξ, θ, ϕ).

The Jacobians relating the Cartesian and SSC take on the following form

$$J_{i''}^{i'} = \begin{Bmatrix} De^{\xi}\cos\theta & -De^{\xi}\sin\theta & 0 \\ De^{\xi}\sin\theta\cos\phi & De^{\xi}\cos\theta\cos\phi & -De^{\xi}\sin\theta\sin\phi \\ De^{\xi}\sin\theta\sin\phi & De^{\xi}\cos\theta\sin\phi & De^{\xi}\sin\theta\cos\phi, \end{Bmatrix} \tag{2.83}$$

and

$$J_{i'}^{i''} = \begin{Bmatrix} \cos\theta\left(De^{\xi}\right)^{-1} & \sin\theta\cos\phi\left(De^{\xi}\right)^{-1} & \sin\theta\sin\phi\left(De^{\xi}\right)^{-1} \\ -\sin\theta\left(De^{\xi}\right)^{-1} & \cos\theta\cos\phi\left(De^{\xi}\right)^{-1} & \cos\theta\sin\phi\left(De^{\xi}\right)^{-1} \\ 0 & -\sin\phi\left(De^{\xi}\sin\theta\right)^{-1} & \cos\phi\left(De^{\xi}\sin\theta\right)^{-1} \end{Bmatrix}, \tag{2.84}$$

which yield the following covariant- and contravariant metric tensors

$$z_{i''j''} = \begin{Bmatrix} \left(De^{\xi}\right)^{2} & 0 & 0 \\ 0 & \left(De^{\xi}\right)^{2} & 0 \\ 0 & 0 & \left(De^{\xi}\sin\theta\right)^{2} \end{Bmatrix}, \tag{2.85}$$

and

$$z^{i''j''} = \begin{Bmatrix} \left(De^{\xi}\right)^{-2} & 0 & 0 \\ 0 & \left(De^{\xi}\right)^{-2} & 0 \\ 0 & 0 & \left(De^{\xi}\sin\theta\right)^{-2} \end{Bmatrix}. \tag{2.86}$$

Parallels can be drawn here with the similarity coordinates. The logarithmic stretching of the coordinate system in the streamwise direction

is expressed in both cases by the second power of the δ- and De^{ξ} of all elements of the covariant metric tensors. The orthogonality of the SSC is confirmed by the diagonality of the metric tensors, and thereby reduces the number of cross-coupling terms in the formulation of the equations of motion. The determinant of the covariant metric tensor is then

$$Z = \left(De^{\xi}\right)^{6} \sin^2\theta, \tag{2.87}$$

and the non-zero elements of the Christoffel-symbols evaluate to

$$\Gamma^1_{11} = 1 \ , \ \Gamma^1_{22} = -1 \ , \ \Gamma^1_{33} = -\sin^2\theta \tag{2.88}$$

$$\Gamma^2_{12} = 1 \ , \ \Gamma^2_{33} = -\sin\theta\cos\theta \tag{2.89}$$

$$\Gamma^3_{13} = 1 \ , \ \Gamma^3_{23} = \frac{\cos\theta}{\sin\theta}. \tag{2.90}$$

These represent a total of ten non-zero elements due to the symmetry of the lower index of the Christoffel symbol. The physical velocity components in SSC are then expressed in terms of Cartesian velocity components as

$$V^{\xi} = V^x\cos\theta + V^y\sin\theta\cos\phi + V^z\sin\theta\sin\phi, \tag{2.91}$$

$$V^{\theta} = V^y\cos\theta\cos\phi - V^x\sin\theta + V^z\cos\theta\sin\phi, \tag{2.92}$$

$$V^{\phi} = V^z\cos\phi - V^y\sin\phi. \tag{2.93}$$

It is now possible to formulate the governing equations in SSC, analogously to the procedure applied in the case of similarity coordinates.

2.3.4 Governing equations in SSC

The contravariant form of the continuity equation is then obtained using the determinant of the metric tensor, (2.87), and can be written as follows

$$\frac{\partial V^i}{\partial z^i} + \frac{V^2}{\tan z^2} + 3V^1 = 0. \tag{2.94}$$

The continuity equation in physical form is then

$$\frac{\partial V^{\xi}}{\partial \xi} + \frac{\partial V^{\theta}}{\partial \theta} + \frac{1}{\sin\theta}\frac{\partial V^{\phi}}{\partial \phi} + \frac{V^{\theta}}{\tan\theta} + 2V^{\xi} = 0, \tag{2.95}$$

and we note the singularity at $\theta = 0$, due to the nature of the spherical coordinate system.

2.3.4.1 The advective term

The non-linear advective term is evaluated, which takes on the following form in a well-defined coordinate system on a Euclidean manifold

$$V^j \nabla_j V^i = V^j \left(\frac{\partial V^i}{\partial z^j} + \Gamma^i_{jk} V^k \right). \tag{2.96}$$

The non-zero components of the advective term are then

$$\begin{aligned} V^j \nabla_j V^1 &= V^j \frac{\partial V^1}{\partial z^j} + \left(V^1\right)^2 - \left(V^2\right)^2 - \left(V^3\right)^2 \sin^2\left(z^2\right), \\ V^j \nabla_j V^2 &= V^j \frac{\partial V^2}{\partial z^j} + 2V^1 V^2 - \sin\left(z^2\right) \cos\left(z^2\right) \left(V^3\right)^2, \\ V^j \nabla_j V^3 &= V^j \frac{\partial V^3}{\partial z^j} + 2V^1 V^3 + \frac{2V^2 V^3}{\tan\left(z^2\right)}. \end{aligned}$$

2.3.4.2 The pressure gradient

Since the pressure is a scalar, the covariant derivative reduces to a partial derivative

$$\nabla^i P = z^{ij} \nabla_j P \tag{2.97}$$

$$= z^{ij} \frac{\partial P}{\partial z^j}. \tag{2.98}$$

The pressure term then reduces to the following three terms for the three components

$$\nabla^1 P = z^{11} \frac{\partial P}{\partial z^1} \tag{2.99}$$

$$\nabla^2 P = z^{22} \frac{\partial P}{\partial z^2} \tag{2.100}$$

$$\nabla^3 P = z^{33} \frac{\partial P}{\partial z^3}. \tag{2.101}$$

As opposed to the similarity coordinates the pressure terms consist of a single term for each components in SSC.

2.3.4.3 The Laplacian

In curvilinear coordinates the Laplacian of the contravariant velocity component takes the following form (see Appendix B for the derivation

of this form)

$$\nabla^j \nabla_j V^i = z^{jk} \left(\frac{\partial^2 V^i}{\partial z^j z^k} - \Gamma^l_{jk} \frac{\partial V^i}{\partial z^l} + 2\Gamma^i_{jl} \frac{\partial V^l}{\partial z^k} + \right. \\ \left. + v^m \left(\frac{\partial \Gamma^i_{jm}}{\partial z^k} + \Gamma^i_{kl} \Gamma^l_{jm} - \Gamma^l_{jk} \Gamma^i_{lm} \right) \right). \quad (2.102)$$

Evaluating (2.68) in SSC yields the following terms for the three components

$$\begin{aligned} \nabla^j \nabla_j V^1 &= z^{ij} \frac{\partial^2 V^1}{\partial z^i \partial z^j} + z^{11} \frac{\partial V^1}{\partial z^1} + z^{22} \left(\frac{\partial V^1}{\partial z^1} - 2 \frac{\partial V^2}{\partial z^2} \right) \\ &+ z^{33} \left(\frac{\partial V^1}{\partial z^1} \sin^2 z^2 + \frac{\partial V^1}{\partial z^1} \sin z^2 \cos z^2 + \right. \\ &- \left. 2 \sin^2 z^2 \frac{\partial V^3}{\partial z^3} - 2 V^2 \sin z^2 \cos z^2 \right) \quad (2.103) \\ \nabla^j \nabla_j V^2 &= z^{ij} \frac{\partial^2 V^2}{\partial z^i \partial z^j} + z^{11} \left(\frac{\partial V^2}{\partial z^1} + V^1 \right) + \\ &+ z^{22} \left(\frac{\partial V^2}{\partial z^1} + 2 \frac{\partial V^1}{\partial z^2} - V^2 \right) + \\ &+ z^{33} \left(\frac{\partial V^2}{\partial z^1} \sin^2 z^2 + \frac{\partial V^2}{\partial z^2} \sin z^2 \cos z^2 + \right. \quad (2.104) \\ &- \left. \frac{\partial V^3}{\partial z^3} \sin z^2 \cos z^2 + V^2 \sin^2 z^2 - V^3 \cos^2 z^2 \right) \\ \nabla^j \nabla_j V^3 &= z^{ij} \frac{\partial^2 V^3}{\partial z^i \partial z^j} + z^{11} \left(\frac{\partial V^3}{\partial z^1} + V^3 \right) + \\ &+ z^{22} \left(\frac{\partial V^3}{\partial z^1} + \frac{2}{\tan \theta} \frac{\partial V^3}{\partial z^2} - \frac{V^3}{\sin^2 \theta} + \frac{V^3}{\tan^2 \theta} \right) + \quad (2.105) \\ &+ z^{33} \left(\frac{\partial V^3}{\partial z^1} \sin^2 \theta + \frac{\partial V^3}{\partial z^2} \sin \theta \cos \theta + \frac{1}{\tan \theta} \frac{\partial V^2}{\partial z^3} + V^3 \right) \end{aligned}$$

The Navier-Stokes equations can now be written in SSC in terms of the physical velocity components.

2.3.4.4 Navier-Stokes equations in SSC

The Navier-Stokes are then formulated in physical form in SSC. The three-momentum equations corresponding to the three velocity compo-

nents, V^ξ, V^θ, and V^ϕ, are given in the following. The ξ-component

$$\begin{aligned}
\frac{\partial V^\xi}{\partial t} &+ \frac{V^\xi}{\sqrt{z_{11}}}\left(\frac{\partial V^\xi}{\partial \xi} - V^\xi\right) + \frac{V^\theta}{\sqrt{z_{22}}}\frac{\partial V^\xi}{\partial \theta} + \frac{V^\phi}{\sqrt{z_{33}}}\frac{\partial V^\xi}{\partial \phi} + \\
&+ \frac{\left(V^\xi\right)^2}{\sqrt{z_{11}}} - \frac{\left(V^\theta\right)^2}{\sqrt{z_{22}}} - \frac{\left(V^\phi\right)^2}{\sqrt{z_{11}}} = -\frac{\sqrt{z^{11}}}{\rho}\frac{\partial P}{\partial \xi} + \\
&+ \nu z^{11}\Bigg[\frac{\partial^2 V^\xi}{\partial \xi^2} + \frac{\partial^2 V^\xi}{\partial \theta^2} + \frac{1}{\sin^2\theta}\frac{\partial^2 V^\xi}{\partial \phi^2} + \frac{\partial V^\xi}{\partial \xi} - 2\frac{\partial V^\theta}{\partial \theta} + \\
&+ \frac{1}{\tan\theta}\left(\frac{\partial V^\xi}{\partial \xi} - V^\xi\right) - \frac{2}{\sin\theta}\frac{\partial V^\phi}{\partial \phi} - V^\xi - 2 z_{11} V^\theta \sin\theta\cos\theta\Bigg],
\end{aligned} \tag{2.106}$$

the θ-component

$$\begin{aligned}
\frac{\partial V^\theta}{\partial t} &+ \frac{V^\xi}{\sqrt{z_{11}}}\left(\frac{\partial V^\theta}{\partial \xi} - V^\theta\right) + \frac{V^\theta}{\sqrt{z_{22}}}\frac{\partial V^\theta}{\partial \theta} + \frac{V^\phi}{\sqrt{z_{33}}}\frac{\partial V^\theta}{\partial \phi} + \\
&+ 2\frac{V^\xi V^\theta}{\sqrt{z_{11}}} - \frac{1}{\tan\theta}\frac{\left(V^\phi\right)^2}{\sqrt{z_{11}}} = -\frac{\sqrt{z^{22}}}{\rho}\frac{\partial P}{\partial \theta} + \nu z^{22}\Bigg[\frac{\partial^2 V^\theta}{\partial \xi^2} + \\
&+ \frac{\partial^2 V^\theta}{\partial \theta^2} + \frac{1}{\sin^2\theta}\frac{\partial^2 V^\theta}{\partial \phi^2} + \frac{\partial V^\theta}{\partial \xi} + 2\frac{\partial V^\xi}{\partial \theta} + \frac{1}{\tan\theta}\frac{\partial V^\theta}{\partial \theta} + \\
&- \frac{1}{\tan\theta}\frac{\partial V^\theta}{\partial \phi} - \frac{V^\phi}{\tan^2\theta\sin\theta} + V^\xi - V^\theta\left(1 + z_{22}\right)\Bigg],
\end{aligned} \tag{2.107}$$

and the ϕ-component

$$\begin{aligned}
\frac{\partial V^\phi}{\partial t} &+ \frac{V^\xi}{\sqrt{z_{11}}}\frac{\partial V^\phi}{\partial \xi} + \frac{V^\theta}{\sqrt{z_{22}}}\frac{\partial V^\phi}{\partial \theta} + \frac{V^\phi}{\sqrt{z_{33}}}\frac{\partial V^\phi}{\partial \phi} + \\
&+ \frac{1}{\tan\theta}\frac{V^\theta V^\phi}{\sqrt{z_{11}}} = -\frac{\sqrt{z^{33}}}{\rho}\frac{\partial P}{\partial \theta} + \nu z^{33}\Bigg[\frac{\partial^2 V^\phi}{\partial \xi^2} + \frac{\partial^2 V^\phi}{\partial \theta^2} + \\
&+ \frac{1}{\sin^2\theta}\frac{\partial^2 V^\phi}{\partial \phi^2} - \frac{\partial V^\phi}{\partial \xi} + \frac{2}{\sin\theta}\left(\frac{\partial V^\phi}{\partial \xi} - V^\phi\right) + \\
&+ 3\frac{\cos\theta}{\sin^3\theta}\left(\frac{\partial V^\phi}{\partial \theta}\sin\theta - V^\phi\right) + \frac{\cos\theta}{\sin^3\theta}\frac{\partial V^\theta}{\partial \phi} + \frac{V^\phi}{\sin^3\theta} + \\
&+ V^\phi\left(\frac{1}{\sin\theta} + \frac{1}{\sin\theta\tan^2\theta}\right)\Bigg].
\end{aligned} \tag{2.108}$$

This form of the equations does not suffer from additional cross-couplings between components, due to the orthogonality of the coordinate system.

CHAPTER 3

Decomposition and Reconstruction of Vector Fields

The application of the LD has generally been restricted to fields expressed in orthogonal coordinate systems, at least within the fluid mechanics community. Due to the complexity of the similarity coordinates, we wish to obtain a general expression for the LD integral in order to easily relate the modes to the corresponding governing equations in similarity coordinates, or any other coordinate system for that matter. Our aim is in other words, to formulate the LD integral in tensor form. It is worth underlining that the eigenfunctions of the LD integral should be viewed as the constituents of a high-dimensional basis that spans the vector field. In the light of the previous chapter, the LD modes can be viewed as a set of globally orthogonal (covariant/contravariant) basis vectors - orthogonal in Hilbert space - but locally representing a curvilinear coordinate system which, in general, is not orthogonal. The analogies between the eigenfunctions and the covariant basis vectors are evident, as is the perception of the covariant basis as a vector field in its own right. The eigenfunctions are in this regard a more efficient basis in terms of spanning the velocity field, since the magnitude of their components decrease statistically for every added basis vector. The solution of the LD integral is thus a new optimized and locally curvilinear coordinate system, extracted from the velocity field itself.

3.1 The LD in Curvilinear Coordinates

The solution to the LD integral is a set of curvilinear coordinates, which are represented by the eigenfunctions. These are characterized by their statistical parallelism with the velocity field in Hilbert space, a feature quantified by the eigenvalues. The basis vectors we are searching to project the vector field onto are ensured to have two useful properties: 1) mutual orthogonality and 2) convergence. The former implies that the inner product of two different basis functions in Hilbert space is zero, while the latter implies that the cumulative sum of basis functions is guaranteed to converge towards the original velocity field as the number of bases are added.

The vector space choice for the projection is defined through the definition of the inner product, $(\cdot, \cdot)$. By requiring the vector space to be L^2 we are ensuring that the basis functions with which we wish to

span the velocity field constitute a Hilbert space, and thereby possess the advantageous properties mentioned above.

3.1.1 The LD formalism

In the formulation of the LD integral we restrict the function space to the weighted L^2-space for vector-valued functions

$$L^2_w\left(\Omega,\mathbb{C}^3\right) := \left\{\overline{\Phi} : \Omega \to \mathbb{C}^3 \middle| \int_\Omega \|\overline{\Phi}\|^2 w d\mu < \infty\right\}, \tag{3.1}$$

where $\Omega \subseteq \mathbb{R}^3 \times t$. The weighted L^2-inner product, $(\cdot,\cdot)_w$, of two vector-valued functions, $\overline{\Phi},\overline{\Psi} \in \Omega$, with the weight, $w : \mathbb{R} \mapsto \mathbb{R}_{>0}$, is defined in terms of the inner product

$$(\cdot,\cdot) : \mathbb{C}^3 \times \mathbb{C}^3 \mapsto \mathbb{C}, \tag{3.2}$$

such that

$$\left(\overline{\Phi},\overline{\Psi}\right) = \overline{\Phi}\cdot\overline{\Psi}^*, \tag{3.3}$$

where

$$\|\overline{\Phi}\| = (\overline{\Phi},\overline{\Phi})^{\frac{1}{2}}. \tag{3.4}$$

The L^2_w-inner product can then be formulated as

$$(\overline{\Phi},\overline{\Psi})_w = \int_\Omega \left(\overline{\Phi},\overline{\Psi}\right) w d\mu. \tag{3.5}$$

Here μ collectively designates the differential volume for both space and time, $\mu = \left\{z^i, t\right\}$ and the corresponding norm is defined as

$$\|\overline{\Phi}\|_w = (\overline{\Phi},\overline{\Phi})^{\frac{1}{2}}_w. \tag{3.6}$$

Since $L^2_w\left(\Omega,\mathbb{C}^3\right)$ is a Hilbert space the LD integral takes the form, Holmes, Lumley, and Berkooz 2012

$$\overline{R}\,\overline{\Phi} = \left\langle \overline{v}\left(\overline{\Phi},\overline{v}\right)_w\right\rangle = \lambda\overline{\Phi}, \tag{3.7}$$

where $\overline{R}$ is self-adjoint with respect to the L^2_w-inner product (Appendix C).

We then formulate the inner product in curvilinear coordinates by decomposing $\overline{\Phi}$ and $\overline{v}$ in terms of their covariant basis vectors and by introducing the tensor notation

$$\left(\overline{\Phi},\overline{v}\right)_w = \int_\Omega v^*_{\hat{i}}\varphi^{\hat{i}}\hat{w}d\hat{\mu}, \tag{3.8}$$

where the hat over the index is used to indicate the coordinate that is being integrated over, and the asterisk denotes the complex conjugate. The expression (3.7) can be written compactly in invariant form as

$$\int_{\Omega} \overline{G} d\hat{\mu} = \lambda \overline{\Phi}, \tag{3.9}$$

where

$$\overline{G} = \left\langle \overline{v} v_{\hat{i}}^{*} \right\rangle \varphi^{\hat{i}} \widehat{w}. \tag{3.10}$$

Taking the divergence of (3.9) shows that for a divergence-free fluid, the eigenvectors are also divergence-free. By decomposing $\overline{v}$ and $\overline{\Phi}$ in terms of their covariant basis vectors, $\overline{v} = v^i \overline{z}_i$ and $\overline{\Phi} = \varphi^i \overline{z}_i$, we can rewrite (3.9) in component form

$$\boxed{\int_{\Omega} R_{\cdot\hat{i}}^{i} \varphi^{\hat{i}} \widehat{w} d\hat{\mu} = \lambda \varphi^{i},} \tag{3.11}$$

where the two-point covariant-contravariant correlation tensor is defined as $R_{\cdot\hat{i}}^{i} = \left\langle v^i v_{\hat{i}}^{*} \right\rangle$, and, $(\cdot)$, is used as a placeholder to indicate the ordering of the indices in the second order mixed tensor. This expression can be converted to arithmetic form in order to yield

$$\boxed{\int_{\Omega} R_{\cdot\hat{i}}^{i} \varphi^{\hat{i}} \widehat{w} \sqrt{\widehat{Z}} d\mu^{\widehat{4}} = \lambda \varphi^{i},} \tag{3.12}$$

where $\widehat{Z}$ is the determinant of the covariant metric tensor evaluated at the integration point, and $d\mu^{\hat{4}}$ represents the four differential elements of the coordinate system.

Extending the tensor notation to elements of $L_w^2\left(\Omega, \mathbb{C}^3\right)$, the inner product between bases can be expressed as

$$\delta_{\beta}^{\alpha} = \left(\overline{\Phi}^{\alpha}, \overline{\Phi}_{\beta} \right)_w, \tag{3.13}$$

where the Greek indices denote the basis elements in $L_w^2\left(\Omega, \mathbb{C}^3\right)$. Since the bases are orthonormal the placement of the Greek indices in the sub- and superscript is chosen in order to support the Einstein summation convention. It is therefore worth noting that lowering the index in (3.13) yields the metric tensor. Since this tensor is an identity operator due to the orthonormality criterion, it is likewise denoted by a delta

$$\delta_{\alpha\beta} = \left(\overline{\Phi}_{\alpha}, \overline{\Phi}_{\beta} \right)_w. \tag{3.14}$$

Analogous to the decomposition of the vector field with respect to the covariant basis, we can decompose $\overline{v}$ in terms of the eigenfunctions

$$\overline{v} = v^{\alpha} \overline{\Phi}_{\alpha}, \tag{3.15}$$

where the vector coefficients are obtained by a projection of the instantaneous field onto the new basis. This is achieved by taking the inner product of (3.15) and $\overline{\Phi}^{\beta}$ to yield

$$v^{\alpha} = \left(\overline{v}, \overline{\Phi}^{\alpha}\right)_{w}. \tag{3.16}$$

The indices are $\alpha = 1, 2, ..., n$, where n is the dimensionality of the new space. Observe, that we have chosen to denote the coefficients in (3.15), in a very similar manner to the contravariant vector components in (2.2), namely with the letter, v. The difference between the components in the two spaces is designated by the Greek indices which will consistently be used for elements of L^2_w. From this it is clear that the v^{α} are the " velocity" components with respect to the covariant basis vectors $\overline{\Phi}_{\alpha}$.

The total kinetic energy of the field can be obtained from the eigenfunctions by the L^2_w-inner product of the velocity field with itself, by decomposing the velocity components as (3.15)

$$\left(\overline{v}, \overline{v}\right)_{w} = v^{\alpha} v^{*}_{\alpha}. \tag{3.17}$$

Ensemble averaging (3.17), yields the averaged total kinetic energy of the field

$$\lambda = \left\langle v^{\alpha} v^{*}_{\alpha} \right\rangle. \tag{3.18}$$

The formulation of the LD in curvilinear coordinates, (3.12) allows us to evaluate certain flows and coordinate systems in terms of the optimal basis functions in that particular coordinate system. Coordinate transforms can be applied in combination with (3.12) in the search for symmetries between the integrand and the right-hand-side of (3.12). And if symmetries can be shown to exist, the optimal family of eigenfunctions can be identified. This form is especially practical for self-preserving flows, such as far-field regions of jets and wakes, and possibly even fully developed boundary layers. It even allows the application of convected coordinates where the metric tensor is time-dependent, which may be useful in case of accelerated flows.

In the introduction of this chapter the vector-valued basis functions in $L^2_w\left(\mathbb{R}^3\right)$ were described as globally orthogonal and locally curvilinear. This is worth demonstrating, since there is a subtle distinction between the definition of orthogonality between elements in $L^2_w\left(\mathbb{R}\right)$ and those in $L^2_w\left(\mathbb{R}^3\right)$. Since the elements of the two vector spaces are one- and three-dimensional scalar- and vector valued functions, respectively, the latter involves a summation over the components, i, in addition to the integration over the domain. This is seen by expanding (3.13) and invoking the self-adjoint property of the covariant basis vectors

$$\delta^{\alpha}_{\beta} = \left(\varphi^{i\alpha}, \varphi_{i\beta}\right)_{w}, \tag{3.19}$$

which means that $\varphi^{i\alpha}$ and $\varphi_{j\alpha}$ are in general not orthogonal with respect to the L^2_w-inner product. This inner product can therefore be written as

$$\gamma^i_j \delta^\alpha_\beta = \left(\varphi^{i\alpha}, \varphi_{j\beta}\right)_w , \tag{3.20}$$

where the elements of γ^i_j are not restricted to the values 0 and 1. The expression (3.20) only reduces to the orthogonality criterion, (3.13), if $j = i$. This means that even for a Cartesian coordinate system spanning $\mathbb{R}^3$ the assumption of orthogonality between individual components of the L^2_w-basis is in general incorrect for $\alpha \neq \beta$.

For a curvilinear coordinate system spanning $\mathbb{R}^3$ we can rewrite (3.19) to a contravariant form

$$\delta^\alpha_\beta = \left(z_{ij}\varphi^{i\alpha}, \varphi^j_\beta\right)_w , \tag{3.21}$$

and we discover that the right-hand-side of (3.21) can represent up to nine non-zero terms, as opposed to the three non-zero contributions for orthogonal coordinates. Note that it is then possible to identify any contribution to the TKE in a general coordinate system by expanding the averaged canonical inner product in (3.17) in terms of the eigenfunctions

$$\langle(\overline{v}, \overline{v})\rangle = \lambda z_{ij}\varphi^{i\alpha}\varphi^{j*}_\alpha , \tag{3.22}$$

which means that in general coordinates, some contributions to the TKE come from the shear-stresses, e.g. in the case of $i = 1$ and $j = 2$.

In the following, the expression (3.12) will be used to deduce the eigenfunctions in similarity coordinates and in SSC. This will lead to a discussion regarding the effect dimensionality of the domain has on the eigenfunctions, and the role of the weight function in the definition of the inner product.

3.1.2 The LD in similarity coordinates

The far-field region of the flow has two important characteristics that are relevant for this analysis: the streamwise mean velocity evolution, and the turbulent scale evolution with streamwise position. One could then ask if it is possible to choose a coordinate system such that the flow becomes homogeneous with respect to this new basis. This is analogous to asking whether there exists a coordinate system such that the two-point correlation tensor - volume element product, $R^i_{i'}\sqrt{Z'}$, is exclusively a function of the separation coordinate, $\zeta = \xi' - \xi$ along the ξ-coordinate. If so, it would infer that the eigenfunctions are trigonometric polynomials with respect to this new basis, Lumley 1967a. In order to test whether the coordinate system proposed by Ewing et al. 2007 yields a homogeneous flow field in the case of the turbulent jet, we

note that the mean velocity evolves as $1/\delta(x)$ and the scale growth is proportional to $\delta(x)$ in Cartesian coordinates. The proposed system involves a logarithmic stretching of the streamwise coordinate, motivated by the linear growth of scales with streamwise position. The logarithmic stretching is imposed in order to "counteract" the growth of scales in the new system, (2.40). This is demonstrated by evaluating the distance measure along the ξ-coordinate

$$\zeta = \xi' - \xi = \ln\left(1 + \frac{r}{x - x_0}\right), \tag{3.23}$$

where $r = |x' - x|$, is the Euclidean distance along the streamwise coordinate. Note that (3.23) can be approximated as, $\ln(1 + r/x)$ for $x >> x_0$. This shows that if the scale growth is proportional to the streamwise coordinate, $r \propto x$, then ζ is constant.

The second factor to consider is the evolution of the streamwise mean velocity, U_c. Since for Cartesian coordinates, $U_c(x) = ABM_0^{1/2}/\delta$, Hussein, Capp, and George 1994, where $B = 2/\sqrt{\pi}B_u$ is the velocity decay constant and $M_0 = \pi/4U_0^2D^2$, where U_0 is the velocity at the nozzle lip. This implies that the mean streamwise velocity component with respect to the covariant basis of the similarity coordinates is defined as

$$\widetilde{U}_c = \frac{A^2BM_0^{\frac{1}{2}}}{\delta^2}. \tag{3.24}$$

By decomposing the contravariant velocity components, and metric tensor, and introducing the weight function

$$v^i = \tilde{v}^i\widetilde{U}_c, \tag{3.25}$$

$$z_{\hat{i}\hat{j}} = \tilde{z}_{\hat{i}\hat{j}}\hat{\delta}^2, \tag{3.26}$$

$$\widehat{w} = e^{-\hat{\xi}}, \tag{3.27}$$

the following form of the four-dimensional LD integral in similarity coordinates is obtained from (3.12)

$$\int_\Omega \widetilde{R}^j_{\cdot\hat{j}}\tilde{\varphi}^{\hat{j}}\widehat{\eta}d\mu^{\widehat{4}} = \tilde{\lambda}\tilde{\varphi}^j, \tag{3.28}$$

where

$$\widetilde{R}^j_{\cdot\hat{j}} = \tilde{z}_{\hat{j}\hat{k}}\left\langle\tilde{v}^j\tilde{v}^{\hat{k}}\right\rangle, \tag{3.29}$$

$$\tilde{\varphi}^{\hat{j}} = \hat{\delta}^2\varphi^{\hat{j}}, \tag{3.30}$$

$$\tilde{\varphi}^j = \delta^2\varphi^j, \tag{3.31}$$

$$\tilde{\lambda} = \lambda/\left(A^4B^2DM_0\right). \tag{3.32}$$

The scaled correlation tensor, $\widetilde{R}^j_{\hat{j}}$, is exclusively a function of the separation in the ξ-direction. The exponentially decaying weight function, (3.27), is applied in order to remove the dependence of the integrand on e^{ξ}. Note that this choice of weight function fulfills the necessary requirements in order for the weighted inner product space, (3.1), to be a Hilbert space. The weight function is necessary if the eigenfunctions in the ξ-direction are to be identified as Fourier coefficients. This has gone unnoticed prior to the present work. In the work of Ewing 1995 and Wänström 2009 the velocities that were applied in the LD were the cylindrical physical velocity components scaled by the local centerline velocity. The volume element i.e. $\sqrt{Z}$, for the similarity coordinates was then assumed to be η. Here it is shown that the latter is in fact ξ-dependent as seen from (2.49). Note that the same weight function, (3.27), appears in the inner product of Laguerre polynomials, in order to ensure their integrability. In the current case the weight effectively ensures that the new differential element in the streamwise direction remains constant

$$const = d\xi = Adx/\delta, \tag{3.33}$$

where dx represents the differential element in Cartesian coordinates. From this it is seen that a constant $d\xi$ in fact implies an increasing differential element, dx, in physical space for increasing x. In practice, for the jet far-field, the weight means that the inner-product must be defined with respect to this weight as well, as indicated throughout section 3.1.1.

We now introduce the following coordinate transformations, Ewing et al. 2007, Wänström 2009

$$\zeta = \widehat{\xi} - \xi, \tag{3.34}$$

$$\Theta = \widehat{\theta} - \theta, \tag{3.35}$$

$$T = \widehat{t} - t, \tag{3.36}$$

which yields the following form of the LD integral

$$\int \eta \int \widetilde{R}^j_{\cdot\hat{j}} \tilde{\varphi}^{\hat{j}} d\zeta d(\hat{\cdot}) = \tilde{\lambda} \tilde{\varphi}^j. \tag{3.37}$$

This means that $\tilde{\varphi}^i$ in (3.28), can be represented by a Fourier expansion along the ξ-coordinate, by following an analogous rationale to that of Lumley 1967b for the case of homogeneous turbulence in Cartesian coordinates. We assume the following form, but for the contravariant, scaled eigenfunctions in similarity coordinates

$$\boxed{\tilde{\varphi}^j = \widetilde{\Psi}^j(\omega, \kappa, \eta, m) e^{i(t\omega + \kappa\xi + m\theta)},} \tag{3.38}$$

where Ψ^j are the eigenfunctions along the η-coordinate. We then obtain the following expression for the LD integral in similarity coordinates

$$\boxed{\int \Omega^j_{\cdot\hat{j}} \Psi^{\hat{j}} \hat{\eta} d\hat{\eta} = \tilde{\lambda} \Psi^j,} \tag{3.39}$$

where

$$\boxed{\Omega^j_{\cdot\hat{j}} = \int\int\int \tilde{R}^j_{\cdot\hat{j}} e^{-i(T\omega+\kappa\zeta+m\Theta)} dT d\zeta d\Theta.} \tag{3.40}$$

It is worth mentioning that the Fourier transform defined on L^2_w requires the function in question, to be well-defined on L^2_w. In practice, this is not an issue, since the extent of the domain is limited. For an ideal turbulent free jet, however, this creates a problem since the vector field is unbounded in the ξ-direction. This is addressed by redefining the weight-function, (3.27), to $w = e^{-\xi(1+\xi)}$.

The contravariant components of the eigenfunctions are retrieved from (3.31) in order to obtain

$$\boxed{\varphi^j = \Psi^j \frac{e^{i(t\omega+\kappa\xi+m\theta)}}{\delta^2}.} \tag{3.41}$$

The expression (3.41) shows that the contravariant components of the modes in similarity coordinates are spatially decaying Fourier modes. Since φ^j is a tensor the eigenfunctions transform to any well-defined coordinate system, Z'', by applying the Jacobian operator

$$\varphi^{j''} = \varphi^j J^{j''}_j, \tag{3.42}$$

which is useful for evaluating the modes in more familiar coordinate systems (such as Cartesian or cylindrical coordinates). The physical components for the similarity coordinates can be obtained from (2.10) and (2.47) in order to yield

$$\varphi[1] = \Psi^1 \sqrt{\eta^2 + A^{-2}} \frac{e^{i(t\omega+\kappa\xi+m\theta)}}{\delta}, \tag{3.43}$$

$$\varphi[2] = \Psi^2 \frac{e^{i(t\omega+\kappa\xi+m\theta)}}{\delta}, \tag{3.44}$$

$$\varphi[3] = \Psi^3 \eta \frac{e^{i(t\omega+\kappa\xi+m\theta)}}{\delta}. \tag{3.45}$$

The magnitudes of the eigenfunctions in (3.43) vary slightly along η (see figure 2.1), due to the non-orthogonality of similarity coordinates. This magnitude variation due to the varying bases is less than 4% across the width of the jet.

Attempts have been made before to formulate the modes in the streamwise direction of the jet by Ewing et al. 2007 who suggested that the streamwise direction would be Fourier modes for the scaled field. This was later implemented by Wänström 2009. Neither, however, realized the streamwise variation of the basis vectors, in their formulation of the velocity field. The current derivation yields the modes for the physical velocities themselves, and not the scaled velocity field, which is usually the approach required by equilibrium-similarity theory. It thus provides an expression for the eigenfunctions which correspond to the common intuition one has about the far-field. Namely that it is not homogeneous along ξ, but that it can nevertheless be expressed in terms of Fourier coefficients - with a decaying amplitude. The additional insight, however, is that the inner product for the jet far-field must be defined in terms of the weight function, (3.27) if the modes are to be identified as Fourier modes in similarity coordinates.

It is easily demonstrated that decaying Fourier modes are obtained for a weight function of value unity if the coordinate system is defined in two dimensions. This is seen by setting $\theta = 0$ in the definition of the similarity coordinates (2.40)-(2.42). In two spatial dimensions the volume element, (2.49), becomes an area element and the modes can again be defined as decaying Fourier modes. It is worth noting, however, that the decaying amplitude of the streamwise modes is a strict necessity in order to maintain a constant energy flux through each cross-section of the fully-developed region. As the wavelength increases with ξ, due to the logarithmic stretching, the amplitude of the wave must decrease correspondingly. Parallels can be drawn here to water waves progressing along a linear inclination towards the shore. The linear waves increase in height and decrease in length as they move up the slope in order to (in the ideal case) conserve their energy. In this regard, the current eigenfunctions represent the reversed case where waves progress away from shore, such that the wave height decreases with increasing wave length.

3.1.3 The LD in SSC

The self-adjointness of the operator $\overline{R}$ in (3.7) is only one of two criteria that have to be met if we wish to decompose the flow field with respect to orthonormal modes using regular matrix operations. The second criteria is Hermitian symmetry of the matrix representation of $\overline{R}$. The latter is in general not guaranteed by the self-adjointness of the operator, even in finite dimensional spaces. Its importance becomes evident when solving the LD integral using matrix operations, where the orthogonality of the LD modes is only guaranteed if the operator is self-adjoint *and* its matrix representation is Hermitian symmetric. It is seen from (3.40) that $\Omega^{j}_{\cdot\hat{j}}$

is not equal to its Hermitian counterpart. In other words

$$\Omega_{\hat{j}}^{\cdot j} - \Omega_{j}^{\cdot \hat{j}*} = 0, \tag{3.46}$$

is only guaranteed in orthonormal coordinate systems, Gel fand 1961, Lax 2007, Grinfeld 2013, and therefore fails to hold in similarity coordinates.

In similarity coordinates, the non-zero off-diagonal terms introduce an asymmetry in the two-point correlation matrix. The symmetrization of this matrix may, however, be achievable through similarity transformations (these are not to be confused with the similarity coordinates used in this work), Golub and Van Loan 2013, which involve rewriting an asymmetric matrix in terms of a matrix-product of two symmetric matrices. This procedure, however, is not straight forward for the case of the two-point correlation matrix in similarity coordinates. Instead the LD will be expressed in SSC (see figure 2.2) which have the advantage of spanning an orthogonal system.

We now introduce a new definition of the characteristic velocity in SSC, which depends on the absolute distance from $x = x_0$. From (3.24) we can rewrite the scaled centerline velocity as

$$\widetilde{U}_c = \frac{B M_0^{\frac{1}{2}}}{\left(De^{\xi}\right)^2}, \tag{3.47}$$

such that we can write the velocity components, metric tensor and weight function as

$$v^i = \tilde{v}^i \widetilde{U}_c \tag{3.48}$$

$$z_{\hat{i}\hat{j}} = \tilde{z}_{\hat{i}\hat{j}} D^2 e^{2\hat{\xi}} \tag{3.49}$$

$$\widehat{w} = e^{-\hat{\xi}}. \tag{3.50}$$

From the following definitions of coordinates

$$\zeta = \widehat{\xi} - \xi, \tag{3.51}$$

$$\Theta = \widehat{\phi} - \phi, \tag{3.52}$$

$$T = \widehat{t} - t, \tag{3.53}$$

the LD integral in SSC takes on the following form

$$\int \widetilde{R}_{\cdot \hat{j}}^{j} \tilde{\varphi}^{\hat{j}} \sin\widehat{\theta} d\widehat{\mu^4} = \tilde{\lambda} \tilde{\varphi}^{j}, \tag{3.54}$$

where

$$\widetilde{R}^{j}_{\cdot\hat{j}} = \tilde{z}_{\hat{j}\hat{k}} \left\langle \tilde{v}^{j} \tilde{v}^{\hat{k}} \right\rangle, \tag{3.55}$$

$$\tilde{\varphi}^{\hat{j}} = D^2 e^{2\hat{\xi}} \varphi^{\hat{j}}, \tag{3.56}$$

$$\tilde{\varphi}^{j} = D^2 e^{2\hat{\xi}} \varphi^{j}. \tag{3.57}$$

$$\tilde{\lambda} = \lambda / \left(B^2 D M_0 \right). \tag{3.58}$$

It is then possible to perform the equivalent procedure to the one in section 3.1.2 in order to obtain the following expression for the decomposition of the flow with respect to Fourier modes in t and in the ξ-, and ϕ-direction. Writing the eigenfunctions in the following form

$$\boxed{\tilde{\varphi}^{j} = \widetilde{\Psi}^{j}(\omega, \kappa, \theta, m) e^{i(t\omega + \kappa\xi + m\phi)},} \tag{3.59}$$

where $\widetilde{\Psi}^{j}$ are the eigenfunctions along the θ-coordinate, we obtain the following expression for the LD integral in SSC

$$\boxed{\int \widetilde{\Omega}^{j}_{\cdot\hat{j}} \widetilde{\Psi}^{\hat{j}} d\hat{\theta} = \tilde{\lambda} \widetilde{\Psi}^{j},} \tag{3.60}$$

where

$$\boxed{\widetilde{\Omega}^{j}_{\cdot\hat{j}} = \int\int\int \tilde{R}^{j}_{\cdot\hat{j}} e^{-i(T\omega + \kappa\zeta + m\Theta)} \sqrt{\sin\theta \sin\hat{\theta}} dT d\zeta d\Theta.} \tag{3.61}$$

This form resembles greatly the form (3.40), where the only difference is that (3.46) is satisfied. Note that we have applied a similarity transformation of the integrand in (3.60), by

$$\widetilde{\Psi}^{j} = \Psi^{j} / \sqrt{\sin\theta}. \tag{3.62}$$

We now have the formulation of the LD in SSC which allows us to solve the integral equation using standard matrix operations. One should note that the two-point correlation in SSC, unlike the case of similarity coordinates, is taken along a curved line (circle segment), in the θ-direction. The fact that the modes do not expand the flow at the same points in space makes a direct comparison between the modes in the two coordinates more complicated. An argument can, however, be made that for small θ the θ-coordinates resembles straight lines. This assumption can be invoked for the cross-plane measurements (chapter 5), where data was sampled on a flat plane, contrary to a spherical shell dictated by the SSC.

3.2 Galerkin projection

With the aim of gaining a deeper understanding of the energy transport in the turbulent jet far-field, the velocity field can be spanned by the modes themselves. It is therefore possible to reconstruct the terms of the energy equation, (2.33), using the eigenfunctions as a basis. With this purpose in mind, we constrain the set of basis functions to $L^2_w\left(\Omega, \mathbb{C}^3\right)$, and define the vector field in terms of this basis. From the invariance of the fluctuating part of the velocity we can write

$$v^i \overline{z}_i = v^\alpha \overline{\Phi}_\alpha, \tag{3.63}$$

where $\overline{\Phi}_\alpha = \varphi^i_\alpha \overline{z}_i$. By suppressing the covariant basis vectors, the relation (3.63) yields

$$v^i = v^\alpha \varphi^i_\alpha. \tag{3.64}$$

This means that φ^i_α plays the role of a shift-tensor and is therefore an operator that projects a tensor onto the n-dimensional manifold spanned by the eigenfunctions. Note, however, that the use of the term here should be understood in terms of zero curvature, which is a direct consequence of the linearity of the LD operator. In the following, we will discuss the interpretations of the terms of the ensemble averaged TKE equation, and not least what they can tell us about the turbulent jet far-field as well as turbulent flows in general.

3.2.1 Turbulence kinetic energy equation

Expanding the energy equation in terms of the basis functions yields the following expressions for the terms in (2.33)

$$I : \frac{D}{Dt}\frac{1}{2}\left\langle v_\alpha v^{\beta *} \varphi^\alpha_i \varphi^{i*}_\beta \right\rangle, \tag{3.65a}$$

$$II : \left\langle v_\alpha v^{\beta *} \varphi^\alpha_i \varphi^{j*}_\beta \right\rangle \nabla_j \left\langle V^i \right\rangle, \tag{3.65b}$$

$$III : \frac{1}{2}\nabla_j \left\langle v_\alpha v^{\beta *} v^\gamma \varphi^\alpha_i \varphi^{i*}_\beta \varphi^j_\gamma \right\rangle, \tag{3.65c}$$

$$IV : \frac{1}{\rho}\nabla_i \left\langle v^\alpha \varphi^i_\alpha p \right\rangle, \tag{3.65d}$$

$$V : \nu\left(\nabla_j \left\langle v^\alpha \varphi_{i\alpha} \nabla^j v^{\beta *} \varphi^{i*}_\beta \right\rangle + \nabla_j \left\langle v^\alpha \varphi_{i\alpha} \nabla^i v^{\beta *} \varphi^{j*}_\beta \right\rangle\right), \tag{3.65e}$$

$$VI : \nu\left\langle \nabla^j v^\alpha \varphi^i_\alpha \nabla_j v^{\beta *} \varphi^*_{i\beta} + \nabla^i v^\alpha \varphi^j_\alpha \nabla_j v^{\beta *} \varphi^*_{i\beta} \right\rangle. \tag{3.65f}$$

Since the eigenfunctions are deterministic and the coefficients are coordinate independent, we can rewrite $I - VI$ by invoking (3.18) to obtain

the following forms of the ensemble averaged energy equation

$$I : \frac{\lambda}{2}\frac{D}{Dt}\varphi_i^\alpha \varphi_\alpha^{i*}, \tag{3.66a}$$

$$II : \lambda \varphi_i^\alpha \varphi_\alpha^{j*} \nabla_j \left\langle V^i \right\rangle, \tag{3.66b}$$

$$III : \frac{1}{2}\left\langle v_\alpha v^{\beta *} v^\gamma \right\rangle \varphi_\gamma^j \nabla_j \varphi_i^\alpha \varphi_\beta^{i*}, \tag{3.66c}$$

$$IV : \frac{1}{\rho}\varphi_\alpha^i \left\langle v^\alpha \nabla_i p \right\rangle, \tag{3.66d}$$

$$V : \nu\lambda \left(\nabla_j \left(\varphi_i^\alpha \nabla^j \varphi_\alpha^{i*} \right) + \nabla_j \left(\varphi_i^\alpha \nabla^i \varphi_\alpha^{j*} \right) \right), \tag{3.66e}$$

$$VI : \nu\lambda \left(\nabla^j \varphi^{i\alpha} \nabla_j \varphi_{i\alpha}^* + \nabla^i \varphi^{j\alpha} \nabla_j \varphi_{i\alpha}^* \right). \tag{3.66f}$$

We note that in (3.66) a summation over repeating indices is implied, where the eigenvalue $\lambda = \lambda^\alpha$ should be included in the summation. The interpretation of the turbulence energy equation (3.66) is subject to the definition of the $L_w^2(\Omega, \mathbb{C}^3)$-inner product, which in this case is determined by the choice of the weight. In case of a unit weight the λ^α represent the total turbulence kinetic energy of the field related to mode α. In case of a non-unit weight (3.66) should be viewed as a weighted energy equation.

For a self-adjoint LD operator, the eigenvalues are guaranteed to be non-zero. Since self-adjointness ensures that φ_α^i cannot be zero in the *entire* domain *simultaneously*, for turbulent flows characterized by a self-adjoint LD operator this directly implies that *all modes* must exchange energy with the mean flow in the presence of mean gradients. The degree to which this occurs in the domain is determined by the corresponding eigenvalue-eigenfunction combination. Note that this is the necessary theoretical support for the hypothesis in Wänström 2009 stating that multiple modes are able to obtain their energy directly from the mean flow. This energy transport from the mean flow to a wide range of modes is, in the presence of mean gradients, closer to being the norm than the exception.

Term III governs the non-linear energy transport caused by velocity fluctuations. We see that the term regulates the energy fluxes within- and across modes and this energy exchange is not directly dependent on the mean TKE, λ, but is instead dependent on the instantaneous TKE with a v^γ modulation, where the latter works as a Lagrangian multiplier together with φ_γ^j. The process is governed by the modal interactions between modes α, β, and γ, which in the case of Fourier modes is traditionally coined as *triadic interactions*. From prior discussions, we know that all modes must have non-zero coefficients, which means that the coefficients in (3.66b) determine the intensity of the modal energy transport across the jet. The key, however, to understanding the spatial

distribution of the energy transport can be found in the eigenfunctions. We can immediately infer that the energy transfer is zero at all nodes of φ_γ^j. We see that there is no energy transfer when the spatial derivatives of $\varphi_i^\alpha \varphi_\beta^{i*}$ are zero. We also observe that the energy transfer is maximized in flow regions where the local extrema of φ_γ^j coincide with the maximum gradient of $\varphi_i^\alpha \varphi_\beta^{i*}$. For $\alpha = \beta = \gamma$ expression (3.66b) defines the non-linear energy transfer within a given mode - or in other words the extent to which the individual modes redistribute their energy over the domain (space and time).

If α, β, and γ in (3.66b) correspond to the most energetic modes, we would expect the eigenfunctions to exhibit negligible spatial gradients. This is because the distance between the local extrema would be relatively large i.e., the number of local extrema would be relatively small over the span of the flow, which would infer smaller gradients. For low-energy eigenfunctions, where the number of local extrema is generally high over the span of the flow we see from (3.66b) that the non-linear energy transfer would be significant. On average, energy transfer would be greatest between modes with similar energy-levels, a phenomenon that is most commmonly seen at high mode numbers (corresponding to low energies). Since φ_i^α are continuously varying over the domain, it shows that the process of energy transport is very dynamic indeed, and for most turbulent flows it is continuously varying. It is especially interesting to classify the extent of energy exchanged between adjacent modes especially those which are closely spaced in terms of energy as well as the non-linear energy transfer in regions where the energy spectra exhibit the $-5/3$-slope.

Terms V and VI are the modal representations of the viscous transport and dissipation. Both terms are dependent on nonzero modal gradients in order to be present in the flow. Furthermore, since both terms are proportional to λ and are finite we note that the suprema of V and VI must necessarily be bounded by the opposing characteristics of the eigenvalues (representing the turbulence kinetic energy) and modal gradients; large eigenvalues must be balanced by small modal gradients in order to ensure a balanced energy dissipation. We also note that since the eigenvalues are non-zero dissipation also remains non-zero for all modes, since the solutions of (3.7) are non-trivial. If we assume that dissipation takes place predominantly at high mode numbers we notice that unlike the energy production, it will necessarily be distributed more or less homogeneously across the entire domain, due to the increasing number of local extrema related to high mode numbers. In fact, as will be seen in section 4.3.3, high mode number eigenfunctions have significant complex parts. The dissipation of a given mode may in some way be related to

the imaginary part of the modes, and this characteristic may potentially be used as a indicator of the level of dissipation a given mode produces. If there is a direct relation between the magnitude of the imaginary part and the level of dissipation a given mode produces, it may have a profound effect on efficient modeling of dissipation in general turbulence flows. Moreover, it could be used to determine how forcing, such as accelerations affect the dissipation in a turbulent flows and which modes are responsible for these effects.

3.3 Numerical implementation of LD in SSC

It is the aim of this section to illustrate how the matrix implementation of the LD in SSC should be performed. In the following the implementation will be performed with respect to scaled contravariant velocity components consistent with the preceding sections. In order to formulate the integral eigenvalue problem in similarity coordinates, (3.39), in matrix form we must first formulate the Jacobian operator and the metric tensor in matrix form. The first and second indices of the tensors refer to rows and columns, respectively, where the upper index of the Jacobian is considered to designate the row number. Initially, the contravariant velocity components are obtained from the Cartesian velocity components using standard linear algebraic methods. Hereafter, the implementation of the LD is defined for the full four-dimensional decomposition.

3.3.1 Contravariant velocity components

The contravariant velocity components in similarity coordinates are defined in vector form in the following manner

$$\mathbf{v} = \left[v^1 v^2 v^3\right]^T, \tag{3.67}$$

where the T in the superscript designates the transpose operator. The Jacobian operators are expressed analogously to the tensors

$$\mathbf{J} = \begin{bmatrix} \cos\theta/De^{\xi} & \sin\theta\cos\phi/De^{\xi} & \sin\theta\sin\phi/De^{\xi} \\ -\sin\theta/De^{\xi} & \cos\theta\cos\phi/De^{\xi} & \cos\theta\sin\phi/De^{\xi} \\ 0 & -\sin\phi/De^{\xi}\sin\theta & \cos\phi/De^{\xi}\sin\theta \end{bmatrix} \tag{3.68}$$

$$\mathbf{J}^{-1} = \begin{bmatrix} De^{\xi}\cos\theta & -De^{\xi}\sin\theta & 0 \\ De^{\xi}\sin\theta\cos\phi & De^{\xi}\cos\phi & -De^{\xi}\sin\theta\sin\phi \\ De^{\xi}\sin\theta\sin\phi & De^{\xi}\cos\theta\sin\phi & De^{\xi}\sin\theta\cos\phi \end{bmatrix} \tag{3.69}$$

and the covariant metric tensor is written from (2.47) as

$$\mathbf{Z} = \begin{bmatrix} D^2 e^{2\xi} & 0 & 0 \\ 0 & D^2 e^{2\xi} & 0 \\ 0 & 0 & D^2 e^{2\xi} \sin^2\theta \end{bmatrix}. \tag{3.70}$$

The contravariant metric tensor in matrix form is then the inverse of (3.70)

$$\mathbf{Z}^{-1} = \begin{bmatrix} 1/D^2 e^{2\xi} & 0 & 0 \\ 0 & 1/D^2 e^{2\xi} & 0 \\ 0 & 0 & 1/D^2 e^{2\xi} \sin^2\theta \end{bmatrix}. \tag{3.71}$$

The reciprocal relationship between the covariant- and contravariant metric tensors and Jacobian operators is manifested by the inverse relation between the corresponding matrix forms, which yields the identity matrix

$$\mathbf{I} = \mathbf{J}\mathbf{J}^{-1} = \mathbf{Z}\mathbf{Z}^{-1}. \tag{3.72}$$

The contravariant velocities in similarity coordinates, $\mathbf{v}$, are obtained from the Cartesian components, $\mathbf{v}'$, through the following matrix-vector product

$$\mathbf{v} = \mathbf{J}\mathbf{v}'. \tag{3.73}$$

Note that since the Jacobian is varying spatially, this transformation has to be performed for every spatial location in order to obtain the local contravariant velocity components.

3.3.2 Matrix implementation of the LD

In the current work the classical LD is applied exclusively along the inhomogeneous direction, which is the θ-coordinate for the SSC, whereas the projections along the ξ- and ϕ-directions are performed on trigonometric polynomials. The construction of the corresponding block matrix in SSC is seen from the analytical formulation of the integral eigenvalue problem of Fourier coefficients, (3.61), since we are in fact seeking to find the Ψ^j eigenfunctions in (3.60). For each combination of j and $\hat{j}$, $\widetilde{\Omega}^j_{\cdot\hat{j}}$ represents a square cross-correlation sub-matrix, each of which is an element of the block matrix, $\widetilde{\mathbf{\Omega}}^{(\kappa,m,n)}$. As indicated by the superscripts, the resulting operator is represented by a block matrix for each wavenumber κ, azimuthal harmonic m, and frequency n

$$\widetilde{\mathbf{\Omega}}^{(\kappa,m,n)} = \begin{bmatrix} \widetilde{\mathbf{\Omega}}^1_{\hat{1}} & \widetilde{\mathbf{\Omega}}^1_{\hat{2}} & \widetilde{\mathbf{\Omega}}^1_{\hat{3}} \\ \widetilde{\mathbf{\Omega}}^2_{\hat{1}} & \widetilde{\mathbf{\Omega}}^2_{\hat{2}} & \widetilde{\mathbf{\Omega}}^2_{\hat{3}} \\ \widetilde{\mathbf{\Omega}}^3_{\hat{1}} & \widetilde{\mathbf{\Omega}}^3_{\hat{2}} & \widetilde{\mathbf{\Omega}}^3_{\hat{3}} \end{bmatrix}, \tag{3.74}$$

where $\widetilde{\mathbf{\Omega}}^{j}_{\hat{j}} \in \mathbb{C}^{N\times N}$, and N is the number of discretization points in the radial direction. We can designate the discrete θ-coordinates as the sequence $\{\theta_k\}_{k=1}^{N}$ of equally spaced grid points with spacing $\Delta\theta$ and find the empirical eigenvalues and eigenvectors of (3.74). In the case when data is only obtained from a single plane the dimensions of the problem are naturally reduced.

CHAPTER 4

Streamwise Experiment

In the current chapter data from the streamwise PIV experiment of Hodzic 2014 is analyzed. The experiment was designed on the basis of the experiment of Wänström 2009, Wänström, George, and Meyer 2012, but was performed using higher resolution cameras. While the main analysis of the physical velocities will be performed in SSC, the analysis of data in similarity coordinates will be covered briefly in order to illustrate the impact that non-orthogonality of the coordinate system has on the representation of the field. It will be shown that especially the cross spectra will suffer large distortion at high wavenumbers due to this effect. Since the SSC and similarity coordinates do not coincide along the non-homogeneous coordinates θ and η, respectively for the two coordinate systems, it is not straight forward to compare the data between the systems. An attempt, will however be made to present the differences between the results of the two systems. The LD analysis, will on the other hand, only be performed in SSC due to the lack of Hermitian symmetry that similarity coordinates impose on the cross-correlation matrix (see section 3.1.3).

4.1 Experimental procedure

The experiment was performed in a tent with dimensions $2.5 \times 3.0 \times 10.0\,\mathrm{m}^3$, in order to minimize the induced backflow due to confinement, Hussein, Capp, and George 1994. The tent was sealed off during measurements and was seeded with tracer particles generated by an in-house seeding generator equipped with an atomizing laskin plexiglass nozzle producing glycerin droplets of approximately $2 - 3\,\mu$m. A fan was driving the flow and was placed inside the tent in order to ensure that air inside the jet-box had a similar concentration of seeding particles to the bulk of air inside the tent.

The fan supplied air through the back-side of a jet-box with inner dimensions $58.5 \times 58.5 \times 59\,\mathrm{cm}^3$, this particular jet-box was used originally in Gamard, Jung, and George 2004 and subsequently by Wänström 2009 in order to generate their $D = 1$cm jet. It was equipped with baffles and screens in order to break down any transient structures, and thus provide a nearly constant pressure field across the nozzle inlet. The axi-symmetrical nozzle design was based on fifth-order polynomials in order to create smooth contraction ratios from 60 mm to $D = 10\,\mathrm{mm}$. Before

commencing the data acquisition the fan was left running for approximately one hour in order to ensure that any transient effects have passed, as well as to ensure that the particle concentration had approached a homogeneous distribution inside the tent.

4.1.1 Data acquisition

The data were acquired using an experimental setup shown in figure 4.1. The 2C-PIV system consisted of two 16 MPix (4872×3248 pix) Dantec FlowSenseEO cameras, with a pixel pitch of 7.4 μm using 60 mm Nikon lenses with an aperture of $f^{\#}$ 2.8. The particles were illuminated by a 200 mJ ND:YAG 532 nm laser equipped with dual cavities.

In order to reduce the distorting effect of windowing (spectral leakage) on the stream-wise energy spectra, the cameras needed to cover a sufficient extent of the jet in the stream-wise direction. This effect was modeled by Wänström 2009 assuming a correlation function for homogeneous turbulence of the shape $\exp(-|\Xi|/I_\xi)c$, where Ξ is the spatial separation in the homogeneous direction, ξ, between two interrogation points, c is the variance of the stream-wise velocity component and I_ξ is the integral length scale in the ξ-direction measured in terms of the ξ-distance. Since the energy spectrum of the correlation functions shows noticeable distortions when a rectangular window is applied, for $|\Xi| < 10I_\xi$, the conservative window size measured in ξ-coordinates

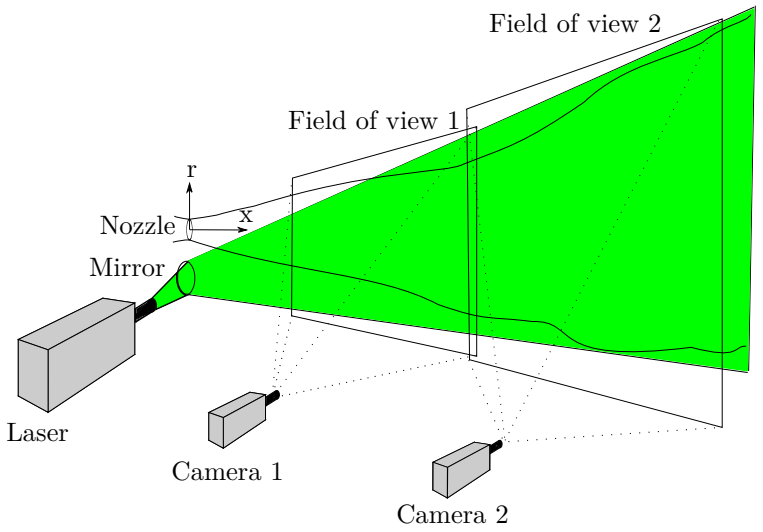

Figure 4.1: Sketch of the experimental setup for the streamwise experiment.

in the current experiments was ≈ 1.25, corresponding to a window size of $75D$ in physical space. The time between pulses, Δt, was carefully optimized in correspondence with the dynamic range of the field by analyzing measurements for various Δt. This was done to ensure that the captured dynamic range was as large as possible, by reducing particle loss at the beginning of the field-of-view (FOV) of camera 1 and reducing the peak-locking bias at the end of the FOV of camera 2. $150\,\mu$s was found to be optimal.

The minimum sampling rate in order to ensure uncorrelated fields, was estimated from preliminary measurements of the downstream flow field. For measurements to be uncorrelated at any given point in the measuring space, the minimum time between samples was required to be two integral time scales, corresponding to 0.12 s. This was estimated using Taylor's hypothesis along the centerline from the range $x/D = [70 : 100]$ downstream of the nozzle, applying a convection velocity corresponding to the local mean velocity at one jet half-width (corresponding to 50% of the local centerline velocity). A sampling rate of 1 Hz was used in the experiments and the data was acquired in a single sitting in order to obtain 11 000 uncorrelated realizations.

4.1.2 Data processing

The velocity fields were obtained from processing the particle images using the Dantec software DynamicSudio v4.0 with a correlation-based interrogation scheme (adaptive PIV). This uses a multi-grid processing of the data with outlier detection, resulting in a final grid of 16×16 pix interrogation areas with 50% overlap, corresponding to a physical interrogation window size of $\Delta^2 = (1.7\,\mathrm{mm})^2$ and $(2.6\,\mathrm{mm})^2$ for cameras 1 and 2 . Window shifting with moving averages was applied in order to increase the dynamic range of particle displacement estimates.

4.2 Results in similarity coordinates

As discussed in Chapter 2, historically in the studies of jets - herein the works of George 1989, Panchapakesan and Lumley 1993a, Panchapakesan and Lumley 1993b, Hussein, Capp, and George 1994, and Ewing et al. 2007 - the far-field statistics were represented in terms of normalized cylindrical velocity components obtained from the so-called similarity analysis. These velocity components, however, were evaluated along coordinate lines of the similarity coordinate system and not the cylindrical coordinate system. This introduces some confusion to the geometrical interpretation of the velocity field in what is known as similarity space. The distinction to be made here is subtle, but proves to be central for the

exact physical interpretation of the analytical eigenfunctions obtained from the Lumley Decomposition. In an attempt to clarify the ambiguous character of these velocity components in similarity space, the components obtained from the simiarity scaling in George 1989, Panchapakesan and Lumley 1993a-Panchapakesan and Lumley 1993b, Ewing et al. 2007 and Wänström 2009 are in the current chapter as well as in Chapter 5 designated as *cylindrical* velocity components and should be understood as centerline velocity scaled cylindrical velocity components evaluated in points referred to the similarity coordinate system, (2.40)-(2.42) (p. 18). The confusion regarding the geometrical interpretation of the velocity components in similarity coordinates is formally rooted in the failure of invariance preservation under the coordinate transformations of the field, namely that the historical representation of the scaled field in similarity coordinates implicitly refers to the cylindrical basis vectors although, a coordinate transformation from cylindrical to similarity coordinates is performed. A useful analogy to explain the problem is the notion of presenting Cartesian velocity components (v^x, v^y, v^z) in place of cylindrical velocity components for a field expressed in cylindrical coordinates - which is clearly erroneous.

An important consequence of any choice of coordinates is the variation of single- and multi-point statistics herein the Reynolds stresses. Unlike the invariant turbulence kinetic energy and dissipation, the Reynolds stresses are *variants* and are therefore as much an artifact of the coordinate system as they are of the flow itself. They do serve a purpose, however, since they are useful for our intuitive understanding of the flow dynamics in for instance describing the amount of shear experienced along constant coordinate lines (e.g. along constant η in similarity coordinates). For the analysis of e.g. shear-related effects across turbulent shear-flows defined in different coordinate systems, it is important to preserve a definition of shear-stresses that is consistent with the coordinate transformation. This will in-fact prove to be useful in section 4.3 when comparing spatial spectra produced from the current flow to the theoretical results of Lumley 1967a in the prediction of the $-7/3$-law of the cross-spectrum for constant shear flows.

The points underlined in the preceding paragraph have illustrated some of the complications resulting from the choice of esoteric coordinate systems. The intended aim of the transformations of the jet far-field to similarity coordinates has nevertheless been to obtain an additional coordinate along which the LD modes can be identified as analytical functions (in addition to the temporal and azimuthal coordinates which are identified as Fourier modes) through which a more intuitive understanding of the flow field can be obtained. The consequence of this transformation is, as demonstrated in Chapter 2, that the equations of motion as well as the velocity components must be expressed in terms

of a basis that is less intuitive than say the Cartesian basis, due to the curvilinear nature of the similarity coordinates (see Figure 2.1 on p. 21). This is exemplified by the varying angle between the ξ- and η bases for different η-coordinates. The current section along with section 4.3 serve as an attempt to familiarize the reader with the flow field in this somewhat abstract setting of similarity coordinates and SSC, by depicting the single-point statistics in both systems and comparing these to the traditional representation of jet statistics in cylindrical coordinates. This section will introduce the far-field statistics in the new coordinate basis and aims to eradicate any confusions that were consequently introduced by the quasi coordinate transformations, while preserving the invariance principle and the supporting mathematical rigidity of tensor calculus.

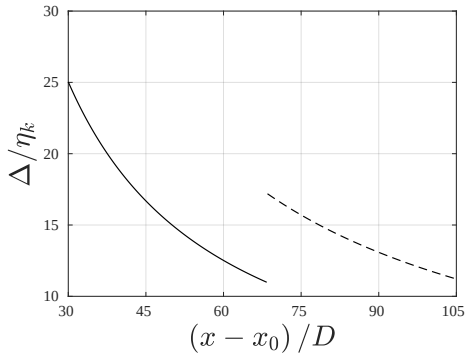

Figure 4.2: The effective spatial resolution ratio of 16 Mpix cameras. The resolution is normalized by the Kolmogorov microscale estimate. The discontinuity is caused by the relative distances between the laser-sheet and the cameras.

Applying equilibrium similarity analysis, George 1989, Hussein, Capp, and George 1994, to the one-dimensional energy spectrum the following expression for the Kolmogorov microscale can be deduced in the fully developed region of the jet

$$\eta_\kappa(x) = \underbrace{\left(\tilde{\varepsilon}(B_u Re_D)^3\right)^{-\frac{1}{4}}}_{\tilde{\eta}_\kappa}(x - x_0), \tag{4.1}$$

where the non-dimensional dissipation, $\tilde{\varepsilon} = 0.26$, was directly measured using the local axisymmetric estimate in Hussein 1991. The constants $B_u = 5.8$ and $x_0 = 4D$ are the centerline velocity decay rate and virtual origin (figure 1.2), respectively, obtained from a non-linear optimization scheme of a Gaussian to the mean stream-wise velocities.

The resolution normalized by the Kolmogorov microscale, Δ/η_k, is seen in Figure 4.2 and shows the effective resolution variation due to the increase of scales with downstream position. The discontinuity, due to the transition between fields-of-view of the two cameras only affects small scale estimates, as these are below the cut-off wavenumber caused by spatial filtering. This threshold value can be estimated from figures 4.2, and (4.1) by estimating the cutoff wavelength as

$$\Delta_{c,s} \approx 25\tilde{\eta}_\kappa\left(x\right). \tag{4.2}$$

We can then approximate the dimensionless cut-off wavenumber as $\tilde{\kappa}_{c,s} = \pi/\Delta_{c,s}$, which can be evaluated to be $\kappa_{c,s} \approx 560$. Since the discontinuous "jump" must represent a κ-value greater than $\tilde{\kappa}_{c,s}$, it means that the corresponding effects on the spectrum are located after the roll-off wavenumber, caused by spatial filtering. The effect on the discontinuity can therefore be neglected in the present analysis.

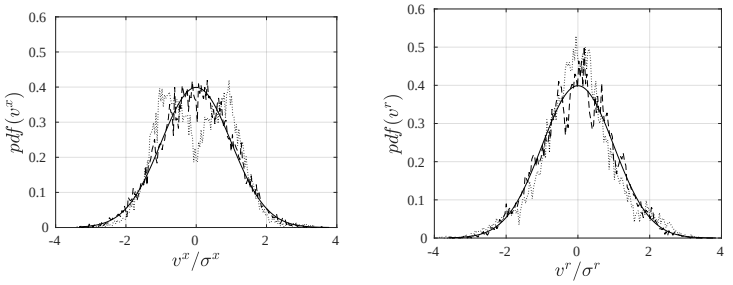

Figure 4.3: Pdf's of the fluctuating parts of the velocity along the centerline. (a): stream-wise component, (b): radial component. ——— : normal distribution, – – – – : $(x - x_0)/D = 30$, ····· : $(x - x_0)/D = 105$.

Due to the large domain span, peak-locking effects has been investigated across the domain. Figure 4.3 shows probability density functions for the stream-wise and radial fluctuations at $x - x_0 = 30D$ and $x - x_0 = 105D$ at the jet centerline. Note that the largest deviations from the normal distribution are found at the downstream position. These are expected due to the much smaller particle displacement downstream compared to the upstream part of the measurement domain. The deviations were confirmed to be caused by the peak-locking. This effect has been investigated in the past (Foucaut et al. 2004, Foucaut, Carlier, and Stanislas 2004) for similar-looking pdf's obtained from PIV measurements, and were shown to have a negligible effect on the energy

density spectra, corresponding to approximately a 3% white noise level in Fourier space. For this reason, the current deviations from the normal distribution are assumed to have a negligible effect on the results given the specific analysis performed in the current work.

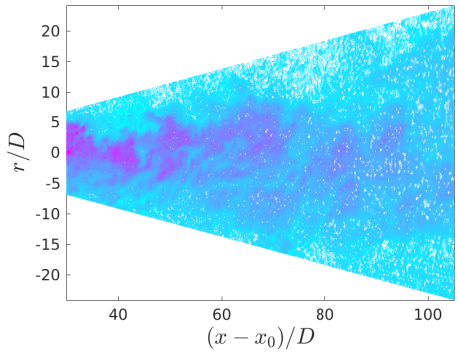

(a)

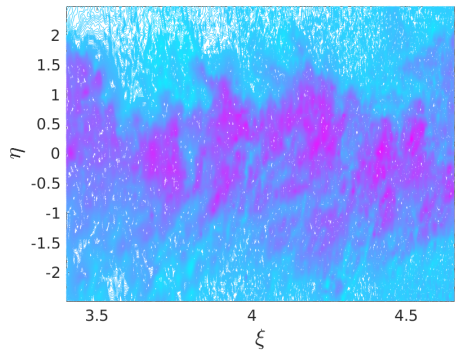

(b)

Figure 4.4: Instantaneous velocity magnitudes (a): Physical velocity field in cylindrical coordinates (b): Velocity field in similarity coordinates scaled with the local centerline velocity.

The instantaneous velocity magnitude in cylindrical coordinates is shown in figure 4.4(a), where the fields-of-view have been truncated at $\eta = 2.475$ for both cameras. Velocities have been interpolated using third-order polynomials resulting in a smooth transition between the two fields-of-view. Figure 4.4(b) on the other hand shows the instantaneous veloc-

ity magnitude in similarity coordinates scaled by the centerline velocity illustrating the homogeneity of the scaled field in similarity coordinates, which is the inspiration for decomposing the flow along the ξ-direction by means of the Fourier transform.

4.2.1 Single-point Statistics in Similarity Coordinates

The similarity coordinate profiles of the static first- and second-order moments for the jet far-field are seen in Figure 4.5, where data from the following downstream distances are shown:
$(x - x_0)/D = [30, 34, 38, 43, 49, 55, 63, 71, 80, 90, 102]$. The data collapse to a high degree over the covered range of the cameras, bearing in mind the increasing effective resolution with downstream position due to the increasing scale sizes, Wanstrom et al. 2007. The advantage of applying similarity coordinates is that the representation of the velocity field is greatly simplified, as seen in Figure 4.4(b). The jet is a flow that has been studied extensively in the past, and is usually represented in cylindrical coordinates. When equilibrium similarity theory is applied, the cylindrical components are simply scaled by the centerline velocity.

Figure 4.6 compares the single-point statistics of the scaled velocity components averaged over the length of the domain and the corresponding cylindrical scaled velocity components. The mean streamwise velocity component (Figure 4.6(a)) exhibits a close resemblance to the cylindrical component. This is expected due to the limited impact of the coordinate change, see (2.54). There are, however, notable differences between the mean η-component and the corresponding cylindrical radial velocity component, V^r, as seen in Figure 4.6(b). The characteristic zero-crossing of the cylindrical mean component, V^r, around $\eta = 1.5$ stands in stark contrast to the shape of the V^η-profile. The latter describes the entrainment process in the jet (e.g. Figure 4.4(b)), by a continuously negative contribution, meaning that in this coordinate system the jet is entraining the flow across the entire width of its extent. This simplifies the understanding of the entrainment process of the jet greatly, and give a much more intuitive picture of the engulfment of the fluid. In Figure 4.6(b) the η-component of the velocity, V^η, has been included as calculated using the measured mean streamwise velocity and the continuity equation, (2.58), such that the scaled η-component is expressed through V^ξ by

$$V^\eta = -\frac{1}{\eta}\int_0^\infty \frac{V^\xi \eta}{\sqrt{\eta^2 + A^{-2}}} d\eta. \tag{4.3}$$

This equation was used to model V^η and as seen from Figure 4.6(b) it is a good fit for $\eta < 1$. Hereafter the effect of the backflow caused by the enclosure of the tent is the most likely cause for the deviation

from (4.3). The second noticeable difference between the components of the two coordinate systems is seen in the normal stresses in the η-direction (Figure 4.6(d)). In similarity coordinates the stresses have a narrower profile due to the negative contribution term in (2.55). The shear-stresses are seen in Figure 4.6(e) and are severely impacted by the non-orthogonality of the system, and are much smaller in similarity coordinates than in cylindrical coordinates. For any solenoidal shear flow, maximum shear would be observed at any location in the flow between orthogonal velocity components and would decreases as the angle between the coordinate lines decreases. The transformation from cylindrical to similarity coordinates follows this conclusion and is the cause for the significantly reduced shear stresses. Figures 4.6(e) and 4.6(f) show that the shear-stresses decrease with η in similarity coordinates compared to cylindrical coordinates, such that the former are 35% lower at $\eta = 1$ and nearly an order of magnitude lower at the edge of the flow.

The reduced levels of mean shear are relevant for the analysis of the energy production term in the turbulence energy equation, (2.33). Although the energy production is an invariant, the energy contributions from shear-stresses as opposed to normal stresses are dependent on the coordinate system. By expanding the production term (II) in (2.33) we get the following contributions to the turbulence kinetic energy production

$$\begin{aligned}
\mathcal{P} &= \underbrace{\left\langle v^1 v^1 \right\rangle \left(z_{11} \nabla_1 \left\langle V^1 \right\rangle + z_{12} \nabla_1 \left\langle V^2 \right\rangle \right)}_{\mathcal{P}^{11}} + \\
&+ \underbrace{\left\langle v^2 v^2 \right\rangle \left(z_{22} \nabla_2 \left\langle V^2 \right\rangle + z_{12} \nabla_2 \left\langle V^1 \right\rangle \right)}_{\mathcal{P}^{22}} + \\
&+ \underbrace{\left\langle v^1 v^2 \right\rangle \left(z_{12} \nabla_1 \left\langle V^1 \right\rangle + z_{11} \nabla_2 \left\langle V^1 \right\rangle + z_{22} \nabla_1 \left\langle V^2 \right\rangle + z_{12} \nabla_2 \left\langle V^2 \right\rangle \right)}_{\mathcal{P}^{12}}.
\end{aligned} \tag{4.4}$$

It is apparent that the azimuthal components do not play a part in the TKE production, due to axi-symmetry and the lack of mean swirl in the flow. Figure 4.7(a) shows the contributing terms as a function of η together with the aggregate profile. The relative contributions of $\mathcal{P}^{11}$, $\mathcal{P}^{22}$, and $\mathcal{P}^{12}$ in (4.4), are 25.6%, 5.3% and 69.1% of $\mathcal{P}$, respectively. The relative contributions from the scaled cylindrical velocity components, $\mathcal{P}_c^{ij}$, are also shown. The production related to shear-stresses has shifted a significant portion of the energy production contribution from the shear-stresses ($\mathcal{P}^{12}$) to the streamwise stresses ($\mathcal{P}_c^{11}$) whereas the change to $\mathcal{P}^{22}$ is negligible. In fact 99% of the energy production was related to the streamwise-radial shear-stresses in cylindrical coordinates. Note that since all contributions in the production budget must integrate to the same curve, $\mathcal{P}$ in any coordinate system, we can conclude

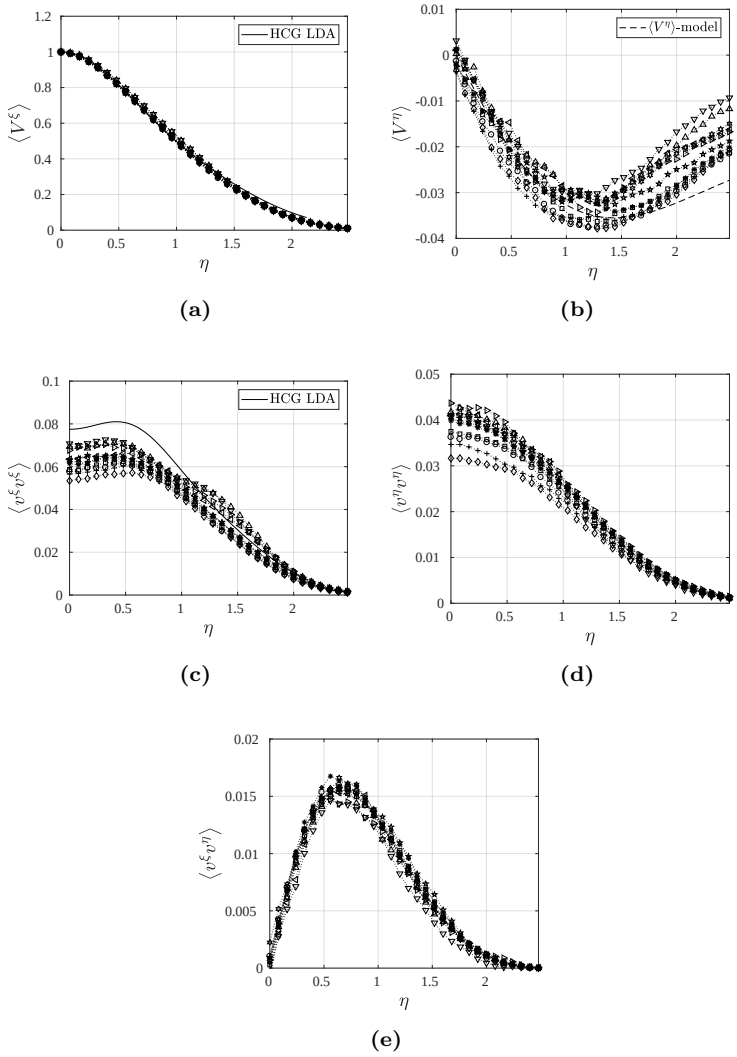

Figure 4.5: Single-point statistics in similarity coordinates sampled at the following streamwise coordinates $(x - x_0)/D = [30, 34, 38, 43, 49, 55, 63, 71, 80, 90, 102]$. Note the greatly expanded scale in the second axis in figures (b)-(e). The increase in intensities downstream is consistent with the increasing spatial resolution, Wanstrom et al. 2007.

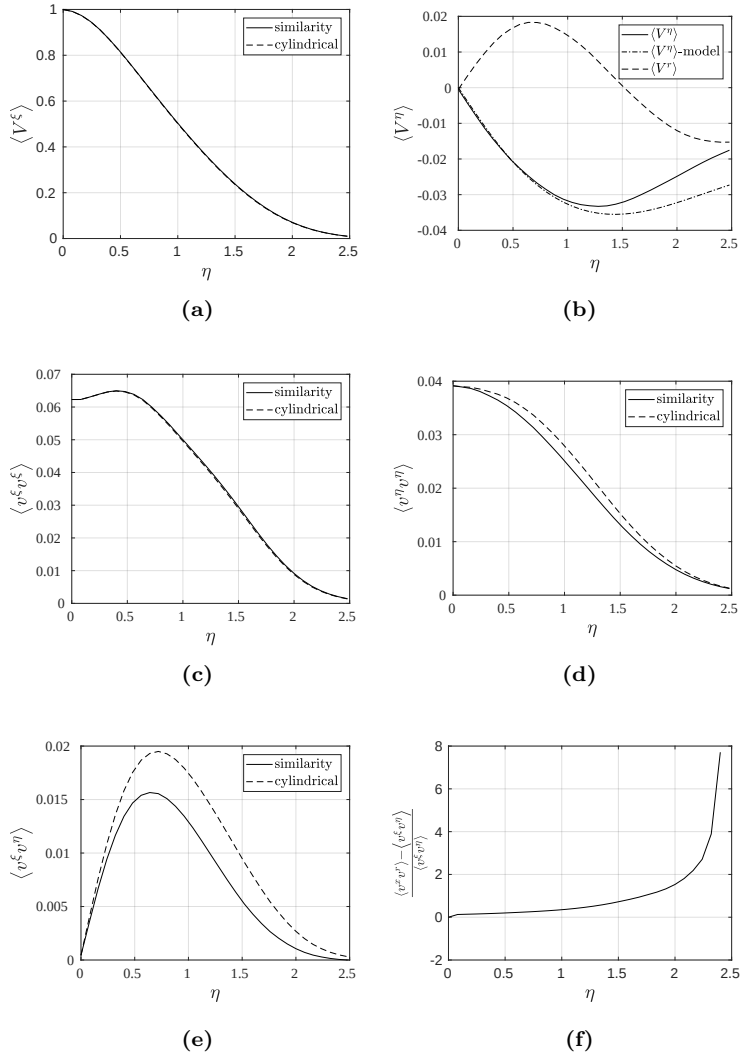

Figure 4.6: Averaged single-point statistics using cylindrical- and similarity velocity components in similarity coordinates. (a): Mean streamwise velocity, (b): mean radial velocity, (c): normal stresses in the streamwise direction, (d): normal stresses in the radial direction, (e): shear-stresses, (f): local ratio between the shear stresses in similarity and cylindrical coordinates. It is seen that the change to similarity coordinates has a more moderate impact on the profiles of $\langle V^\eta \rangle$ and shear-stresses, where the latter is seen to decrease drastically due to the coordinate change.

that the streamwise normal stresses play a much more significant part in the TKE production in similarity coordinates. It is therefore evident that the transformation from cylindrical velocity components to similarity components has changed the energy contribution of the Reynolds stresses, while conserving the total energy production of the flow.

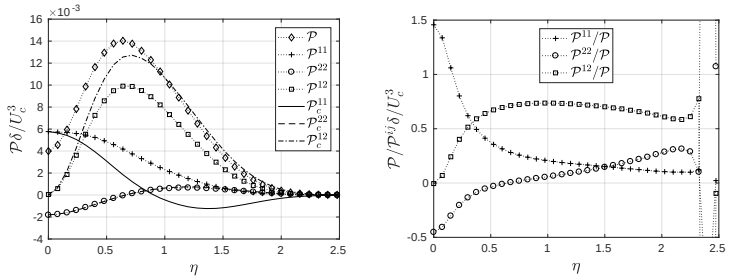

(a) **(b)**

Figure 4.7: (a): Contributions to the turbulence kinetic energy production, (b): Pointwise contributions to the turbulence kinetic energy production of normal and shear-stresses.

The example above illustrates how the notion of stresses is related to the particular coordinate system, and how non-orthogonality of the coordinates may cause significant distortions to our perception of energy production in turbulent flows. This is especially important when working in more abstract coordinate systems, for example by viewing the far-field region of the turbulent jet as Figure 4.4(b) rather than the notion 4.4(a). We are therefore forced to rely more heavily on mathematical formulations in understanding the physics of the flow. In the following the energy density spectra in similarity coordinates will be analyzed, and here some peculiar characteristics will become evident as result of the coordinate transformation. It will be shown that non-orthogonality of the system will give rise to unexpected phenomena in the cross-spectra.

4.2.2 Spatial spectra in similarity coordinates

In the numerical implementation of energy spectra in similarity coordinates, it was assumed that the length of the domain across the jet is constant. Note, however, that this is not entirely true. As seen from figure 2.1, the domain length, L_ξ, is in fact an increasing function of η. This is seen by comparing lengths of constant η-lines at two-different η-coordinates. Since the variation of L_ξ from $\eta = 0$ to $\eta = 2.5$ is 2.7%

across the jet, it has been neglected in the current case. One should, however, keep in mind in the case of the two-point cross-correlation tensor of Fourier coefficients, that in the numerical formulation of the Fourier transform an equidistant step size must be ensured for all η. This is simply due to the orthogonality between different Fourier bases for different wavenumbers, George 2013. In the analytical case this is not an issue due to the infinite number of Fourier bases. In the discrete case, however, one would mistakenly correlate Fourier coefficients at two different η-coordinates corresponding to different wavenumbers. The issue may be addressed in the numerical implementation by ensuring that the ξ-coordinates of interpolation points varies with η such that the same wavenumbers are correlated across the span of the flow.

Figures 4.8-4.11 show the normal- and cross-spectra in similarity coordinates at various η-locations. Since these are spatial spectra, these do not suffer from the approximation errors related to Taylor's frozen field hypothesis which is usually applied in the conversion process of temporal spectra to energy spectra e.g. from data obtained from hot-wire measurements. This has an advantageous effect on the accuracy of the spectra at high wavenumbers, representing the small scales of the flow where Taylor's hypothesis does not apply due to their convection by the large scales, Lumley 1965, Champagne, Friehe, and LaRue 1977, Buchhave and Velte 2017. In the processing of the current data, a Parzen window was applied in order to reduce the distortion effects of spectral leakage from low to high wavenumbers. Note that in this case the leakage results from the finite record length.

The resulting component energy spectra are seen to exhibit the $-5/3$-range - as expected for high-Reynolds number flows - over several decades of κ for all η-coordinates. Note that this was initially identified by Wänström 2009, but from spectra of scaled cylindrical fluctuations in the far-field region of the jet. While the exact bounds of the $-5/3$-range vary with the η-coordinate the range is found to lie between 40 and 300.

One effect caused by the non-orthogonality of the coordinate system is the profound increase in the cross-spectra at large η. This effect is seen to increase towards the periphery of the jet. It is worth underlining, that this behavior is not observed in the cross-spectra in Wänström 2009 nor in the current data when the cylindrical velocity components are applied in similarity coordinates. It is exclusively an effect of the similarity coordinate system when using the corresponding velocity components in that system. Transforming the shear-stresses from cylindrical to similarity coordinates and mapping the resulting expressions to Fourier space, the following relation appears

$$\left\langle \widehat{v^{\xi} v^{\eta}} \right\rangle = A\sqrt{\eta^2 + A^{-2}} \left(\left\langle \widehat{v^{x} v^{r}} \right\rangle - A\eta \left\langle \widehat{v^{x} v^{x}} \right\rangle \right). \tag{4.5}$$

It illustrates the effect that the non-orthogonality of the similarity coordinate system has on the cross-spectrum in similarity space. It is seen that the energy spectrum of the x-fluctuations is projected onto the cross-spectrum, with the effect varying with η. For small η the projection is negligible, but has a substantial effect at large η, since the autospectrum on the right-hand side of (4.5) is several orders of magnitude larger than the cross-spectrum. This effect is strongest at large wavenumbers, where the differences in energy levels of auto- and cross-spectra are most profound. As a result the cross-correlation increases, seen most evidently in Figures 4.10(g)-4.11(h), where the cross-correlation spectrum approaches the autocorrelation with increasing η. It is worth keeping in mind that both terms on the right-hand side of (4.5) are complex-valued, while the cross-spectra plotted in Figures 4.8-4.11 represent the absolute value of (4.5). Therefore, the effect of $\langle\widehat{v^x v^x}\rangle$ on the cross-spectrum in similarity coordinates also depends on the phase information of both terms on the right-hand side in (4.5).

We can thus conclude that the spectra obtained in similarity coordinates using the corresponding velocity components of that coordinate system introduces distorting phenomena to the cross-spectra that are not observed for spectra obtained from homogeneous constant shear flows. This is yet another indication (the first being the failure of Hermitian symmetry of the cross-correlation matrix in the LD integral) that the similarity coordinates are not ideal for decomposing the jet. This is the motivation for analyzing the jet far-field in SSC, a coordinate system which does not suffer from the aforementioned issues due to their orthogonality and thereby their decoupling of the streamwise- and spanwise velocity components. The rest of this chapter will therefore focus on the analysis of the jet in SSC which in many ways proves to be the more natural choice of coordinates for the jet, allowing us to compare the jet data more easily with other flows without the residual effects of non-orthogonal coordinates.

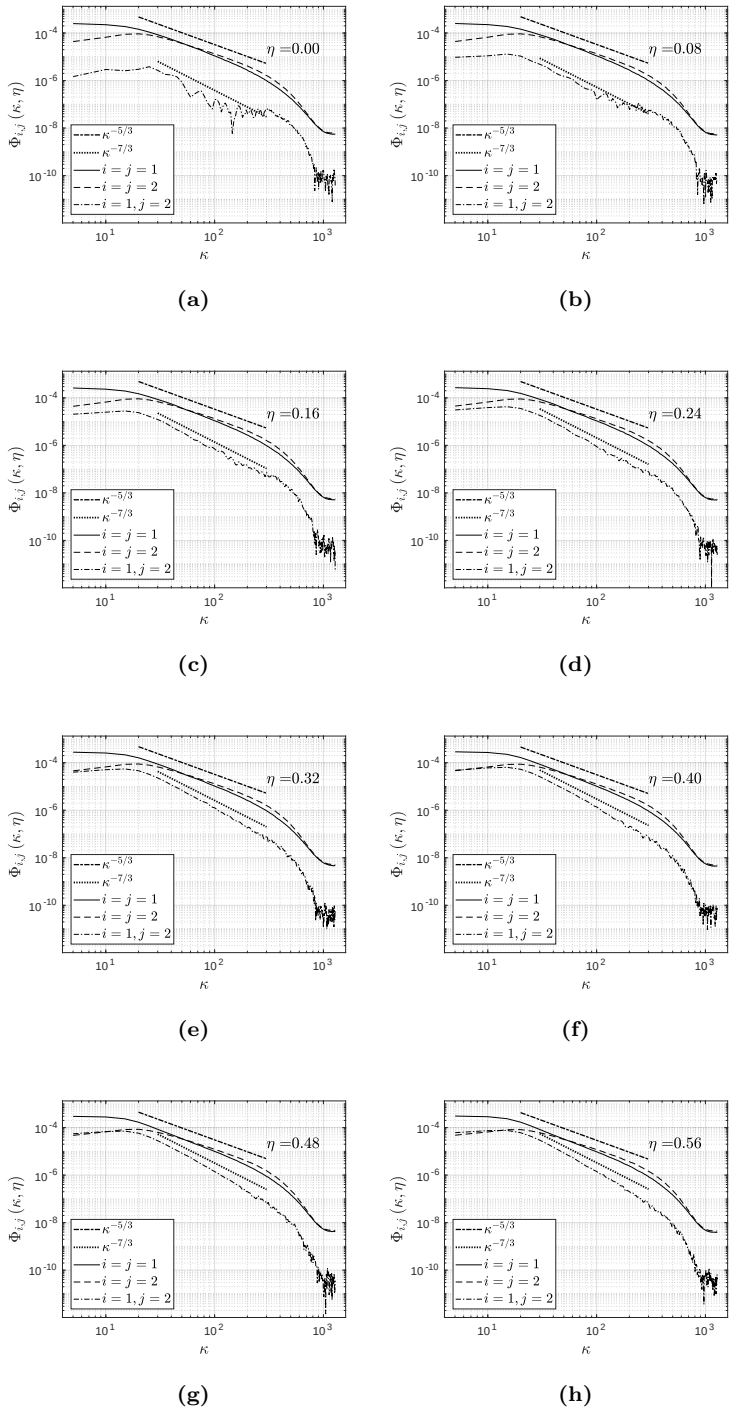

Figure 4.8: Energy density spectra, and cross-spectra at various η-coordinates for the velocity ξ- and η- velocity components.

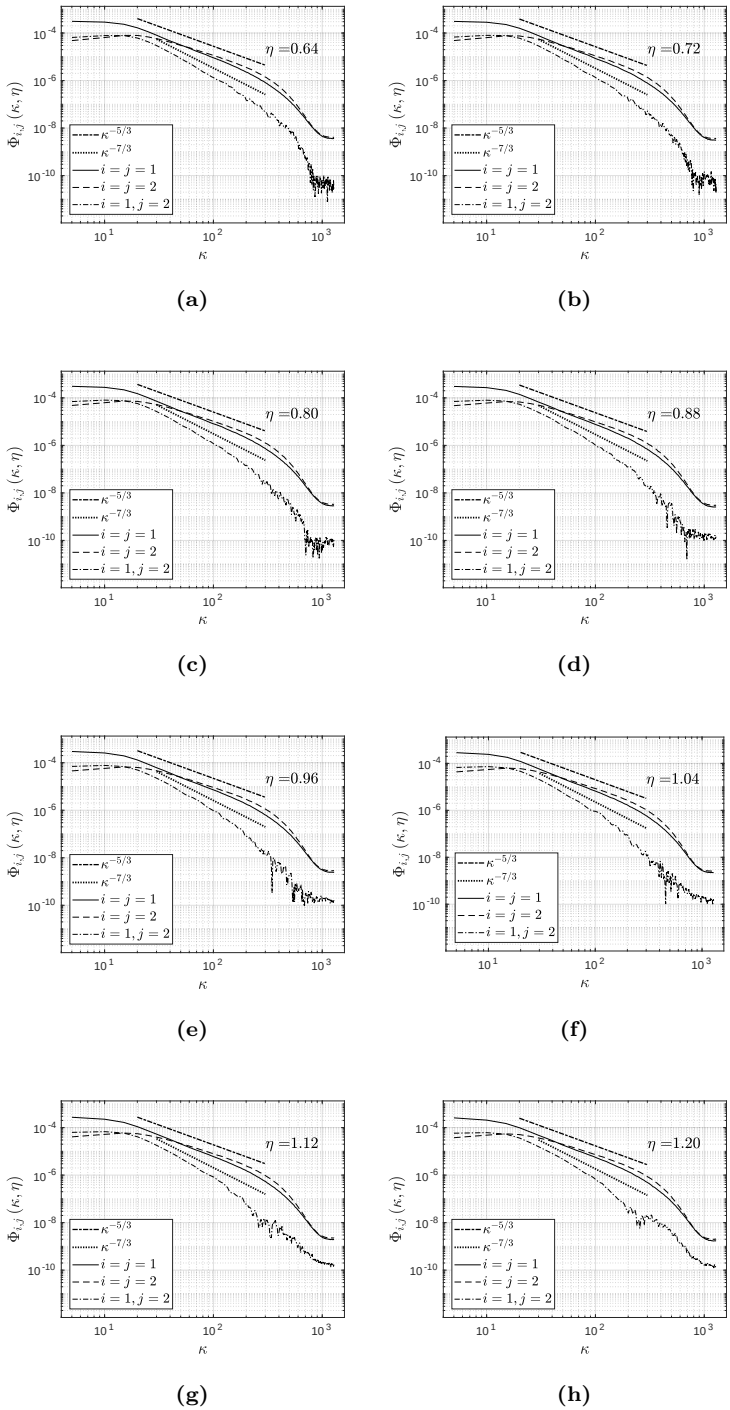

Figure 4.9: Energy density spectra, and cross-spectra at various η-coordinates for the velocity ξ- and η- velocity components.

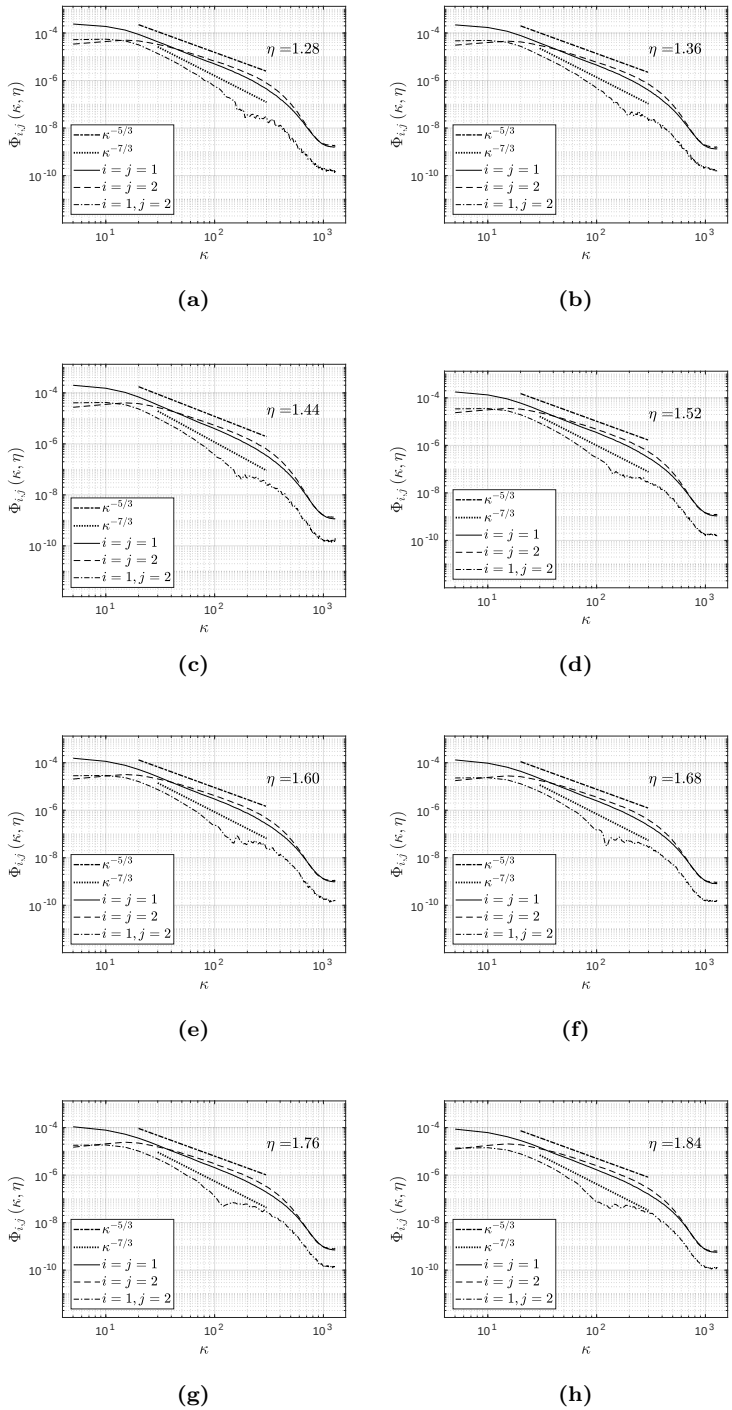

Figure 4.10: Energy density spectra, and cross-spectra at various η-coordinates for the velocity ξ- and η- velocity components.

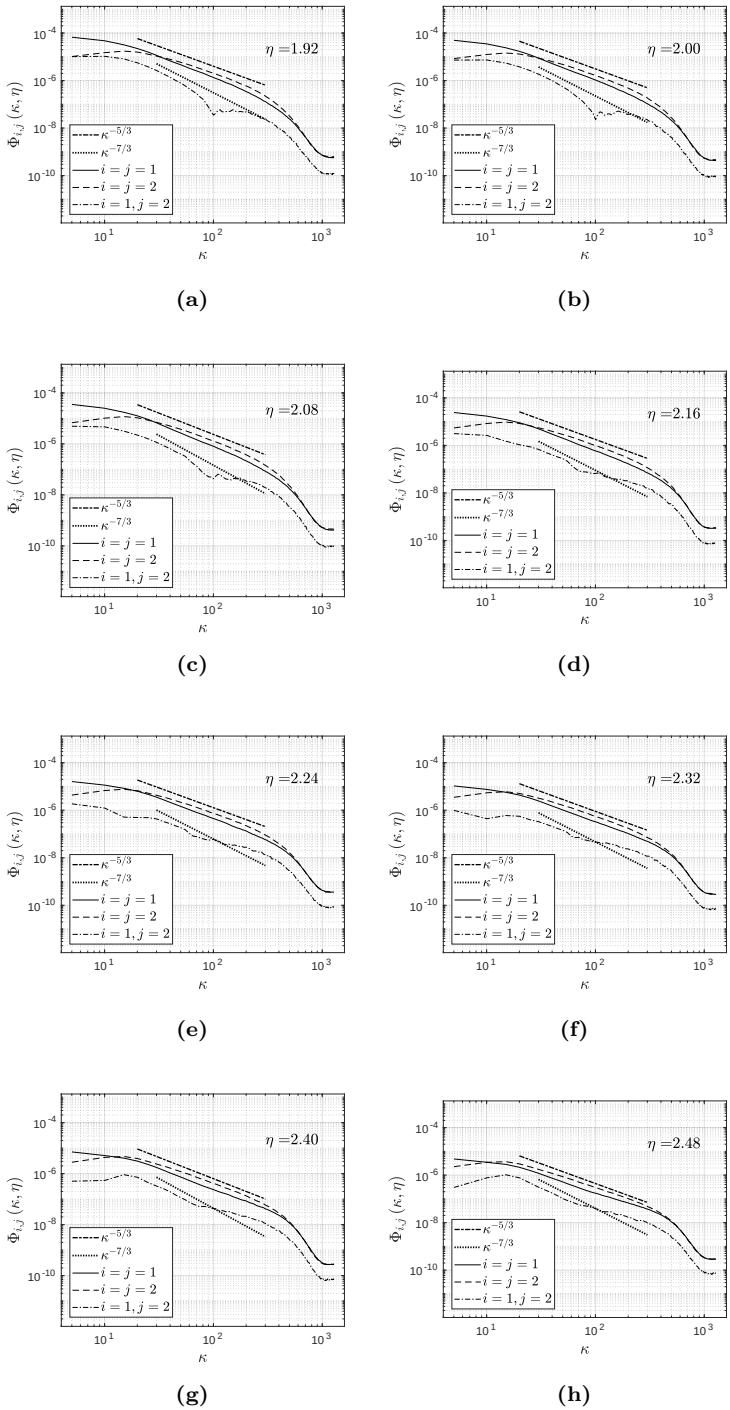

Figure 4.11: Energy density spectra, and cross-spectra at various η-coordinates for the velocity ξ- and η- velocity components.

4.3 Results in SSC

Having investigated the effects of the similarity coordinates on the single-point statistics and spectral representation of the field, we continue with the main representation of the measured data, namely in SSC. The single-point statistics and spectra will be presented in these coordinates, where the advantage of orthogonality will be applied in order to decompose the velocity field in terms of LD modes. Furthermore, a closer study of the modal building blocks of the spectra will be performed. The analysis will lead to conclusions on which modes constitute the main contributions to the reconstruction of the *energy production range*, and the *inertial subrange*, and if any individual modes reconstruct the $-5/3$ and $-7/3$-slopes in the energy- and cross-spectra, respectively. Inspired by the preceding section the analysis in SSC will cover the energy production contributions across the jet width, but now in terms of its modal building blocks, and the prominent role that the shear-stresses have in this regard, when presented in SSC.

4.3.1 Single-point Statistics

The instantaneous SSC velocities are seen in Figure 4.12, where the arc of constant ξ is seen at the beginning and end of the domains in Figure 4.12(a). For a constant ξ-coordinate in a self-similar flow, the deviation of the single-point statistics between the representation in SSC and cylindrical coordinates is strictly due to the rotation of the coordinate system. Therefore, identical profiles to those seen in Figure 4.14 could theoretically be captured from data sampled from a plane perpendicular to the centerline of the jet and a rotation of the coordinate system. This, however, is not true in the case of two-point statistics, since the two-point correlation is dependent on the instantaneous field at multiple points in space. Even for a self-similar flow, the correlation between two points, $P_A = (\xi_1, \theta_1, 0)$ and $P_B = (\xi_2, \theta_2, 0)$, would not be the same as between point P_A and $P_C = (\xi_1 + \Delta\xi, \theta_2, 0)$ - where $\Delta\xi$ is chosen such that point C is located perpendicular to the centerline directly above point $(\xi_1, 0, 0)$. This is naturally due to the inhomogeneity of the turbulence represented by the scaled flow field.

The mean velocity profiles and the Reynolds stresses in figures 4.13 and 4.14, show the same traits as the profiles in similarity coordinates. Note that the negative $\langle V^\theta \rangle$-component can be compared to the $\langle V^\eta \rangle$-component in similarity coordinates. The $\langle V^\theta \rangle$-profiles are again modeled from the continuity equation in SSC using the following expression for an incompressible flow

$$\langle V^\theta \rangle = -\frac{1}{\sin\theta} \int_0^\infty \langle V^\xi \rangle \sin\theta d\theta, \tag{4.6}$$

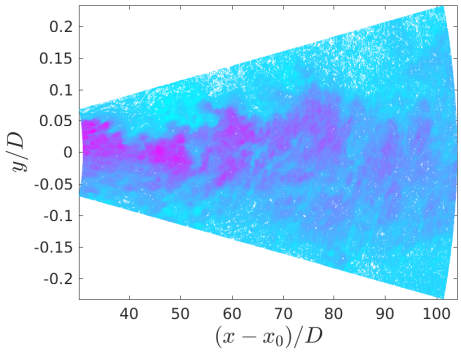

(a)

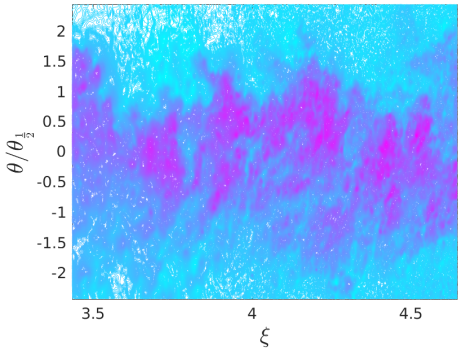

(b)

Figure 4.12: (a): Velocity magnitude in spherical coordinates and (b): scaled magnitude in SSC.

and is shown in Figure 4.13(b).

The simplicity of (4.6) should not be taken lightly. An optimal coordinate system simplifies the expression of the dynamics that it depicts. This is most easily understood by noting that in an ideal coordinate system the contravariant velocity components would be unity at all points in space and time. For a turbulent flow this would, of course, entail that the coordinate system would be time dependent which would unavoidably make it complicated. Nevertheless, it would successfully depict very simple velocity components. A coordinate system basis should not be viewed differently than the velocity vectors themselves. Obtaining

the *ideal* coordinate system is completely equivalent to finding the exact solution to the governing equations. For the far-field region of the jet the SSC seem to depict the velocity field in a more elegant way than any other immediate coordinate system - herein the similarity coordinates as demonstrated by comparing (4.6) and (4.3). We note that the simpler the statistical profiles of the contravariant velocity components are the closer the coordinate system is to the velocity field itself - simplicity can here be quantified as the minimization of the integrated curvature of the profiles. In addition to this, when the coordinate system itself has a simple geometrical formulation such as (2.80)-(2.82), there is a strong argument for depicting the turbulent jet far-field in SSC in general.

The Reynolds stresses are seen in figures 4.14(c)-4.14(e), where some variation of the profiles is caused by the coordinate transformation from cylindrical to SSC-coordinates. The $\langle v^\xi v^\xi \rangle$ and $\langle v^\theta v^\theta \rangle$ are narrower and wider, respectively, than the corresponding profiles in cylindrical coordinates, and the biggest impact of the coordinate transformation is reflected in the shear-stresses. The shear-stresses in SSC are smaller than in cylindrical coordinates, but on the other hand more shear is produced than in similarity coordinates.

Figure 4.15(a) depicts the energy production term, II, in (2.33), which reduces to the following form in SSC

$$\begin{aligned} \mathcal{P} &= \underbrace{z_{11} \langle v^1 v^1 \rangle \nabla_1 \langle V^1 \rangle}_{\mathcal{P}^{11}} + \underbrace{z_{22} \langle v^2 v^2 \rangle \nabla_2 \langle V^2 \rangle}_{\mathcal{P}^{22}} \\ &+ \underbrace{\langle v^1 v^2 \rangle (z_{11} \nabla_2 \langle V^1 \rangle + z_{22} \nabla_1 \langle V^2 \rangle)}_{\mathcal{P}^{12}}, \end{aligned} \tag{4.7}$$

which again is a simpler formulation than (4.4), due to the non-zero off-diagonal terms of the metric tensor. These production distributions are seen in Figure 4.15(a) where they have been normalized by the total of the energy production. The figure depicts a continuously negative contribution to the energy production of $\mathcal{P}^{22}$, unlike the representations in cylindrical- and similarity coordinates. The energy production from mean shear is also smaller than in cylindrical coordinates. The energy contributions of the various components to the total energy production are 27.9%, -10.2% and 82.3% for $\mathcal{P}^{11}$, $\mathcal{P}^{22}$, and $\mathcal{P}^{12}$ respectively. Therefore, a majority of the energy production is related to the shear-stresses, representing a 16.7% decrease in energy production compared to the shear-stresses in cylindrical coordinates. Figure 4.15(b) shows the relative contributions of the terms in (4.7) normalized by the total energy. The relatively small variations of the contributions between $\theta/\theta_{\frac{1}{2}} = 0.5$ and 2 are striking. The energy production fractions are nearly constant for $\mathcal{P}^{22}$ over this range. The gradual increase of the shear-stress

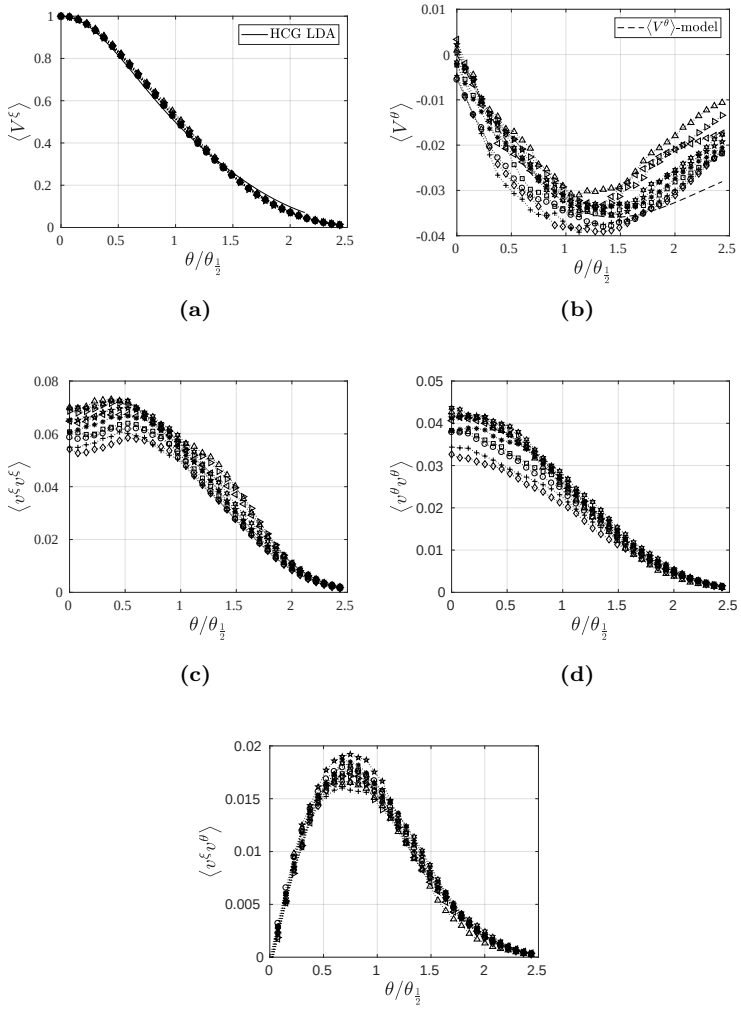

Figure 4.13: Single-point statistics sampled at the following streamwise coordinates $(x - x_0)/D = [30, 34, 38, 43, 49, 55, 63, 71, 80, 90, 102]$. (a): Mean streamwise velocity, (b): mean radial velocity, (c): normal stresses in the streamwise direction, (d): normal stresses in the radial direction, (e): shear-stresses

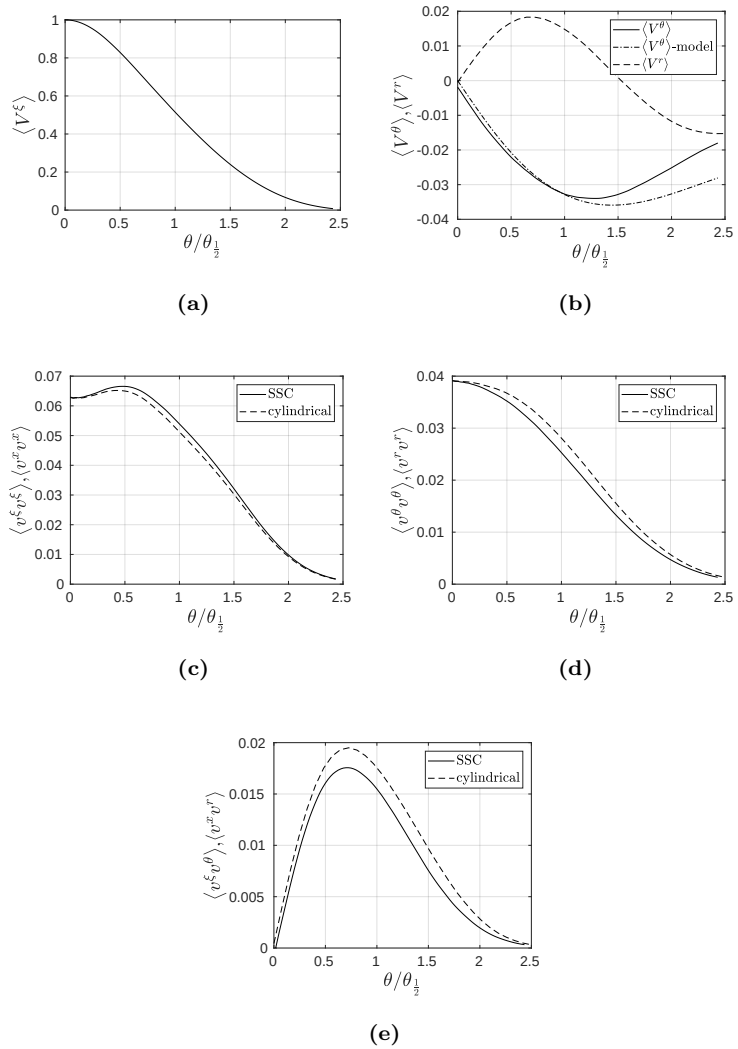

Figure 4.14: Streamwise averaged single-point statistics using cylindrical- and SSC velocity components. (a): Mean streamwise velocity, (b): mean radial velocity, (c): normal stresses in the streamwise direction, (d): normal stresses in the radial direction, (e): shear-stresses, (f): local ratio between the shear stresses in similarity and cylindrical coordinates. It is seen that the change to similarity coordinates has an impact on the profiles of $\langle V^\theta \rangle$ and shear-stresses.

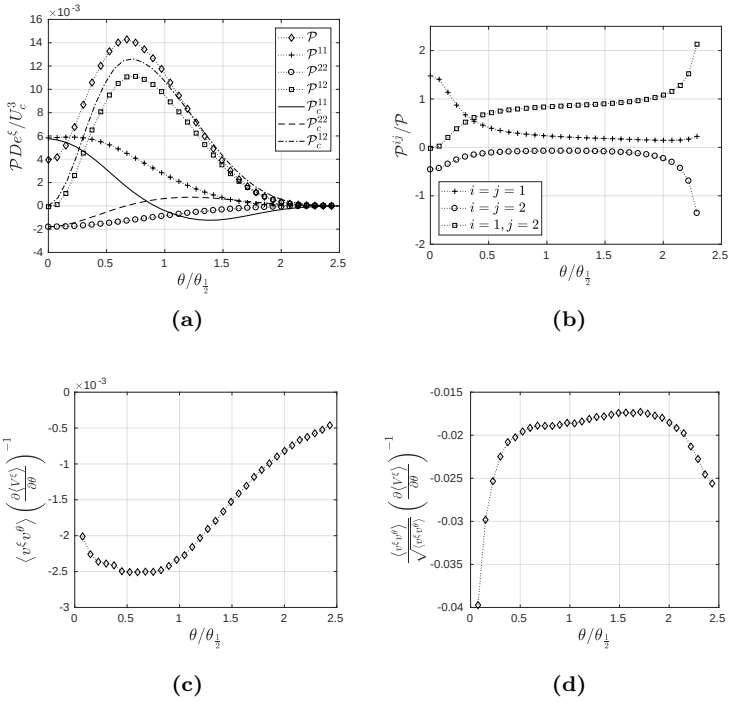

Figure 4.15: (a): TKE production components for SSC, (b): Relative contributions to the turbulence kinetic energy production of normal and shear-stresses, (c): Proportionality of shear-stresses and mean velocity gradient, (d): Scaled proportionality of shear-stresses and mean velocity gradient.

contribution from approximately 70% to 105% over the same jet-span is due to the corresponding decrease of $\mathcal{P}^{11}$. This means that moving away from the centerline of the jet, the contribution of the shear-stresses to the turbulence kinetic energy production increases, while the role of the normal stresses decreases. At the periphery of the jet the shear-stress contribution increases immensely due to the dominance of the second terms in (2.91) and (2.92) for large θ. It is evident that the most dynamic region in the turbulent jet far-field is the region around one half-width. Many of the characteristic profiles have their extrema around this region and the depiction of the mean spanwise velocity component, (4.6), indicates that large turbulent structures are located in this region. These may very well have a significant influence on the location of the extremum of the $\langle V^{\theta}\rangle$, and thereby the entrainment rate.

In the following sections, the flow is investigated further by means of spectral analysis. It is especially interesting to view the decomposition of the spectra in terms of their LD modes. It is particularly the energy production distribution between stresses which is relevant for the reconstruction of the energy production term in section 4.3.4. This will reveal why some stresses are reconstructed faster than others, and which modes participate in the energy production of the flow.

4.3.2 Spatial spectra in SSC

It is the property of the PIV technique that allows true experimental spatial spectra to be computed for high Reynolds number flows, and velocity components along tilted coordinate axes, as in the case of the SSC. Similar multi-component measurements would be difficult, if not impossible to perform using hot-wires. Away from the centerline high turbulence intensities would reduce the validity of Taylor's hypothesis and make effective separation of the velocity components more challenging.

The 1D energy density spectra are shown together with the cross-spectra for various θ-coordinates in Figures 4.17-4.20. A Parzen-window has been applied in order to reduce the spectral leakage at higher wavenumbers related to the finite window length. The spectra are seen to exhibit the $-5/3$- and $-7/3$-slopes already from $\theta/\theta_{\frac{1}{2}} = 0.07$. The inertial subrange is estimated to be in $\kappa \in [20 : 300]$. But the upper limit is probably due to the spatial filtering from the finite measuring volume (since $\kappa\eta << 0.1$).

The $-7/3$-slope in the cross-spectra was predicted to exist in flows where turbulence was sustained by a uniform mean shear gradient by Lumley 1967a. Lumley's model was based on the assumption that shear-stresses were proportional to the mean shear, which in the current case means that

$$\left\langle v^{\xi} v^{\theta} \right\rangle \propto \frac{\partial \left\langle V^{\xi} \right\rangle}{\partial \theta}, \tag{4.8}$$

where the shear-stresses are obtained by integrating the cross-spectrum, and arguing that the Reynolds shear-stress production is dependent exclusively on κ, the turbulent energy spectral flux, ϵ_{κ}, and the mean shear. Dimensional analysis then implies that the shear-stress production is manifested in the universal equilibrium range in terms of a $-7/3$-slope of the cross-spectrum, Lumley 1967a

$$\left\langle \widehat{v^{\xi} v^{\theta}} \right\rangle \propto \epsilon^{1/3} \kappa^{-7/3} \frac{\partial \left\langle V^{\xi} \right\rangle}{\partial \theta}. \tag{4.9}$$

Note that the coefficient will be universal only if the turbulence at these wavenumbers is as well, an idea which is very much in dispute, Cham-

pagne 1978, George 2014. The cross-spectra in Figure 4.8 indeed exhibit a $-7/3$-slope for wavenumbers between 20 and 250, with the exception of the spectra in the vicinity of the centerline, where the low spectra are in correspondence with the negligible shear-stresses in this region. The slope increases rapidly away from the centerline due to the increase of mean shear (Figure 4.15(c)). Beyond $\theta/\theta_{\frac{1}{2}} = 0.72$ (Figure 4.9(b)), the $-7/3$ range is slowly eradicated for large κ. The reason for this can be understood by examining the assumptions underlying Lumley's model leading to the prediction of the $-7/3$-range. The manifestation of the $-7/3$-range traces back to regions in which the shear-stresses are proportional to the mean gradient, corresponding to the assumption (4.8). Although the $-5/3$-slope of the energy spectra can be identified across the entire span of the jet, the $-7/3$-slope diminishes with increasing θ, as the underlying assumption of proportionality

$$\left\langle v^{\xi} v^{\theta} \right\rangle \propto \frac{\partial \left\langle V^{\xi} \right\rangle}{\partial \theta}, \tag{4.10}$$

becomes weaker. Figure 4.15(c) reveals that the proportionality described by (4.10) is valid in the range $0.25 < \theta/\theta_{\frac{1}{2}} < 1$. This correlates with the diminishing $-7/3$-slope for high κ-values as one moves beyond one jet half-width. The existence of the $-7/3$-range for small θ-coordinates indicates, that in the region where shear-stresses are proportional to the mean velocity gradient, a wide range of scales contribute to the energy production through shear-stresses, as seen from (4.7) and Figure 4.15(a). Note that most of the contribution to the energy production from shear-stresses is obtained from low wavenumbers. In the absence of three-dimensional spectra, it is difficult to draw conclusions from this since the low wavenumbers suffer from aliasing from the other directions.

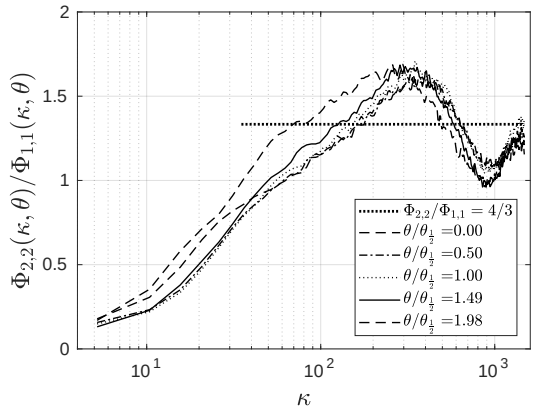

Figure 4.16: Ratio of the component spectra. The assumption of isotropy requires $\Phi_{2,2}/\Phi_{1,1} = 4/3$, Hinze 1975.

It is worth mentioning that the notion of isotropy is not clearly manifested in the current spectra. Although both energy component spectra exhibit the $-5/3$-slope these are manifested in different wavenumber regions, which means that the ratio between the component energy spectra is varying with wavenumber. A prerequisite for isotropy in the inertial subrange is, Hinze 1975

$$\Phi_{2,2}/\Phi_{1,1} = 4/3. \tag{4.11}$$

Figure 4.16 shows the noticeable variability of $\Phi_{2,2}/\Phi_{1,1}$ around 4/3 for various positions across the jet indicating that the turbulence is not isotropic. The reason for this may be that the Reynolds number of 20 000 is too low in order for this flow to exhibit isotropy at these scales, as predicted by the Kolmogorov theory. Note, however, that the decomposition applied in the current work does not assume isotropy for any turbulent scale.

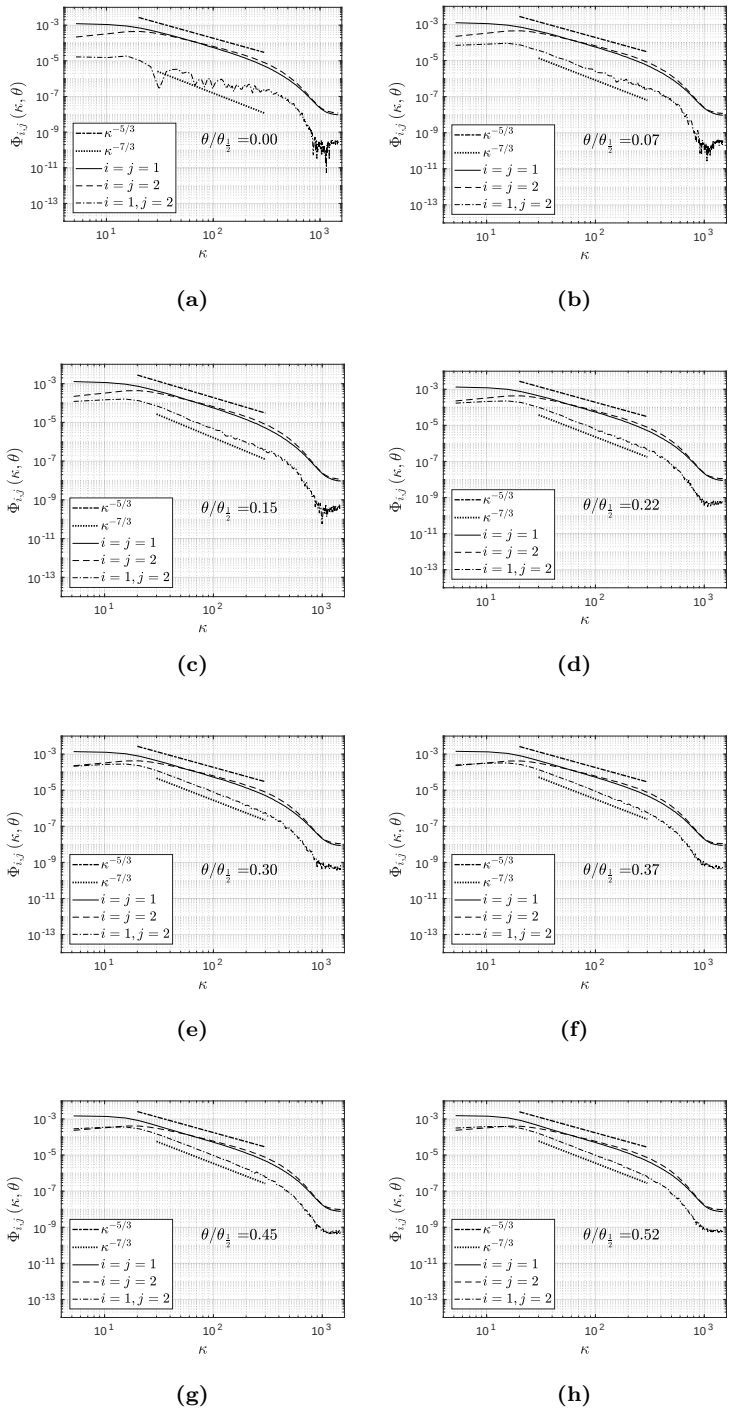

(a) **(b)**

(c) **(d)**

(e) **(f)**

(g) **(h)**

Figure 4.17: Spatial spectra in SCC from various spanwise coordinates, $\theta/\theta_{\frac{1}{2}}$.

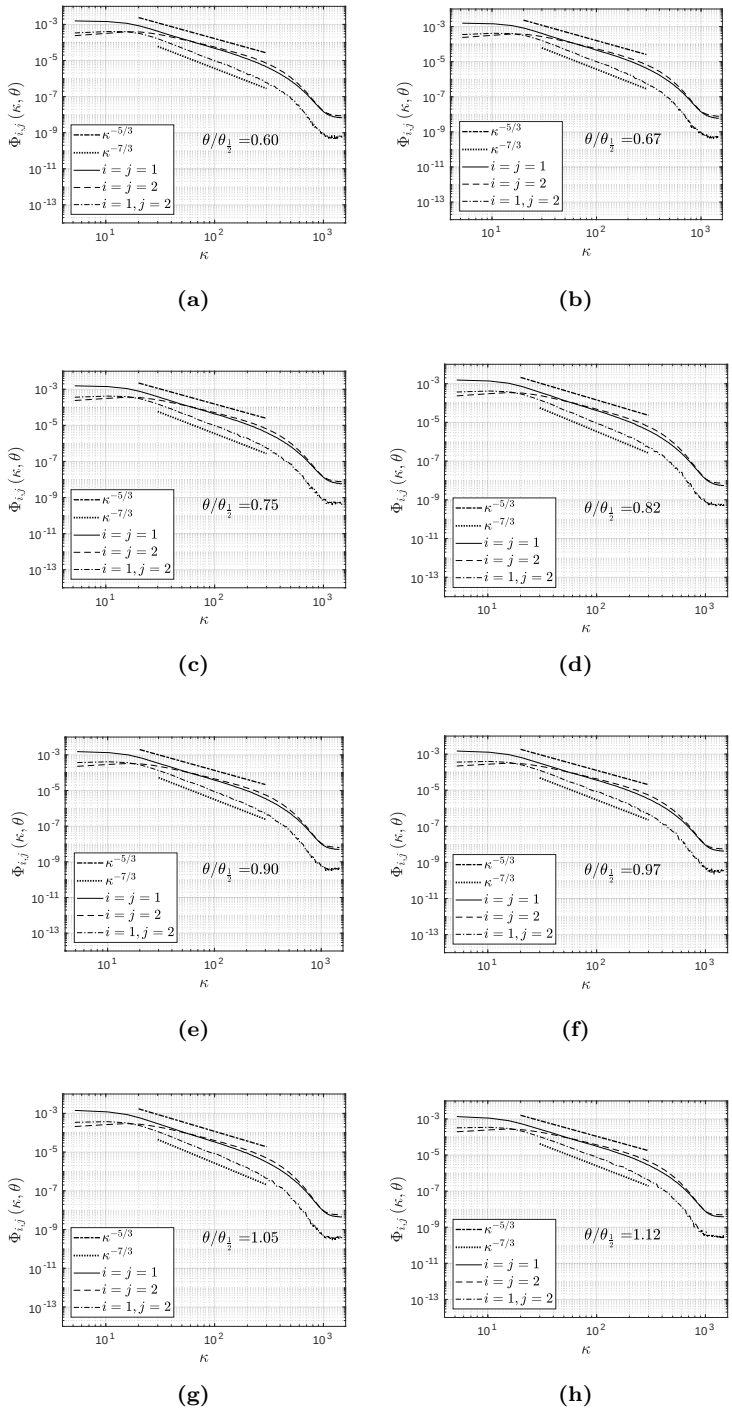

(a) **(b)** **(c)** **(d)** **(e)** **(f)** **(g)** **(h)**

Figure 4.18: Spatial spectra in SCC from various spanwise coordinates, $\theta/\theta_{\frac{1}{2}}$.

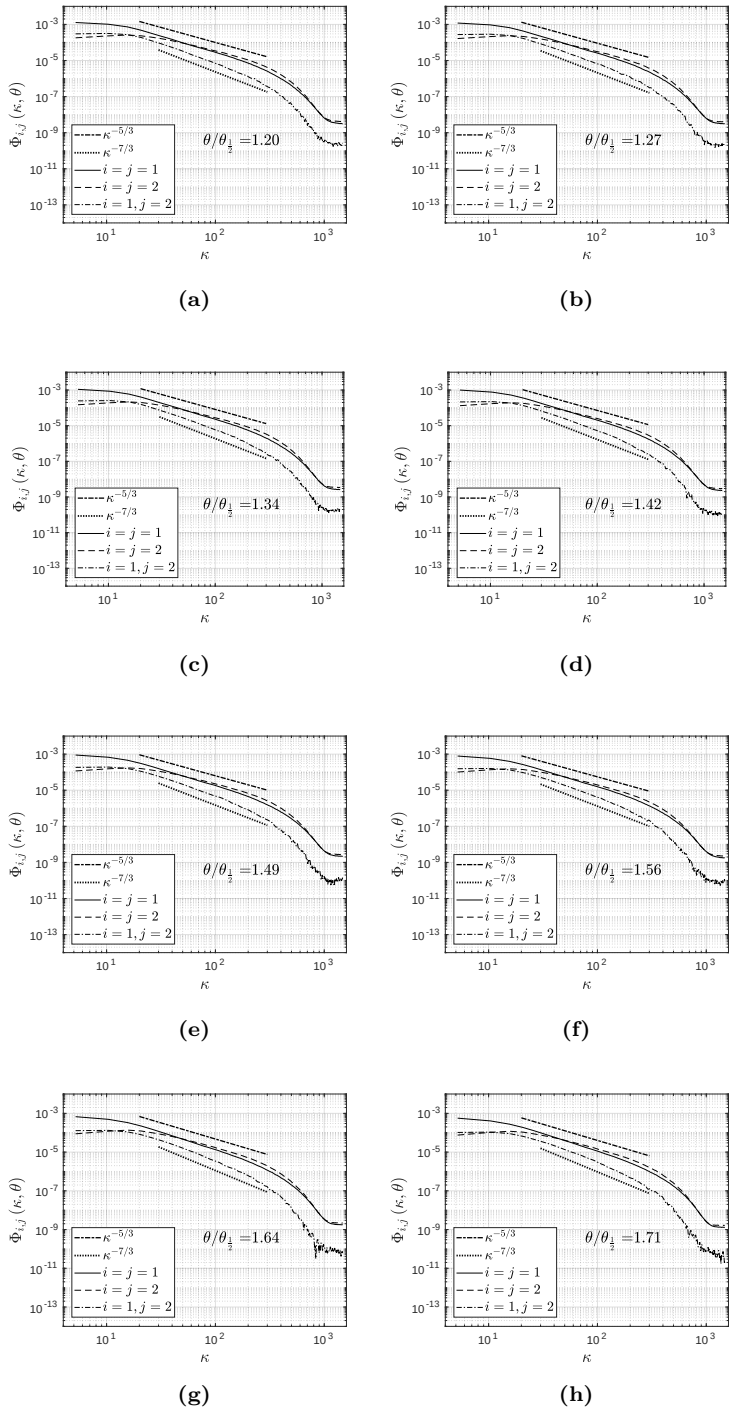

(a) **(b)** **(c)** **(d)** **(e)** **(f)** **(g)** **(h)**

Figure 4.19: Spatial spectra in SCC from various spanwise coordinates, $\theta/\theta_{\frac{1}{2}}$.

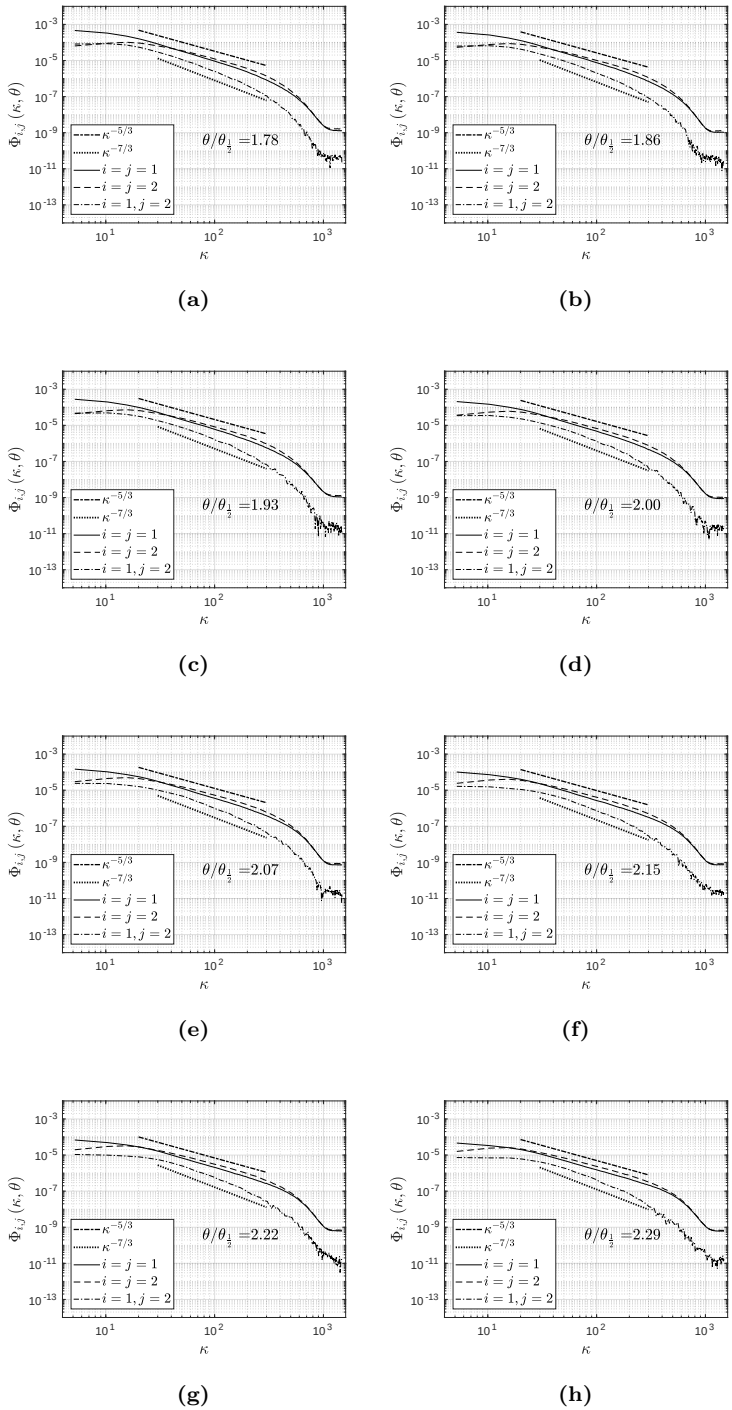

(a) **(b)** **(c)** **(d)** **(e)** **(f)** **(g)** **(h)**

Figure 4.20: Spatial spectra in SCC from various spanwise coordinates, $\theta/\theta_{\frac{1}{2}}$.

4.3.3 Decomposition of the Velocity field in $L^2_w\left(\Omega, \mathbb{C}^3\right)$

We note that the streamwise components of the LD modes for the turbulent jet far-field can be identified to be stretched amplitude-decaying Fourier modes. This is concluded by introducing a specific inner product weight, as discussed in Chapter 3. We note that this means that the Fourier basis is optimal for the space $L^2_w(\Omega, \mathbb{C}^3)$, and not for $L^2(\Omega, \mathbb{C}^3)$. This must be taken into consideration in the physical interpretation of the modes as well as the equations that are expanded by the modes from the Galerkin projection. In the current work only the production term of the turbulence energy equation has been expanded with respect to the $L^2_w(\Omega, \mathbb{C}^3)$-inner product, which means that the energy equation we are analyzing must be distinguished from the regular turbulence kinetic energy equation describing the thermodynamic energy of the system. The eigenvalues are thus no longer directly representative of the TKE content of a given mode which is apparent from the definition of the eigenvalues in $L^2_w(\Omega, \mathbb{C}^3)$

$$\lambda^{(\alpha)} = \left\langle \left| \left(\overline{V}, \overline{\Phi}^{\alpha} \right)_w \right|^2 \right\rangle . \tag{4.12}$$

This is a consequence of the choice of coordinate system and basis functions combination (see section 3.1.3, p. 41). The eigenvalues in (4.12) represent the spatially weighted energy in the streamwise direction. The additional e^{ξ}-term appearing in the inner product which motivated the introduction of a neutralizing weight function appears due to the logarithmic stretching of the coordinate system in the ξ-direction and can be compared to the radial component appearing as the Jacobian in the transformation from Cartesian to polar coordinates. The stretching in the latter case is naturally a result of the linearly increasing displacement between adjacent azimuthal coordinates with increasing radial coordinate. The problem is then essentially reduced to finding a bounded operator, f, which transforms the eigenfunctions back to physical space

$$f : L^2_w\left(\Omega, \mathbb{C}^3\right) \rightarrow L^2\left(\Omega, \mathbb{C}^3\right). \tag{4.13}$$

This may indeed prove to be difficult as it very much resembles the problem in classical Fourier analysis of extracting the 'true' energy spectrum from a one that is windowed. A hint regarding the form of f, however, may be found from the notion that if we define the domain as $\Omega \subseteq \mathbb{R}^2 \times t$, where the azimuthal dimension in three-dimensional space is neglected in the LD integral, we see that the streamwise component of the Fourier modes are identified as the analogue to the stretched amplitude decaying Fourier in $L^2\left(\Omega, \mathbb{C}^3\right)$. At the time of writing of this thesis, however, the function f is unknown for $\Omega \subseteq \mathbb{R}^3 \times t$. Due to this, we are limited to the

analysis of the eigenfunctions in the weighted space which unfortunately blurs our understanding of some of the physical characteristics of the flow.

The LD was performed by discretizing the θ-coordinate into $n = 100$ points between $\theta/\theta_{\frac{1}{2}} = 0$ and 2.475. This resulted in a total of 200 LD modes for each Fourier coefficient. The normalized energy distribution of the LD modes are shown in Figure 4.21(a), and the cumulative sum is shown in Figure 4.21(b). The first mode contains 38.3% of the total energy of the field while the first seven modes contain 80% of the total energy in the flow. Figure 4.21(c) shows further that 80% of the energy of the first seven modes is contained in the region below $\kappa = 80$. The relative energies and the cumulative sums, χ_n, are summarized in Table 4.1 for the first eight modes. The absolute real parts of the first eight modes for the components ξ- and θ are seen in Figures 4.22 and 4.23.

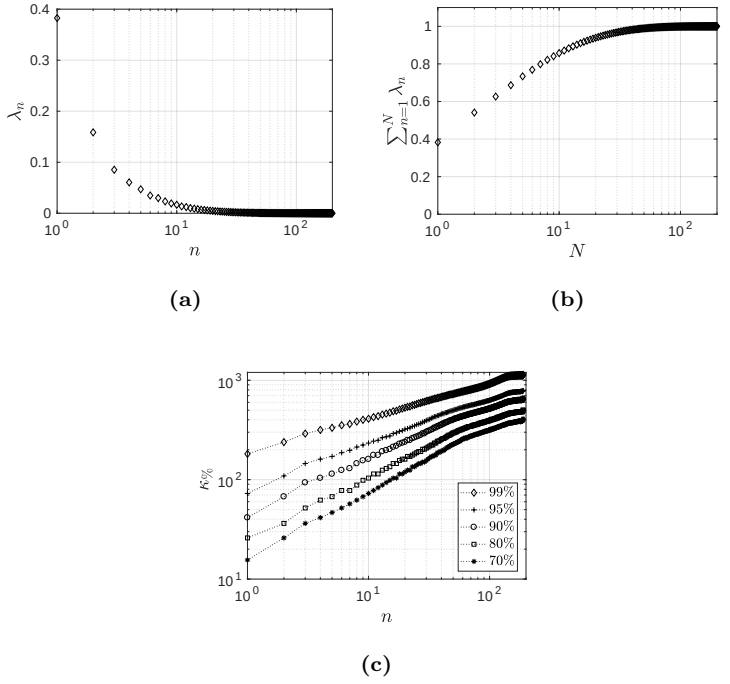

(a) **(b)**

(c)

Figure 4.21: (a): Normalized eigenvalues integrated over wavenumbers, (b): cumulative sum over normalized eigenvalues, (c): wavenumbers defining percentiles of energy across mode numbers, n.

As expected, most of the energy is contained in the low wavenumber re-

gion as it is seen that the contours subside for increasing κ-values. Part of this is due to the aliasing from the missing spatial direction. Note that the Parzen filter effectively removes the spectrally leaked energy to high wavenumbers which was seen in Wänström 2009. Otherwise, the contours between the current experiment and that of Wänström 2009 show a great resemblence although they were performed independently using different experimental setups and that the scaled cylindrical velocity components in similarity coordinates were applied in Wänström 2009.

Table 4.1: Relative modal energies and cumulative sums for the first eight modes.

n	1	2	3	4	5	6	7	8
λ_n	0.383	0.159	0.085	0.061	0.047	0.035	0.030	0.023
χ_n	0.383	0.542	0.627	0.688	0.735	0.770	0.800	0.822

Note that the normalization of the LD modes does not affect their orthogonality. This can be seen from (3.13), since for any constant scaling of eigenvectors this multiplier can be taken out of the inner product. Since only non-trivial solutions to the LD integral are found, the multiplier is guaranteed to be non-zero i.e. the absolute value of the eigenfunction itself is guaranteed to be non-zero.

Figures 4.26 and 4.27 show the normalized LD modes for the ξ- and θ-components. It is noteworthy that the two most distinct modes are 1 and 2 seen in Figure 4.26 and that these have the most distinct eigenvalues. Modes 5 and 7, and 6 and 8 are very similar, and so are modes $9-16$. The striking similarity between ξ-components of the modes even for low mode numbers, suggests that a significant number of these may quite successfully be modelled by the same eigenfunction with an appropriate phase-shift. Since the difference between adjecent eigenvalues is seen to decrease rapidly for $\alpha > 4$ (Figure 4.21(a)) this correlates with the notion that modes with similar eigenvalues often describe related dynamic processes.

From Figures 4.23(a)-and 4.23(b), 4.27(a), and 4.27(b), the most energetic modes $(1-4)$ have negligible θ-components at low wavenumbers. This is expected since Figures 4.15(a) and 4.15(b) illustrate that the θ-component of velocity in general has negligible energy production and therefore can only play a key part in the energy transport across wavenumbers. This may be understood by perceiving the shear-stresses as the θ-transport of v^ξ by v^θ distributing the energy most effectively across the jet in regions where mean shear peaks, in a

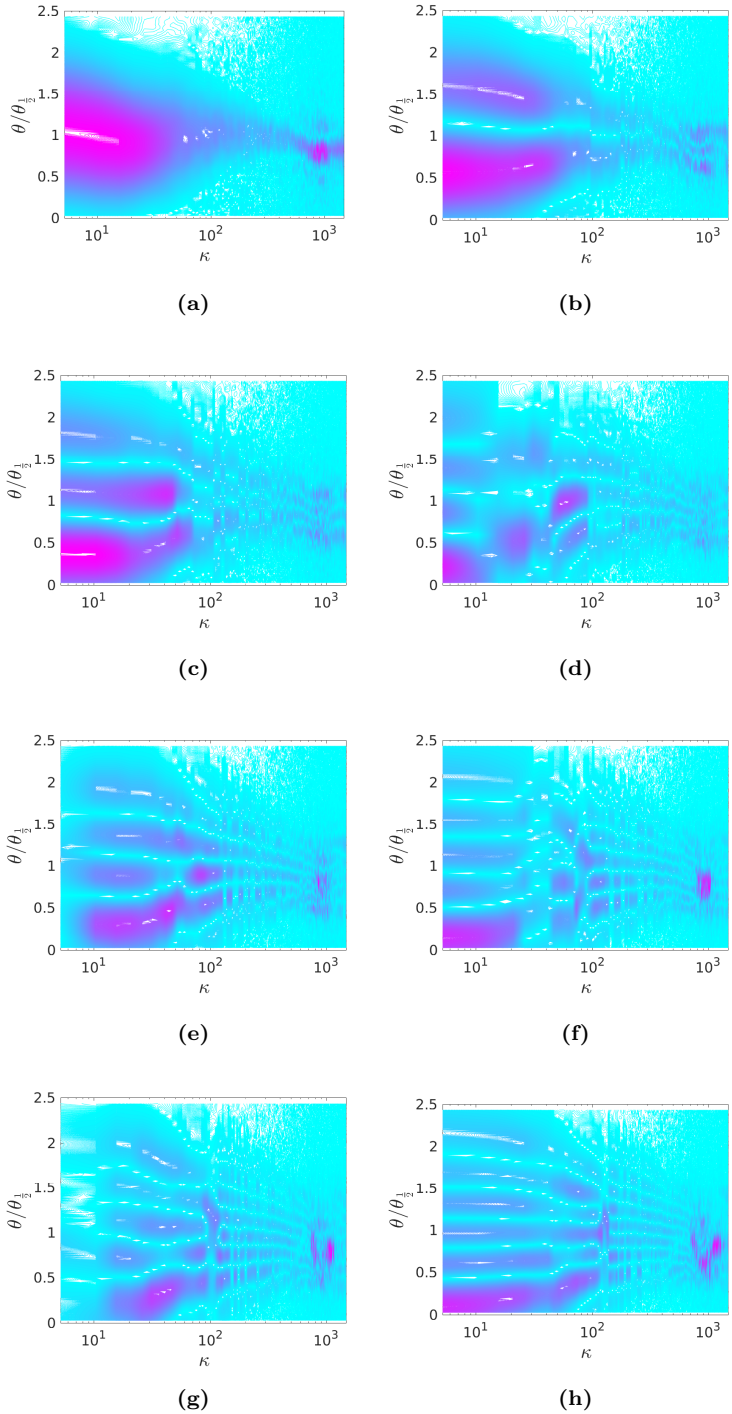

Figure 4.22: The absolute real parts of ξ-components of the LD modes $\alpha = 1 - 8$, as a function of dimensionless wavenumber, $|\Re\left\{\Psi_\alpha^\xi(\kappa, \theta)\right\}|$.

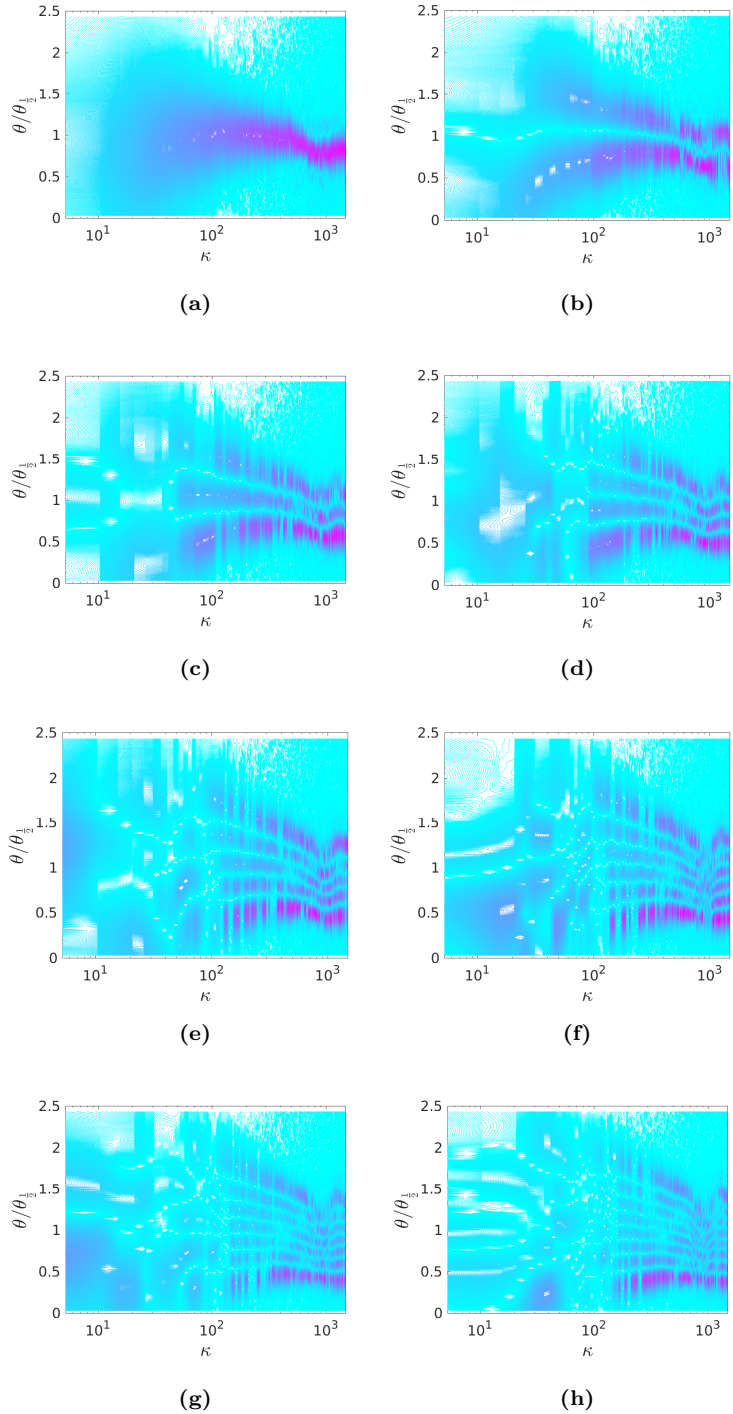

Figure 4.23: The absolute real parts of θ-components of the LD modes $\alpha = 1 - 8$, as a function of dimensionless wavenumber, $|\Re\left\{\Psi_\alpha^\theta(\kappa, \theta)\right\}|$.

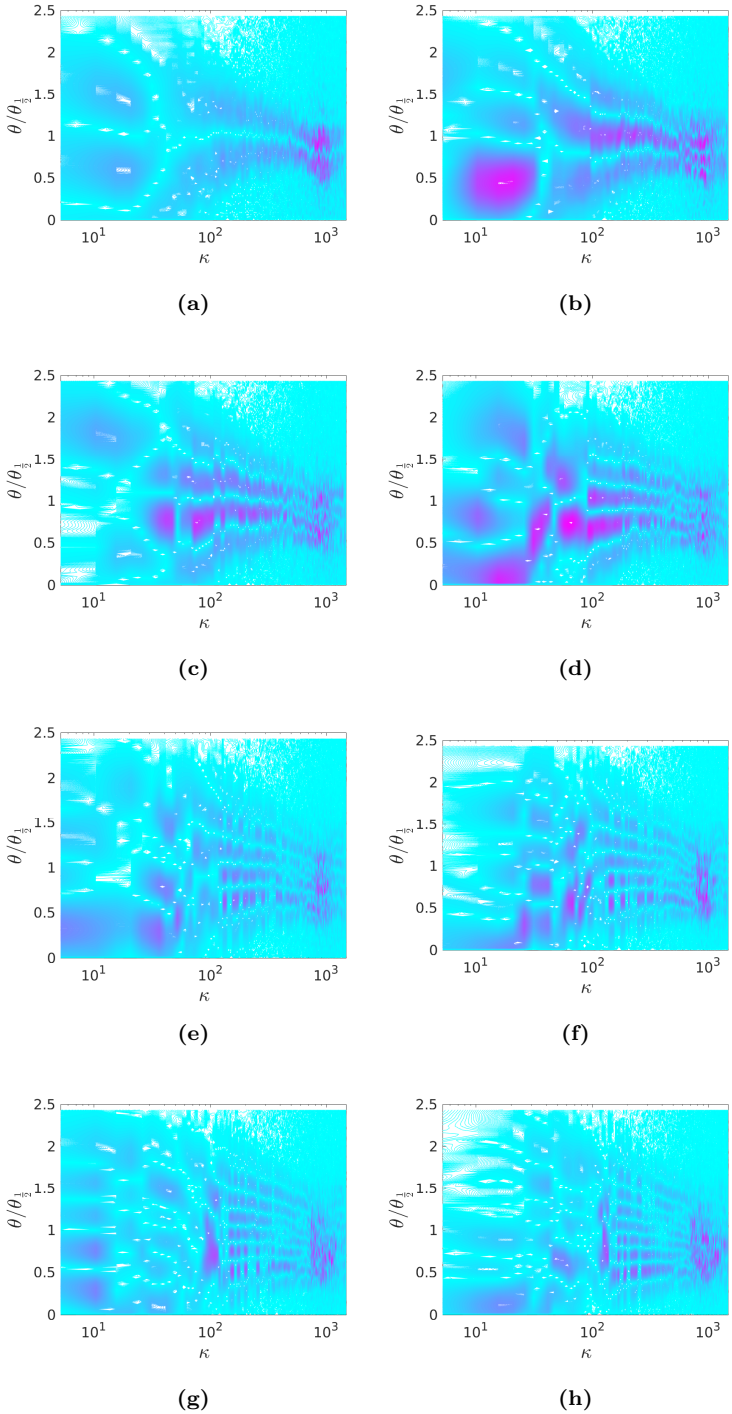

Figure 4.24: The absolute imaginary parts of ξ-components of the LD modes $\alpha = 1 - 8$, as a function of dimensionless wavenumber, $|\Im\left\{\Psi_\alpha^\xi(\kappa,\theta)\right\}|$.

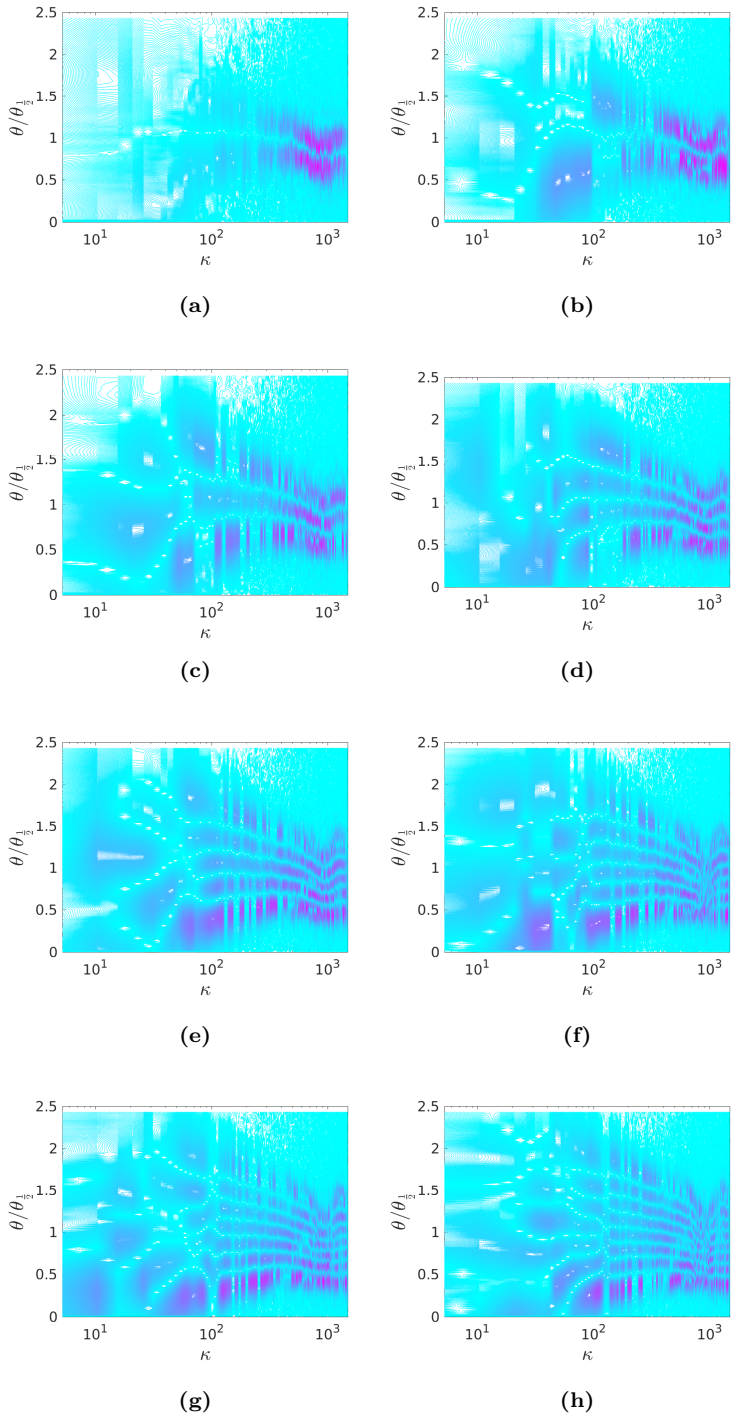

Figure 4.25: The absolute imaginary parts of θ-components of the LD modes $\alpha = 1 - 8$, as a function of dimensionless wavenumber, $|\Im\left\{\Psi_\alpha^\theta(\kappa,\theta)\right\}|$.

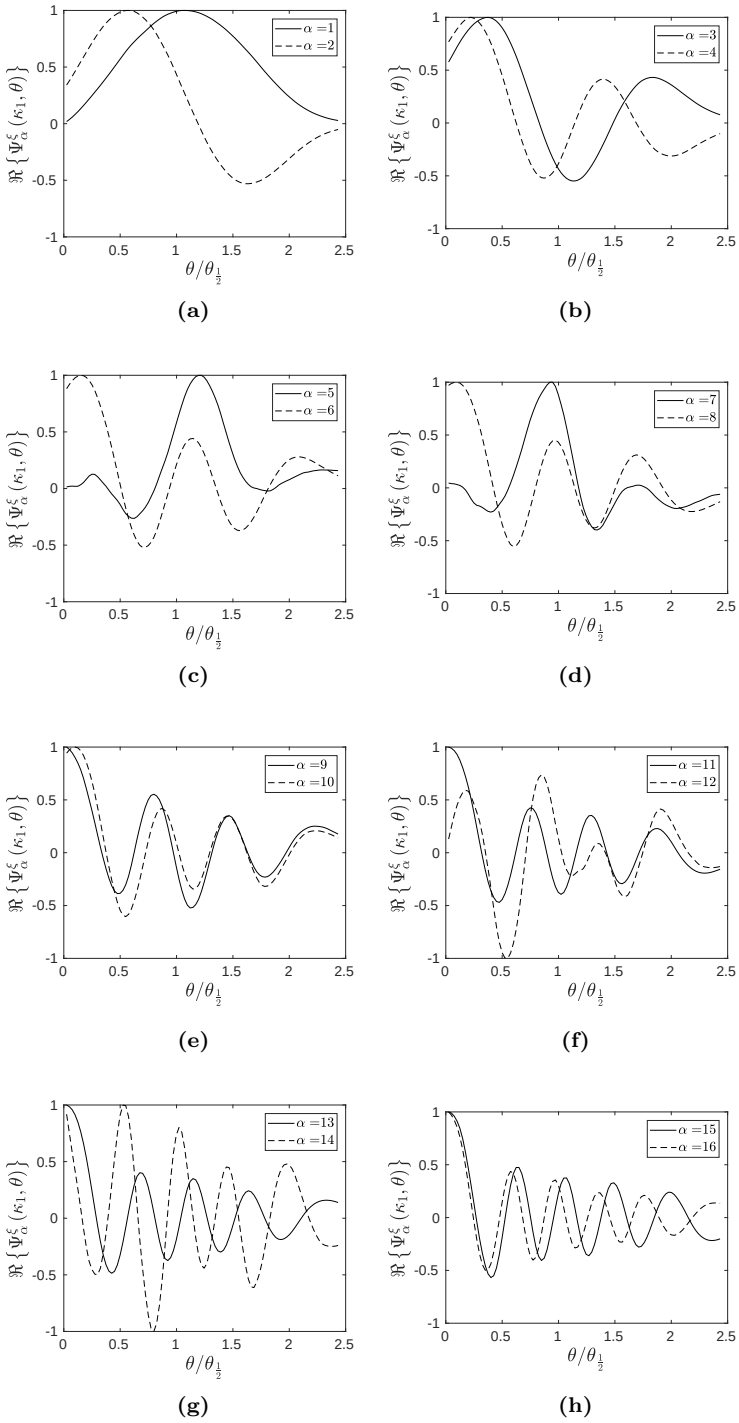

Figure 4.26: The real parts of the ξ-components of LD modes $\alpha = 1-16$ related to the first wavenumber, $\Re\left\{\Psi_\alpha^\xi(\kappa_1,\theta)\right\}$.

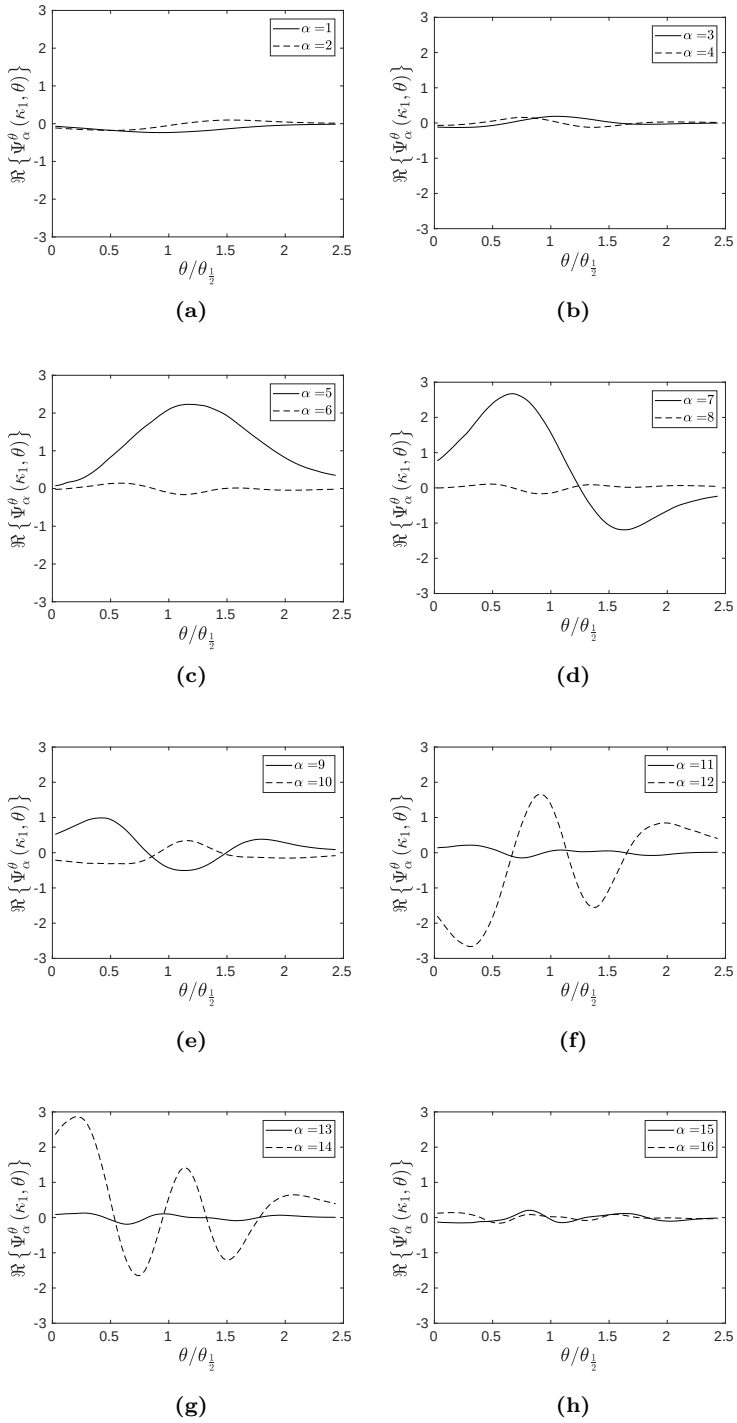

Figure 4.27: The real parts of the θ-components of LD modes $\alpha = 1-16$ related to the first wavenumber, $\Re\left\{\Psi_\alpha^\theta(\kappa_1,\theta)\right\}$.

classical Boussinesq-type fashion. Since the low-wavenumber region of the energy spectra represents the region related to TKE production the θ-components of the LD modes must necessarily be very limited in this same wavenumber region, as they would otherwise contribute significantly to the TKE production through the reconstruction of $\Phi_{1,2}$. This is confirmed by Figures 4.23(a)-4.23(d) where significant amplitudes only appear in the inertial subrange. We shall return to this discussion in the reconstruction of the spectra in section 4.3.4.

Since the modes along ξ are represented by waves of the physical form, $e^{i\kappa\xi-\xi}$ their correlation is represented by Figures 4.22-4.23. In fully developed turbulence the group velocities of the longest waves are often correlated with the local mean velocity. For shorter wavelengths this is less often the case, due to the velocity induced on them by larger scales. Therefore we note that waves in general are expected to move with very different group velocities across the jet-width. The correlation between these waveforms - which is what the modes are representing - is therefore determined by the extent to which the waves across the jet share the same phase velocity.

4.3.4 Reconstruction of the Velocity field in SSC

In Wänström 2009 it was stated that several azimuthal (Fourier) modes of the jet are able to obtain a significant part of their energy directly from the mean flow, thereby circumventing a Richardson-like energy cascade from low- to high mode numbers. From the current measurements, we can examine directly the modal contributions to the reconstruction of the energy production term, (4.7), as well as the variations of these contributions across the jet (Figure 4.15(a)). Note that while the mean turbulence kinetic energy is dominated by the streamwise Reynolds-stresses the energy production term is dominated by the shear-stresses. This characterization of the principal modal contributions to the energy production will provide information regarding the effect of the mean shear gradient - which is varying greatly across the jet. Also, we can examine the modal contributions to the component energy density spectra and cross-spectra. The building blocks required to reconstruct the characteristic $-5/3$-range across the span of the flow will be provided in order to investigate which modes are dominant participants in the energy transfer between scales. Finally, in order to gain a broader understanding of the self-similarity hypothesis posed by Lumley 1967a in terms of its modal building blocks, the $-7/3$-range of the cross-spectrum will be reconstructed. This discussion will lead to the notion of modal *self-similarity.*

4.3.4.1 Analysis of component spectral topology

The individual contributions of modes $1-8$ to the spectra $\Phi_{1,1}$, $\Phi_{2,2}$, and $\Phi_{1,2}$ are shown in Figures 4.28-4.30. The figures give an overview of the individual contributions of the first eight modes for all wavenumbers and illustrate an important point regarding the contribution of the first mode to the spectra. The role of the θ-component of the modes as well as the contribution of this component to the energy production will be demonstrated more clearly in the paragraphs to follow, but it is clear from the contour lines in Figures 4.28(a) and 4.29(a), that unlike $\Phi^{(1)}_{1,1}$ the peak of $\Phi^{(1)}_{2,2}$ occurs at higher wavenumbers in the production range than for $\Phi^{(1)}_{1,1}$. As noted earlier in Wänström 2009, this is consistent with what is observed in homogeneous isotropic turbulence Tennekes and Lumley 1972, where it is a direct consequence of incompressibility. It is probably significant that it is observed in this turbulence as well - at least in SSC.

Comparing the peaks of Figures 4.28(a) and 4.29(a) indicates that significant energy production through mean shear can only occur from the wavenumber range where significant contributions from both $\Phi^{(1)}_{1,1}$ and $\Phi^{(1)}_{2,2}$ overlap. Therefore, the contribution of the first mode to the reconstruction of the cross-spectrum, $\Phi^{(1)}_{1,2}$, in Figure 4.30(a) shows that the maximum energy production is related to slightly higher wavenumbers than for $\Phi^{(1)}_{1,1}$. This means that the most significant energy productions from normal- and shear stresses occur for different wavenumbers. However, aliasing of high wavenumber energy into lower wavenumbers of one-dimensional spectra introduces uncertainties in this regard.

Upon closer inspection - and in stark contrast to the low-wavenumber region - it is seen that each modal contribution to the reconstruction of the spectra retains its shape in the inertial subrange. This should be interpreted as *modal self-similarity* across wavenumbers, and can be considered statistical proof of time averaged scale invariance across the jet-width. It can be considered an extension of the idea proposed by Lumley 1967a (section 4.3.2) for constant shear flows for modelling the cross-spectral similarity in the inertial subrange across the entire span of the jet. The modal self-similarity of higher modes in fact seems independent of the large velocity gradient variations over the span of the flow. Symmetry of the turbulence is suggested by the similarity between the respective modal contributions to $\Phi^{(n)}_{1,1}$ and $\Phi^{(n)}_{2,2}$ in figures 4.28 and 4.29 in the inertial subrange.

The cumulative sums of the modal contributions to the reconstruction of energy density- and cross-spectra are shown in Figures 4.31-4.33. It is characteristic that various modes are rebuilding the spectra initially

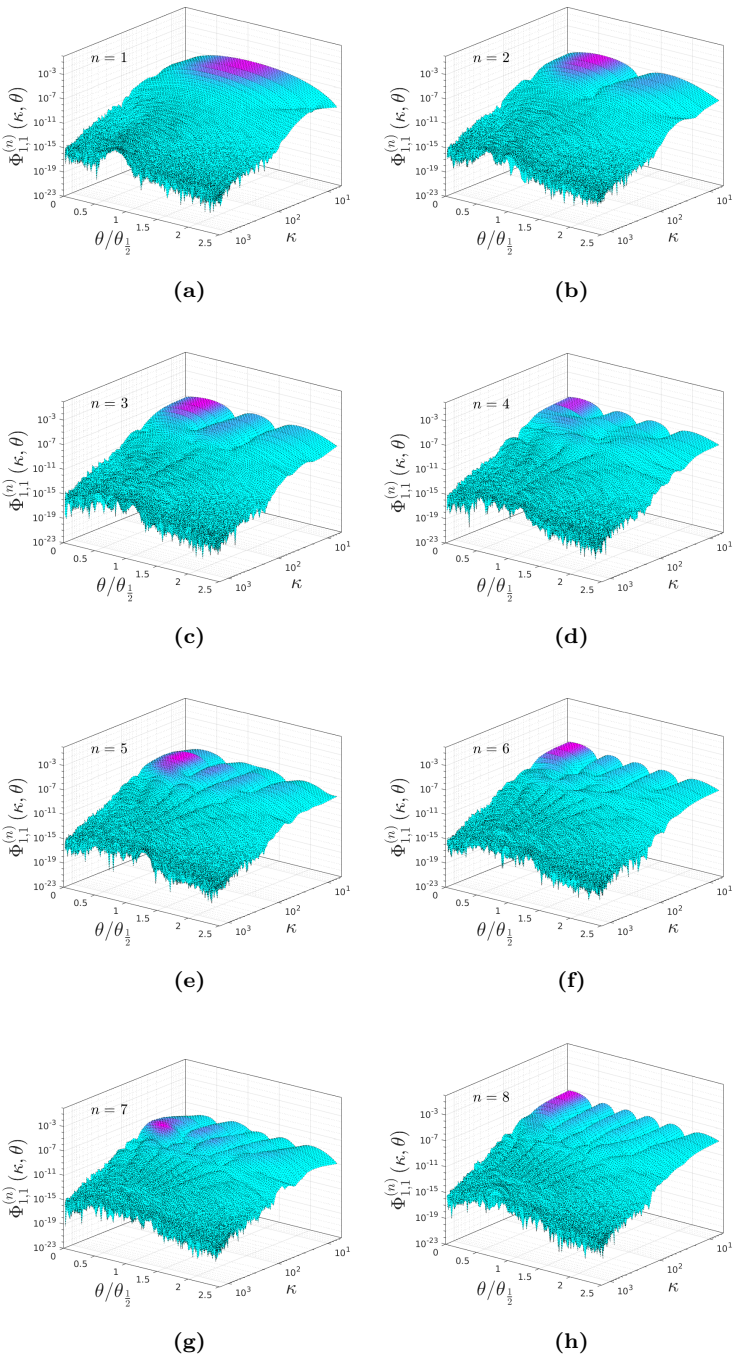

Figure 4.28: Modal contributions to the reconstruction of the streamwise energy spectrum, $\Phi_{1,1}$, of modes $n = 1 - 8$.

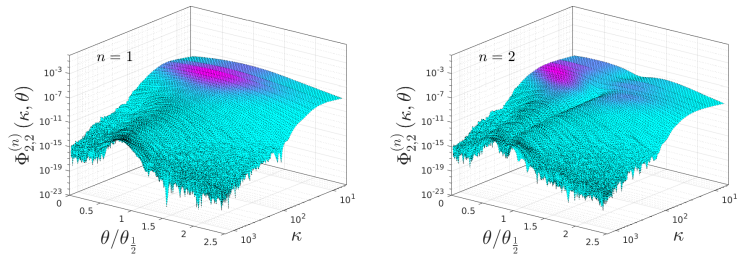

(a)

(b)

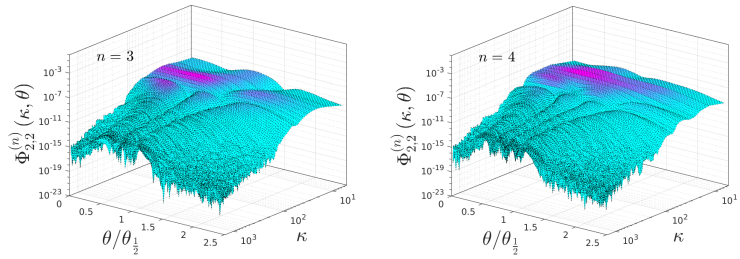

(c)

(d)

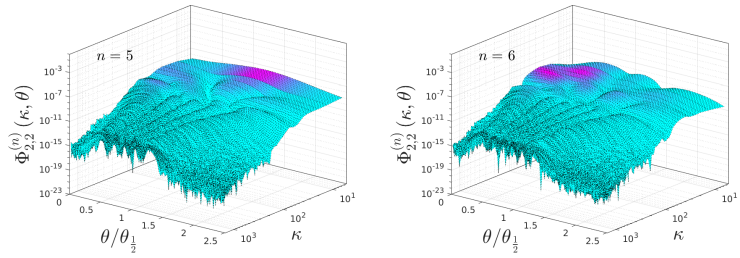

(e)

(f)

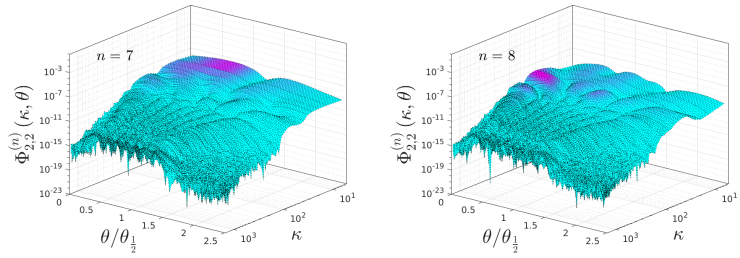

(g)

(h)

Figure 4.29: Modal contributions to the reconstruction of the radial energy spectrum, $\Phi_{2,2}$, of modes $n = 1 - 8$.

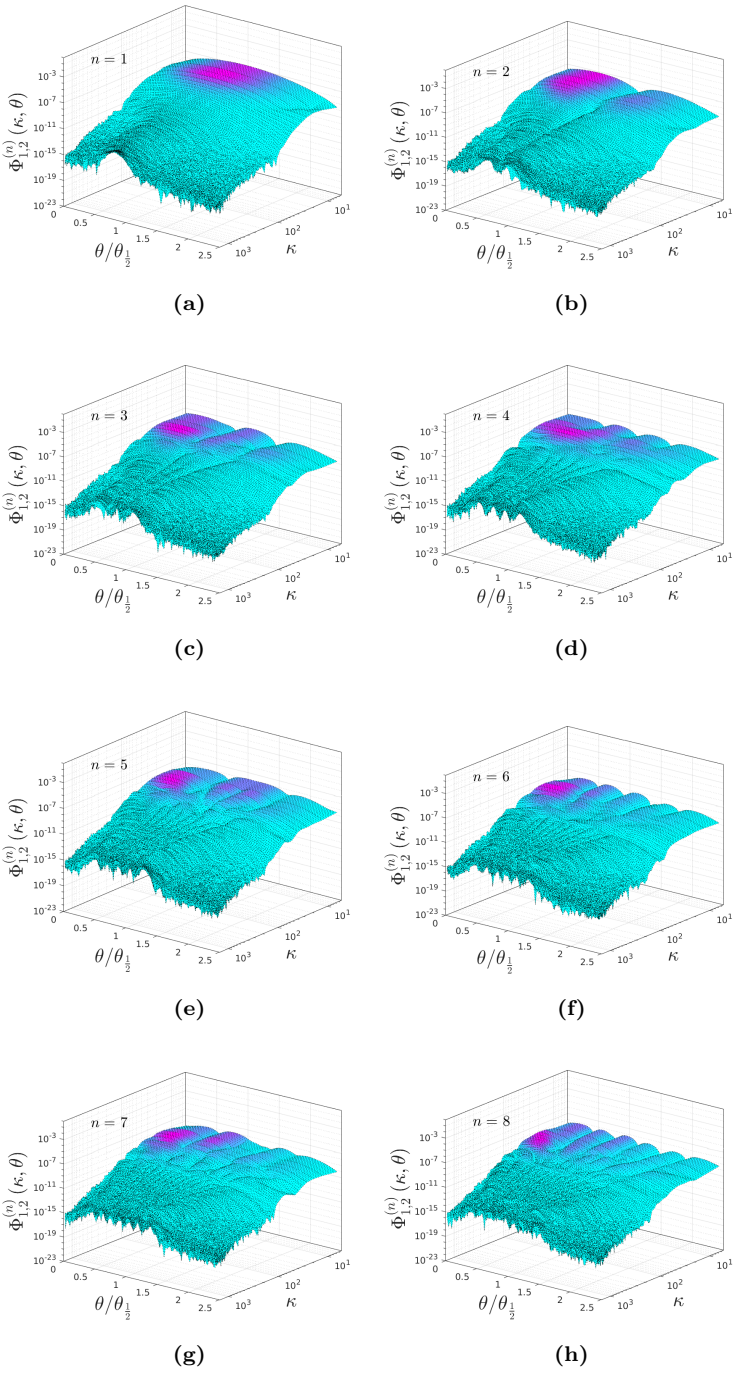

Figure 4.30: Modal contributions to the reconstruction of the cross-spectrum, $\Phi_{1,2}$, of modes $n = 1 - 8$.

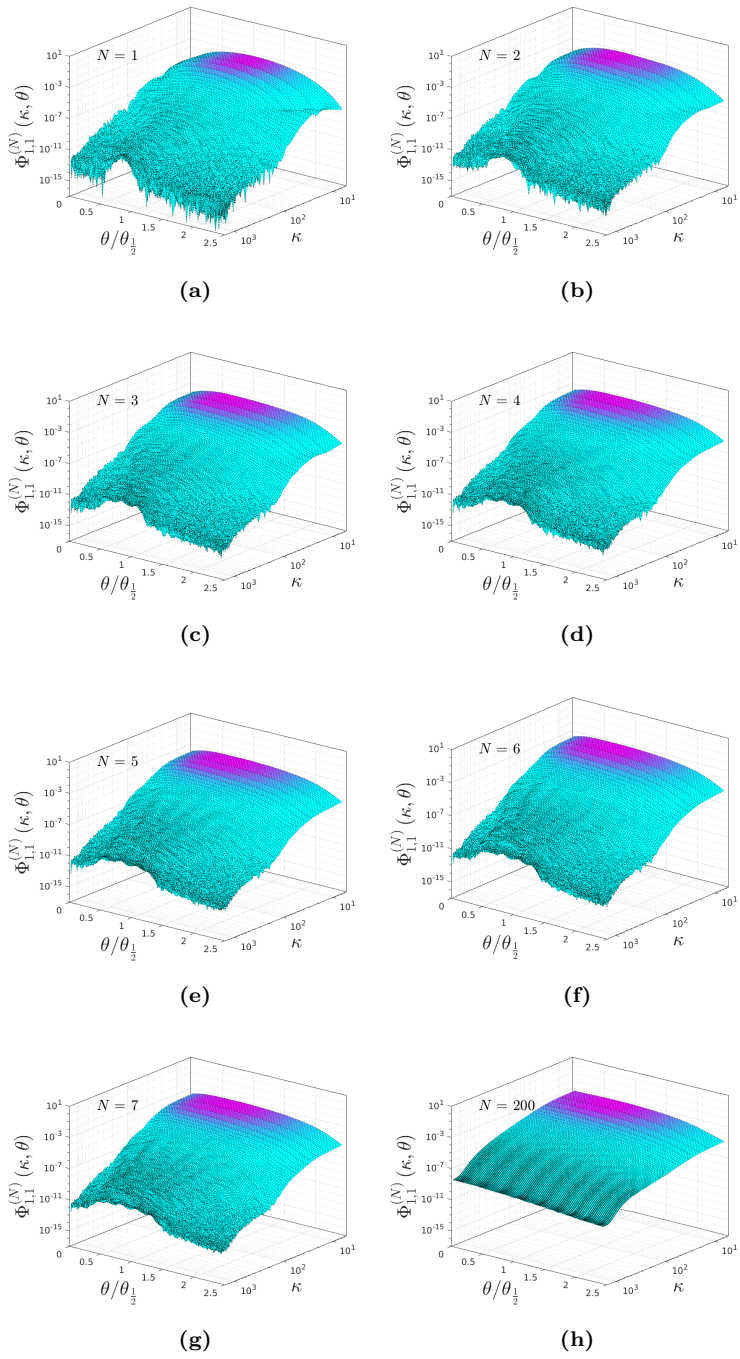

Figure 4.31: Modal cumulative contributions to the reconstruction of the streamwise energy spectrum, $\Phi_{1,1}$, of the cumulative sums $N = [1, 2, 3, 4, 5, 6, 7, 200]$.

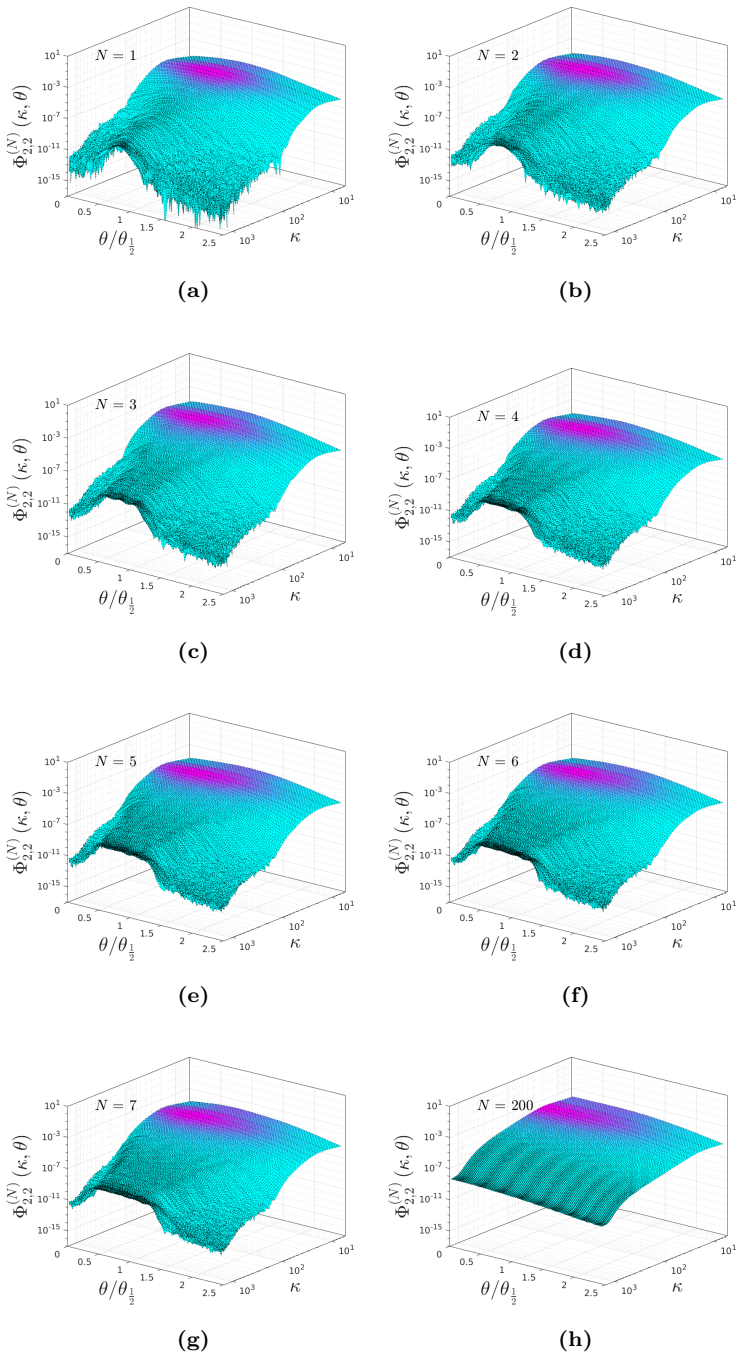

Figure 4.32: Modal cumulative contributions to the reconstruction of the radial energy spectrum, $\Phi_{2,2}$, of the cumulative sums $N = [1, 2, 3, 4, 5, 6, 7, 200]$.

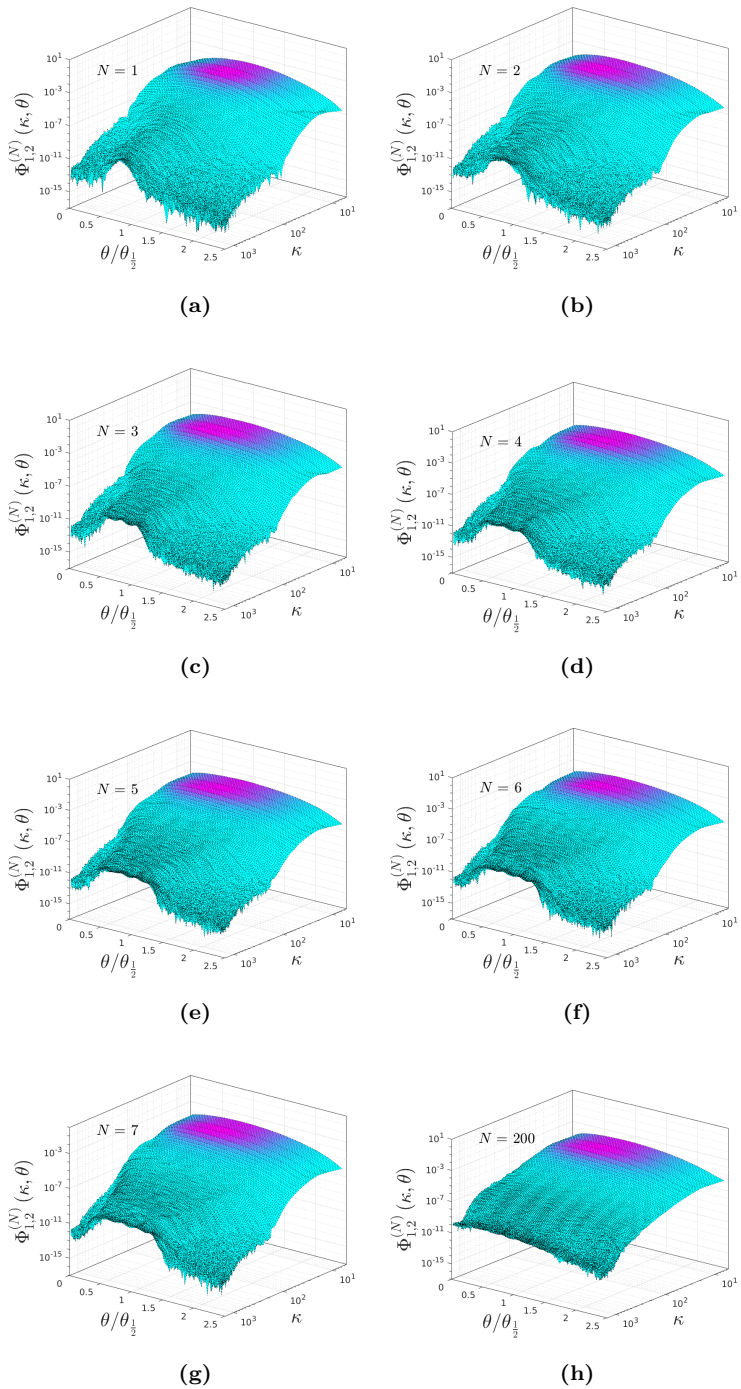

Figure 4.33: Modal cumulative contributions to the reconstruction of the cross-spectrum, $\Phi_{1,2}$, of the cumulative sums $N = [1, 2, 3, 4, 5, 6, 7, 200]$.

from $\theta/\theta_0 = 1$. It is seen that these modes are very efficiently constructing a *flat* topology around the region of one half-width, which is related to it being the most energetic region in the flow. By comparing the total reconstruction seen in Figures 4.31(h), 4.32(h), and 4.33(h) it is evident that the high wavenumber regions very close to the centerline as well as at the edge of the jet are very slowly reconstructed. This will become more evident later, when the Reynolds stresses are reconstructed.

4.3.4.2 Modal reconstruction of component spectra

Figures 4.34-4.39 show the individual modal contributions in the reconstruction of $\Phi_{i,j}$ for various θ-position across the jet. Figures 4.40-4.45 show the cumulative modal contributions. These figures are shown in order to analyze the reconstruction of the $-5/3$- and $-7/3$-slope ranges at various θ-coordinates. Specifically we are interested in finding out whether individual modal building blocks reconstruct these slopes, or whether it is a combination of modes that is required to achieve the reconstruction.

The individual modal contributions for the reconstruction of $\Phi_{1,1}$ are seen in Figures 4.34-4.35. The individual modal contributions have closer values towards the end of the $-5/3$-region around $\theta/\theta_0 = 1$, than elsewhere. Recall from Figures 4.17-4.20 that the $-5/3$-range is already manifested from $\theta/\theta_{\frac{1}{2}} = 0.07$ and stretches across the entire width. However, the first eight modal contributions in Figures 4.34-4.35 show that none of these reflect the $-5/3$-slope. The cumulative sum seen in 4.40-4.41, shows the first eight modal contributions to $\Phi_{1,1}$, as well as the full reconstructed spectrum. It can be seen that the $-5/3$-slope is reconstructed only when contributions of higher modes are added. This means that the $-5/3$-slope in $\Phi_{1,1}$ is defined by low-energy modes, each of which are of course topologically different.

Now the case is different for the reconstruction of the $\Phi_{2,2}$-spectrum. The individual modal contributions to $\Phi_{2,2}$ are shown in Figures 4.36-4.37. As one moves from the centerline towards the $\theta/\theta_{\frac{1}{2}}$-region, the number of modes contributing to the reconstruction of the $-5/3$-range is diminishing. Upon closer inspection it is seen that it takes both modes 1 and 2 to reconstruct the $-5/3$-slope at $\theta/\theta_{\frac{1}{2}} = 0.67$, whereas the $-5/3$-range is reconstructed entirely by the the first mode around $\theta/\theta_{\frac{1}{2}} = 1$. This process is reversed as we move towards the jet boundary, where multiple modes are again observed to contribute to the reconstruction of the $-5/3$-slope of the spectrum. This is supported by the collapse around $\theta/\theta_{\frac{1}{2}} = 1$ of the cumulative contributions to the reconstruction of $\Phi_{2,2}$ which are shown in Figures 4.42-4.43. From the earlier discussion in sections 4.3.1 and 4.3.3 regarding the role of the θ-velocity component to the energy transport, it is clear that the θ-components of the modes

are optimized in terms of the energy transport, which is intriguing. The reconstruction of the $-5/3$-region with the first mode only is a direct consequence of this.

Observing the reconstruction of the cross-spectra by the individual modal contributions in figures 4.38-4.39 as well as the cumulative contributions in figures 4.44-4.45, similar traits to the reconstruction of $\Phi_{2,2}$ are seen. Note, however, that the modes reconstruct the $-7/3$-slope around $\theta/\theta_{\frac{1}{2}}$ with the first mode alone. This result is quite astonishing demonstrating that the shear-stress production is defined almost completely by the first LD mode. It will in fact later be shown that unlike the Reynolds normal stresses, the shear-stress profile will be reconstructed almost entirely with the first mode at all θ-coordinates. This is also indicated by the cumulative reconstruction of cross-spectra in figures 4.44-4.45, due to the collapse of the modal contributions over a very wide range of the jet-width, indicating that each additional mode contributes very little to the total spectrum. Note, that these results not only confirm the spectral similarty from Lumley 1967a which was somewhat indicated by the modal self-similarity discussed earlier, but also demonstrate that shear-stress producing structures in the inertial subrange are completely defined by the first LD mode in regions with high constant shear in the jet, namely around $\theta/\theta_{\frac{1}{2}} = 1$. This correlates with the fact that high shear regions may produce significant TKE at a wide range of scales, as seen directly from (4.7) in case of large mean gradients.

In the following a more in-depth energy production analysis will be performed focusing on the local energy production of the modes. The analysis will test the extent to which the hypothesis posed in Wänström 2009 holds, namely that multiple modes obtain significant and relatively constant parts of their energy directly from the mean flow. This will lead to a quantification of the eigenvalue normalized production of each mode.

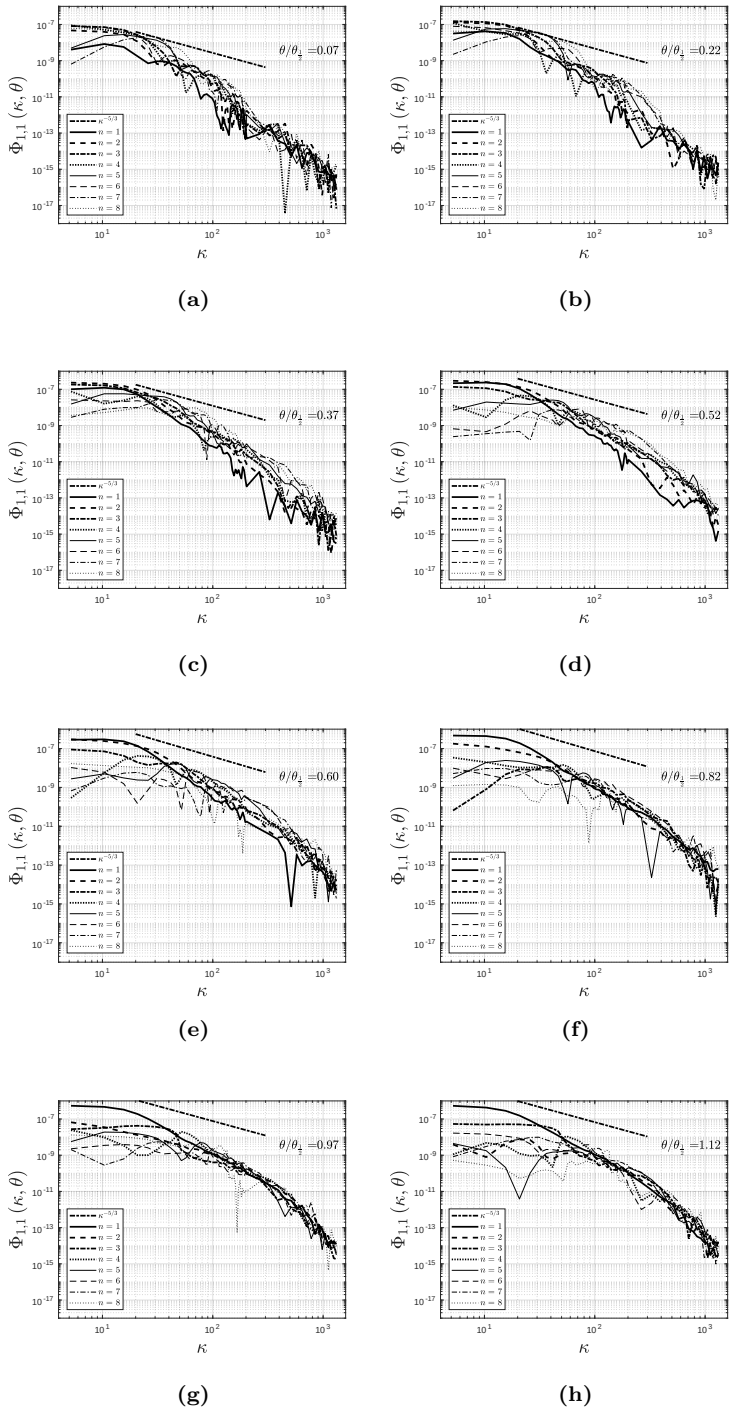

Figure 4.34: Modal components of single-point spatial spectra, $\Phi^n_{1,1}$, at various spanwise coordinates, $\theta/\theta_{\frac{1}{2}}$.

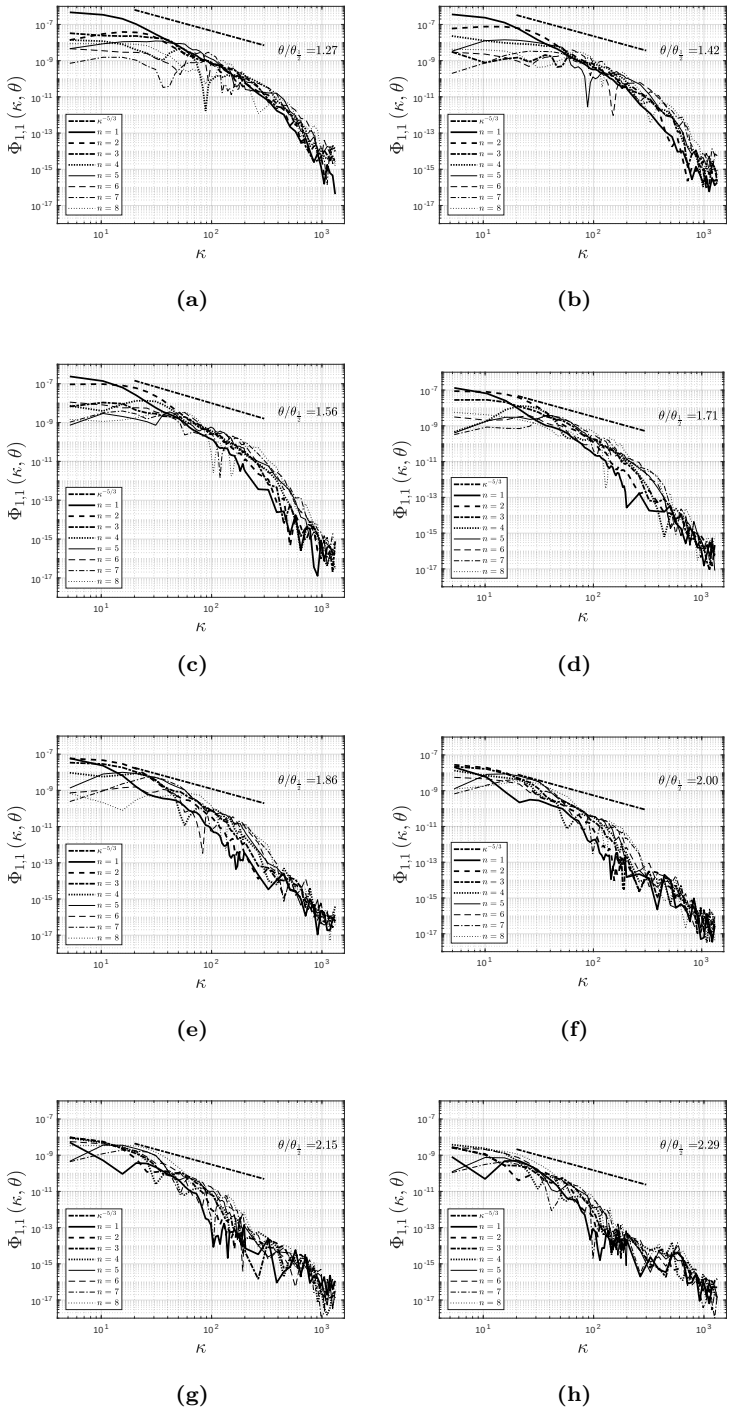

Figure 4.35: Modal components of single-point spatial spectra, $\Phi^n_{1,1}$, at various spanwise coordinates, $\theta/\theta_{\frac{1}{2}}$.

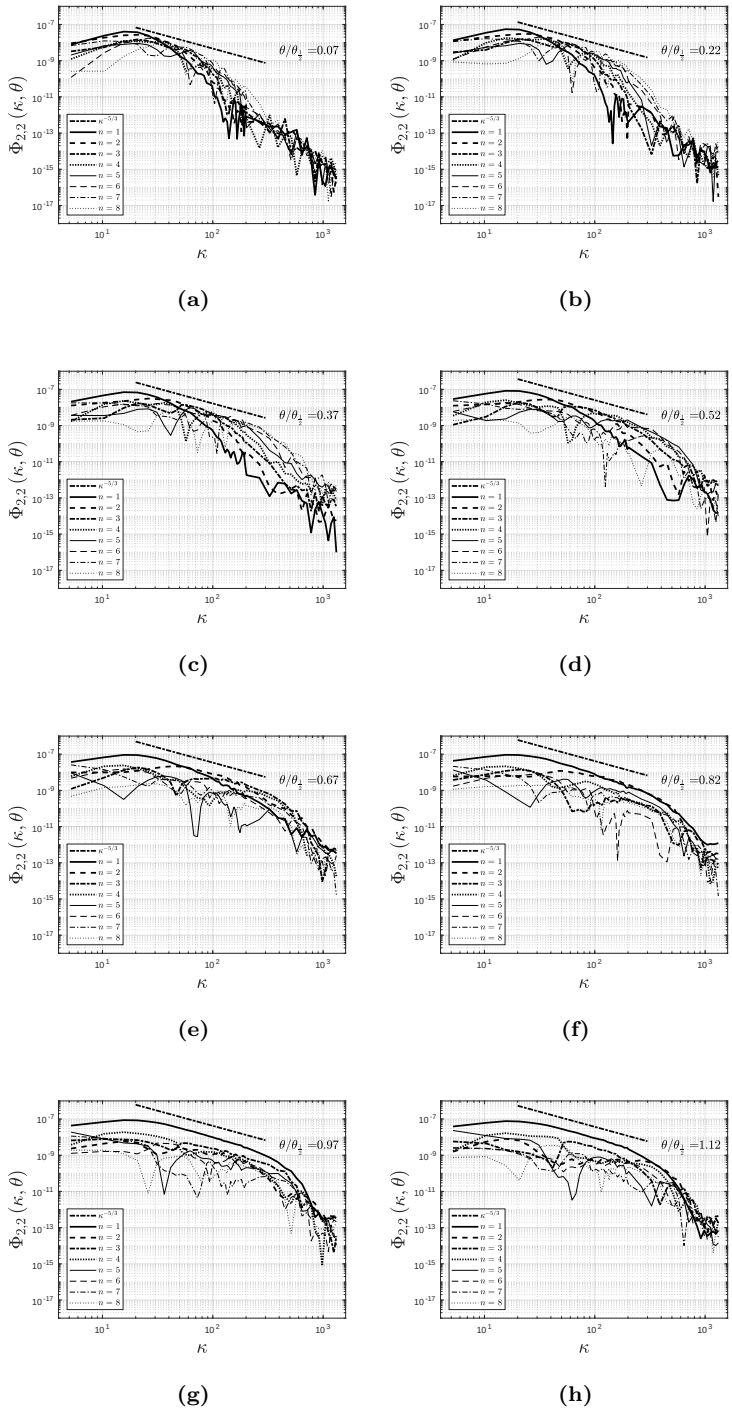

Figure 4.36: Modal components of single-point spatial spectra, $\Phi^n_{2,2}$, at various spanwise coordinates, $\theta/\theta_{\frac{1}{2}}$.

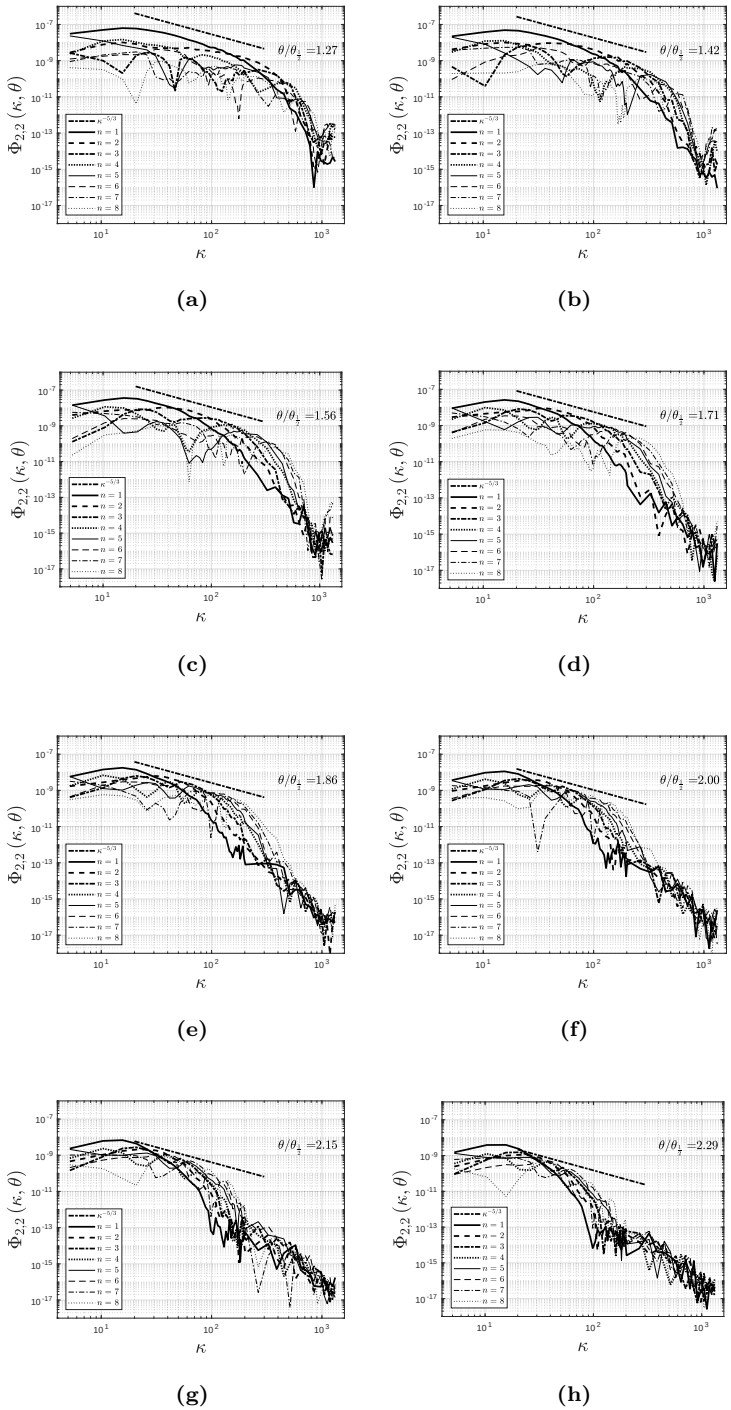

Figure 4.37: Modal components of single-point spatial spectra, $\Phi^n_{2,2}$, at various spanwise coordinates, $\theta/\theta_{\frac{1}{2}}$.

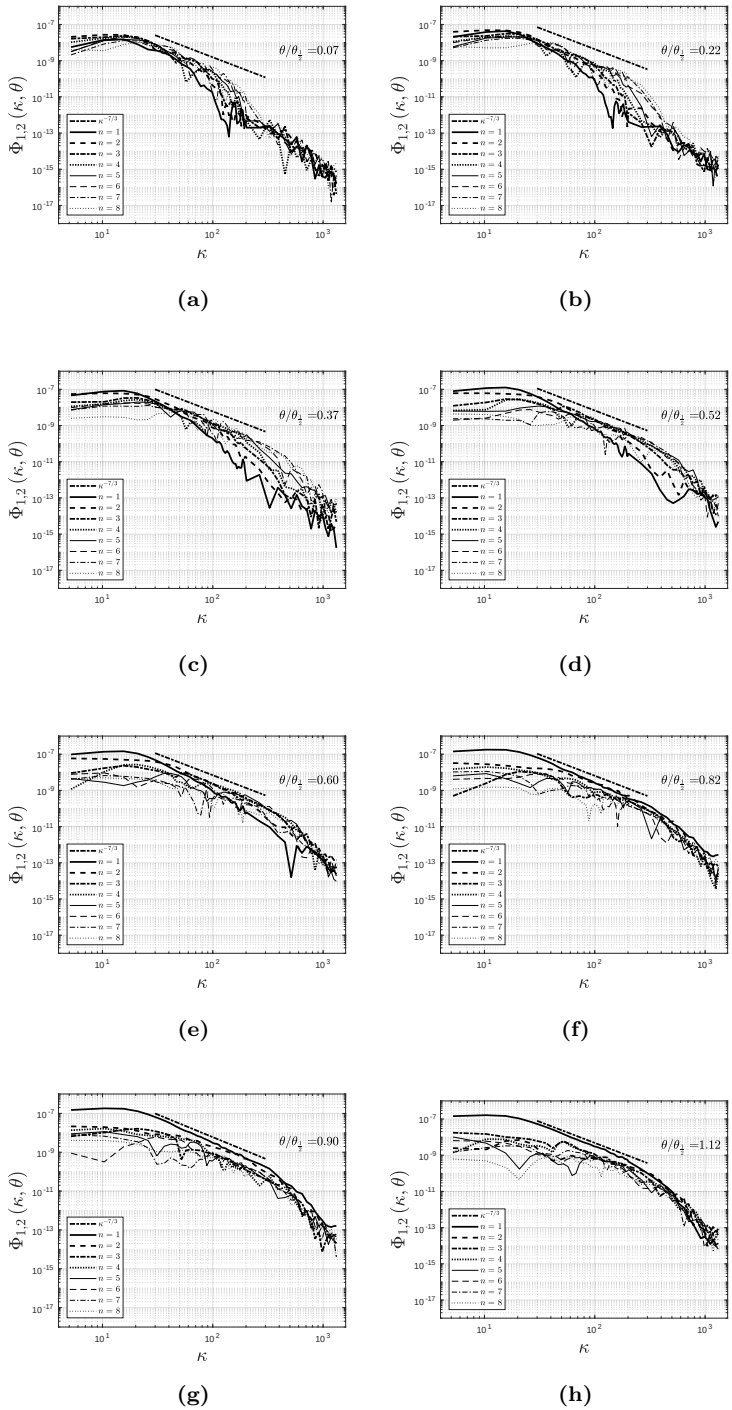

(a) **(b)**

(c) **(d)**

(e) **(f)**

(g) **(h)**

Figure 4.38: Modal components of single-point spatial spectra, $\Phi^n_{1,2}$, at various spanwise coordinates, $\theta/\theta_{\frac{1}{2}}$.

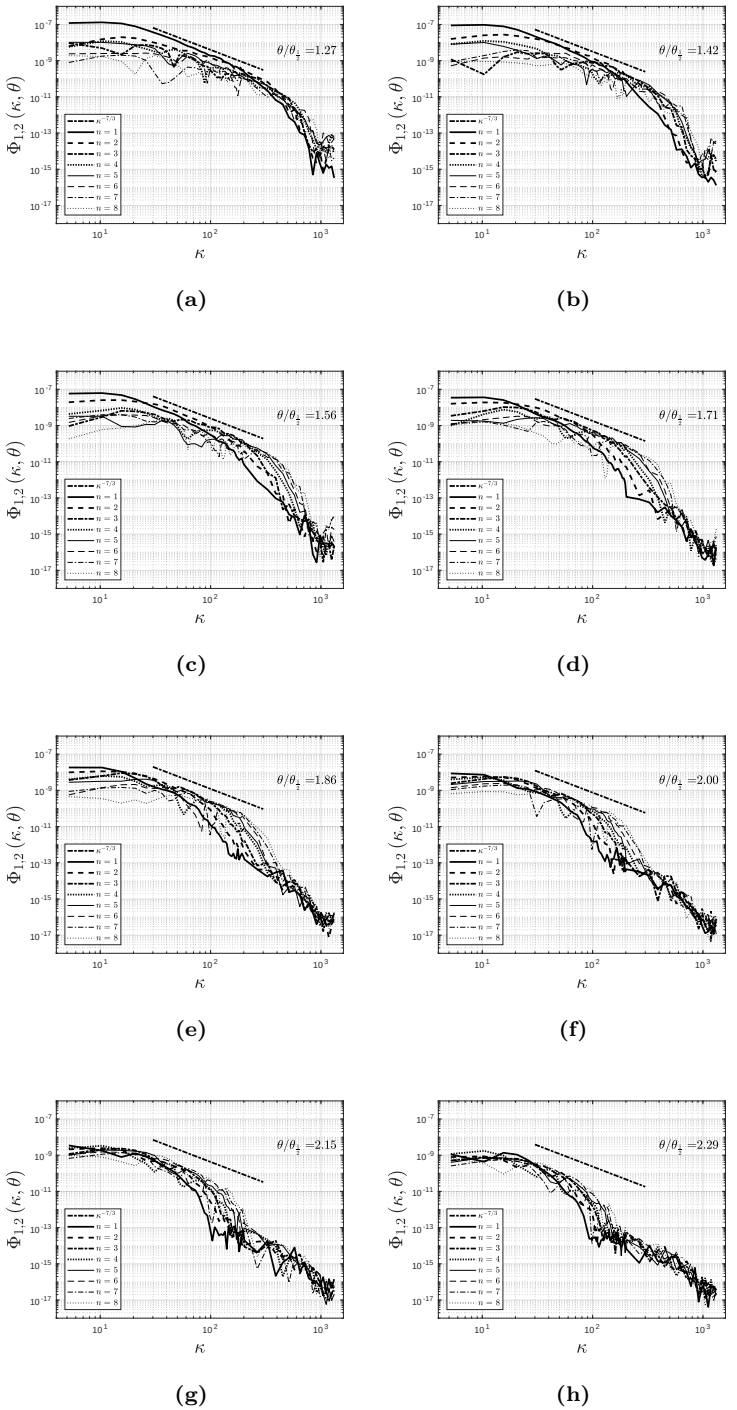

Figure 4.39: Modal components of single-point spatial spectra, $\Phi^n_{1,2}$, at various spanwise coordinates, $\theta/\theta_{\frac{1}{2}}$.

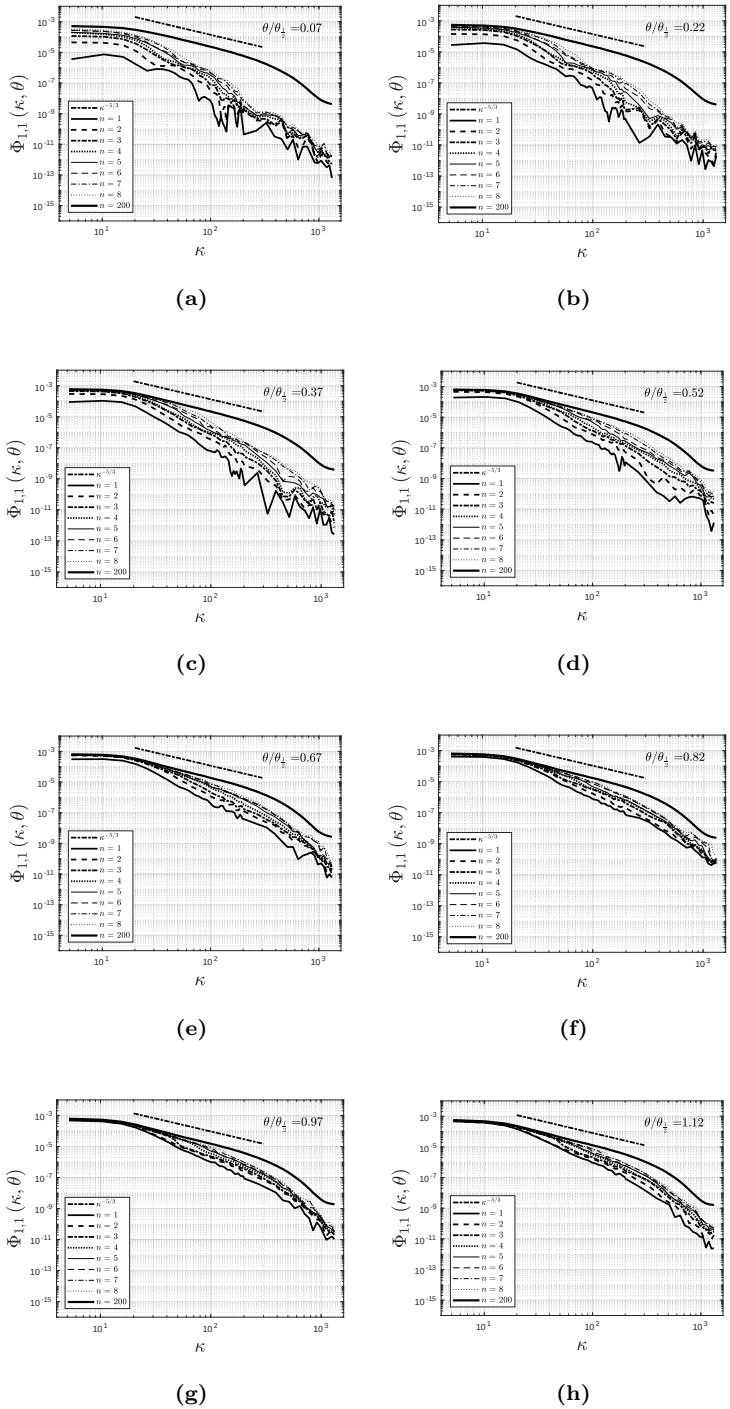

Figure 4.40: Cumulative modal components of single-point spatial spectra, $\Phi^N_{1,1}$, at various spanwise coordinates, $\theta/\theta_{\frac{1}{2}}$, where $\sum_{N=1}^{n} \Phi^N_{1,1}$.

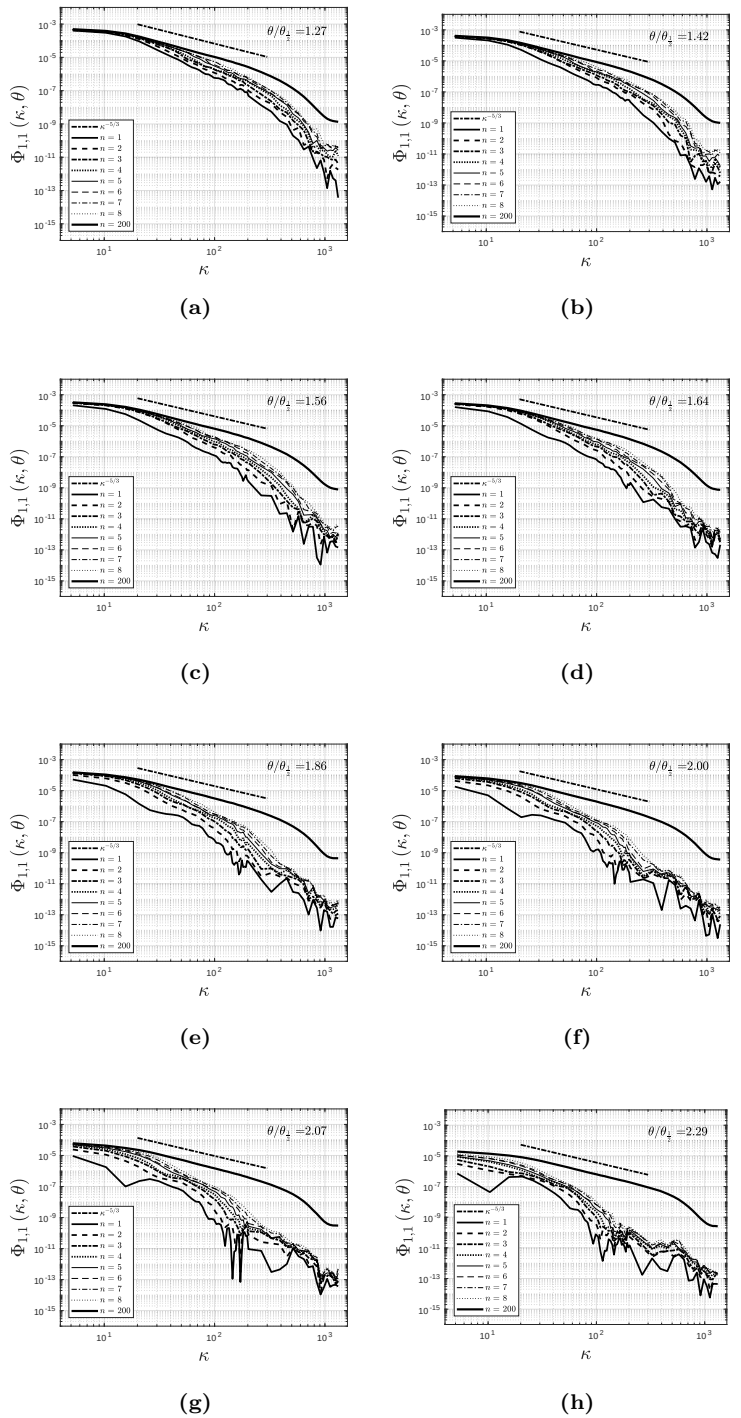

Figure 4.41: Cumulative modal components of single-point spatial spectra, $\Phi^N_{1,1}$, at various spanwise coordinates, $\theta/\theta_{\frac{1}{2}}$, where $\sum_{N=1}^{n} \Phi^N_{1,1}$.

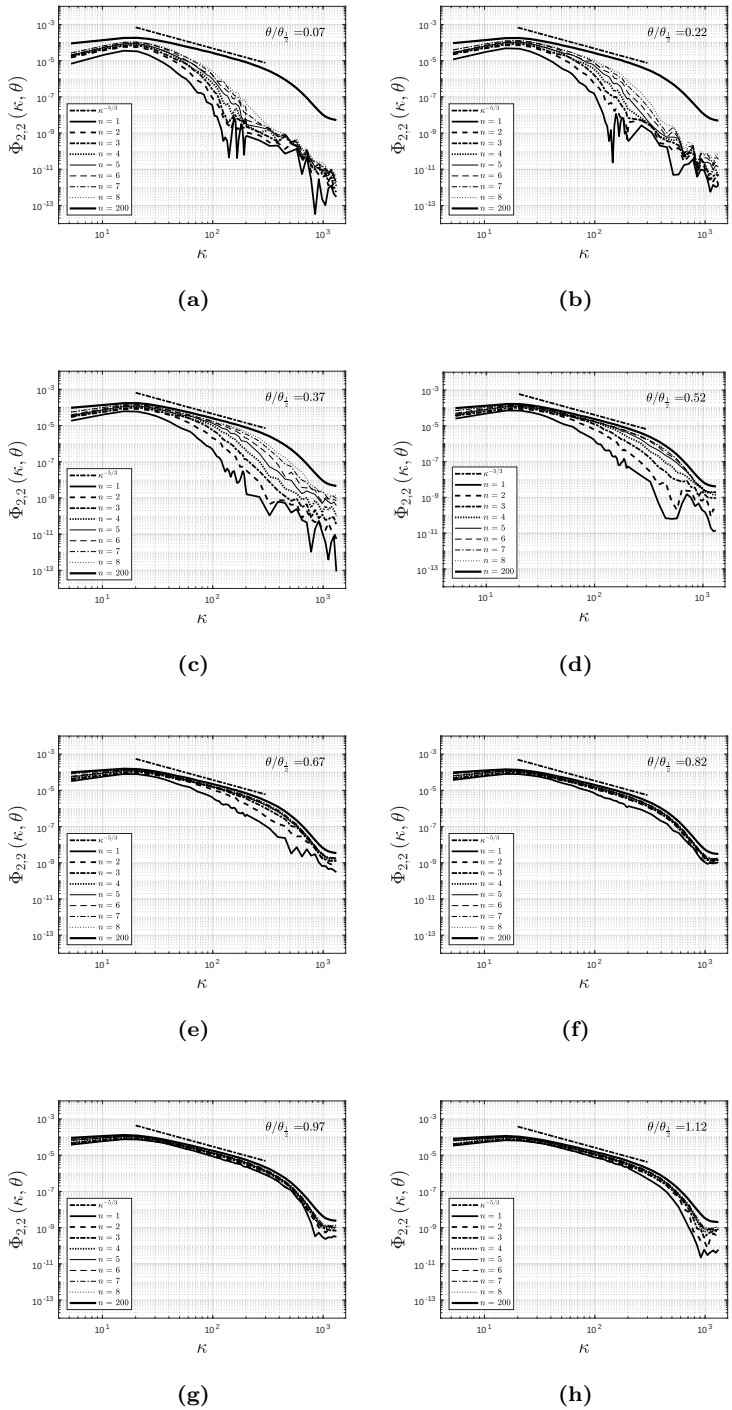

Figure 4.42: Cumulative modal components of single-point spatial spectra, $\Phi^N_{2,2}$, at various spanwise coordinates, $\theta/\theta_{\frac{1}{2}}$, where $\sum_{N=1}^{n} \Phi^N_{2,2}$.

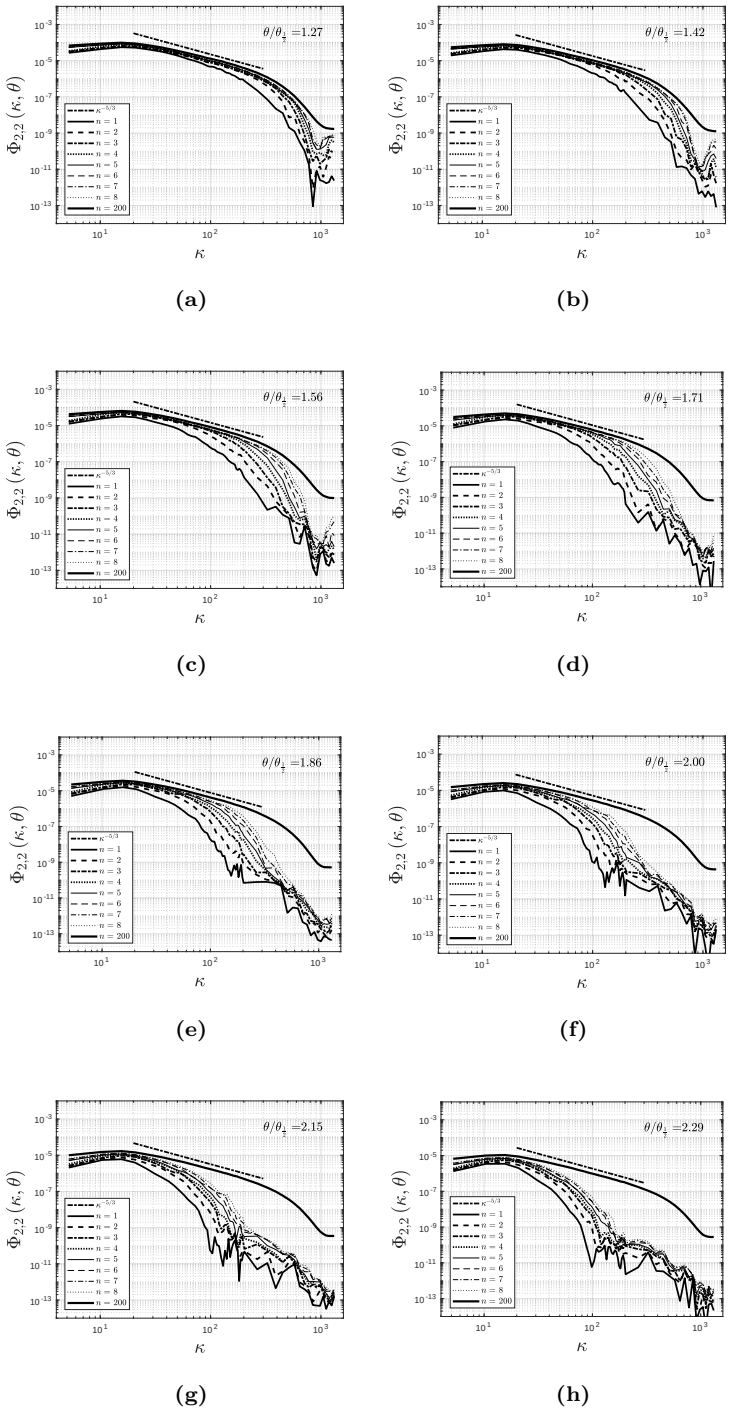

Figure 4.43: Cumulative modal components of single-point spatial spectra, $\Phi^N_{2,2}$, at various spanwise coordinates, $\theta/\theta_{\frac{1}{2}}$, where $\sum_{N=1}^{n} \Phi^N_{2,2}$.

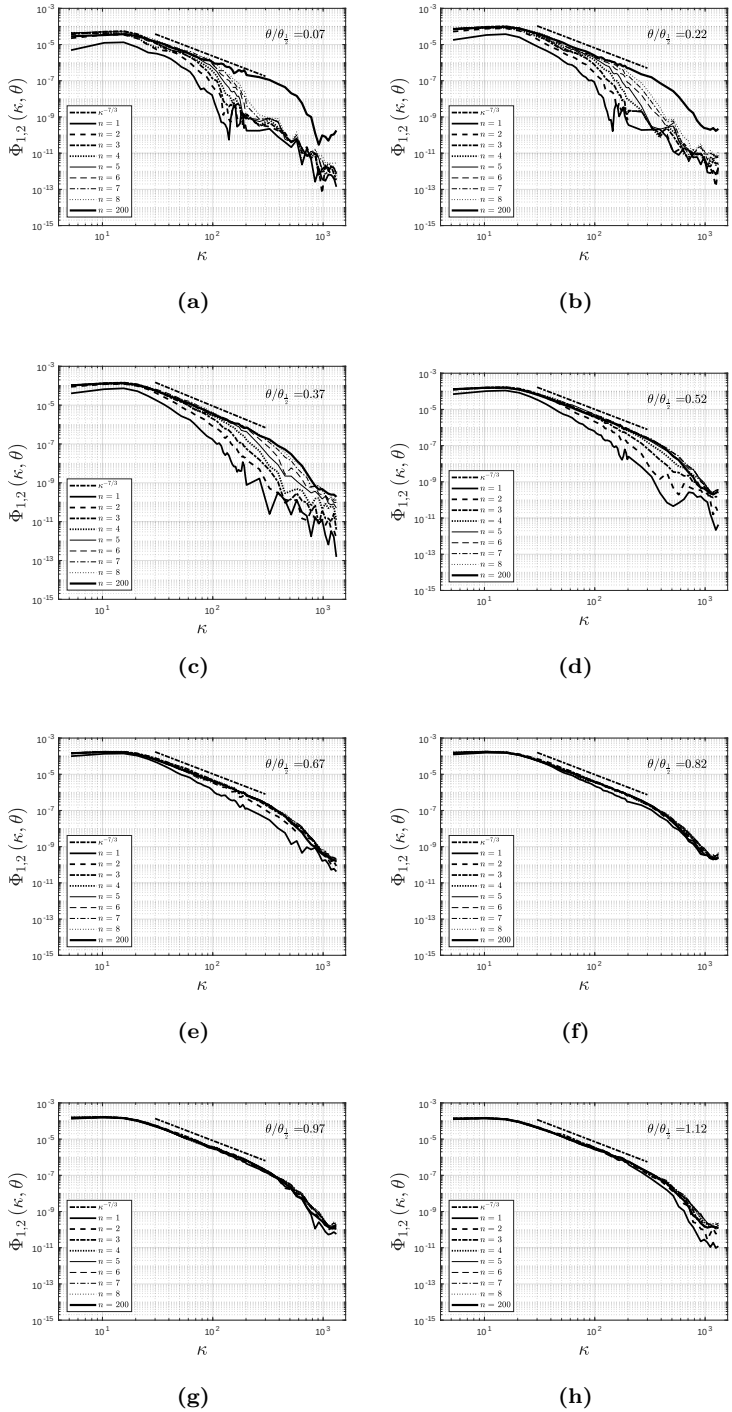

Figure 4.44: Cumulative modal components of single-point spatial spectra, $\Phi^N_{1,2}$, at various spanwise coordinates, $\theta/\theta_{\frac{1}{2}}$, where $\sum_{N=1}^{n} \Phi^N_{1,2}$.

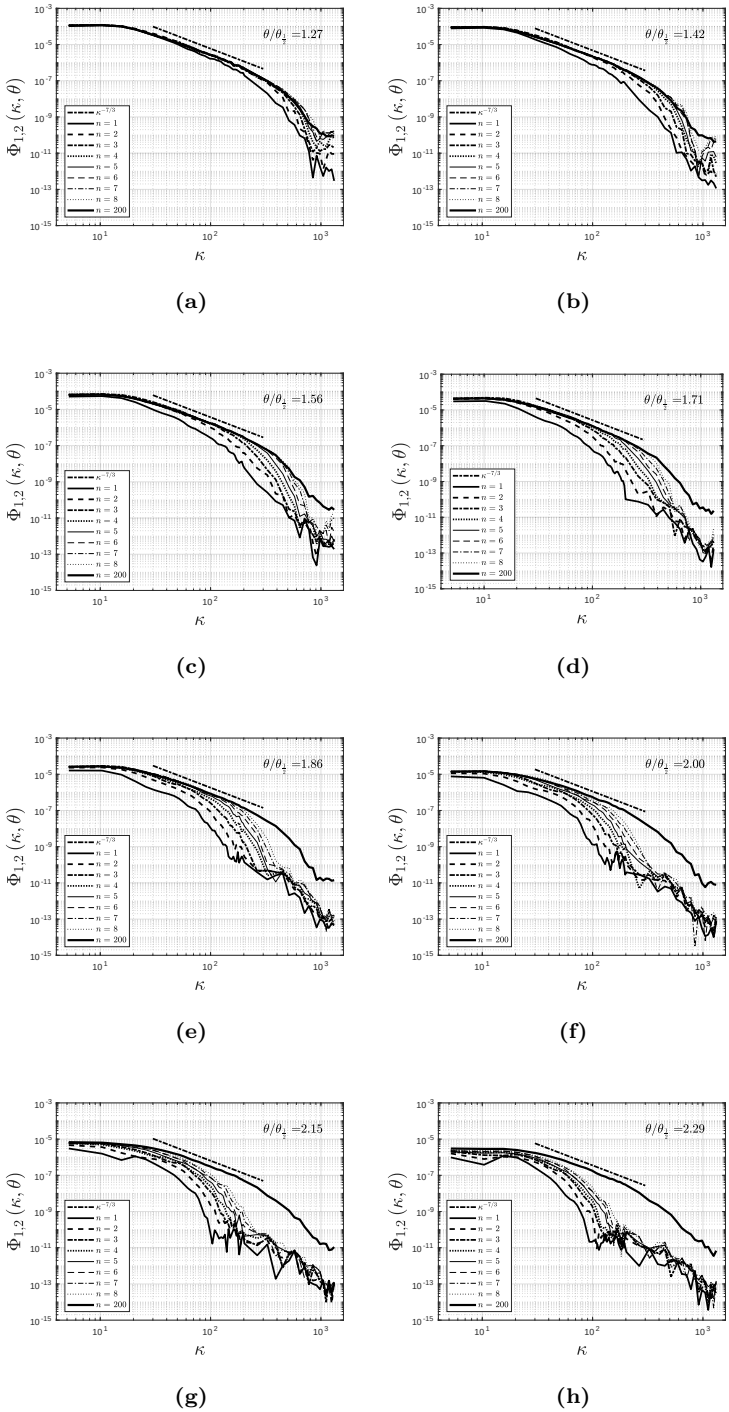

Figure 4.45: Cumulative modal components of single-point spatial spectra, $\Phi^N_{1,2}$, at various spanwise coordinates, $\theta/\theta_{\frac{1}{2}}$, where $\sum_{N=1}^{n} \Phi^N_{1,2}$.

4.3.4.3 Energy production analysis

The term *statistical equilibrium* is generally applied in relation to the averaged turbulence spectra, in particular in wavenumber regions where these exhibit the characteristic $-5/3$-range predicted by the classical Kolmogorov theory. In fact also the dissipation spectrum is hypothesized by the Kolmogorov theory to have a universal similarity form. It is worth keeping in mind, however, that the LD is in fact itself a statistical decomposition, and the modes (eigenfunctions) represent component parts of a probability density functions, which describes the dynamics of the entire field. The fact that the modes are the building blocks of this pdf is seen directly from the orthogonality criterion of (3.19). The criterion implies that the integrand of the $L^2_w(\Omega, \mathbb{C}^3)$-inner product of two eigenfunctions is a pdf when summed over all mode numbers. This is due to the fact that any integral equaling unity directly implies that the integrand can be perceived as a pdf. Since the energy spectra are reconstructed from these eigenfunctions, the components of the spectral reconstruction should be viewed as a more detailed statistical representation of the spectrum, namely one that is weighted by the degree of correlation of wavenumbers across the width of the jet.

The energy production term is the only term in (3.66) for which the full spatial reconstruction is possible to perform from the current data. Although the temporal dimension is unavailable, the spatial data can nevertheless provide much information about the energy contributions of the eigenfunctions. For a full space-time energy production budget for a channel flow, see Muralidhar et al. 2018. The relative energy production in terms of mode number, wavenumber, and θ, is obtained by normalizing II in (3.66) by its eigenvalues, such that we obtain the following expression for the elementwise modal contributions to the production term denoted as the *eigenvalue normalized production* (ENP)

$$\mathcal{P}_\lambda = \varphi_i^\alpha \varphi_\alpha^{j*} \nabla_j \left\langle V^i \right\rangle . \tag{4.14}$$

This expression represents the normalized energy production for each mode for a given point in the domain. By scaling the terms of the energy equation by δ/U_c^3, all terms become independent of the streamwise coordinate. We then note that the resulting expression is a function of α, κ and θ by means of the non-homogeneous eigenfunctions along θ. In order to obtain the total relative production density in terms of mode number and wavenumber, we integrate over the inhomogeneous coordinate

$$\int \delta/U_c^3 \mathcal{P}_\lambda \sin\theta d\theta. \tag{4.15}$$

This yields the relative energy production distributions in terms of LD mode number and wavenumber, shown in Figure 4.46. We note that

(4.14) is complex-valued, for which the real-, and imaginary parts, the arguments and the absolute values of $\mathcal{P}_\lambda$ are shown in Figures 4.46(a), 4.46(b), 4.46(c), and 4.46(d), respectively. It is seen from (4.14) that any imaginary parts are directly affiliated with energy production due to shear-stresses. This is because the production related to normal stresses are entirely real, since we have that $\varphi_i^\alpha \varphi_\alpha^{j*} = |\varphi_i^\alpha|^2$ for $i = j$ and $\alpha = const.$ The real parts in Figure 4.46(a) therefore must contain the aggregate contributions from both shear and normal stresses, while the imaginary parts exclusively contain the information related to shear stresses. From Figure 4.46(d) we can see that the energy production is concentrated around low wave- and mode numbers and that the production levels peak around 0.66. In the most energy productive region of the spectrum the production is characterized by real modes, which is seen from the arguments of $\mathcal{P}_\lambda$, since these are negligible for the corresponding α-m combinations (Figure 4.46(c)). It is profound to note that ENP levels are relatively constant over a relatively wide range of α and κ, as hypothesized by Wänström 2009. Figure 4.46 therefore quantifies which modes produce TKE in proportion to their energy content. For modes related to the $-5/3$-range identified from the energy spectra for $20 < \kappa < 300$ (section 4.3.2), we note the somewhat diminishing ENP values for increasing κ, indicating that modes related to higher wavenumbers play a relatively larger part in the transport of energy than the modes related to lower κ - although significant ENP levels are still seen in the case of the latter. Since (4.15) is in effect a ENP density integrated over the spatial domain, it means that regions in the jet characterized by negligible shear weigh in on the results in Figure 4.46 with insignificant energy production levels effectively reducing the total ENP. This also means that local regions in the integration domain characterized by much higher ENP levels may be found. This can be seen by evaluating (4.14) for each individual α, which shows the ENP distribution over θ and m.

Figure 4.47 exposes the modal contributions of the non-dimensionalized energy production, $\delta/U_c^3\mathcal{P}$, where

$$\mathcal{P} = \lambda \varphi_i^\alpha \varphi_\alpha^{j*} \nabla_j \left\langle V^i \right\rangle, \tag{4.16}$$

while Figure 4.48 shows the eigenvalue normalized energy productions, defined by (4.14). From Figure 4.47 we see that most of the absolute energy is produced below $\kappa = 100$ around the high shear region at low mode numbers. However, for $\alpha = 1$ in Figure 4.48(a) we see that the mode retains much of its energy production over a wide wavenumber range around $\theta/\theta_{\frac{1}{2}} = 1$, throughout the entire κ-range shown in Figure 4.48(a). Upon closer inspection we note that this ratio diminishes from $1.05\,\mathrm{s}^2/\mathrm{m}^2$ at $\kappa = 26$ to $0.78\,\mathrm{s}^2/\mathrm{m}^2$ at $\kappa = 104$ and is fluctuating between

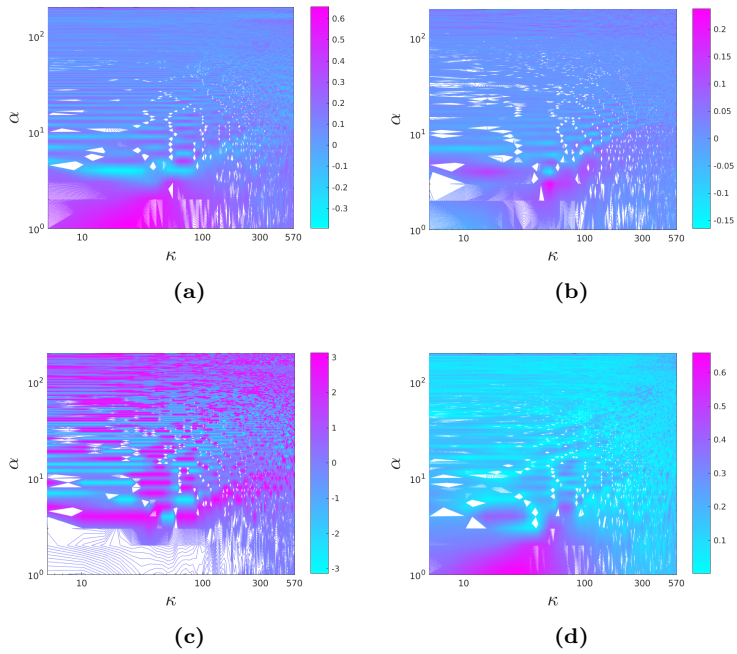

Figure 4.46: Production spectra normalized by the local eigenvalues. (a): $\Re\left\{\delta/U_c^3\mathcal{P}_\lambda\right\}$, (b): $\Im\left\{\delta/U_c^3\mathcal{P}_\lambda\right\}$, (c): $Arg(\delta/U_c^3\mathcal{P}_\lambda)$ (d): $\left|\delta/U_c^3\mathcal{P}_\lambda\right|$.

$0.75\,\mathrm{s}^2/\mathrm{m}^2$ and $0.65\,\mathrm{s}^2/\mathrm{m}^2$ in the range $\kappa = 120-200$. We recall that the range $\kappa = 120-200$ is well within the $-5/3$-region which was identified in section 4.3.2 to be in $\kappa \in [20:300]$. Similar tendencies are seen for the remaining modes in Figure 4.48(a), indicating that this indeed is a general trend for all modes.

Since the half-width region is characterized by high mean shear it is not surprising that even higher modes affiliated to higher κ-values are able to produce significant levels of their own energy content. This is closely related to the earlier discussions regarding the $-7/3$-region of the cross-spectra in section 4.3.2 and their relation to the production of shear-stresses. We recall that the cross-spectra in the high-shear region were recovered from the first mode alone. From the relatively constant ENP levels observed over a wide range of wavenumbers (including the $-5/3$-region) in Figure 4.48(a), we see that a wide range of modes obtain significant portions of their energy directly from the mean flow - especially in the vicinity of high mean shear regions, namely $\theta/\theta_{\frac{1}{2}} = 0.5-1.5$. Outside these θ-ranges energy transfer between LD modes becomes

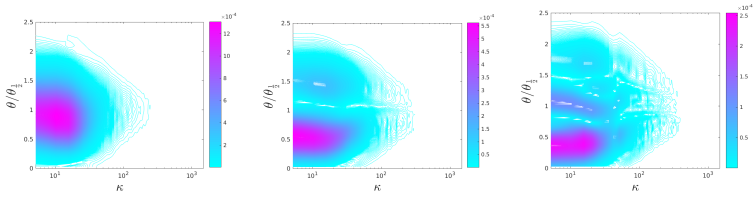

(a) $\alpha = 1$ **(b)** $\alpha = 2$ **(c)** $\alpha = 3$

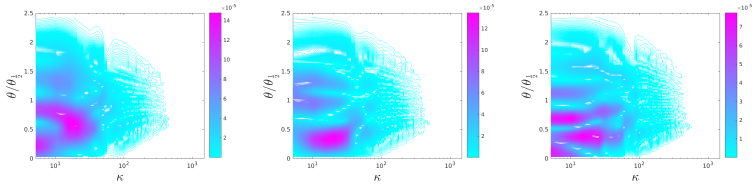

(d) $\alpha = 4$ **(e)** $\alpha = 5$ **(f)** $\alpha = 6$

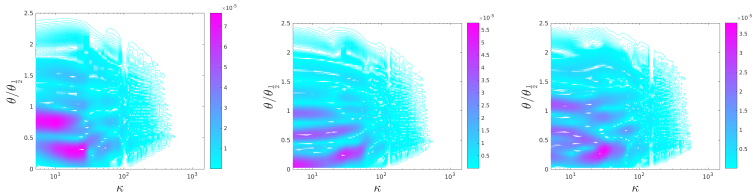

(g) $\alpha = 7$ **(h)** $\alpha = 8$ **(i)** $\alpha = 9$

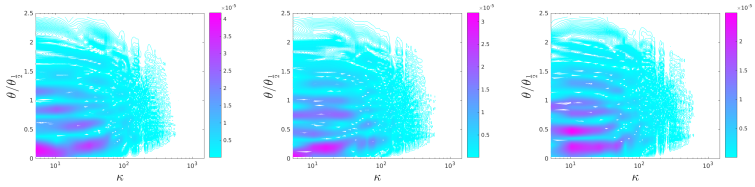

(j) $\alpha = 10$ **(k)** $\alpha = 11$ **(l)** $\alpha = 12$

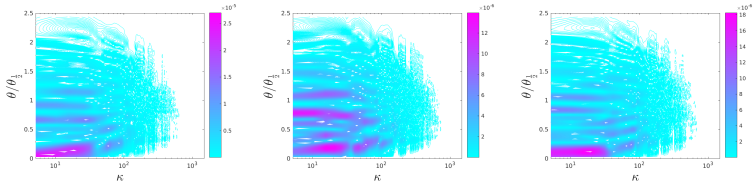

(m) $\alpha = 13$ **(n)** $\alpha = 14$ **(o)** $\alpha = 15$

Figure 4.47: Modal components $\alpha = 1..15$ of the non-dimensionalized term II as a function of wavenumber and span of the jet.

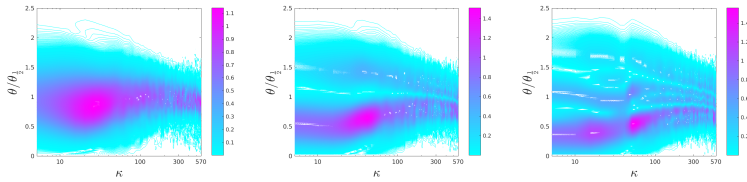

(a) $\alpha = 1$ **(b)** $\alpha = 2$ **(c)** $\alpha = 3$

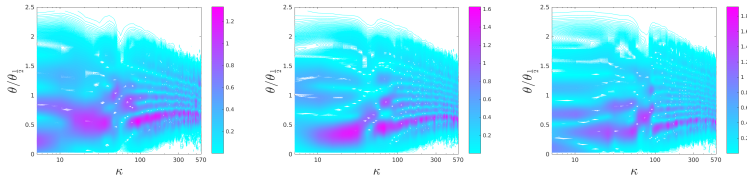

(d) $\alpha = 4$ **(e)** $\alpha = 5$ **(f)** $\alpha = 6$

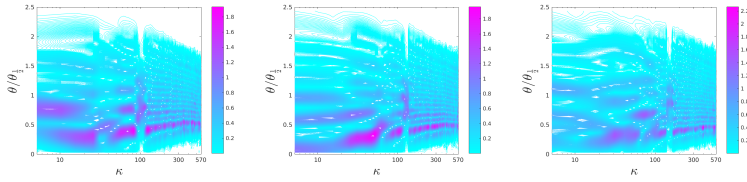

(g) $\alpha = 7$ **(h)** $\alpha = 8$ **(i)** $\alpha = 9$

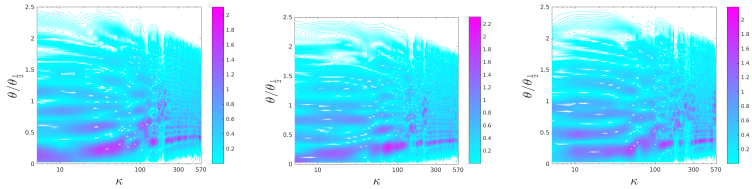

(j) $\alpha = 10$ **(k)** $\alpha = 11$ **(l)** $\alpha = 12$

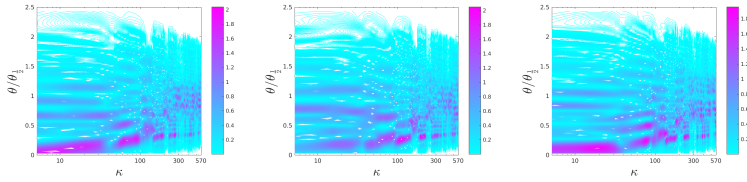

(m) $\alpha = 13$ **(n)** $\alpha = 14$ **(o)** $\alpha = 15$

Figure 4.48: Eigenvalue-normalized modal components $\alpha = 1..15$ of term II as a function of wavenumber and span of the jet. These illustrate the turbulence energy production capacity as a function of θ and κ for each LD mode, relative to the local eigenvalue.

increasingly important in order to facilitate the energy transfer across wavenumbers and eventually down to the dissipative scales. This follows directly from the diminishing ENP for large α and κ observed from the data.

We note that this - at least locally - contradicts the classical Kolmogorov theory. The latter states that the $-5/3$-range is characterized exclusively by energy transfers across scales, and thereby very little energy is produced. This statement only holds true in terms of the absolute energy contributions of the individual modes in Figure 4.47, for which it is true that the total turbulence energy production is limited in comparison to low mode and wavenumber regions. However, the *relative* production levels in Figure 4.48(a) are shown to be significant especially in high shear regions. As we reach the high wavenumber range of the $-5/3$-region we do note a decrease in the ENP. However, the decrease in ENP is merely $28-38\%$ from $\kappa = 26$ to $\kappa = 200$. This shows that energy is in fact introduced over a wide range of scales and this process is not confined to the low wavenumber range - the so-called energy production range as discussed in section 3.2.1 p. 45.

4.3.4.4 Non-linear energy transport analysis

Having concluded that multiple modes produce significant levels of TKE, we are interested in analyzing the non-linear energy transfer within- and across modes, which has proved to be more significant for higher κ-values from earlier results. With this in mind, the variation of modal components of the spectra seen in figures 4.34-4.45 can be analyzed in terms of the spectral energy flux. From dimensional grounds, we can infer that the energy spectrum must exhibit a $-5/3$-range on average in regions where global (in terms of wavenumber) production and dissipation can be deemed insignificant. From this follows that the one-dimensional spectra can be modeled as, Tennekes and Lumley 1972

$$\Phi_{1,1} = \alpha \frac{9}{55} \epsilon_\kappa^{2/3} \kappa^{-5/3}, \tag{4.17}$$

$$\Phi_{2,2} = \alpha \frac{12}{55} \epsilon_\kappa^{2/3} \kappa^{-5/3}, \tag{4.18}$$

in the case of isotropic turbulence, where ϵ_κ is the net energy spectral flux across a given wavenumber, κ. It is worth noting that (4.17) and (4.18) assume that only the local spectral flux is of significance, since the underlying dimensional analysis of the expressions is based on assumptions of insignificant energy production and dissipation in this range. Note that the locality of the spectral flux is indicated by the subscripted κ and is therefore an important deviation from the traditional assumption of statistical equilibrium of the turbulence. Therefore, since the

gradient of the component energy spectra, (4.17) and (4.18), can only deviate from $-5/3$ if ϵ_κ is dependent on the wavenumber Figures 4.34-4.37 tell us that most modal contributions are in fact characterized by varying spectral fluxes. The net fluxes have a tendency to change signs over the same wavenumber range where the mean spectrum exhibits the characteristic $-5/3$-gradient, demonstrating negative as well as positive net spectral fluxes across wavenumbers. It is only the aggregate of the modal contributions that reproduces the $-5/3$-range in the energy spectra - at least away from regions where the mean shear is significant. The spectral reconstruction produces spectra characterized by component contributions in which only the minority are defined by a constant energy flux across wavenumbers.

Although comprising a minority, these do exists in regions where mean shear dominates. Several of the most energetic modal contributions of $\Phi_{2,2}$ exhibit a constant spectral energy flux across wavenumbers, particularly around $\theta/\theta_{\frac{1}{2}} = 1$ (e.g. Figure 4.36(g)). This is seen from their preservation of the $-5/3$-gradients. Similarly, the rapid reconstructions of the $-7/3$-range in Figures 4.38(f)-4.38(h), also indicate a constant spectral flux across wavenumbers for modes $1-3$ approximately. As discussed in section 4.3.3, the modal reconstruction of $\Phi_{2,2}$ is characterized by the $-5/3$-range due to the key role that v^θ plays in the transport of v^ξ across the jet. These results indicate that for statistically stationary high mean shear flows, there exists a statistical equilibrium within the spectral energy transport for individual LD modes. This means that within individual LD modes there exists a constant energy flux across κ-values. While the detailed nature of these energy transfers is not entirely clear in terms of the ratio between the energy transport across LD modes and the energy flux within individual modes, the current data does indicate that the most energetic modes are in a state of equilibrium around the half-width region.

From the $\Phi_{1,1}$ reconstruction, it is seen that the constant spectral flux is not exhibited in any wavenumber range for the first eight modes in the jet. A general decrease in gradients with increasing mode number in the $-5/3$-region indicates that the net negative energy fluxes across wavenumbers are decreasing as the mode number increases, even around $\theta/\theta_{\frac{1}{2}} = 1$. This stands in contrast to what was observed from the same modes in the reconstruction of $\Phi_{2,2}$. It indicates that the energy transfer across mode numbers must play a considerable role as no signs of spectral equilibrium across wavenumbers are observed in individual modes.

The less energetic modes, however, tell a different story. If we first examine the cumulative sum of modes that reconstruct $\Phi_{2,2}$ in the intermediate mean shear region, namely in Figures 4.42(c)-4.42(d), it is seen that the most energetic modes increase the energy levels in the

$-5/3$-range across wavenumbers. The contributions of the less energetic modes, $4-8$, are weighted towards increasing the energy levels at higher wavenumbers, such that the higher end of the spectrum approaches the $-5/3$-slope. This is more clearly seen by the individual modal contributions to the $\Phi_{2,2}$-spectra in Figures 4.36(c)-4.36(d). The spectrum is reconstructed progressively from low- to high wavenumbers for increasing mode numbers. This indicates that for higher wavenumbers the energy contributions of higher mode numbers are dominant, and support the idea of a energy cascade from lower- to higher mode numbers in the $-5/3$-region.

4.3.4.5 Modal reconstruction of single-point statistics

The reconstruction of single-point statistics can be seen in Figure 4.49. Note that a Parzen window was applied on the data before the spectral analysis, resulting in a reduction of turbulence kinetic energy in Figure 4.49, compared to the profiles in Figure 4.14. In order to avoid this, the LD analysis could be performed on the raw signal without the Parzen window. But since the windowing effect would have a more profound effect on the spectra and the LD modes, the current approach was chosen. Nevertheless, the lower energy does not affect our interpretation of the reconstructed single-point statistics.

Figures 4.49(a), 4.49(c), and 4.49(e) show the reconstruction of the Reynolds stresses, whereas figures 4.49(b), 4.49(d), and 4.49(f) show the reconstruction of the corresponding $\mathcal{P}^{ij}$-terms in (4.7). The shear-stresses in Figure 4.49(e) are seen to converge to their final form rapidly. In fact, only two LD modes reconstruct the shear-stress profile. The normal stresses are seen to converge much slower, and as figures 4.49(a) and 4.49(c) show, the convergence rate is slowest around the centerline. Since the modes are determined due to their energy content, it is expected that the energy content of the modes is highest away from the centerline, due to the increasing levels of the Jacobian moving away from the centerline. Near the centerline the modal contribution to the energy reconstruction is very limited due to this fact. Since the shear-stresses are responsible for most of the production, unless significant energy transport is dominating, the TKE will have a similar profile. This is substantiated by the total turbulence kinetic energy production profile shown in Figure 4.49(h). The profile is nearly fully reconstructed after the contribution of only two modes.

Multiplying the normal stresses by $\sin\theta$ we obtain the cumulative modal contributions to the turbulence kinetic energy integrand, which is shown in Figure 4.49(g). From this it becomes apparent that the LD optimizes the modes in terms of maximizing their total

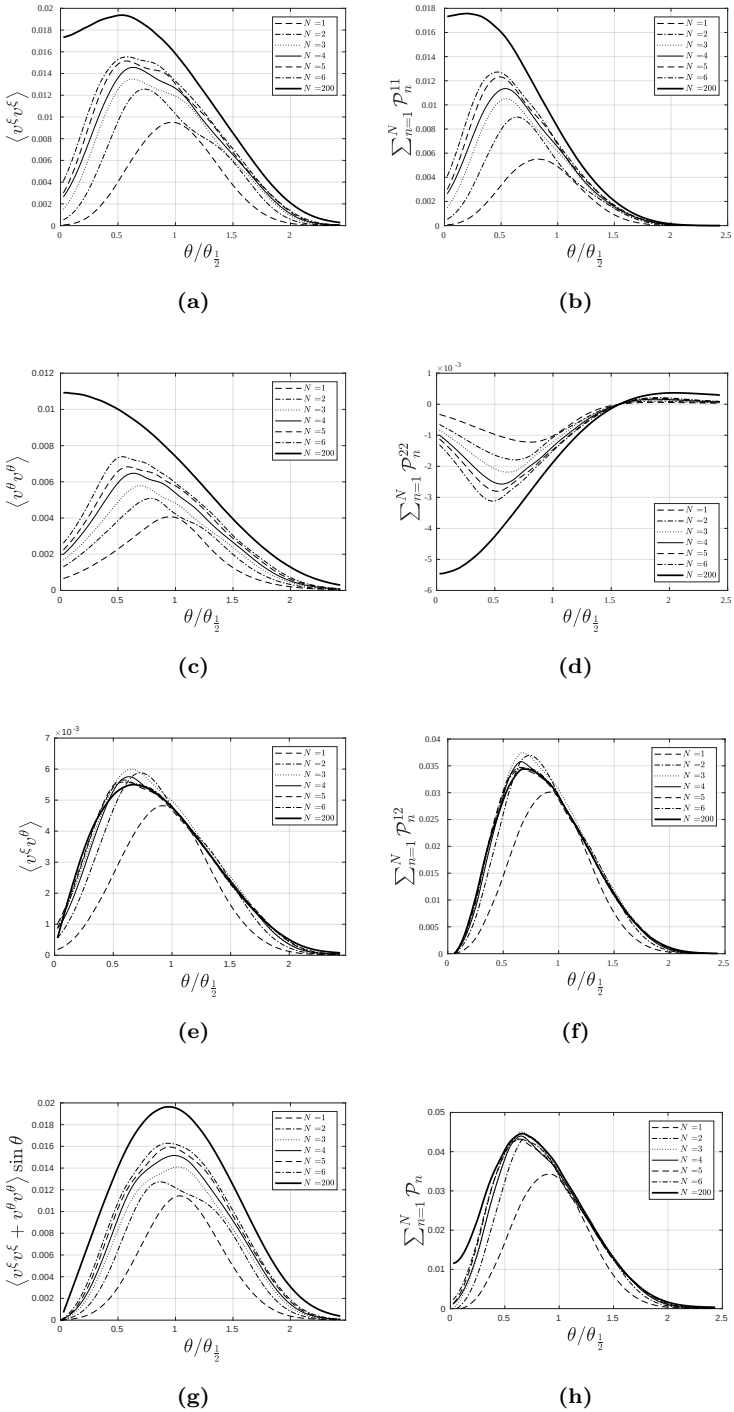

Figure 4.49: Reconstruction of Reynolds stresses and the terms of the energy production, II.

turbulence kinetic energy representation, since every contribution to the reconstruction is a self-similar profile to the preceding and each bell-shaped contribution is centered around $\theta/\theta_{\frac{1}{2}} \approx 1$.

CHAPTER 5

Crossplane experiment

It is a well known property of the LD that the modes are dependent on the dimensionality of the problem. Only the ξ- and θ-components of the velocity field were sampled in the streamwise experiments, but the LD was nevertheless applied in SSC, which is symmetrical around the centerline. Since only two velocity components were applied in this system, the ξ- and θ components have been weighted to a higher degree than they should in the search for the optimal basis. In the current measurements the objective is to analyze the modal reconstruction of the cross-plane measurements performed using stereoscopic PIV. The aim of this chapter is then to decompose and reconstruct the energy production and from these results obtain an idea of the energy transport mechanisms which can be compared to the streamwise experiment. The LD analysis will be performed in cylindrical coordinates, whereafter the modes will be transformed to similarity coordinates, as these are tensors and therefore follow the rules of tensor calculus. Note that a direct transformation to SSC is not possible since the latter required data sampling outside of the measurement plane. Finally, the reconstruction of the Reynolds stresses and the turbulence kinetic energy will follow, in order to evaluate the impact of the additional dimension compared to the streamwise measurements. Although we have added a spatial dimension by performing the cross-plane experiment, we are still missing the temporal component. This means that time is still aliased into the other dimensions of the modes, George 2017.

5.1 Experimental Setup

The cross-plane measurements were performed using the facility which was used for the streamwise experiment in chapter 4 and is identical to the setup applied in Wänström 2009. The experimental setup was located in the same $2.5 \times 3.0 \times 10\text{m}^3$ tent seeded with DEHS-particles with a diameter of approximately $1-2\mu$m. A sketch of the experimental setup is seen in Figure 5.1.

The setup consisted of 200mJ ND:YAG 532nm laser with dual cavities positioned in a forward Mie scatterring configuration with two Dantec FlowSenseEO 16Mpix cameras with a resolution 4872×3248pix and a pixel pitch of $7.4\mu m$. The cameras were positioned on mountings such that the Scheimpflug angle could be adjusted. The laser sheet was lo-

cated in the fully developed region of the jet at $x/D = 40$ from the nozzle. The cameras were equipped with 60mm Nikon lenses with an aperture of $f^{\#}4.0$. The two cameras were positioned in a 45° angle with the laser sheet, which had a thickness of approximately 2mm over the sampling region. The calibration was performed with a calibration target which was manufactured specifically for the experiment in order to cover three half widths of the jet. The target was traversed to five positions across the laser in 2mm steps from in order to ranging well beyond the width of the sheet. A linear transform of the image was performed in order to project the image onto the CCD chip. The sampling was performed with a frequency of 2Hz with a time between pulses of $80\mu s$, and a total of 1000 samples were acquired. Dynamic Studio v4.0 was used for the data processing using the Adaptive PIV interrogation scheme with 50% overlap between the 16×16pix-interrogation windows with subpixel interpolation.

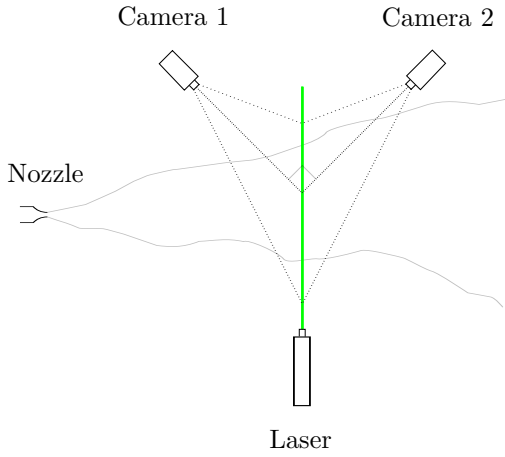

Figure 5.1: Sketch of the experimental setup for the crossplane experiment.

Figure 5.2 shows the instantaneous cylindrical velocity components in the cross plane for the V^x-, V^r-, and V^θ-components, where the contours have been normalized with respect to the maximum velocity in the V^x-component. In the following the data will be evaluated in similarity coordinates using the single-point statistics before analyzing the decomposition as well as the reconstruction of the velocity field.

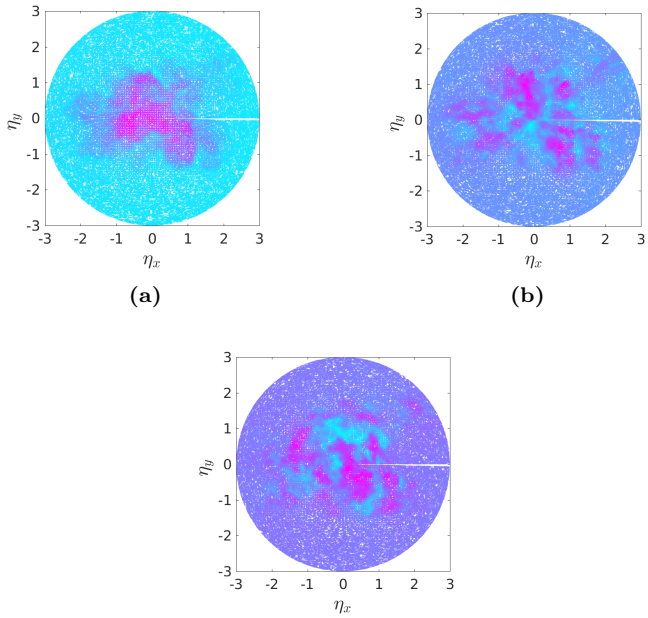

Figure 5.2: Instantaneous velocity contours. (a): v^x, (b): v^r, (c): v^θ.

5.2 Results in similarity coordinates

The analysis in the current work focuses on the quantification of each mode's energy production capacity both globally and locally, in terms of the variation of this property across the span of the jet. It is furthermore interesting to compare these results to the ones obtained in Chapter 4, and to the ENP ratios obtained from the streamwise decomposition. Since both experiments are disadvantaged spatially in terms of covering different dimensions of the velocity field the current analysis will quantify the differences of each experiment by expanding invariants such as the energy production distribution across the domain. Since the measurement techniques applied in the sampling of data are restricted to limited regions of the flow domain the comparison of modes from both planes reveal only projections of the full four-dimensional decomposition in space and time, George 2017.

In the following single-point statistics will be examined in order to ensure that these are comparable to the corresponding results in Chapter 4 and thereby serve as a validation of the measurements.

5.2.1 Single-point Statistics

The single-point statistics in similarity coordinates are shown in Figure 5.3, with an azimuthal spacing between the profiles of $\pi/3$ rad. The scaling parameters were determined to be $A = 0.0934$, $x_0 = 6.0D$, and $B_u = 6.0$, using a least-square optimization scheme and show a good collapse of the azimuthal profiles. The cut-off Fourier mode number, m_c, is a function of η and is estimated to be

$$m_c \sim 63\eta, \tag{5.1}$$

based on the assumption that the smallest resolvable scales are 2Δ where the spatial resolution, $\Delta = 1.58$ mm.

The transformation to similarity coordinates was applied due to the resemblance of the similarity velocity components and those of the SSC seen from the similar variations of the ξ-bases in the two systems. Another reason for applying the similarity coordinates is the correspondence between the linear plane spanned by the η-θ-bases and the sampling region, represented by the planar laser sheet in Figure 5.1. As noted earlier, the direct transformation to the SSC for constant ξ-coordinates would require sampling in a spherical measurement plane and is therefore impractical. Note that it is possible to transform the sampled velocity field to SSC. Although the single-point statistics in this case would be equivalent in two systems for $\theta/\theta_{\frac{1}{2}} = \eta$, the two-point statistics would not, since the correlation along the second coordinate in the two systems would essentially be taken along different surfaces in the domain (η in similarity coordinates and θ-in SSC).

The mean velocity profile in Figure 5.3(a) and the normal stresses in figures 5.3(c) and 5.3(d) are here compared to the cylindrical velocity profiles from Hussein, Capp, and George 1994 and are in good agreement. The spatial filtering is significantly reduced compared to Wänström 2009, due to the high resolution PIV cameras used. The mean radial profile in Figure 5.3(b) is compared to the mean η-velocity model from the continuity equation, (4.3), and shows good agreement even for large η-coordinates where the velocity magnitudes are particularly low.

The azimuthally averaged profiles are seen in Figure 5.4 together with the cylindrical velocity profiles. These exhibit similar tendencies to the profiles in Figures 4.6, but with slightly lower energy levels. This is expected, since the effective spatial resolution of the current measurements is limited by the physical interrogation window size of 1.58×1.58mm. The effective resolution for the current measurements can then be quantified in terms of the estimated Kolmogorov scale to be $\Delta/\eta_k = 21.3$ at $(x - x_0)/D = 34.0$. The effective resolution of the streamwise measurements at $(x - x_0)/D = 34.0$ is $\Delta/\eta_k = 22.0$ (see Figure 4.2 in Chapter 4), which means that the effective resolutions of the two experiments

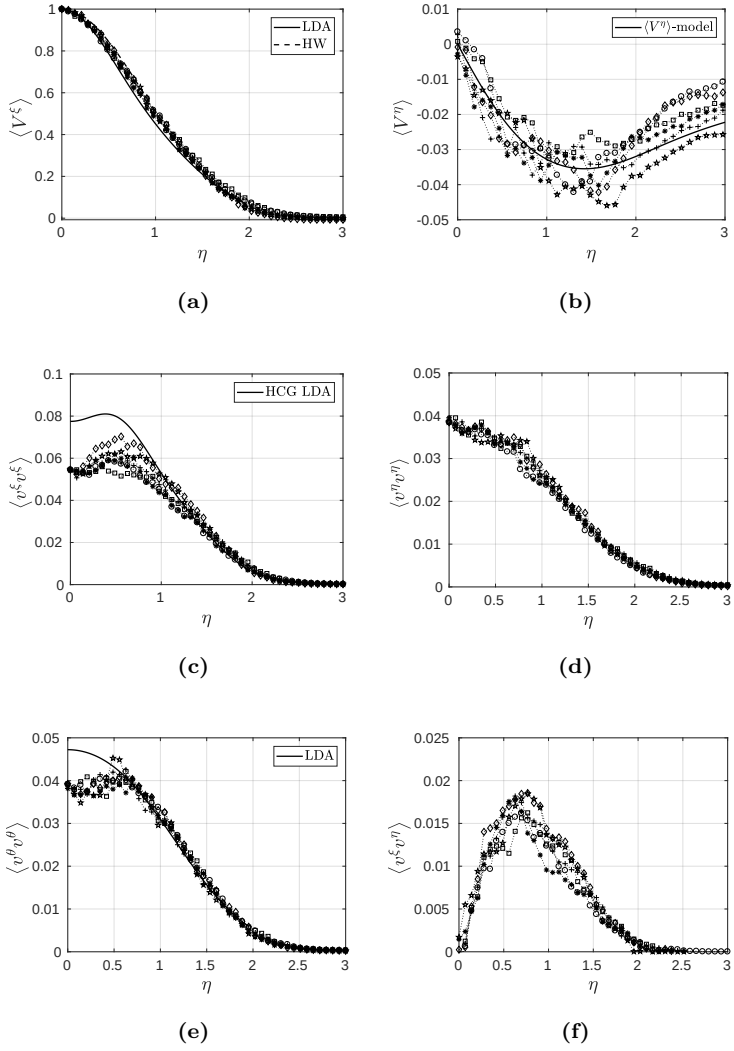

Figure 5.3: Single-point statistics sampled at $(x - x_0)/D = 34$. (a): Mean streamwise velocity, (b): mean η-velocity, (c): normal stresses in the ξ-direction, (d): normal stresses in the η-direction, (e): normal stresses in the θ-direction, (f): shear-stresses.

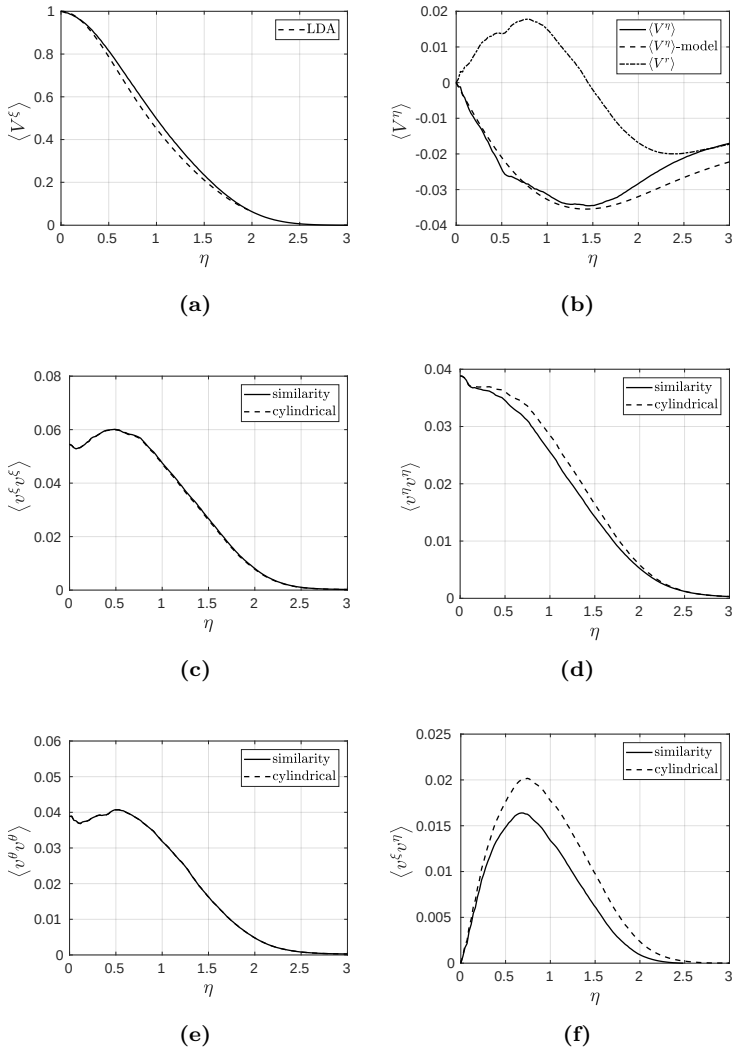

Figure 5.4: Azimuthally averaged single-point statistics using cylindrical- and similarity velocity components. (a): Mean streamwise velocity compared to LDA data from Hussein, Capp, and George 1994, (b): mean radial velocity compared to cylindrical radial velocity component and the mean velocity model from (4.3), (c): normal stresses in ξ-direction, (d): normal stresses in the η-direction, (e): normal stresses in the θ-direction, (f): shear-stresses.

are very close at $(x - x_0)/D = 34.0$, where the two sampling campaigns coincide. Comparing the normal stresses between crossplane- and streamwise experiments at this location we find that they are nearly identical. The slightly higher levels seen in the streamwise-averaged Reynolds stresses in Figures 4.6(c) and 4.6(d) compared to those in figures 5.4(c) and 5.4(d) are due to the effective increase of the spatial resolution with downstream distance from the nozzle. This results in slightly higher mean stress levels in the streamwise experiment.

The energy production contributions are shown in Figure 5.5 and are seen to agree very well with the contributions in Figure 4.7 on p. 62. Since the current measurements cover a wider region of the jet, namely up to three jet half-widths, we can see a rapid increase in the local contributions of the energy production around $\eta = 2.46$. This is due to the small values of $\mathcal{P}$ in this region resulting in a sudden increase in the value of $\mathcal{P}^{ij}/\mathcal{P}$ in Figure 5.5(b). Similar tendencies can be seen in Figure 4.7(b), although this profile is limited to 2.475 jet half-widths.

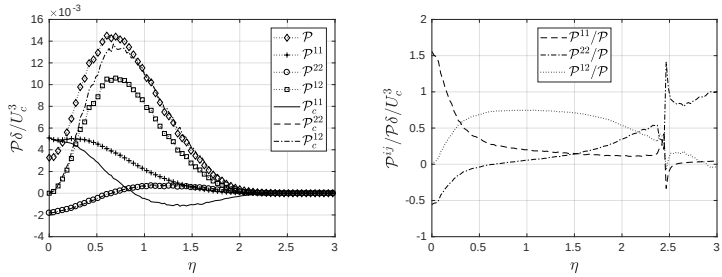

(a) **(b)**

Figure 5.5: TKE production. (a): Component parts of the energy production term. (b): Component parts normalized by the local energy production.

From the statistical analysis it can be concluded that data from the streamwise- and cross-plane experiments are in good agreement, and are thus acceptable for identifying differences between any two decompositions which are related to the difference of dimensionality of the problem. A further analysis, relevant for the physical understanding of the modes, will require quantification of how these basis functions differ in reconstructing the single-point statistics and invariants such as the turbulence kinetic energy, as well as the energy production of the flow.

5.2.2 Decomposition of the Velocity field

The LD of the velocity field was performed in cylindrical coordinates due to the self-adjoint property of two-point correlation matrix in this system. Hereafter the modes were transformed to similarity coordinates by a regular coordinate transformation (see (3.42) p. 33) i.e.

$$\varphi^{j'} = \varphi^{j} J_{j}^{j'}. \tag{5.2}$$

Figures 5.6(a)-5.6(d) show the normalized energy distribution over α, the cumulative sum over α, the energy distribution over m, and the percentile energy content over α and m, respectively.

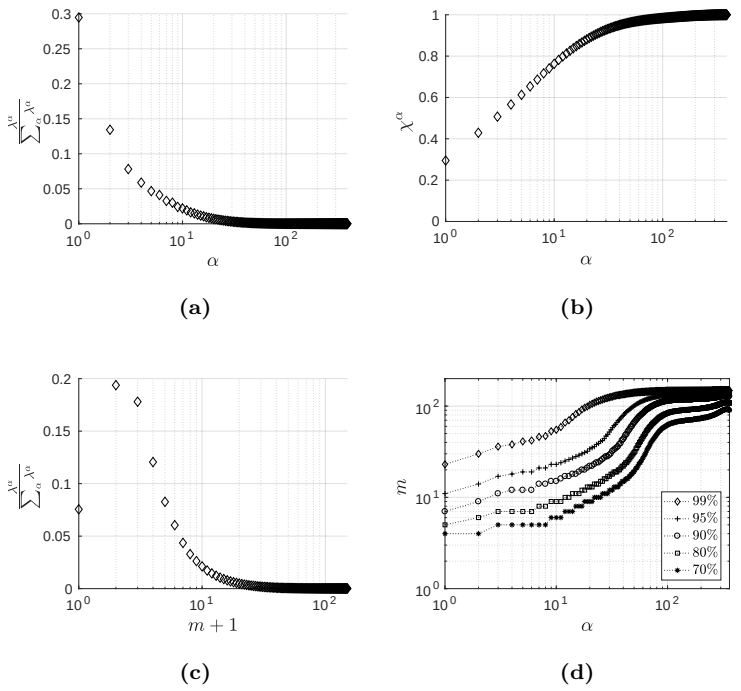

Figure 5.6: Eigenvalues. (a): Eigenvalues normalized by the total energy in the flow, (b): Normalized energy over azimuthal mode number, (c): Energy distribution over Fourier and LD-mode number, (d): azimuthal mode numbers defining percentiles of energy across LD mode numbers, α.

It is seen that $\alpha = 1$ contains 29.5 % over the energy, whereas the first ten modes contain 76.3 % of the energy. The distribution over azimuthal

mode number, m, show that $m = 1$ and 2 are the two most energetic azimuthal modes and we see that 80 % of the energy content of the first ten LD-modes is contained for $m < 10$. These results show that the energy is highly concentrated in a small number of α-m modes. This is also seen from the eigenspectrum as a function of α, and m shown in linear and log-log representations in Figures 5.7(a) and 5.7(b), respectively. Figures 5.7(c)-5.7(f) are the magnitudes of the single-point correlations of the azimuthal Fourier modes as a function of α and η. An elaborate historical review of the modal dominance in the jet can be found in Wänström 2009. It is briefly stated here that the historically varying conclusions regarding the dominance of certain azimuthal modes in the far-field found in litterature (Citriniti and George 2000, Jung, Gamard, and George 2004, Gamard, Jung, and George 2004, Iqbal and Thomas 2007, Tinney, Glauser, and Ukeiley 2008) depend on the region of the flow. These are also determined by the missing dimensions of the decomposition of the flow. The dominance of mode 1 in the current work is in agreement with the conclusions drawn in Wänström 2009 where this same characteristic is observed. However, the current measurements, cover three jet-half widths and are characterized by a higher effective resolution than those in Wänström 2009 thereby capturing a larger fraction of the turbulence kinetic energy of the field.

The real, imaginary, and absolute values of modes $\alpha = 1 : 5$ are shown in Figures 5.8, 5.9, and 5.10, respectively. The three columns of subfigures in figures 5.8-5.10 are the ξ, η, and θ-components of the modes shown as a function of m and η. In general we can see that each modal component has an increasing number of nodes for increasing α. This is most clearly seen from the absolute values in Figure 5.10. Here we observe regions of constant diagonal streaks for increasing m, indicating regions of modal self-similarity behavior which was also observed in the streamwise data in Chapter 4. The self-similar behavior in Figure 5.10 is combined with a translation of the modal antinodes such that these are shifted away from the centerline with increasing m. We note that this tendency is observed for all α and for all components of the modes. From the form of the azimuthal eigenfunctions i.e. $e^{im\theta}$, we can define the wavelength at any η in the following way

$$l = \frac{2\pi\delta\eta}{m}, \tag{5.3}$$

showing that a constant m represents a linearly increasing wavelength for increasing η.

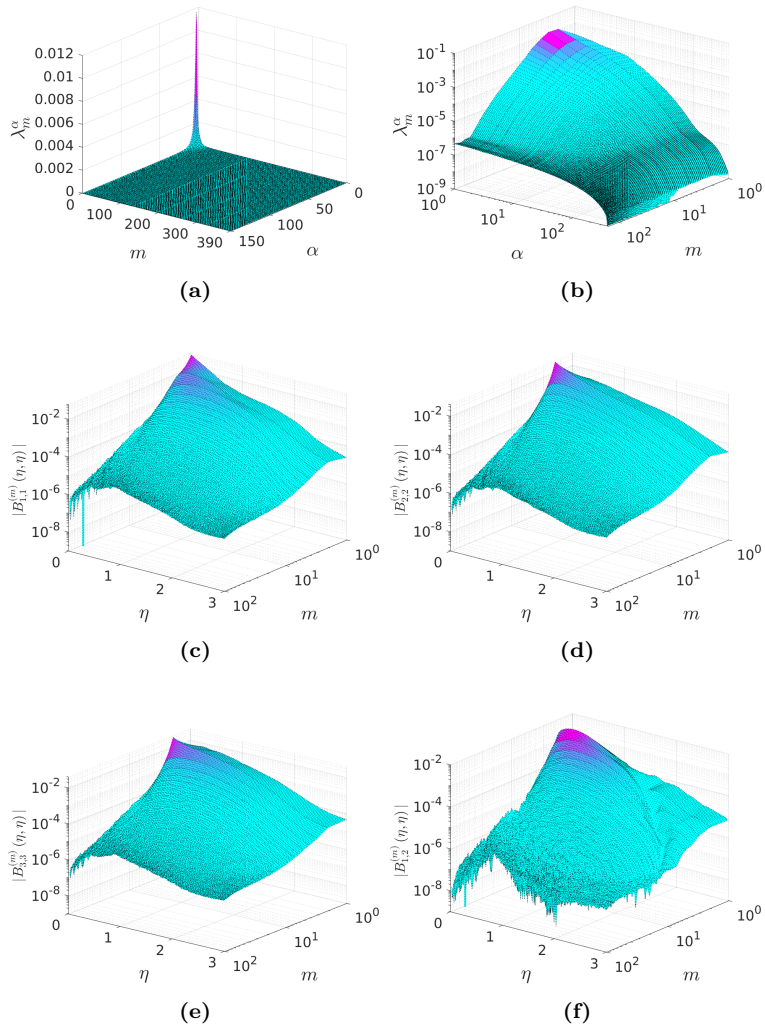

Figure 5.7: (a): Eigenspectrum in linear representation, (b): Eigenspectrum in log-log representation, (c)-(f): single-point correlations of ξ, η, and θ-coefficients in Fourier space.

This means that the same scale sizes are represented by a higher m at the periphery of the flow than at the centerline. It is also important to note that figures 5.8-5.10 are semi-logarithmic representations of the modes, which enhance the appearances of slopes of the diagonal streaks with increasing m. From (5.3) we find the cut-off azimuthal wavenumber, m_c, by requiring (5.3) to be equal to $2\delta\eta_c$ in order to yield the following expression

$$m_c = \frac{\pi\eta}{\eta_c}. \tag{5.4}$$

where $\eta_c = \Delta/\delta$. From this we estimate m_c to be 1.5 at the grid points closest to the centerline, $\eta = 0.023$, while $m_c = 63$ at $\eta = 1$. Table 5.1 summarizes the cut-off mode numbers for various radial position above which results should be neglected, since the eigenfunctions for these m-ranges are unphysical. In figures 5.8-5.10 this limit has been marked by a dotted line, to the right of which data should be neglected. The resulting effect of the azimuthal oversampling for small η is an inherent effect of the cylindrical coordinates, and cannot be avoided due to the requirement posed by the LD-integral of correlating azimuthal Fourier modes with the same mode numbers across the entire span of the jet width. The resulting compromise reduces to an oversampling close to the centerline versus an undersampling at the jet periphery. Note that a related challenge was treated in Citriniti and George 2000 where the number of azimuthal hot-wire probes in the hot-wire rake was regulated such that the data was sampled at the same cutoff azimuthal wavenumber using the lengths of the wires.

This leads to a major distinction between the decomposition performed in the current chapter and the decomposition performed in Chapter 4. In the case of the cross-plane decomposition we are cross-correlating different wavelengths across the jet width, since the wavelength corresponding to a wavenumber m in the region $\eta \sim 0$ is smaller than the wavelength for the same m at e.g. $\eta = 1$. Note that this is not the case in the cross-correlation of Fourier coefficients in the streamwise experiment, where a wavenumber close to the centerline represents the same physical wavelength as a wavenumber in the periphery of the flow. Thus, in the streamwise decomposition we are correlating trigonometric polynomials of the same wavelengths across the jet. It is important to keep this in mind in particular for physical interpretations of the modes. We now see that the LD-modes in the crossplane decomposition represent the intensity of correlations of azimuthal Fourier modes with wavelengths that are directly proportional to the distance between the discrete cylindrical interrogation points. In 5.10(a) for instance the contour lines reveal significant correlation within an η-band corresponding to ~ 0.5 for a wide m-range. This means that for each m (for $\alpha = 1$) the correlation

lengths are of the order of a half jet-width. Note, however, that these are decreasing in terms of energy levels.

Figure 5.5(a) shows that most of the energy is produced between $\eta = 0.5$ and 1. With this in mind we can infer that the modes indicate an active transport of energy away from the energy production range towards the perifery of the flow. This, however, can only be concluded if we assume that a Richardson-like transport of energy across azimuthal Fourier modes is valid - for at least some fraction of the modal energies. With this in mind we oserve a high level of modal self-similarity over wide regions of the flow. Note that this is substantiated by Figure 4.15(d) (p. 74) in Chapter 4, exhibiting nearly constant transport of stresses by velocity fluctuations across a wide regions of the jet. We also observe the likeness of real parts and imaginary parts of η and θ components of modes (figures 5.8 and 5.9), where strong antisymmetries between the real parts of the η-component and the imaginary parts of the θ-components are notice, and vice versa. Generally, from the absolute values of modes $\alpha = 2 : 5$ we see in Figure 5.10 that there is a high degree of symmetry across components; in regions where activity is observed for one component similar activity is observed in the remaining components, indicating a strong presence of three-dimensional coherent motion.

Comparing modes across the streamwise- and cross-plane has proved to be difficult, since the two measurements are covering different dimensions of the flow. Nevertheless, we note that since both experiments must reconstruct the invariants of the flow the decompositions in the two experiments posses much of the same information. It is only the distribution of energy across the basis functions that is different. A more relateable comparison between the modes of the two experiments performed is that of eigenvalue-weighted summation of Fourier modes, since we in this case are comparing the LD modes which span the flow along the inhomogeneous dimension. These weighted modes for the crossplane and streamwise experiments are defined by the following two expressions

$$\phi_\alpha = \sum_{m=0}^{\infty} \lambda \varphi_{\alpha,m} \quad \text{and} \quad \phi_\alpha = \int_{-\infty}^{\infty} \lambda \varphi_\alpha d\kappa. \tag{5.5}$$

By comparing the energy distribution in figures 4.21(a) (p. 83) and 5.6(a) we do not expect the two sets of modes in (5.5) to be equal since we can see that the modes have different energy contents. However, the eigenvalue weighting reduces the differences between the LD-modes in the two experiments to those related to the missing energy caused by the missing θ-component in the streamwise decomposition. The eigenvalue-weighting may therefore be a better comparison than any individual mode comparisons for a specific α-m and α-κ

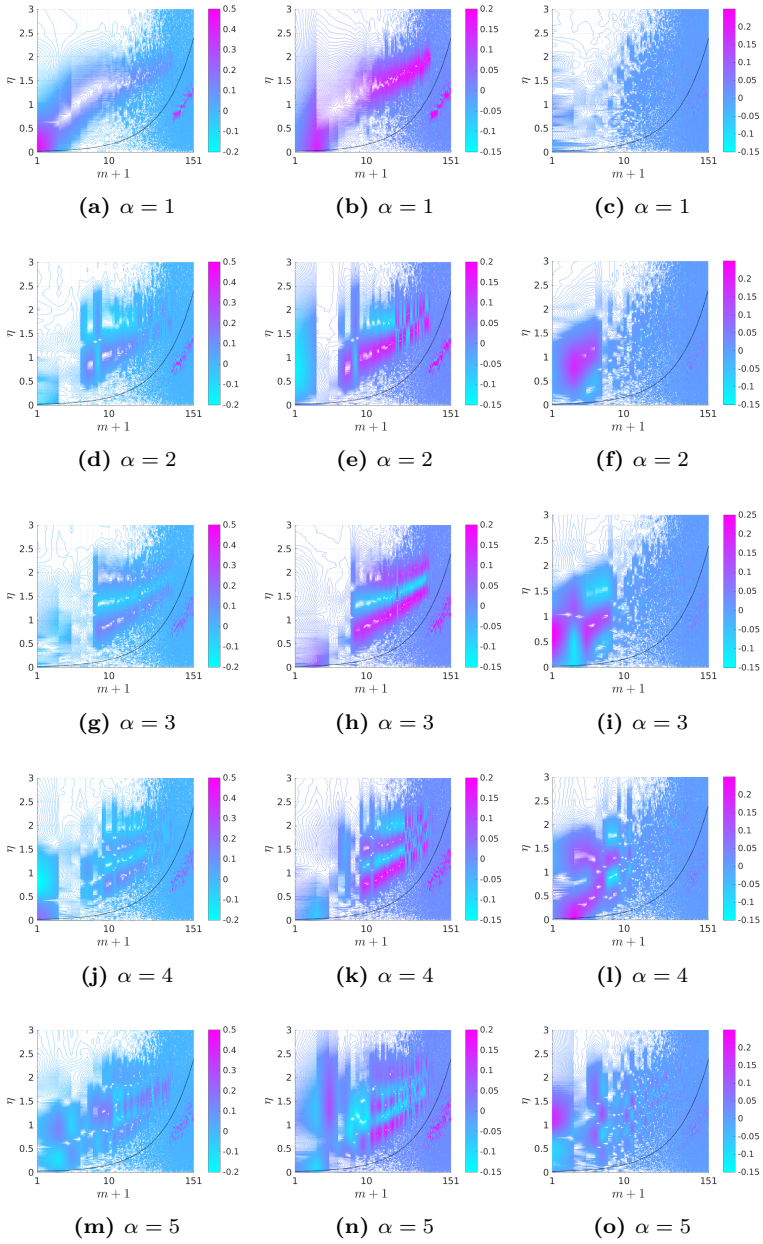

(a) $\alpha = 1$ **(b)** $\alpha = 1$ **(c)** $\alpha = 1$

(d) $\alpha = 2$ **(e)** $\alpha = 2$ **(f)** $\alpha = 2$

(g) $\alpha = 3$ **(h)** $\alpha = 3$ **(i)** $\alpha = 3$

(j) $\alpha = 4$ **(k)** $\alpha = 4$ **(l)** $\alpha = 4$

(m) $\alpha = 5$ **(n)** $\alpha = 5$ **(o)** $\alpha = 5$

Figure 5.8: Real parts of eigenfunctions. The rows of the subfigures represent modes $\alpha = 1 : 5$, respectively, while the ξ, η, θ-components are shown in the first, second and third columns, respectively.

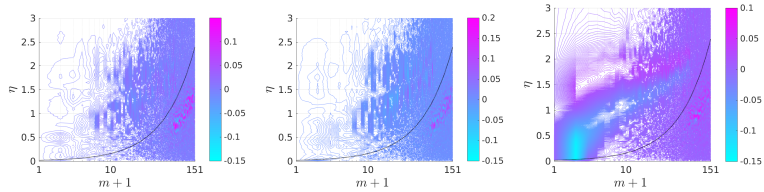

(a) $\alpha = 1$ **(b)** $\alpha = 1$ **(c)** $\alpha = 1$

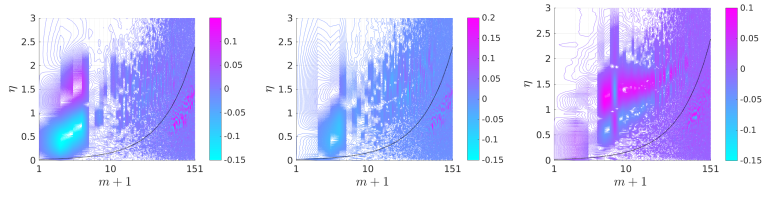

(d) $\alpha = 2$ **(e)** $\alpha = 2$ **(f)** $\alpha = 2$

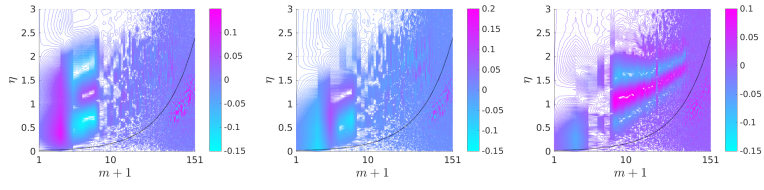

(g) $\alpha = 3$ **(h)** $\alpha = 3$ **(i)** $\alpha = 3$

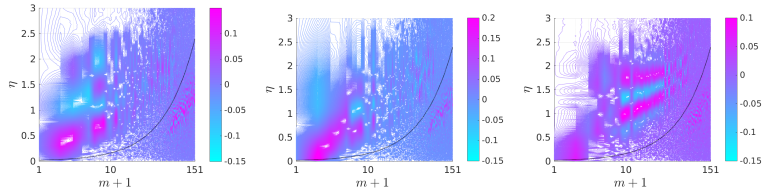

(j) $\alpha = 4$ **(k)** $\alpha = 4$ **(l)** $\alpha = 4$

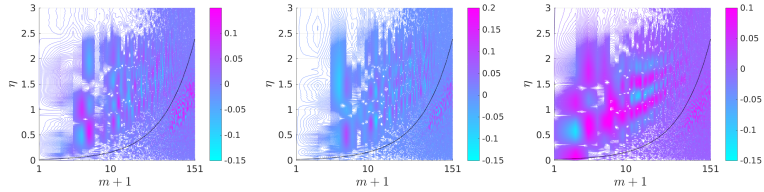

(m) $\alpha = 5$ **(n)** $\alpha = 5$ **(o)** $\alpha = 5$

Figure 5.9: Imaginary parts of eigenfunctions. The rows of the subfigures represent modes $\alpha = 1 : 5$, respectively, while the ξ, η, θ-components are shown in the first, second and third columns, respectively.

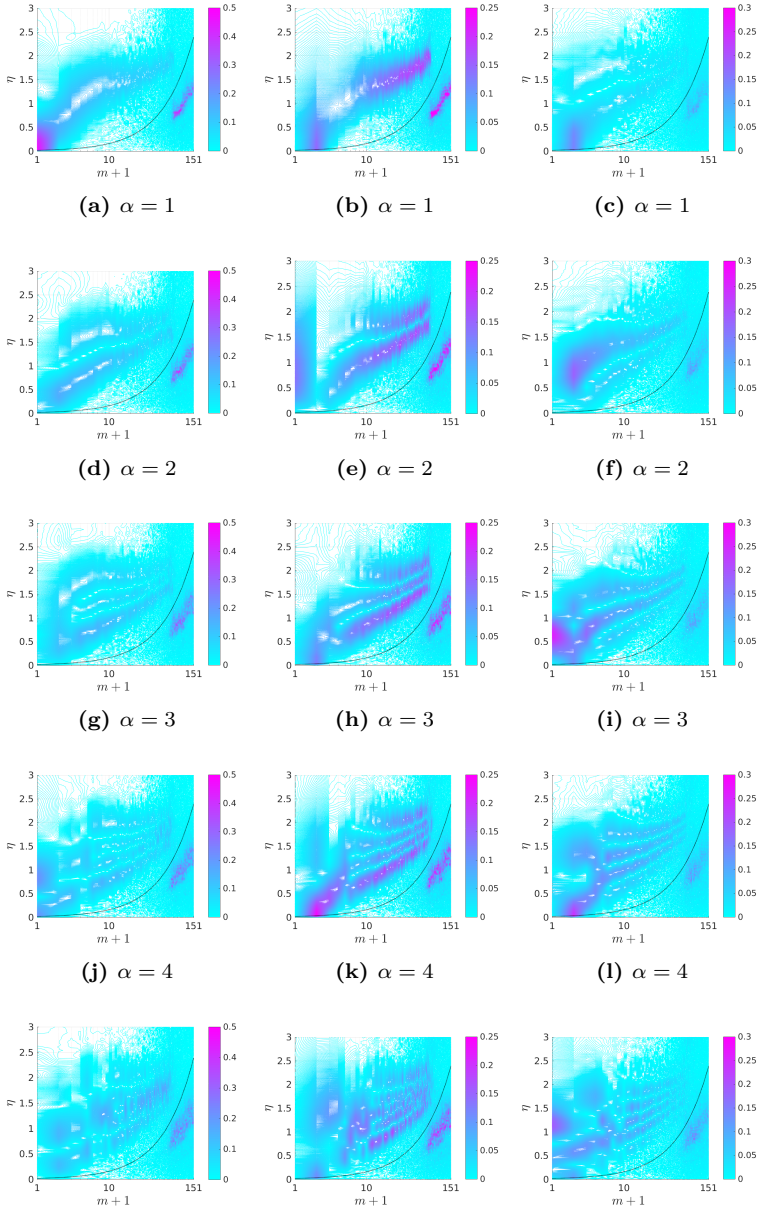

(a) $\alpha = 1$ **(b)** $\alpha = 1$ **(c)** $\alpha = 1$

(d) $\alpha = 2$ **(e)** $\alpha = 2$ **(f)** $\alpha = 2$

(g) $\alpha = 3$ **(h)** $\alpha = 3$ **(i)** $\alpha = 3$

(j) $\alpha = 4$ **(k)** $\alpha = 4$ **(l)** $\alpha = 4$

(m) $\alpha = 5$ **(n)** $\alpha = 5$ **(o)** $\alpha = 5$

Figure 5.10: Absolute values of eigenfunctions. The rows of the subfigures represent modes $\alpha = 1 : 5$, respectively, while the ξ, η, θ-components are shown in the first, second and third columns, respectively.

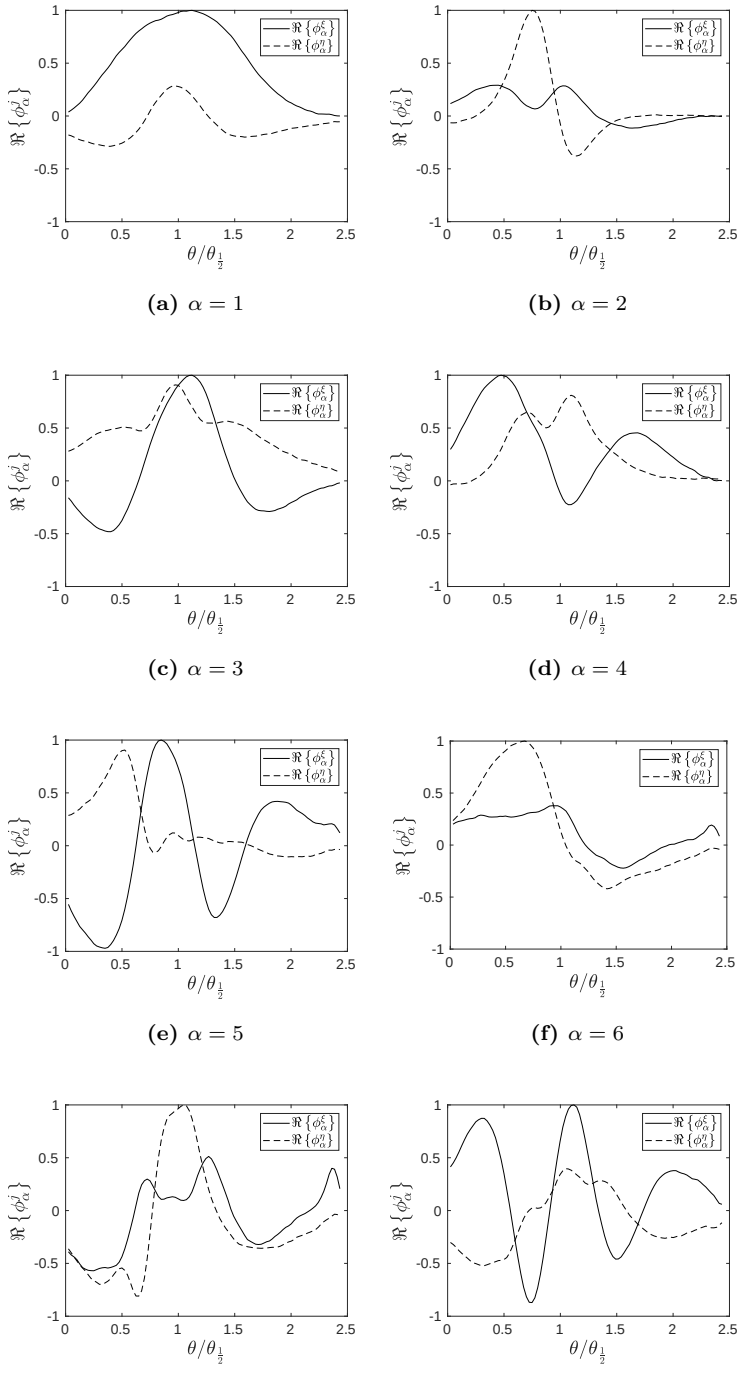

(a) $\alpha = 1$ **(b)** $\alpha = 2$

(c) $\alpha = 3$ **(d)** $\alpha = 4$

(e) $\alpha = 5$ **(f)** $\alpha = 6$

(g) $\alpha = 7$ **(h)** $\alpha = 8$

Figure 5.11: Real parts of eigenvalue-weighted $\alpha = 1 : 8$-mode from the streamwise experiment.

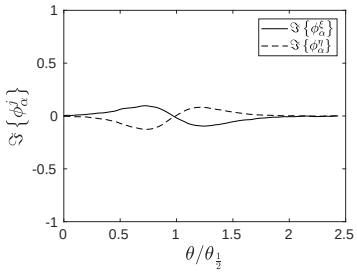

(a) $\alpha = 1$

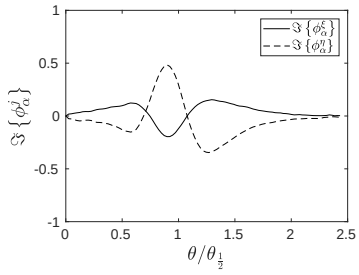

(b) $\alpha = 2$

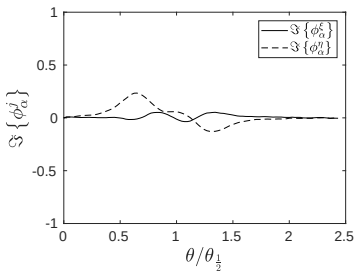

(c) $\alpha = 3$

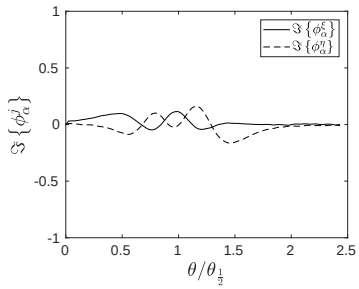

(d) $\alpha = 4$

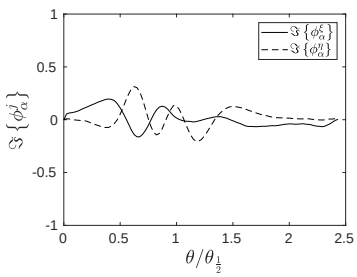

(e) $\alpha = 5$

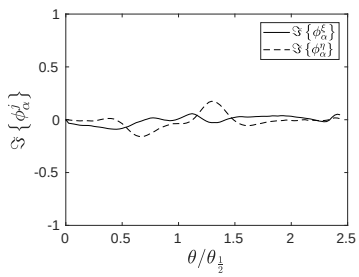

(f) $\alpha = 6$

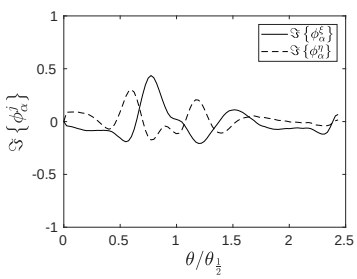

(g) $\alpha = 7$

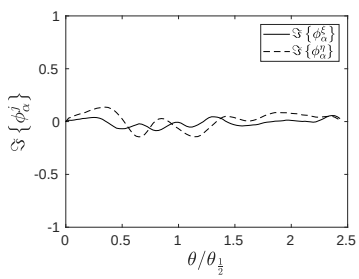

(h) $\alpha = 8$

Figure 5.12: Imaginary parts of eigenvalue-weighted $\alpha = 1 : 8$-mode from the streamwise experiment.

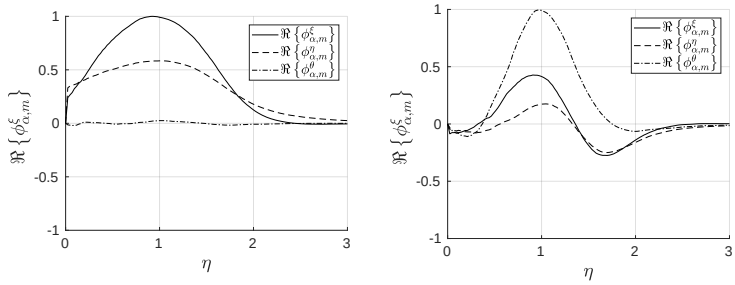

(a) $\alpha = 1$ **(b)** $\alpha = 2$

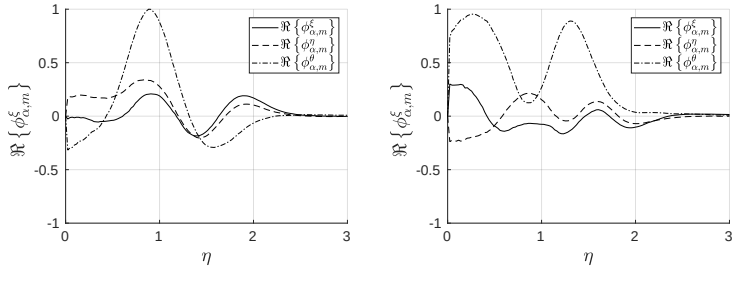

(c) $\alpha = 3$ **(d)** $\alpha = 4$

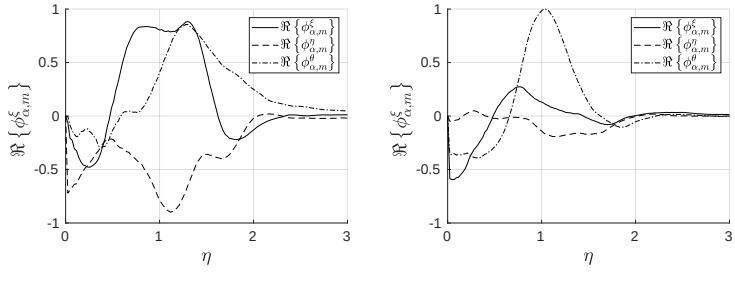

(e) $\alpha = 5$ **(f)** $\alpha = 6$

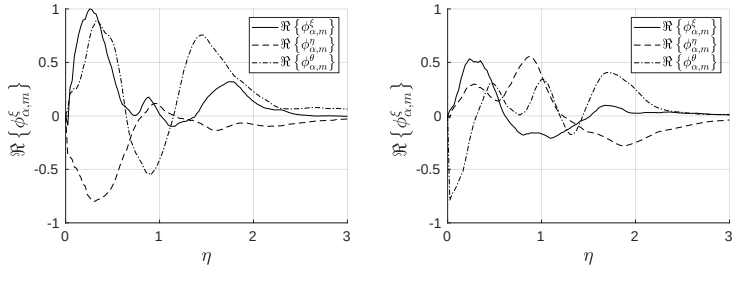

(g) $\alpha = 7$ **(h)** $\alpha = 8$

Figure 5.13: Real parts of eigenvalue-weighted modes $\alpha = 1 : 8$ from the cross-plane experiment.

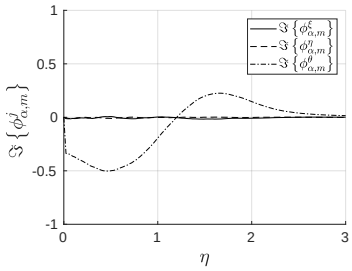

(a) $\alpha = 1$

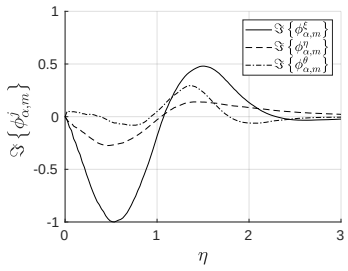

(b) $\alpha = 2$

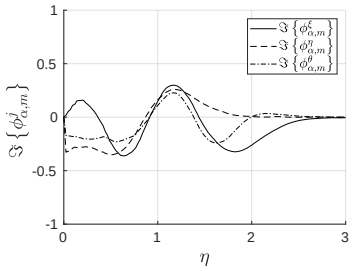

(c) $\alpha = 3$

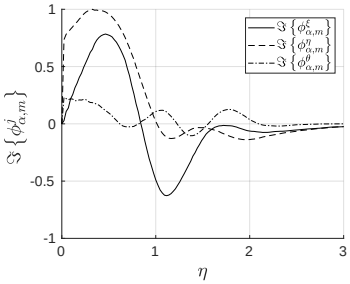

(d) $\alpha = 4$

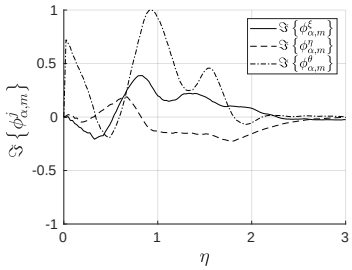

(e) $\alpha = 5$

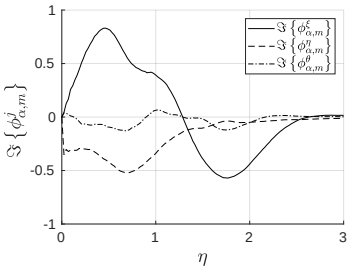

(f) $\alpha = 6$

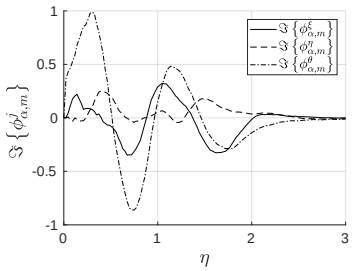

(g) $\alpha = 7$

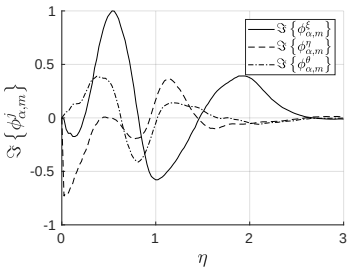

(h) $\alpha = 8$

Figure 5.14: Imaginary parts of eigenvalue-weighted modes $\alpha = 1 : 8$ from the cross-plane experiment.

Table 5.1: The variation of cut-off Fourier mode numbers, m_c, as function over the span of the jet. Mode numbers larger than m_c should be neglected in the analysis.

η	0	0.5	1.0	1.5	2.0	2.5	3.0
m_c	0	32	63	95	126	158	190

combination in the two experiments. The real- and imaginary parts of the first eigenvalue-weighted modes from the streamwise experiment are seen in figures 5.11 and 5.12. The first eight eigenvalue-weighted modes for the crossplane experiment are shown in Figures 5.13 and 5.14 where the real- and imaginary parts for $\alpha = 1 : 8$ are seen, respectively. Comparing the modes across the experiments we see close similarities between the ξ-components for $\alpha = 1$, which contains most of the energy in the two experiments. The missing θ-component in the cross-plane experiment results in a higher weighting on the η-component since it now contains a greater percentage of the measured TKE. The number of antinodes is generally seen to increase with increasing α-values. From the streamwise results in Figure 5.12 the imaginary parts of eigenfunctions are seen to be insignificant for the most energetic LD modes. It is, however, evident from Figures 5.14 that the cross-plane experiment has a more significant imaginary part for $\alpha = 1 : 8$.

5.2.3 Reconstruction of the Velocity field

Analogous to the streamwise experiment we wish to investigate how the modes reconstruct a range of statistical features of the flow. In the preceding section we have investigated the modes as well as their limitations in terms of spatial resolution. In the following the component spectra, and the single-point statistics will be reconstructed analogously to the component energy density spectra in Chapter 4. This section will also include an energy production analysis in which the local and global energy production capabilities of the modes will be quantified and discussed in an analogous manner to the streamwise experiment. We will seek to confirm the general tendencies observed in the energy production analysis in the streamwise experiment, despite the discrepancies related to the change in dimensionality between the two data sets.

5.2.3.1 Modal reconstruction of component spectra

The modal components of the single-point spectra in Figures 5.7(c)-5.7(f) are obtained from the following expression

$$B^{ij} = \lambda \varphi^{i\alpha} \varphi^{j*}_{\alpha}, \tag{5.6}$$

where i, j can each take on the values ξ, η, and θ, representing the three components of the LD-modes. The contributions defined by (5.6) are seen in Figures 5.15-5.18. Similar to the reconstruction of the component energy spectra in Chapter 4 we see that the current spectra exhibit the self-similar behavior for all three modal components. Comparing these results to the modal components of the single-point spectra in figures 5.15(a)-5.18(h) (pp. 144-147) we can identify similar trends between the current data set and the streamwise experiment - keeping in mind that the azimuthal mode number m represents a decomposition along the missing dimension from the data in Chapter 4. Both spectral reconstructions exhibit the same evolution from low to high m and κ, whereafter a self-similar form of the modal components of the spectra follow. This is especially true for low α-values possessing most of the TKE content. Figures 5.15(c), 5.16(b), and 5.17(c) are clear examples of this behavior indicating the existence of an ordered underlying process governing the energy transfer across m-values.

The cumulative reconstruction is achieved from (5.6) by the following expression

$$B^{ij}_{(n)} = \sum_{\alpha=1}^{n} \lambda^{\alpha}_{m} \varphi^{i}_{\alpha,m} \varphi^{j*}_{\alpha,m}, \tag{5.7}$$

where the single-point spectra are reconstructed in Figures 5.19-5.22. Here we see a rapid convergence of the form of the spectra.

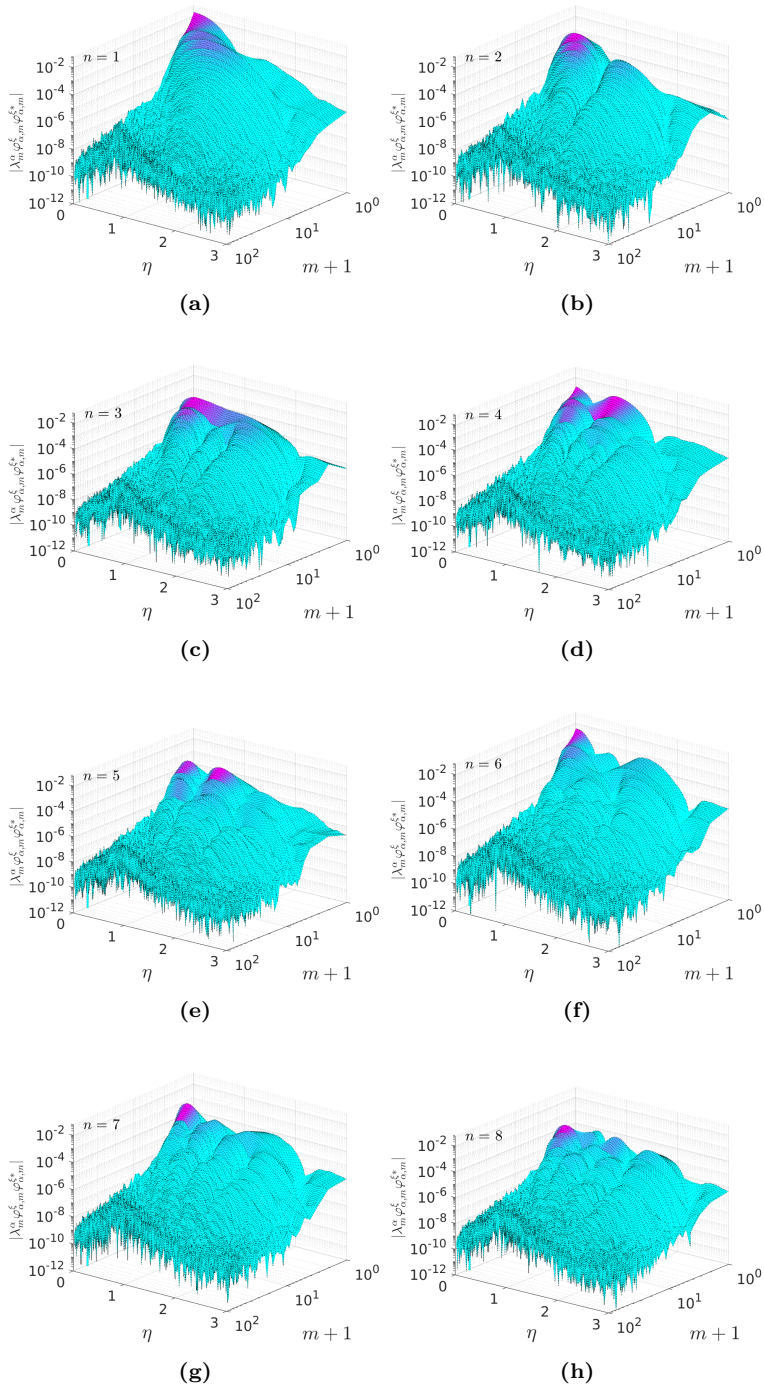

Figure 5.15: Reconstruction of the ξ-component single-point spectra.

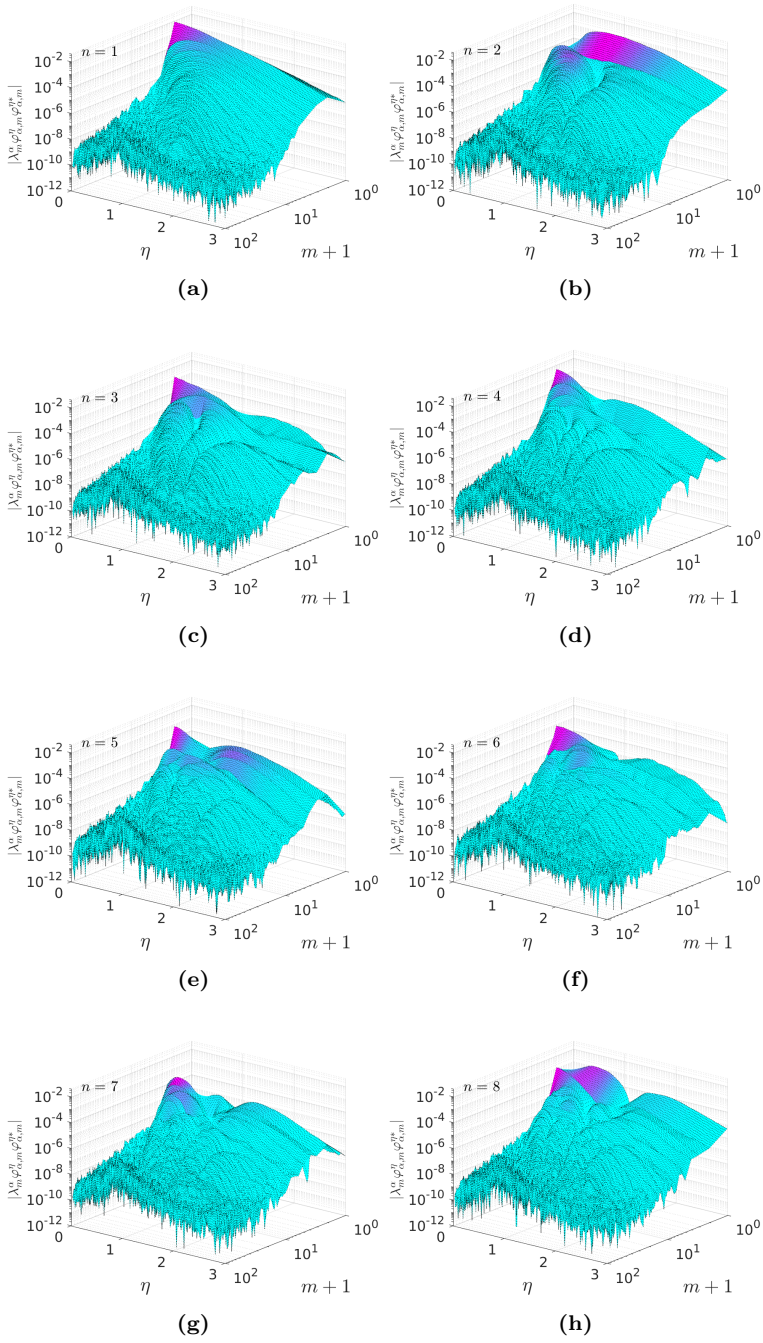

Figure 5.16: Reconstruction of the η-component single-point spectra.

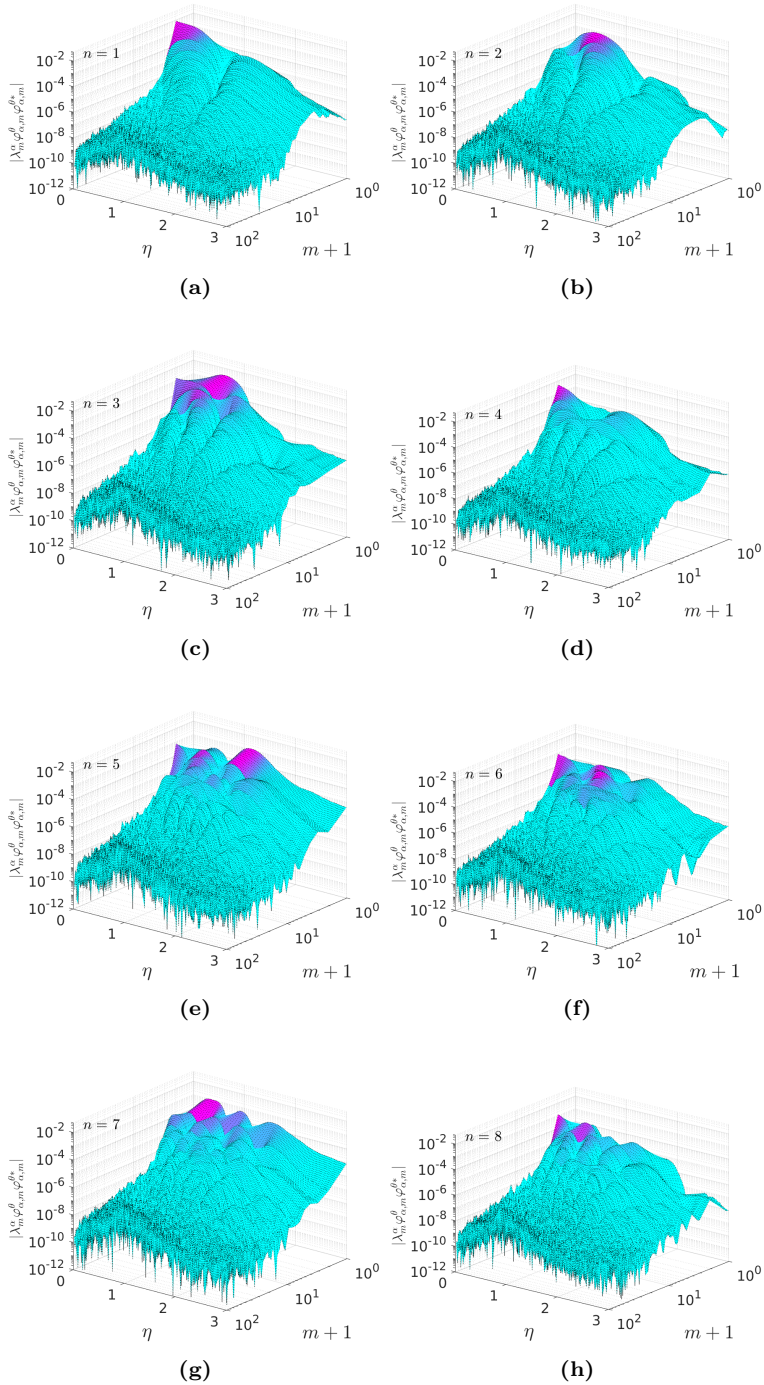

Figure 5.17: Reconstruction of the θ-component single-point spectra.

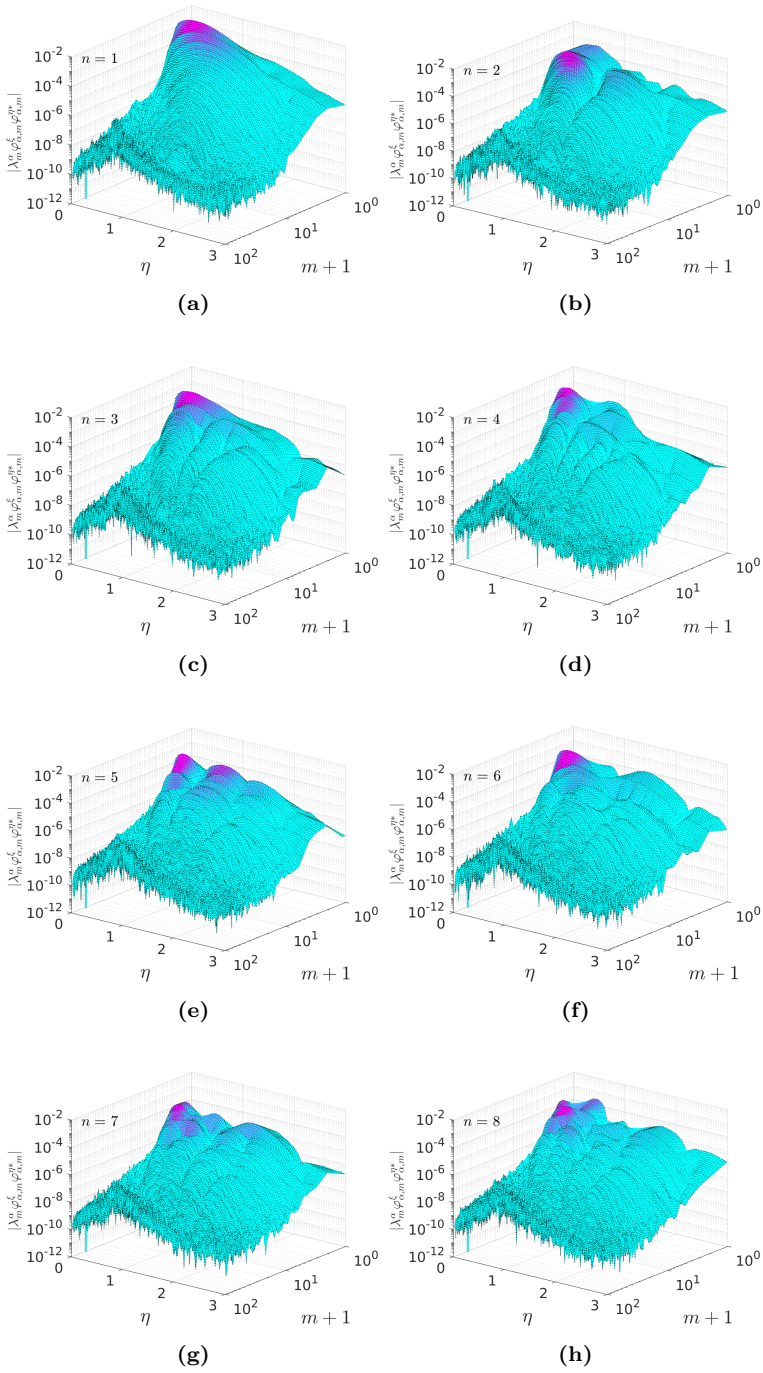

Figure 5.18: Reconstruction of single-point cross-spectra (ξ-η-component).

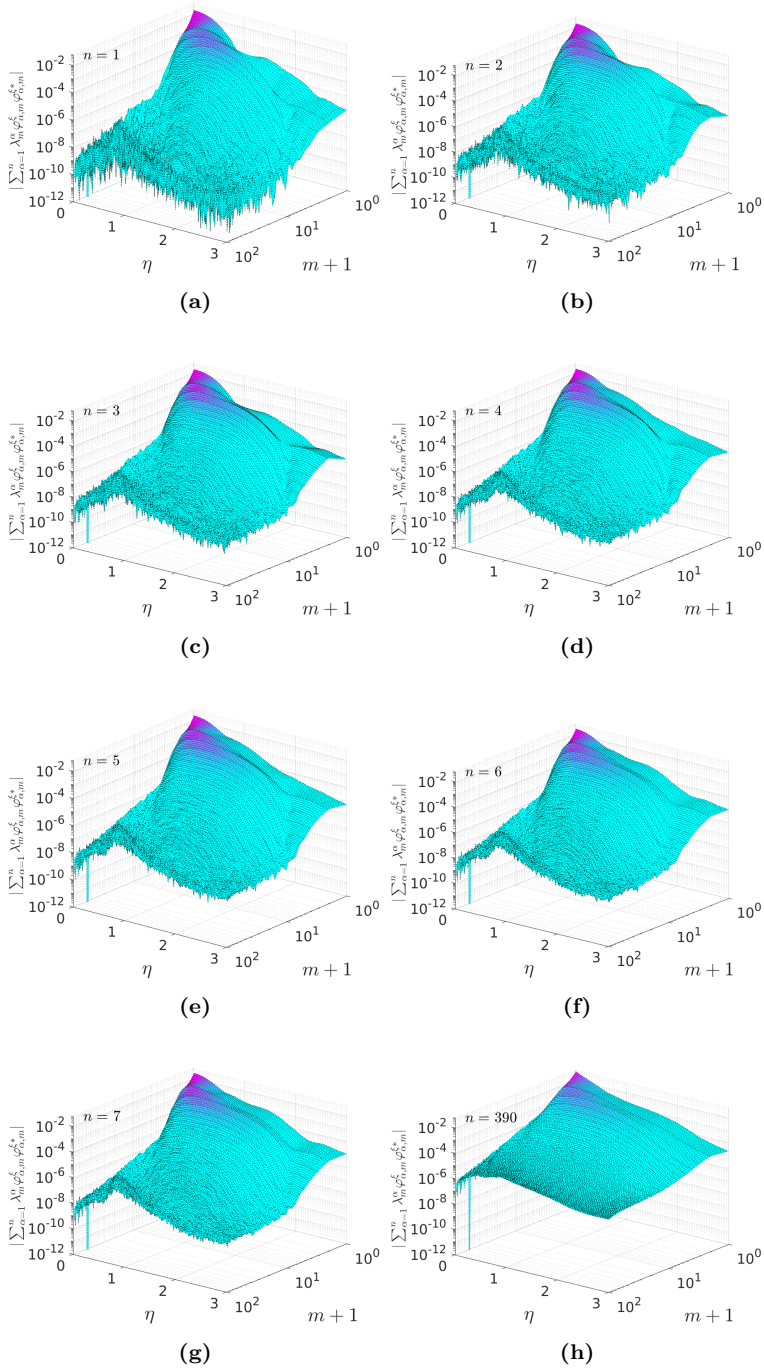

Figure 5.19: Cumulative sum of modal contributions to the ξ-componentof the single-point spectra.

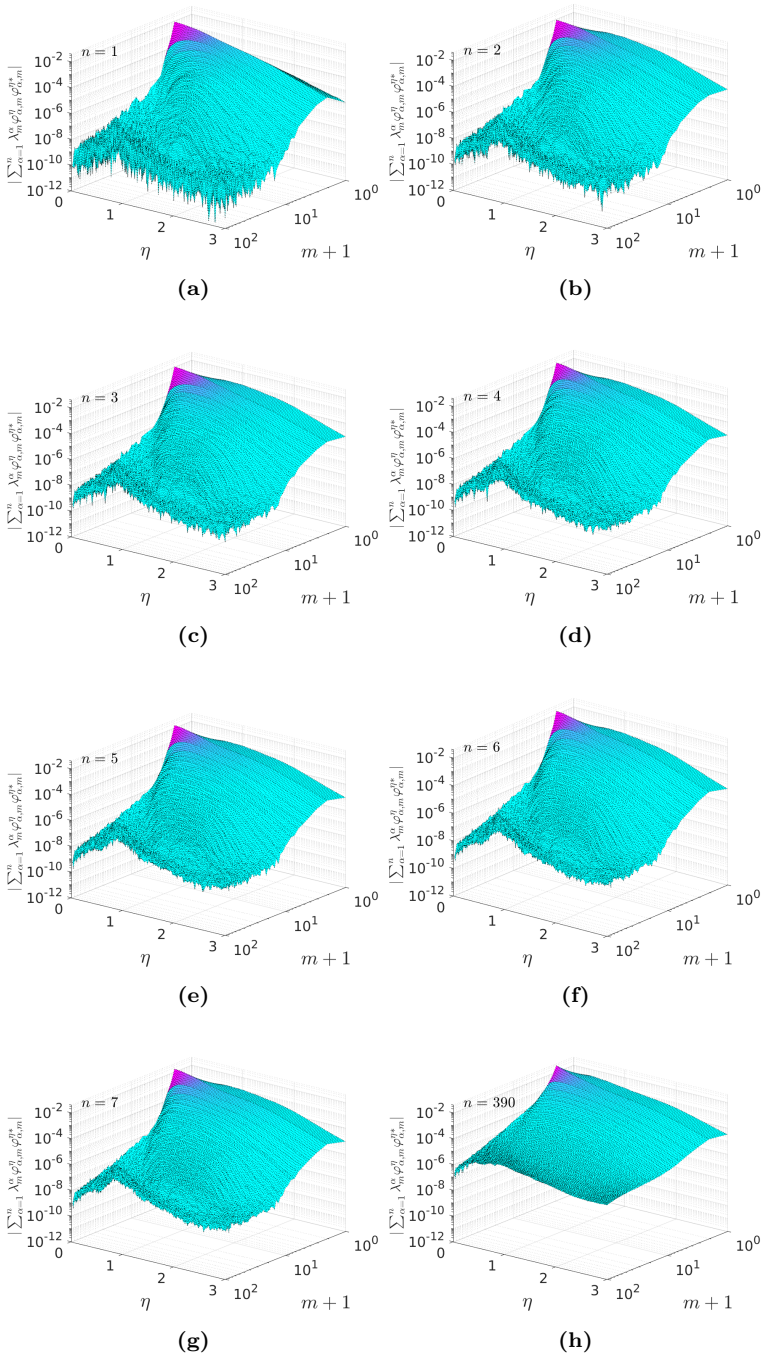

Figure 5.20: Cumulative sum of modal contributions to the η-component single-point spectra.

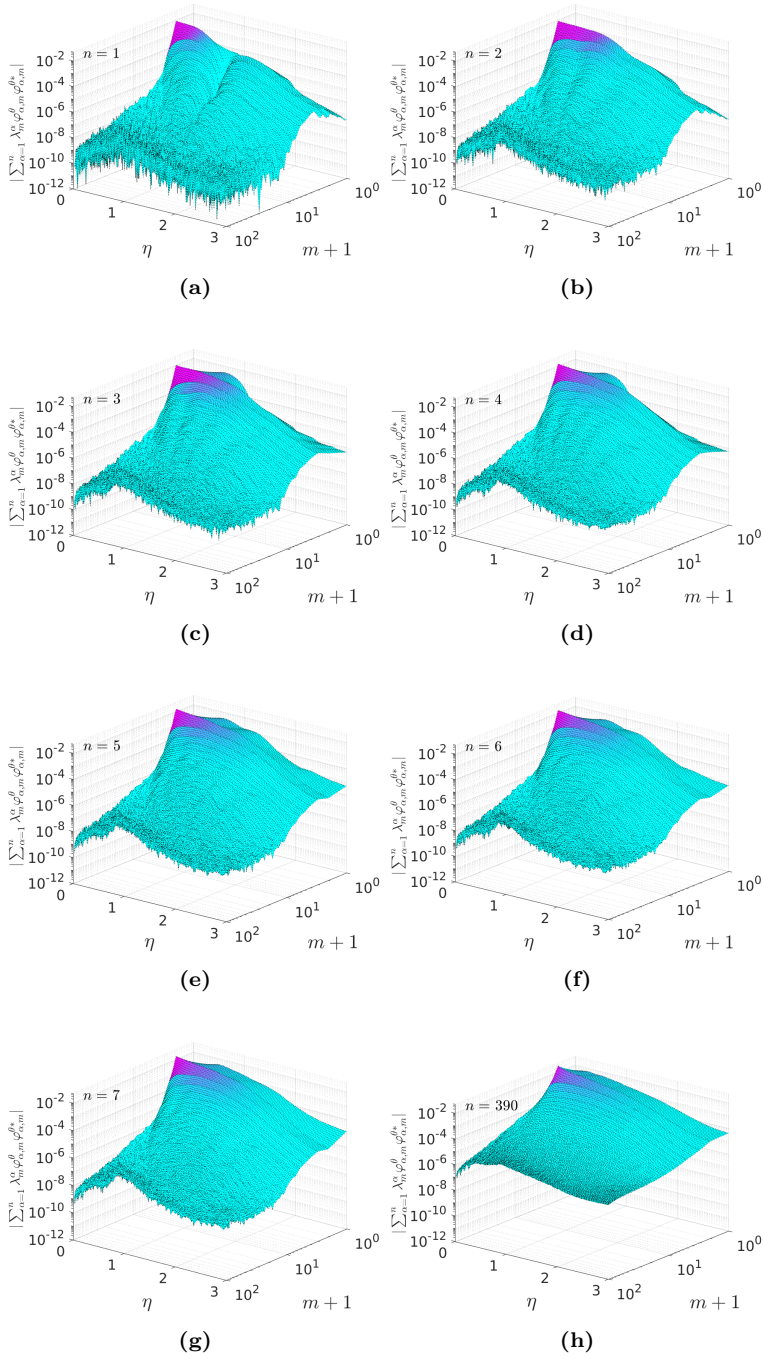

Figure 5.21: Cumulative sum of modal contributions to the θ-component single-point spectra.

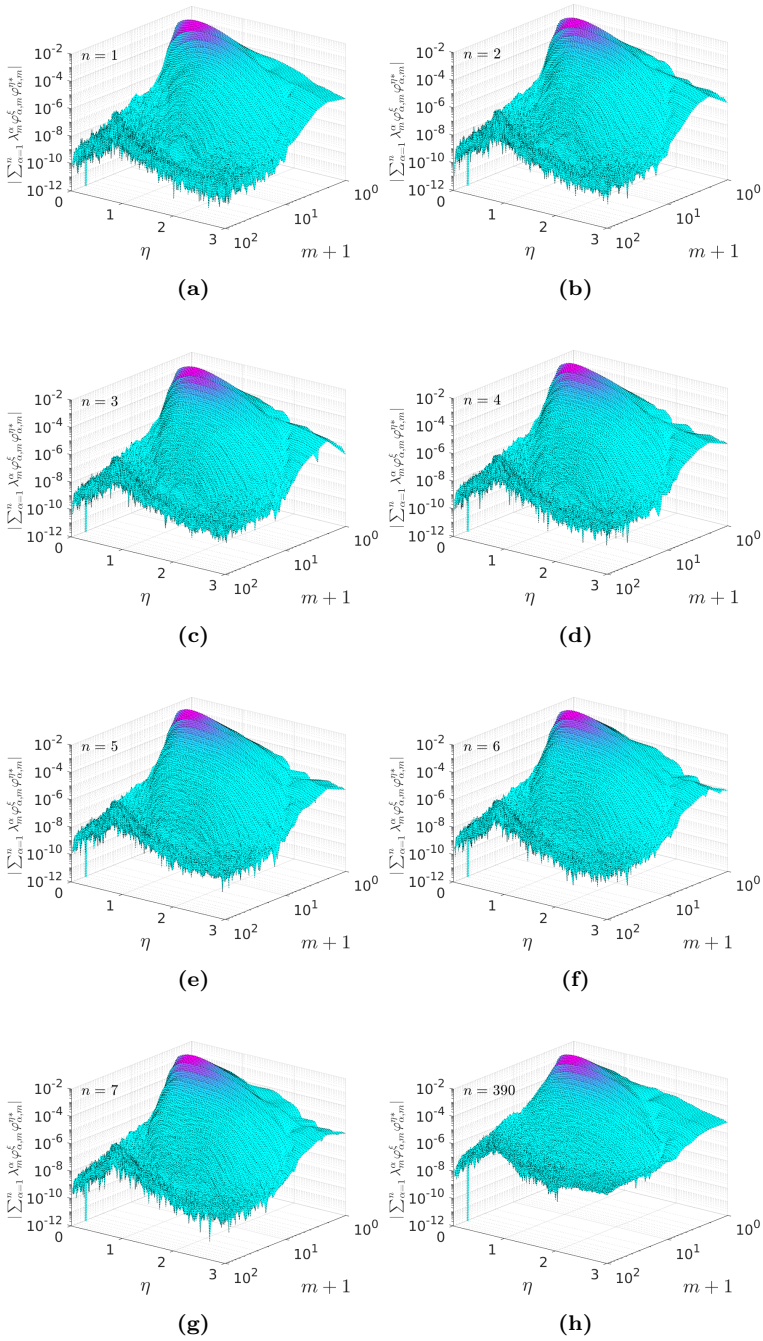

Figure 5.22: Cumulative sum of modal contributions to the cross-spectra (ξ-η-component).

5.2.3.2 Energy production analysis

In order to investigate the ability of the modes to extract energy directly from the mean flow term II in (4.4) is expanded using the modes, analogously to the analysis in section 4.3.4.3 of Chapter 4. We note that in the current case the decomposition is performed for three velocity components, where the azimuthal decomposition represents the additional dimension compared to the decomposition in Chapter 4. Once more we investigate $\delta/U_c^3\mathcal{P}_\lambda$, where

$$\mathcal{P}_\lambda = \varphi_i^\alpha \varphi_\alpha^{j*} \nabla_j V^i, \tag{5.8}$$

representing the eigenvalue normalized production (ENP), but now in the context of the three-dimensional decomposition. We are furthermore interested in the spatially integrated expression, analogous to Chapter 4

$$\int \delta/U_c^3 \mathcal{P}_\lambda \eta d\eta, \tag{5.9}$$

which is shown in Figure 5.23, representing the production density as a function of azimuthal mode number, m and LD-mode number α. Here Figures 5.23(a)-5.23(d) show the real-, the imaginary parts, the argument, and the absolute value of (5.9), respectively. Since these are in a logarithmic representation the first axes in all subfigures are designated as $m+1$ in order to be able to represent the zeroth harmonic, $m=0$. From Figure 5.23(d) see the majority of the energy production contributions arise from low α. It is seen that for low α-values a wide m-range exhibit a constant ENP and only for high m-values do we see a gradual decrease in the ENP from $0.2\,\mathrm{s}^2/\mathrm{m}^2$ at $m=10$ to $0.13\,\mathrm{s}^2/\mathrm{m}^2$ at $m=40$, analogous to the results from the streamwise experiment. This also falls in line with the large degree of modal self-similarity across m-values seen earlier in the analysis of the single-point spectra. The results show negligible ENP levels for the lowest α-m-combinations e.g. $0.05\,\mathrm{s}^2/\mathrm{m}^2$ for $\alpha = 1, m = 0$, as opposed to $0.2\,\mathrm{s}^2/\mathrm{m}^2$ for $\alpha = 1, m = 1:14$. This means that $m=0$ has a comparably relative energy production, while approximately the ENP levels of $0.20\,\mathrm{s}^2/\mathrm{m}^2$ of the higher Fourier modes ($m = 1:14$) are much more significant for $\alpha = 1$. Figure 5.23 also demonstrates that most of the energy production is related to the real-part of the modes similarly to the streamwise experiment. This tendency spans across both experiments in the current work, despite the varying dimensionalities of the two data sets.

Regarding the hypothesis posed by Wänström 2009, these results confirm that for a certain α-m-region the modes obtain a constant fraction of their energy directly from the mean flow. If we compare this to the results of the corresponding analysis in section 4.3.4.3 of Chapter 4, we see similar traits of constant ENP levels where a gradual decrease in

seen for increasing m. Both results therefore support the theory that significant energy is produced locally by the modes and only a fraction must therefore be obtained from higher mode numbers. Both of these results, although in agreement, stimulate questions regarding the nature of the energy transport process. As noted in Chapter 4 section 4.3.4.3, the limited ENP seen here in Figure 5.23 is due to the spatial integration of the energy over the domain which conceals local ENP variations across the width of the jet. Higher levels are expected especially around regions of high mean shear which was shown to be around $\eta = 1$.

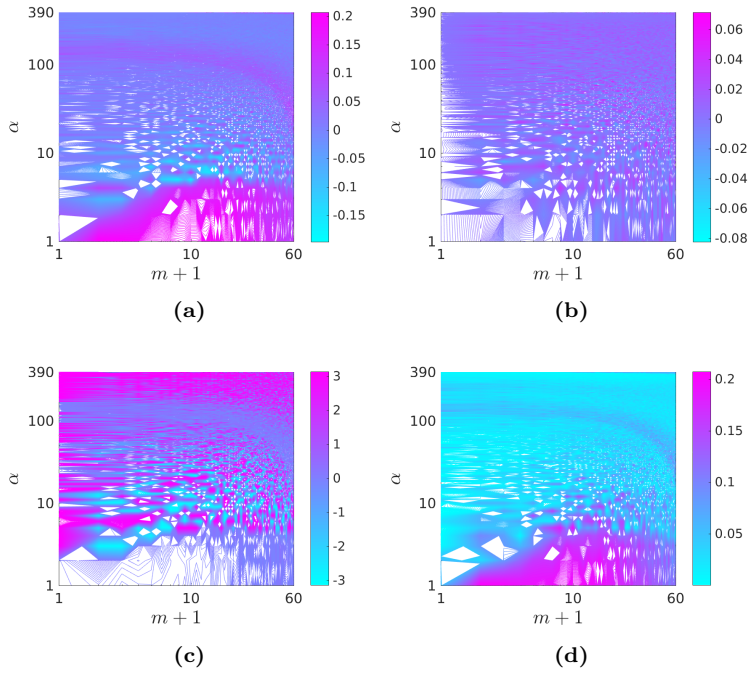

Figure 5.23: Production spectra normalized by the local energy. (a): $\Re\left\{\delta/U_c^3\mathcal{P}_\lambda\right\}$, (b): $\Im\left\{\delta/U_c^3\mathcal{P}_\lambda\right\}$, (c): $Arg(\delta/U_c^3\mathcal{P}_\lambda)$ (d): $\left|\delta/U_c^3\mathcal{P}_\lambda\right|$.

We now investigate the individual LD-modes and their contributions to the energy production as a function of η, that is $\delta/U_c\mathcal{P}$. The spatial distribution of the energy production is shown in terms of the individual modal contributions to the energy production term in Figure 5.24. The majority of the energy production occurs below $m = 10$ for the majority of the production distributions shown.

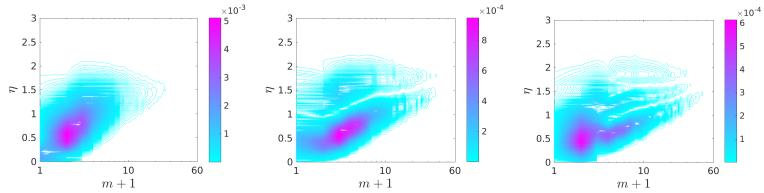

(a) $\alpha = 1$ **(b)** $\alpha = 2$ **(c)** $\alpha = 3$

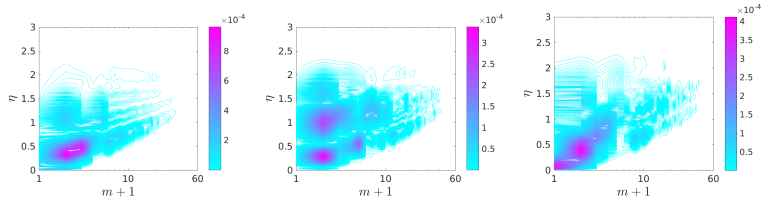

(d) $\alpha = 4$ **(e)** $\alpha = 5$ **(f)** $\alpha = 6$

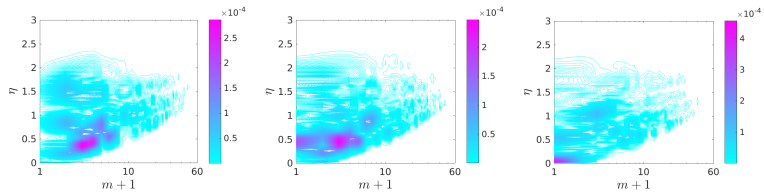

(g) $\alpha = 7$ **(h)** $\alpha = 8$ **(i)** $\alpha = 9$

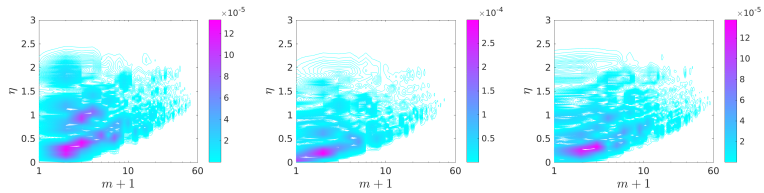

(j) $\alpha = 10$ **(k)** $\alpha = 11$ **(l)** $\alpha = 12$

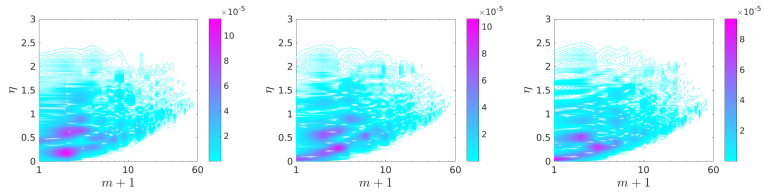

(m) $\alpha = 13$ **(n)** $\alpha = 14$ **(o)** $\alpha = 15$

Figure 5.24: Individual contributions to Term II for $\alpha = 1 : 15$, presented in terms of azimuthal mode number, m, across the span of the jet.

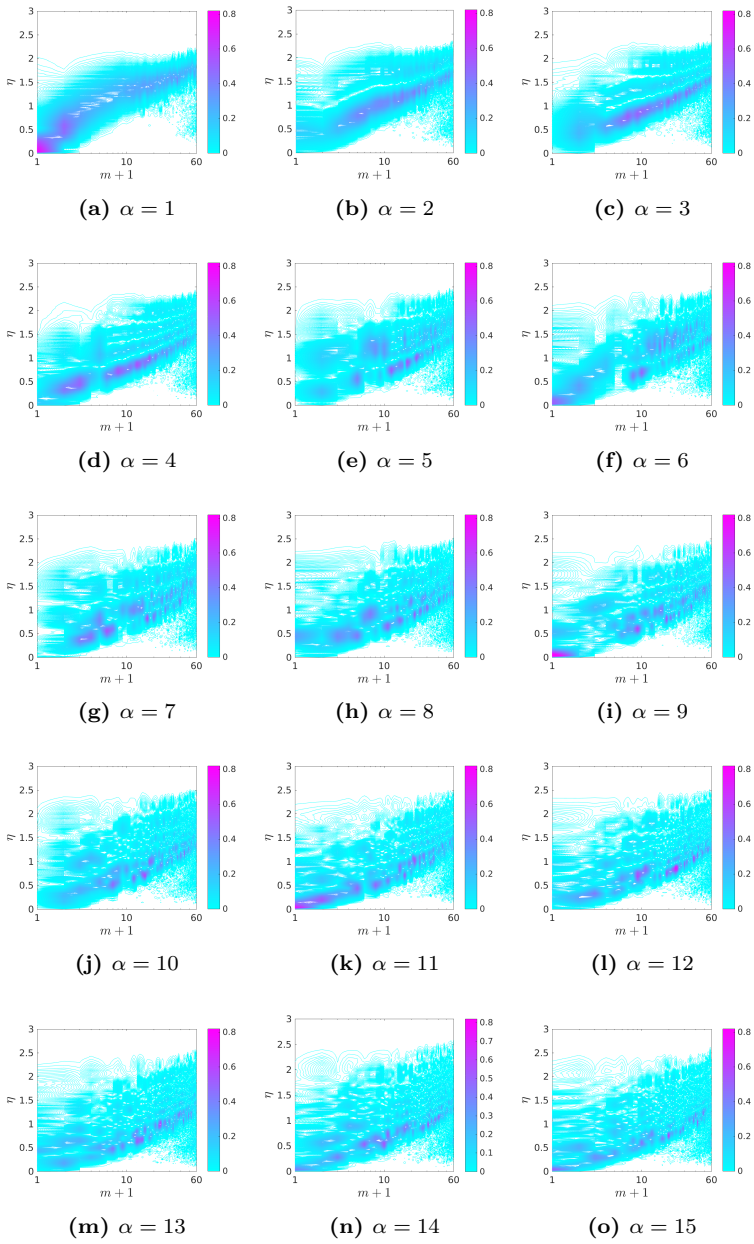

(a) $\alpha = 1$ **(b)** $\alpha = 2$ **(c)** $\alpha = 3$

(d) $\alpha = 4$ **(e)** $\alpha = 5$ **(f)** $\alpha = 6$

(g) $\alpha = 7$ **(h)** $\alpha = 8$ **(i)** $\alpha = 9$

(j) $\alpha = 10$ **(k)** $\alpha = 11$ **(l)** $\alpha = 12$

(m) $\alpha = 13$ **(n)** $\alpha = 14$ **(o)** $\alpha = 15$

Figure 5.25: Energy-scaled contributions to Term II for $\alpha = 1 : 15$, presented in terms of azimuthal mode number, m, across the span of the jet.

The first LD-mode contribution to term II in Figure 5.24(a) is seen to peak around $\eta = 0.50$ for $m = 1$, such that $m = 1$ has the largest local contribution to the energy production in the jet. We note the negligible contributions from $m = 0$ for nearly all η. Although it is characterized by significant energy content - as seen from Figure 5.6(c) - the passivity of $m = 0$ in terms of the energy production indicates that this mode is mostly responsible for the energy transport in the jet. Remnants of these characteristics are seen in the rest of the modes in Figure 5.24, where we also notice peaks in energy production in corresponding α-m-regions. We see that most of the energy production occurs below $\eta = 1$ correlating with regions characterized by significant mean shear. These results show similar traits to those identified in Figure 4.47 in Chapter 4, although a one-to-one correspondence cannot be claimed to exist.

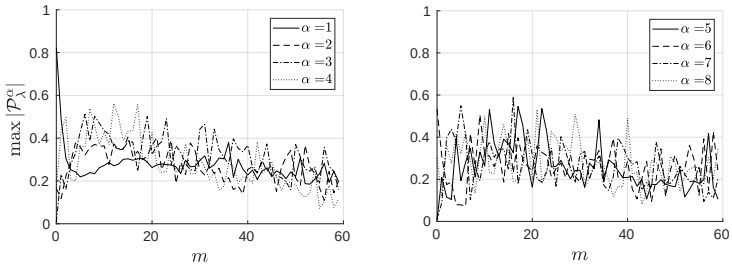

(a) **(b)**

Figure 5.26: Maximum values for $\alpha = 1 : 8$ as a function of m.

Figure 5.25 shows the corresponding ENP distribution across the domain for the LD-modes $1 - 15$. From this we see the energy-scaled contributions of modes and their distributions across the flow domain. We notice the diagonal regions of nearly constant ENP throughout all mode numbers in Figure 5.25. While the most energetic Fourier modes obtain their energy from the high-mean shear regions closer to the jet centerline as would be expected, the less energetic Fourier modes produce energy in regions characterized by relatively low mean shear at the periphery of the flow. For the current data the ENP levels are generally above $0.20\,\mathrm{s}^2/\mathrm{m}^2$ along the characteristic diagonals in Figure 5.25. The maximum levels for $\alpha = 1 : 8$ as a function of m are seen in Figure 5.26, from which we can see that rarely do the ENP levels exceed $0.5\,\mathrm{s}^2/\mathrm{m}^2$, the most notable exception being $m = 0$ for $\alpha = 1$ at the centerline. For higher α the maximum levels increase for $m < 40$ indicating that modes $\alpha = 2 : 4$ obtain a higher percentage of their energy directly from the mean flow, than the more energetic $\alpha = 1$. We also see that

peak levels of ENP are of the same order for all modes in Figure 5.25 which is a similar trait to what was seen in the streamwise experiment. This once more supports the notion that the energy production is a process in which all modes generally participate and that the modes are not exclusively dependent on energy being transferred from lower mode numbers.

5.2.3.3 Modal reconstruction of single-point statistics

The reconstruction of the single-point statistics is shown in Figure 5.27. The profiles are a cumulative sum over α where the m-dependence has been removed by summing over the azimuthal mode numbers. Similarly to the corresponding analysis in Chapter 4 the convergence rate of the shear-stresses is seen to be much faster than the normal stresses. It is also seen that unlike the reconstruction of the analogous profiles in Chapter 4 where the reconstruction started from the $\eta = 1$ region, the modal contributions to the reconstruction of normal stresses extends to the centerline region. From these results one may infer that the slow reconstruction of stresses along the centerline in the streamwise experiment was caused by the spatial aliasing effect of waves crossing the centerline, Tennekes and Lumley 1972. The LD decomposition could be used to eliminate the aliasing effects in the Reynolds stress profiles, but since both experiments are dimensionally limited relative to the decomposition in three-dimensional space, we can argue by analogy to Fourier analysis that the modes in the experiment with the highest concentration of energy at low mode numbers is the most spatially aliased. Comparing the cumulative sum over α in figures 4.21(b) (p. 83) and 5.6(b) we see that the first ten α for the streamwise and crossplane data possess 85.8 % and 76.3 %, respectively, of the total TKE. This indicates that the spatial aliasing is lower in the crossplane data than in the streamwise data.

The reconstructions in Figure 5.27 challenge this postulate, and illustrate that the most significant modal contributions to the normal stress profile reconstructions extend across the entire span of the flow. The reason for this may be found by analyzing the LD-integral, (3.7), in the dimensionally reduced data analyzed in the current work. By neglecting the effects of azimuthal variance in the streamwise experiment, one is implicitly assuming complete axisymmetry for each realization, since we have applied the volume element for a three-dimensional coordinate system in the definition of the LD integral.

The similarity between the two experiments can, however, be found in terms of the reconstruction of the TKE integrand, seen in Figure 5.27(f). These results can be compared to the streamwise analogue in Figure 4.49(g) (p. 121), which shows a similar reconstruction. Since the

LD-modes are optimized in terms of their reconstruction of the TKE the mechanism by which the modes are determined is seen by this comparison to be governed by the same mechanism.

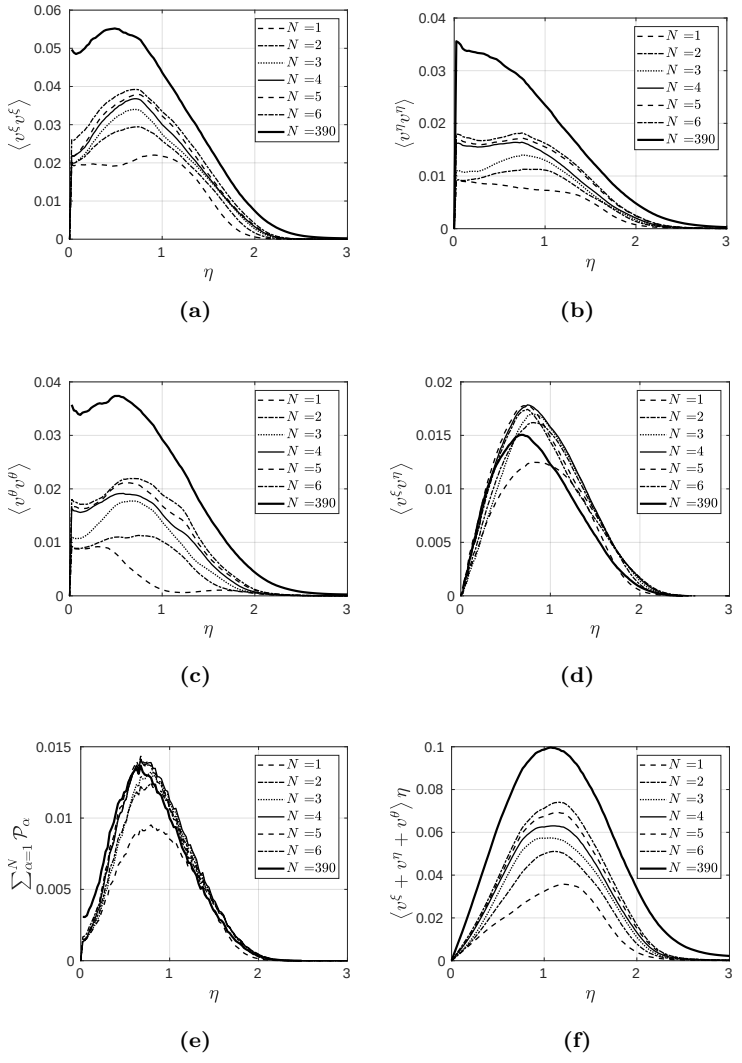

Figure 5.27: Reconstruction of Reynolds stresses and the energy production terms.

CHAPTER 6

Conclusions

In the current work tensor calculus was introduced to equilibrium similarity theory. The new formalism ensures the preservation of invariance of the velocity vectors under coordinate transformation which is required by equilibrium similarity analysis. This provides the possibility of easily performing modal analysis of each term of the energy equation in complex coordinate systems in order to quantify the various processes, herein the energy production, energy dissipation, and the non-linear transport rigorously in terms of the LD eigenfunctions. With the current formalism the current work has paved the way for future investigations of the turbulence kinetic energy transport in the turbulent jet by means of modal expansions in complex coordinate systems.

Furthermore, the work has focused on testing the hypothesis posed in Wänström 2009, namely that multiple modes can extract a constant and significant portion of their relative energies from the mean flow. The expansion of the turbulence kinetic energy transport has demonstrated that for turbulent flows characterized by a self-adjoint LD operator all modes are indeed involved in the global energy production. The analysis has revealed that the energy production capacity of a given mode is varying across the flow domain as well as over wave- and mode numbers. A wide range of modes are observed to obtain significant levels of their energy directly from the mean flow, even at wavenumbers for which the averaged spectra exhibit the characteristic $-5/3$-region. This is particularly shown to be true in high mean shear regions. The reconstruction of the energy spectra revealed that the spectral flux of the individual modal building blocks of the spectra is varying across the $-5/3$-region (in the averaged spectrum) and can be seen to change signs across wavenumbers. This indicates that a more complex energy transport mechanism underlies the averaged spectra and can be investigated in more detail through the analysis of the modal non-linear transport term.

From the cross-plane experiment, the reconstruction of the single-point energy spectra shows similar features of modal similarity compared to the streamwise experiment, where for each LD-mode there modal self-similarity is observed across azimuthal mode numbers. These results, confirm similar features seen in the streamwise plane. The energy production analysis substantiates the results from the streamwise experiments by demonstrating that a wide range of modes (e.g. $\alpha = 1$ and $m = 1 : 14$) obtain relatively constant portions of their energy directly from the mean flow, thereby partially circumventing a classical

Richardson energy cascade stating that less energetic modes obtain their energy exclusively from more energetic modes. The added θ-dimension of the crossplane experiment redistributes the energy-weighing of modes compared to the streamwise experiment. The eigenvalue-weighted LD modes reflect resembling features across the two experiments, whereas the higher modes were characterized by larger differences across the experiments due to the different energy-weighing related to the additional velocity component.

APPENDIX A

The Navier-Stokes equations in curvilinear coordinates

In the following the incompressible Navier-Stokes equations are rewritten from invariant form to curvilinear component form

$$\begin{aligned}
\frac{\partial \overbrace{\overline{V}}^{V^i\overline{z}_i}}{\partial t} + \overbrace{\overline{V}}^{V^j\overline{z}_j} \cdot \underbrace{\nabla}_{\overline{z}_k\nabla^k} \overbrace{\overline{V}}^{V^i\overline{z}_i} &= -\frac{1}{\rho}\underbrace{\nabla}_{\overline{z}_i\nabla^i} p + \\
&+ \nu \underbrace{\nabla^2}_{\overline{z}_j\nabla^j\overline{z}_k\nabla^k} \overbrace{\overline{V}}^{V^i\overline{z}_i}, \qquad \text{(A.1)} \\
\frac{\partial}{\partial t}\left(V^i\overline{z}_i\right) + V^j\overline{z}_j \cdot \overline{z}_k\nabla^k V^i\overline{z}_i &= -\frac{1}{\rho}\overline{z}_i\nabla^i p + \\
&+ \nu\overline{z}_j\nabla^j \cdot \overline{z}_k\nabla^k V^i\overline{z}_i, \qquad \text{(A.2)} \\
\left[\frac{\partial V^i}{\partial t} + V^j \underbrace{z_{jk}\nabla^k}_{\nabla_j} V^i\right]\overline{z}_i &= \left[-\frac{1}{\rho}\nabla^i p + \right. \\
&+ \left. \nu\nabla^j \underbrace{z_{jk}\nabla^k}_{\nabla_j} V^i\right]\overline{z}_i, \qquad \text{(A.3)} \\
\left[\frac{\partial V^i}{\partial t} + V^j\nabla_j V^i\right]\overline{z}_i &= \left[-\frac{1}{\rho}\nabla^i p + \nu\nabla^j\nabla_j V^i\right]\overline{z}_i, \qquad \text{(A.4)}
\end{aligned}$$

where the metrinilic property of the basis has been invoked from (A.1) to (A.2). By supressing the basis-vectors in (A.4) the divergence-free equations take on the following well-known form

$$\frac{\partial V^i}{\partial t} + V^j\nabla_j V^i = -\frac{1}{\rho}\nabla^i p + \nu\nabla^j\nabla_j V^i, \qquad \text{(A.5)}$$

which is valid in any well-defined curvilinear coordinate system defined in Euclidean space.

APPENDIX B

The Laplacian of first-order tensors

The Laplacian in the Navier-Stokes equations operates on vectors defined in $\mathbb{R}^3$. In the spirit of the work at hand, it is important to have a general expression for the Laplacian in curvilinear coordinates in Euclidean space, in order to be able to apply it in general coordinates. In the following the Laplacian of a first-order tensor will be derived for general coordinates.

Due to the tensor-preserving property of the covariant derivative, the Laplacian can be written as a contravariant derivative of a second-order mixed tensor

$$\begin{aligned}
\nabla^j \nabla_j v^i &= z^{jk} \nabla_k T^i_j && \text{(B.1)}\\
&= z^{jk} \left(\frac{\partial T^i_j}{\partial z^k} + \Gamma^i_{kl} T^l_j - \Gamma^l_{jk} T^i_l \right) && \text{(B.2)}\\
&= z^{jk} \Bigg(\frac{\partial}{\partial z^k} \left(\frac{\partial v^i}{\partial z^j} + \Gamma^i_{jl} v^l \right) + && \text{(B.3)}\\
&+ \Gamma^i_{kl} \left(\frac{\partial v^l}{\partial z^j} + \Gamma^l_{jm} v^m \right) - \Gamma^l_{jk} \left(\frac{\partial v^i}{\partial z^l} + \Gamma^i_{lm} v^m \right) \Bigg)\\
&= z^{jk} \Bigg(\frac{\partial^2 v^i}{\partial z^j z^k} + \Gamma^i_{jl} \frac{\partial v^l}{\partial z^k} + v^m \frac{\partial \Gamma^i_{jm}}{\partial z^k} + && \text{(B.4)}\\
&+ \Gamma^i_{kl} \frac{\partial v^l}{\partial z^j} + \Gamma^i_{kl} \Gamma^l_{jm} v^m - \Gamma^l_{jk} \frac{\partial v^i}{\partial z^l} - \Gamma^l_{jk} \Gamma^i_{lm} v^m \Bigg)\\
&= z^{jk} \Bigg(\frac{\partial^2 v^i}{\partial z^j z^k} - \Gamma^l_{jk} \frac{\partial v^i}{\partial z^l} + 2\Gamma^i_{jl} \frac{\partial v^l}{\partial z^k} + && \text{(B.5)}\\
&+ v^m \left(\frac{\partial \Gamma^i_{jm}}{\partial z^k} + \Gamma^i_{kl} \Gamma^l_{jm} - \Gamma^l_{jk} \Gamma^i_{lm} \right) \Bigg).
\end{aligned}$$

The last expression is the reduced form valid in any well-defined coordinate system on manifolds with zero-curvature.

APPENDIX C

The Self-Adjoint Property of $\overline{R}$

In the following we prove that the linear bounded operator $\overline{R} : \mathcal{H} \to \mathcal{H}$ is self-adjoint, where $\mathcal{H}$ is a complex Hilbert space with an inner product $(\cdot, \cdot) : \mathcal{H} \to \mathrm{C}$. From the POD integral the operator is defined as

$$\overline{R}(\cdot) = \left\langle \left(\cdot, \overline{V}\right) \overline{V} \right\rangle . \tag{C.1}$$

We define the adjoint property by the following inner product relation

$$\left(\overline{R}\,\overline{\Phi}, \overline{\Psi}\right) = \left(\overline{\Phi}, \overline{R}^{\dagger}\overline{\Psi}\right), \quad \forall\, \overline{\Phi}, \overline{\Psi} \in \mathcal{H} \tag{C.2}$$

where $\overline{R}^{\dagger}$ is the adjoint operator of $\overline{R}$. The objective is to show that $\overline{R} = \overline{R}^{\dagger}$. We start with the left-hand side of (C.2) and substitute (C.1)

$$\begin{aligned}
\left(\left\langle \left(\overline{\Phi}, \overline{V}\right) \overline{V} \right\rangle, \overline{\Psi}\right) &= \left\langle \left(\left(\overline{\Phi}, \overline{V}\right) \overline{V}, \overline{\Psi}\right) \right\rangle, \\
&= \left\langle \left(\overline{\Phi}, \overline{V}\right) \left(\overline{V}, \overline{\Psi}\right) \right\rangle, \\
&= \left\langle \left(\overline{\Phi}, \left(\overline{V}, \overline{\Psi}\right)^{*} \overline{V}\right) \right\rangle, \\
&= \left(\overline{\Phi}, \left\langle \left(\overline{V}, \overline{\Psi}\right)^{*} \overline{V} \right\rangle\right), \\
&= \left(\overline{\Phi}, \left\langle \left(\overline{\Psi}, \overline{V}\right) \overline{V} \right\rangle\right), \\
&= \left(\overline{\Phi}, \overline{R}^{\dagger}\overline{\Psi}\right).
\end{aligned}$$

From (C.2) and the Riesz' representation theorem, we conclude that $\overline{R} = \overline{R}^{\dagger}$, and therefore (C.1) is self-adjoint. Since $\overline{R}$ is an invariant operator this result means that the tensor formulation of $\overline{R}$ is also self-adjoint.

It is important to underline that the self-adjointness property of the operator in $L^2\left(\Omega, \mathrm{C}^3\right)$ cannot be extended directly to $\mathbb{R}^n$ if the coordinate basis is non-orthogonal. Therefore, the self-adjointness property in linear algebra, usually denoted as Hermitian-symmetry, does not follow for non-orthogonal coordinate systems. Note that this is of central importance for the current work, since the coordinate system proposed for the decomposition by Ewing et al. 2007 is non-orthogonal and is therefore not a coordinate system that can ensure orthogonality nor existence of sufficiantly many eigenvectors to span the basis.

APPENDIX D

Derivation of the POD in scaled similarity variables

The POD in tensor for reads

$$\int_{\Omega} \underbrace{R^{i}_{\cdot\hat{j}}}_{z_{\hat{j}\hat{k}}R^{i\hat{k}}} \varphi^{\hat{j}} \underbrace{\sqrt{\widehat{Z}}}_{\hat{\delta}^3\hat{\eta}/A} \widehat{w} d\widehat{\mu} = \lambda \varphi^{i}. \tag{D.1}$$

We know that we can scale the instanteous physical velocity field by the centerline velocity, which is given by Hussein, Capp, and George 1994

$$U_c = \frac{ABM_0^{1/2}}{\delta}, \tag{D.2}$$

where $\delta = A(x - x_0)$. Since the covariant bases are proportional to $\delta = ADe^{\xi}$, this means that the contravariant velocities at two different points, V^i, and $V^{\hat{i}}$ can be decomposed as as $V^i = \widetilde{V}^i \widetilde{U}_c$ and $V^{\hat{i}} = \widetilde{V}^{\hat{i}} \widehat{\widetilde{U}}_c$, where $\widetilde{U}_c$ and $\widehat{\widetilde{U}}_c$ are the centerline velocities of the contravariant components defined as

$$\widetilde{U}_c = \frac{A^2 B M_0^{1/2}}{\delta^2} \tag{D.3}$$

$$\widehat{\widetilde{U}}_c = \frac{A^2 B M_0^{1/2}}{\widehat{\delta}^2}. \tag{D.4}$$

We know this to be true since we can reconstruct the original velocity field by noting that the physical field is expanded by the covariant basis in the following manner

$$\overline{V} = \underbrace{V^i}_{\widetilde{V}^i \widetilde{U}_c} \overline{z}_i = \underbrace{\widetilde{V}^i \widetilde{U}_c}_{\propto U_c} \overbrace{\overline{z}_i}^{\propto \delta/A}. \tag{D.5}$$

Since we know that the scaled contravariant velocity, $\widetilde{V}^i$, is homogeneous along ξ, it directly implies that $U_c \propto A^2/\delta^2$. We can now rewrite (D.1) as

$$\int_{\Omega} \underbrace{\overbrace{z_{\hat{j}\hat{k}}}^{\tilde{z}_{\hat{j}\hat{k}} A^2 D^2 e^{2\hat{\xi}}} \overbrace{R^{i\hat{k}}}^{\widetilde{U}_c \widehat{\widetilde{U}}_c \widetilde{R}^{i\hat{k}}}}_{\widetilde{R}^{i}_{\hat{j}} \widetilde{U}_c \widehat{\widetilde{U}}_c D^2 e^{2\hat{\xi}}} \varphi^{\hat{j}} \hat{\delta}^3 \hat{\eta}/A \widehat{w} d\widehat{\mu} = \lambda \varphi^{i}, \tag{D.6}$$

which means that

$$AD^2 \int_\Omega \widetilde{R}^i_{\hat{j}} \underbrace{\widetilde{U}_c \widehat{\widetilde{U}}_c}_{\frac{A^4B^2M_0}{(\widehat{\delta\delta})^2}} e^{2\hat{\xi}} \varphi^{\hat{j}} \underbrace{\hat{\delta}^3}_{A^3D^3e^{3\hat{\xi}}} \widehat{\eta}\widehat{w} d\widehat{\mu} = \lambda \varphi^i. \tag{D.7}$$

Note that

$$\left(\delta\widehat{\delta}\right)^{-2} = A^{-4}D^{-4}e^{-2\xi}e^{-2\hat{\xi}}, \tag{D.8}$$

which means that

$$AD^2 \int_\Omega \widetilde{R}^i_{\hat{j}} \frac{A^4B^2M_0}{(\delta\widehat{\delta})^2} e^{2\hat{\xi}} \varphi^{\hat{j}} \hat{\delta}^3 \widehat{\eta}\widehat{w} d\widehat{\mu} = \lambda \varphi^i, \tag{D.9}$$

and after canceling out terms we have

$$A^4B^2DM_0 \int_\Omega \widetilde{R}^i_{\hat{j}} \varphi^{\hat{j}} \frac{e^{3\hat{\xi}}}{e^{2\xi}} \widehat{\eta}\widehat{w} d\widehat{\mu} = \lambda \varphi^i, \tag{D.10}$$

and finally

$$\int_\Omega \widetilde{R}^i_{\hat{j}} \varphi^{\hat{j}} \frac{e^{3\hat{\xi}}}{e^{2\xi}} \widehat{\eta}\widehat{w} d\widehat{\mu} = \widetilde{\lambda} \varphi^i, \tag{D.11}$$

where

$$\widetilde{\lambda} = \frac{\lambda}{A^4B^2DM_0}. \tag{D.12}$$

By setting $\widehat{w} = e^{-\hat{\xi}}$ and defining $\widetilde{\varphi}^i = e^{2\xi}\varphi^i$ and $\widetilde{\varphi}^{\hat{j}} = e^{2\hat{\xi}}\varphi^{\hat{j}}$, we obtain the final non-dimensionalized expression for the POD integral in similarity coordinates

$$\int_\Omega \widetilde{R}^i_{\hat{j}} \widetilde{\varphi}^{\hat{j}} \widehat{\eta} d\widehat{\mu} = \widetilde{\lambda} \widetilde{\varphi}^i. \tag{D.13}$$

Bibliography

Aris, Rutherford (1962). *Vectors, Tensors, and the Basic Equations of Fluid Mechanics*. New York: Dover Publications, Inc. New York.

Buchhave, Preben and Clara M. Velte (2017). "Measurement of turbulent spatial structure and kinetic energy spectrum by exact temporal-to-spatial mapping". In: *Physics of Fluids* 29.8, p. 085109. ISSN: 1070-6631. DOI: 10.1063/1.4999102. URL: http://aip.scitation.org/doi/10.1063/1.4999102.

Champagne, F H (1978). "The fine-scale structure of the turbulent velocity field". In: *Journal of Fluid Mechanics* 86.1, pp. 67–108. ISSN: 0022-1120. DOI: 10.1017/S0022112078001019.

Champagne, F. H., C. A. Friehe, and J. C. LaRue (1977). "Flux Measurements, Flux Estimation Techniques, and Fine-Scale Turbulence Measurements in the Unstable Surface Layer Over Land". In: *Journal of the Atmospheric Sciences* 34.3, pp. 515–530.

Christensen, Ole (2010). *Functions, Spaces, and Expansions*. ISBN: 978-0-8176-4979-1. DOI: 10.1007/978-0-8176-4980-7. arXiv: arXiv:1011.1669v3. URL: http://link.springer.com/10.1007/978-0-8176-4980-7.

Citriniti, J. H. and W. K. George (2000). "Reconstruction of the global velocity field in the axisymmetric mixing layer utilizing the proper orthogonal decomposition". In: *Journal of Fluid Mechanics* 418, pp. 137–166.

Corrsin, Stanley and Alan L. Kistler (1955). *Free-Stream Boudaries of Turbulent Flows*. Tech. rep.

Dirac, Paul Adrien Maurice (1975). *General Theory of Relativity*. John Wiley & Sons.

Ewing, D (1995). "On Multi-Point Similarity Solutions in Turbulent Free-Shear Flows". Ph.D. dissertation. The State Univeristy of New York at Buffalo, p. 261.

Ewing, D. et al. (2007). "Two-point similarity in the round jet". In: *Journal of Fluid Mechanics* 577, pp. 309–330.

Foucaut, J. M., J. Carlier, and M. Stanislas (2004). "PIV optimization for the study of turbulent flow using spectral analysis". In: *Measurement Science and Technology* 15.6, pp. 1046–1058.

Foucaut, J. M. et al. (2004). "Characterization of different PIV Algorithms Using the EUROPIV Synthetic Image Generator and Real Images From a Turbulent Boundary layer". In: *Proceedings of the EUROPIV*. Vol. 2, pp. 163–185.

Gamard, S. et al. (2002). “Application of a ”slice” proper orthogonal decomposition to the far field of an axisymmetric turbulent jet”. In: *Physics of Fluids* 14.7, pp. 2515–2522.

Gamard, Stephan, Daehan Jung, and William K. George (2004). “Downstream evolution of the most energetic modes in a turbulent axisymmetric jet at high Reynolds number. Part 2. The far-field region”. In: *Journal of Fluid Mechanics* 514, pp. 205–230.

Gel fand, I. M. (1961). *Lectures on Linear algebra*. Interscience publishers inc., New York.

George, W. K. (2013). *Lectures in Turbulence for the 21st Century*.

George, William K. (1989). “The self-preservation of turbulent flows and its relation to initial conditions and coherent structures”. In: *Advances in Turbulence, 3973*.

— (2014). “Reconsidering the ‘ Local Equilibrium ’ hypothesis for small scale turbulence”. In: *Turbulence Colloquium Marseille 2011: Fundamental Problems of Turbulence, 50 Years After the Marseille 1961 Conference. Les Ulis, Fr.: EDP Sci.*

— (2017). “A 50-Year Retrospective and the Future”. In: *Whither Turbulence and Big Data in the 21st Century?* Springer, pp. 13–43.

Glauser, M. N., S. J. Leib, and W. K. George (1987). “Coherent Structures in the Axisymmetric Turbulent Jet Mixing Layer”. In: *Fifth International Symposium on Turbulent Shear Flows*. Springer-Verlag Berlin Heidelberg.

Golub, G. H. and C. F. Van Loan (2013). *Matrix Computations*. Fourth. The Johns Hopkins University Press, p. 780.

Grinfeld, Pavel (2013). *Introduction to Tensor Analysis and the Calculus of Moving Surfaces*.

Hinze, J.O. (1975). *Turbulence*. McGraw-Hill.

Hodzic, Azur (2014). “PIV Measurements on a Turbulent Free Jet - Spatial Decomposition of a Turbulent Free Jet using Proper Orthogonal Decomposition”. Master thesis. Kgs. Lyngby: Technical University of Denmark.

Holmes, P, J.L. Lumley, and G Berkooz (2012). *Turbulence, Coherent Structures, Dynamical Systems and Symmetry*. Second edi. Cambridge University Press.

Hussein, Hussein J. (1991). “Locally axisymmetric turbulence”. In: *Journal of Fluid Mechanics* 233.1, pp. 1–23.

Hussein, Hussein J., Steven P. Capp, and William K. George (1994). “Velocity measurements in a high-Reynolds-number, momentum-conserving, axisymmetric, turbulent jet”. In: *Journal of Fluid Mechanics* 258.1, pp. 31–75.

Iqbal, M. O. and F. O. Thomas (2007). *Coherent structure in a turbulent jet via a vector implementation of the proper orthogonal decomposition*. Vol. 571, pp. 281–326.

Jung, Daehan, Stephan Gamard, and William K. George (2004). "Downstream evolution of the most energetic modes in a turbulent axisymmetric jet at high Reynolds number. Part 1. The near-field region". In: *Journal of Fluid Mechanics* 514, pp. 173–204.

Lax, Peter D. (2007). *Linear Algebra and its Applications*. Second edi. New Jersey.

Leib, SJ, MN Glauser, and WK George (1984). "An application of Lumley's orthogonal decomposition to the axisymmetric turbulent jet mixing layer". In: *Proc. 9th Rolla Symp. on Turbulence in Fluids*. Ed. by X. B. Reed, G. K. Patterson, and J. L. Zakin. University of Missoury, Rolla.

Lumley, J. L. (1965). "Interpretation of Time Spectra Measured in High-Intensity Shear Flows". In: *Physics of Fluids* 8.6, pp. 1056–1062.

— (1967a). "Similarity and the turbulent energy spectrum". In: *Physics of Fluids* 10.4, pp. 855–858. ISSN: 00319171. DOI: 10.1063/1.1762200.

— (1970). *Stochastic tools in turbulence*. Academic, New York.

Lumley, John Leask (1967b). "The structure of inhomogeneous turbulent flows". In: *Atmospheric turbulence and radio wave propagation*. Nauka, Moscow, pp. 166–178.

Muralidhar, Srikanth Derebail et al. (2018). "Spatio-temporal Proper Orthogonal Decomposition of turbulent channel flow". In: *ArXiv* 1805.01494. arXiv: 1805.01494. URL: http://arxiv.org/abs/1805.01494.

Panchapakesan, N. R. and J. L. Lumley (1993a). "Turbulence measurements in axisymmetric jets of air and helium. Part 1. Air jet". In: *Journal of Fluid Mechanics* 246, pp. 197–223.

— (1993b). "Turbulence measurements in axisymmetric jets of air and helium. Part 2. Helium jet". In: *Journal of Fluid Mechanics* 246, pp. 225–247.

Schmidt, Oliver T. et al. (2018). "Spectral analysis of jet turbulence". In: *Journal of Fluid Mechanics* 855, pp. 953–982. ISSN: 0022-1120. DOI: 10.1017/jfm.2018.675. arXiv: 1711.06296. URL: http://arxiv.org/abs/1711.06296.

Tennekes, H. and J. L. Lumley (1972). *A First Course in Turbulence*. Cambridge, Massachusetts: MIT Press.

Tinney, C. E., M. N. Glauser, and L. S. Ukeiley (2008). *Low-dimensional characteristics of a transonic jet. Part 1. Proper orthogonal decomposition*. Vol. 612, pp. 107–141.

Towne, Aaron, Oliver T. Schmidt, and Tim Colonius (2018). "Spectral proper orthogonal decomposition and its relationship to dynamic mode decomposition and resolvent analysis". In: *Journal of Fluid Mechanics* 847, pp. 821–867. ISSN: 14697645. DOI: 10.1017/jfm.2018.283. arXiv: 1708.04393.

Townsend, A. A. (1956). *The structure of turbulent shear flows*. Cambridge: Cambridge University Press.

Truesdell, C. (1953). "The Physical components of vectors and Tensors". In: *ZAMM-Journal of Applied Mathematics and Mechanics/Zeitschrift für Angewandte Mathematik und Mechanik* 33.10.11, pp. 345–356.

Wänström, M (2009). "Spatial decompositions of a fully-developed turbulent round jet sampled with particle image velocimetry". Ph.D. thesis. Chalmers University of Technology. ISBN: 9789173853521. URL: `http://swepub.kb.se/bib/swepub:oai:services.scigloo.org:102284?tab2=abs{\%}7B{\&}{\%}7Dlanguage=en`.

Wänström, M., W. K. George, and K. E. Meyer (2006). "Stereoscopic PIV and POD applied to the far turbulent axisymmetric jet". In: *AIAA 20063368*, pp. 1–14.

— (2009). "Spatial Spectra of Jet Turbulence Measured by Particle Image Velocimetry". In: 3.6, pp. 28–31.

Wanstrom, M. et al. (2007). "Identifying Sources of Errors on Stereoscopic PIV Measurements". In: *5th ASME/JSME 2007 Joint Fluids Engineering Conference*, pp. 987–996.

Wänström, Maja, William K. George, and K.E. Meyer (2012). "Streamwise and Radial Decomposition of a Turbulent Axisymmetric Jet". In: *Progress in Turbulence and Wind Energy IV*. Ed. by Martin Oberlack et al. Springer Berlin Heidelberg, pp. 147–150.

Weyl, H. (1952). *Space - Time - Matter*. Dover Publications, Inc., p. 330.

Wygnanski, I. and H. Fiedler (1969). "Some measurements in the self-preserving jet". In: *Journal of Fluid Mechanics* 38.3, pp. 577–612.